TESIS DE LA UNIVERSIDAD DE ZARAGOZA

2011

37

David Paesa García

Reset observers and temperature control for induction hobs

Departamento

Informática e Ingeniería de Sistemas

Director/es

Sagüés Blázquiz, Carlos

López Nicolás, Gonzalo

ISSN 2254-7606

Prensas de la Universidad Universidad Zaragoza

Universidad Zaragoza
1542

Tesis Doctoral

RESET OBSERVERS AND TEMPERATURE CONTROL FOR INDUCTION HOBS

Autor

David Paesa García

Director/es

Sagüés Blázquiz, Carlos
López Nicolás, Gonzalo

UNIVERSIDAD DE ZARAGOZA

Informática e Ingeniería de Sistemas

2011

PhD Thesis

Reset Observers and Temperature Control for Induction Hobs

David Paesa García
October 2011

Advisors:

Carlos Sagues	Universidad de Zaragoza, Spain
Gonzalo Lopez-Nicolas	Universidad de Zaragoza, Spain

Acknowledgment

Summarizing my last four years in this document has been a tough nut to crack. However, it would be even tougher for me if I unintentionally forget to acknowledge some people who have played (and many of them still do) a key role throughout these years. People mostly from Zaragoza, but also from Murcia, Eindhoven and Manchester where I had the opportunity to meet and work with some of the most outstanding people in their field (whatever the field may be). To avoid that, I would prefer not to highlight any specific person. They already know it, and this is all that matters. Sincerely, thank you all!

Resumen

En la actualidad, la tecnología de calentamiento por inducción se encuentra lo suficientemente consolidada como para que resulte difícil encontrar diferencias notables entre las encimeras de inducción de los distintos fabricantes. Todos ellos presentan modelos con similares características electrónicas: potencia máxima suministrable, número y diámetro de los fuegos, disposición de los mismos, etc. Es por ello, que resulta indispensable encontrar nuevos elementos diferenciadores entre las distintas cocinas, que supongan un progreso en el estado del arte y que resulten en una mejora cualitativa y cuantitativa del sistema.

Con este objetivo, se aborda la ambiciosa tarea de desarrollar una cocina de inducción doméstica que permita al usuario controlar directamente la temperatura del recipiente en lugar de la potencia suministrada al mismo. Controlando correctamente la temperatura del recipiente se aseguran las siguientes ventajas:

- Para el usuario: se aumenta la seguridad, ya que se impide alcanzar temperaturas peligrosas. Se incrementa el rendimiento, ya que se minimiza el consumo de energía. Además se facilita el proceso de cocinado, ya que la propia cocina advierte al usuario cuando el recipiente alcanza la temperatura deseada.

- Para los recipientes: al controlar su temperatura se impide que su recubrimiento antiadherente se estropee, aumentando su durabilidad.

- Para los fabricantes de cocinas domésticas: permite obtener un elemento diferenciador para sus productos frente a sus competidores. Al controlar la temperatura del recipiente, se controla también la temperatura que puede alcanzar la superficie de cocción. Por lo que se podrían emplear materiales de bajo coste como el vidrio templado en lugar de cristal vitrocerámico.

El problema del control de temperatura de recipiente se aborda desde dos puntos de vista. El primero, con un carácter marcadamente teórico,

consiste en el desarrollo de algoritmos de observación que permitan estimar la temperatura de recipiente de la manera más precisa posible. El segundo, basado en una aproximación más práctica y experimental, consiste en el desarrollo de nuevos métodos de sensado que permitan disminuir la incertimbre presente en los sensores de temperatura actualmente empleados.

Inspirados por las excelentes propiedades de los sistemas de reset (en términos de tiempo de respuesta y sobreoscilación), se explora en esta Tesis la aplicabilidad de los sistemas de reset al campo de los observadores. Con este fin, se propone una definición formal de un nuevo tipo de observador: el observador de reset. Posteriormente, se evalúa cuál de las condiciones de reset actualmente presentes en la literatura es más adecuada para esta nueva estructura de observación. Adicionalmente, se estudia la posible generalización del observador de reset para distintas clases de sistemas, por ejemplo, sistemas con retraso, no lineales o sujetos a perturbaciones externas. Es destacable que dicho estudio no está limitado al análisis de estabilidad y convergencia, sino que incluye la síntesis automática de los parámetros del observador de reset.

Antes de comprobar la aplicabilidad de los observadores de reset en el control de tempertura de recipiente, se hace un importante esfuerzo para determinar cuál es el sensor de temperatura más adecuado para cada proceso de cocinado. Con este objetivo, no sólo se desarrollan nuevos sensores de temperatura sino que además cada nueva propuesta se compara con los sensores existentes, en términos de robustez, tiempo de respuesta y coste. Una vez determinados los sensores de temperatura a emplear, se hace un desarrollo experimental para implementar los algoritmos de control y estimación propuestos en cocinas de inducción reales. Finalmente, múltiples resultados experimentales y de aplicación demuestran la aplicabilidad de los observadores de reset para el control de temperatura de recipientes en cocinas de inducción.

En resumen, las principales contribuciones de esta Tesis se engloban en:

- El desarrollo de algoritmos eficientes para el observador de reset que pueden ser empleados para estimar y controlar la temperatura del recipiente. Este nuevo observador, el observador de reset, resulta de la aplicación novedosa de la teoría de sistemas de reset al campo de los observadores, y puede ser extendido a una gran variedad de sistemas. Este trabajo incluye tanto el análisis de estabilidad como la síntesis de los parámetros del observador de reset.

- El desarrollo de tres novedosos sistemas de sensado, que son especialmente adecuados para medir la temperatura del recipiente en cocinas de inducción: los *contact spots*, el *sensor line*, y el sensor magnético. Este trabajo incluye una completa comparación entre estas novedosas propuestas y otros métodos ya existentes, y concluye con la selección

del sensor de temperatura más adecuado para nuestro sistema bajo estudio.

- La aplicación de nuestros resultados teóricos (esto es, los observadores de reset) a una aplicación industrial real. Este trabajo incluye el diseño, ajuste y prueba de los algoritmos de control y estimación propuestos. En concreto, esta Tesis contribuye finalmente con el desarrollo de un control de temperatura de recipiente para cocinas de inducción, el cual es adecuado tanto para procesos con alta carga como para los de poca o nula carga. Además, se ilustra mediante exhaustivos experimentos el rendimiento superior de nuestras contribuciones teóricas, y su aplicabilidad al control de temperatura para cocinas de inducción

Abstract

Nowadays, domestic induction heating technology is quite well consolidated in such a manner that it is difficult to find substantial differences between the induction hobs offered by different manufacturers. All of them present induction hobs with similar features: maximum power, size, shape, etc. For this reason, finding new distinguishing features between them is indispensable to the manufacturers.

To this end, we consider as the main objective of this work the development of a pot temperature control for domestic induction hobs, which allows the user to directly control the temperature of the cooking pot rather than the supplied power as standard hobs do. Several advantages are obtained by a proper control of the cooking pot temperature:

- For the user: resultant system is safer and more reliable because dangerously high temperatures are avoided. Overall performance is higher because energy consumption is minimized. It simplifies the cooking process, due to the fact that the hob itself informs the user when the cooking pot reaches the desired temperature.

- For the cooking pot: by controlling its temperature, its nonstick surface cannot be damaged, which increases its durability in the long term.

- For the manufacturers: they obtain distinguishing features with respect to competitors. Moreover, by controlling the cooking pot temperature, the temperature of the cooking surface is under control as well. Therefore, new materials with less demanding thermal properties but considerably cheaper than glass ceramic could be used instead.

Issues concerning cooking pot temperature control are addressed from two standpoints. The first, based on a theoretical perspective, will consist in the development of observation algorithms that allow an accurate estimation of the cooking pot temperature. The second, based on a more practical and

experimental focus, will consist in the design of novel sensing methods that outperform the currently used temperature sensors.

Inspired by the excellent features of reset systems in terms of transient response and lack of overshooting, we will explore throughout this Thesis the applicability of reset systems to the observer framework. To this end, a formal definition of a new sort of observer, the reset observer, will be proposed. The influence of the different reset conditions on the reset observer structure will be studied as well. Additionally, the reset observer formulation will be extended to different sorts of systems, including time-delay systems, non-linear systems, and systems affected by external disturbances. It is worth noting that we will consider not only stability and convergence analysis but also the observer's parameter synthesis.

Before checking the applicability of reset observers in controlling the cooking pot temperature, a significant effort will be made to determine what temperature sensor is more suitable depending on the load of the cooking process. To this end, novel temperature sensors will be developed, and their performance will be compared with the existing ones in terms of robustness, time response and cost. Once this task is done, the proposed control and estimation algorithms will be implemented in actual induction hobs. Finally, exhaustive experimental and application tests will be carried out in order to show the applicability of reset observers for controlling the cooking pot temperature in induction hobs.

Specifically, the main contributions of this Thesis are:

- The development of more efficient algorithms for the reset observer that can be used for estimating and controlling the cooking pot temperature. This new observer, the reset observer, results from the novel application of the reset theory to the observer framework, and can be applied to a wide class of systems. This work includes both, stability analysis and reset observer's parameter synthesis.

- The development of three novel sensing devices specially suitable for measuring the cooking pot temperature in induction hobs: the contact spots, the sensor line and the magnetic sensor. This work includes a complete comparison between these novel proposals and other existing methods so that the most suitable temperature sensor for the system under study can be determined.

- The application of our theoretical results (i.e. the reset observers) to a real industrial application, including the design, tuning, and testing of the proposed control-estimation algorithms. Specifically, this Thesis finally contributes with the development of a temperature cooking pot control for induction hobs that is suitable for high and low load cooking processes. Besides, this Thesis shows by exhaustive experiments the superior performance of our theoretical contributions, and

their applicability to the cooking pot temperature control for induction hobs.

Contents

Table of Acronyms

AO	Adaptive observer
BIBO	Bounded input bounded output
CI	Clegg Integrator
CQLF	Common quadratic Lyapunov function
DO	Disturbance observer
FORE	First order reset element
LMI	Linear matrix inequality
LTI	Linear time invariant
LMIP	Linear matrix inequality problem
MIMO	Multiple input multiple output
NTC	Negative Temperature Coefficient
PTC	Positive Temperature Coefficient
PI	Proportional integral
PO	Proportional observer
PIO	Proportional integral observer
PIAO	Proportional integral adaptive observer
RAO	Robust adaptive observer
ReO	Reset observer
ReAO	Reset adaptive observer
ReDO	Reset disturbance observer
RTD	Resistance temperature detector (in Chapter 2)
	Reset time dependent (otherwise)
RTI	Reset time independent
SISO	Single input single output

Part I

Introduction

Chapter 1

Introduction

1.1 Domestic Induction Cookers

Induction heating is the process of heating electrically conducting objects (generally made of metal) by electromagnetic induction. According to Faraday's law, a voltage is induced in a conductor loop if it is subjected to a time-varying magnetic flux which equation is as follows

$$\epsilon = -\frac{d\phi}{dt} \tag{1.1}$$

where ϵ is the induced voltage and ϕ is the time-varying magnetic flux. As result of this phenomenon, a current flows in the conductor if there exists a closed path.

Induction heating is based on two physical phenomena: induced currents and magnetic hysteresis. On the one hand, when a conducting body instead of a conductor loop is subjected to a time-varying magnetic field, voltages are similarly induced in this body, which consequently generate currents circulating through the conductor [1]. These induced currents (generally called eddy currents or Foucault currents) lead to Joule heating of the conductor itself (see Fig. 1.1). On the other hand, when an external magnetic field is applied to a ferromagnetic body, the atomic dipoles align themselves with the external field, which results in additional energy losses that finally lead to heating. These changes on the alignment of the atomic dipoles can be modeled by a magnetic hysteresis loop, whose width describes the amount of energy losses [2].

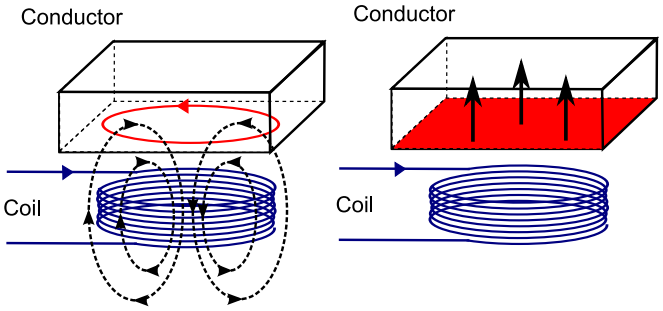

Figure 1.1: Generation of eddy currents in a conductor subjected to a time-varying magnetic field (left picture). Heat generated by Joule heating is transmitted upwards through the conductor itself (right picture).

Induction heating has been successfully applied to a wide variety of applications (Fig. 1.2). They are mostly related to industry processes such as surface hardening [3], [4], melting [5], and soldering [6]. Besides, induction heating has been also applied to household processes. Among them, domestic induction cookers stand out as the most important application of the induction heating phenomena [7].

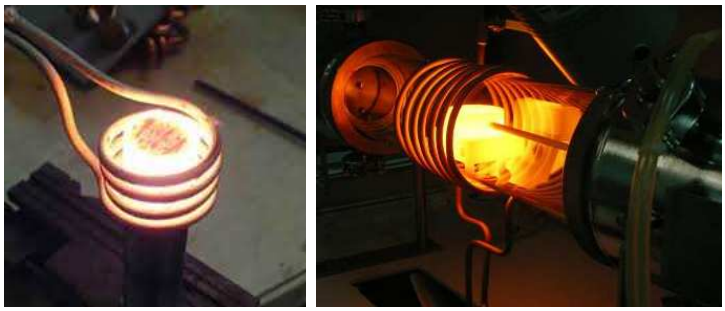

Figure 1.2: Induction heating applications.

Induction cooker is the domestic application of the induction heating phenomena. It basically consists of a cooking surface, an induction coil, and an inverter topology as it is depicted in Fig. 1.3. Induction coil is mounted underneath the cooking surface, and it is fed with a high-frequency current generated by the inverter topology. The current creates an alternating magnetic field. When a ferromagnetic pot is brought close to the cooking surface, the magnetic field induces an electrical current in the pot [1]. The eddy current, flowing through the pot, which behaves as an electrical resistance, causes electrical power to be dissipated as heat, and then the pot gets hot and heats its content by heat conduction [8].

Figure 1.3: Arrangement of an induction hob.

An induction cooker is faster, easier to clean and more energy-efficient than a traditional electric hob. For these reasons, they have become increas-

ingly popular lately. One of its main features is that it allows instant control of cooking energy similar to gas burners. Because induction heats directly the cooking vessel itself, the possibility of burn injury is significantly less than with other methods. The cooking surface is only heated from contact with the vessel, unlike other methods (e.g. traditional electric hobs) which have to heat up the cooking surface before being capable of heating the cooking pan itself.

Main blocks of a domestic induction hob are depicted in Fig. 1.4. Firstly, hob takes the energy from the mains voltage, and then, an electromagnetic compatibility filter removes the voltage disturbances. After that, the voltage is subsequently rectified by a full bridge of diodes to generate a DC (Direct Current) bus. Then, the inverter topology provides to the induction coil the high-frequency current needed to heat up the cooking pot. Finally, the power supplied is controlled modifying the working frequency of the inverter depending on the modulation strategy.

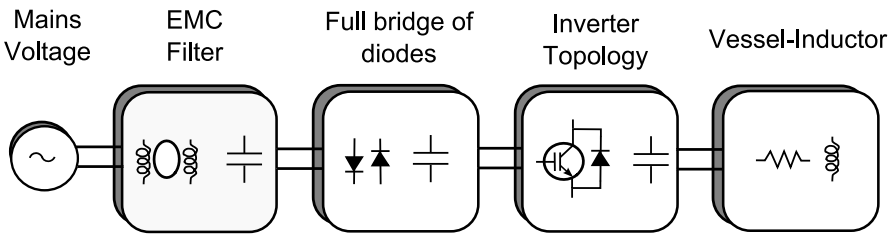

Figure 1.4: Main blocks of an induction hob.

Typically, the energy saving and efficiency on domestic induction hobs has been restricted to the development of highly efficient resonant inverter topologies, modulation strategies, and inductors.

Some relevant contributions on inverter topologies are [9] and [10]. In the former, an in-depth study of the different inverter topologies is carried out. There, the authors underline the weakness and strengths of each topology. In the latter, an upgraded full-bridge inverter with two outputs is proposed. This concept was also applied to the half-bridge inverter. The main contribution of that work is to present a cost-effective proposal that provides new benefits as a quick heating function with an optimal utilization of electronics. Currently, most domestic induction hobs are based on this inverter topology.

As it has been outlined before, the objective of the modulation strategies is to control the delivered power. Typically, it is ranged between 30 W to 3.3 kW. In a series resonant load, supplied power can be controlled by modifying the working frequency of the inverter. The higher the working frequency is, the lesser the power is delivered. Traditional modulation strategies used in domestic induction hobs are the Square Wave (SW) control and the Asymmetrical Duty Cycle (ADC) control [11]. The main drawback of

these controls is their efficiency at the low power range. Since the switching frequency is increased when output power is decreased, the efficiency working at the low power range will be lower than working at the high power range. To overcome this limitation, different novel modulation strategies have been proposed. The Pulse Density Modulation (PDM) strategy tackles this issue varying the intervals in which the current is supplied into the inductors [12]. Another relevant strategy is the Discontinuous Mode Control (DMC) which is based on forcing discontinuous mode that permits to switch at low frequencies controlling the delivered power at the low range [13].

Induction coil is designed to transfer the electrical power delivered by the inverter topology into the pot through a magnetic coupling. The windings for domestic induction heating must fulfill several conditions such as size restrictions, power ratings, and high efficiency in the transmission of the electromagnetic energy. An analytical model of the equivalent impedance of the simpler planar induction system was presented in [14]. This kind of analytical models represents a powerful tool in order to design inductors because it can be used to analyze the magnetic coupling between the pot and the inductor. Another relevant work is [15], where the effect of the temperature on the coupled inductor-pot system is studied in depth.

1.2 Motivation of Pot Temperature Control

From the customer point of view, current induction hobs can be represented by the control scheme depicted in Fig. 1.5. Customer selects the target power of the cooker by using the user interface (e.g. knobs) and the microcontroller automatically modifies the working frequency in such a manner that the power supplied by the inductor and the power desired by the customer are the same. Nonetheless, since the customer does not know how high the temperature of the pot is, he has to modify the target power according to his experience in order to avoid dangerous temperatures. Therefore, cooking results are typically dependent on the cooking skills of the customer.

Some of the problems that usually arise from control schemes based on target power are shown in Fig. 1.6. For instance, too high temperature can damage the nonstick surface of the cooking pan, burn the food, and even worse, cause kitchen fires. These situations take place more often that people might think. In particular, according to [16], in 2005 there were 11000 chip pan fires causing 4000 injuries and 30 fatalities only in United Kingdom. All these dramatic situations could have been avoided by means of a temperature control of the cooking pan, given that the cooker itself would have automatically cut off the power if the pan temperature had been too high.

Additionally, control schemes based on target power have more draw-

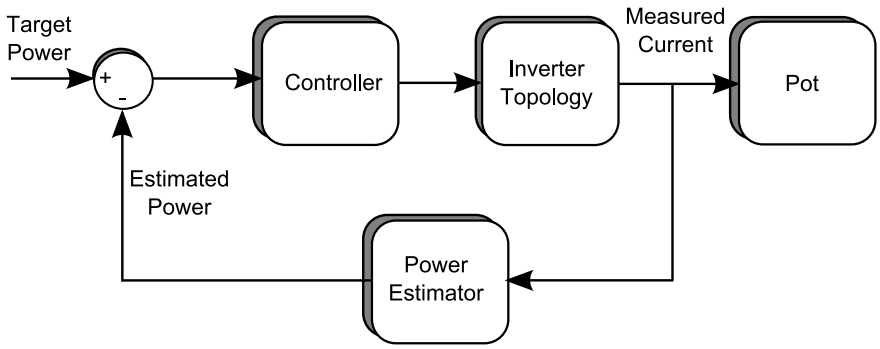

Figure 1.5: Control scheme based on target power.

Figure 1.6: Dangerous situations related to control schemes based on target power.

backs, because with this sort of hobs, customers are prone to use more power that the cooking process actually needs. This waste of energy highly decreases the efficiency of the whole cooking process, although the efficiency of the power electronics is actually very high. Therefore, an improvement in the efficiency during the whole cooking process could be achieved by means of a pot temperature control. As it is shown in Fig. 1.7, the customer directly selects the target temperature and the microcontroller computes how much power is needed so that the temperature of the pot tends to the target temperature.

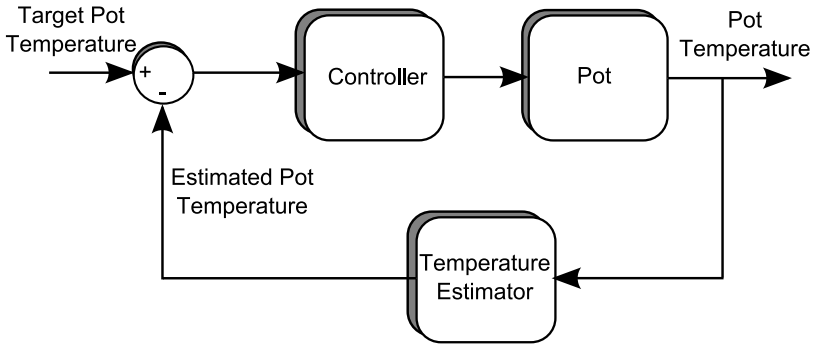

Figure 1.7: Control scheme based on target temperature.

Besides the efficiency improvement, we point out more advantages. For instance, pot temperature control ensures a correct food cooking. Long overshoot might burn the food and long undershoot either increases cooking time, or causes underdone food. Therefore, accurate pot temperature control is very interesting for the users and for the hob manufacturers. A comparison between both approaches is depicted in Fig. 1.8.

Figure 1.8: Comparison between control schemes based on target power and target temperature.

1.3 Research Topics in Pot Temperature Control

From the research point of view, developing a temperature control for an induction hob is interesting and challenging. There is a large number of different pots. Each one has different thermal and physical properties, for instance: diameter, weight, height, concavity and thickness. Since the heat transmission is highly dependent on these parameters, the whole hob-pot system can be understood as a system whose parameters are highly time variant and uncertain. Notice that, existing temperature sensors are mostly situated underneath the cooking surface. Therefore, there is also a huge uncertainty introduced by the indirect measurements of the pot temperature. The contact surface between the pot and the ceramic glass may have some air gap or some food particles that make the measured temperature very imprecise.

Approaches to achieve a reliable temperature control for uncertain industrial application have been traditionally based on improving the used temperature sensors or developing more effective control and/or estimation algorithms. For this reason, we outline here the most feasible approaches

that could be applied to our specific problem.

- Developing new and improved sensing devices. In this case the approach would rely on developing new sensors that provide enhanced measurements in order to decrease the uncertainty of the process. Currently, some induction hobs include a retractable infrared sensor, which is more suitable for high load cooking processes, and two thermistors beneath the glass-ceramic, which are more suitable for low load cooking processes. As a matter of fact, the feasibility of infrared sensors for temperature control of liquids in radiant hobs has already been proved in [17], but it remains to prove whether that promising results can be extended to induction hobs.

  However, there exist no results concerning the feasibility of using NTC-thermistor for controlling low load cooking processes. Despite the fact that some work has been done towards that direction, current results are limited to the development of calibration modes [18]. They basically consist of a two-stage process, first, a predetermined power step is supplied to the cooking pot so that the induction hob's microcontroller can approximately identify the cooking pot thermal parameters, and stored these parameters in the microcontroller's memory. Afterwards, the customer has to inform to the induction hob that the cooking pot to be used has already been identified, in such a manner that the microcontroller uses the previously stored thermal parameters to estimate and control the cooking pot bottom temperature. However, this approach is somewhat bothersome from the customer point of view, and an automatic method to estimate and control the temperature without requiring any previous calibration would be preferable.

  Unfortunately, addressing this issue is far from trivial. As far as the temperature control for domestic cookers is concerned, the uncertainty of the heat transmission from the inductor to the pot, and from the pot to the contact temperature sensors situated underneath of the cooking surface is too high. Moreover, current induction hobs' construction impedes us from measuring where we intended, that is, closer to the cooking pot itself. Therefore, an intuitive approach to minimize the existing uncertainty could be to modify the lay-out of the current temperature sensors.

  Additionally, measurements from different thermal sensors could be combined in order to obtain a more accurate temperature measurement. In theory, by combining the measurements from different sources, the resulting information is in some sense better than the one that would be obtained when these sources were used individually. As a matter of fact the idea of sensor fusion has been extensively used in other fields such as robotics [19] and mechatronics [20].

- Using robust control techniques. There, the aim is to design robust controllers which guarantee the stability of the whole system and meet all the control requirements for all the range of uncertainty of the parameters. Therefore, the obtained controller guarantees the stability of the whole system and meets all the control requirements for all the range of uncertainty of the parameters. The most popular robust control techniques are QFT and H_∞.

  QFT is a robust control technique, which works in the frequency domain, that is especially well suited for control problems with large plant uncertainty [21], [22], [23]. An in-depth survey of QFT for nonlinear systems can be found in [24]. The first step in QFT design is to translate the system uncertainty to frequency domain. For this purpose, the frequency responses of all possible combinations of system parameters are represented in a Nichols chart. Each point plotted represents a possible plant or sensor for a given frequency. Therefore all these points define a region of the uncertainty of the system at the different working frequencies. These regions are known as templates. Afterwards, control requirements have to be translated into boundaries in a Nichols chart. In QFT, each closed-loop specification, such as robust stability, tracking ability and disturbance rejection, generates a boundary. If the nominal open loop gain avoids the boundaries, it is guaranteed that the closed loop specifications are satisfied for all the plants considered in the template. Once the boundaries are computed, the final design step is to compute the open loop gain that fits them in some optimal way. This process is known as loop-shaping and generates directly the robust feedback compensator. Notice that this process is not straightforward and generally it is done heuristically.

  Robust stability or performance objectives can all be formulated as gain attenuation problems with respect to the dynamical or parametric uncertainty. H_∞ control is the cornerstone of the design techniques for this class of problems [25], [26], [27]. The H_∞ approach is based on the computation of some norms by solving linear matrix inequalities [28]. Specifically, the H_∞ norm of a system is defined as its largest input/output RMS (Root Mean Square) gain, which can be interpreted as minimization of the effect of the worst-case disturbance input on the output. Therefore it can be used to address robust stability and performance issues.

  However, robust control techniques such as QFT or H_∞ are somewhat conservative, due to the fact that the resultant controller has to be designed to meet control requirements, for the worst-case behavior between all the considered operation points (i.e. for all the uncertainty of the system). Therefore we could obtain a better performance, if we were able to reduce the uncertainty of the parameters of the cooking

process somehow.

- Using adaptive observers. Here, the idea is to design some sort of recursive algorithm to estimate on-line the state as well as the unknown parameters of a system from the measurements of the system. Observers can be classified according to the sort of representation for the plant to be observed. If the plant is considered to be deterministic, then the observer is a deterministic observer. Otherwise, it is a stochastic observer. Two estimation algorithms that clearly stand out among the others are the seminal works by Kalman in [29] and Luenberger in [30], [31], which are the most popular observers for stochastic and deterministic systems respectively.

  In 1960, R.E. Kalman published his famous paper describing a recursive solution to the discrete-data linear filtering problem [29]. The Kalman filter consists in a set of mathematical equations that provides an efficient computational recursive algorithm to estimate the state of a linear Gaussian stochastic process, in a way that minimizes the mean of the squared error. The Kalman filter averages a prediction of the state variables with a new measurement using a weighted average, which is calculated from their covariances. Its nonlinear version is the Extended Kalman filter which linearizes about the current mean and covariance. Since that time, the Kalman filter has been a topic of extensive research and application, particularly in the area of autonomous or assisted navigation [32] and tracking applications [33].

  In a similar way, a Luenberger observer is a recursive mathematical structure to estimate the state of a linear deterministic process. It combines sensor output and plant input signals with models of both, the plant and sensor to generate a feedback signal that is superior to the sensor output alone. Although it was initially proposed for linear systems, it was quickly extended to the nonlinear framework [34]. Luenberger observers have also been widely studied during the past decades, particularly for fault detection and adaptive control in industrial applications [35]. Its simplicity and ease of tuning might give some advantage over Kalman filters, specially for nonlinear systems [36]. Nonetheless, as it has been pointed out before, determining when to use each type of observer depends on the probabilistic nature of the system to be observed.

  All those works were characterized by having only a proportional feedback term of the output observation error in both state observer and parameter adaptation law. This proportional approach ensures a bounded estimation of the state and the unknown parameter, assuming a persistent excitation condition as well as the lack of disturbances. The performance of proportional adaptive observers was improved by

adding an integral term to the adaptive laws, [37], [38], [39]. This additional term can increase the steady state accuracy and improve the robustness against modeling errors and disturbances.

However, since the adaptive laws are still linear, they have the inherent limitations of linear feedback control. Namely, they cannot decrease the settling time and the overshoot of the estimation process simultaneously. Therefore, a trade-off between both requirements is needed. Nevertheless, this limitation can be solved by adding a reset element. A reset element consists of an integrator and a reset law that resets the output of the integrator as long as the reset condition holds. Reset elements were introduced by Clegg in 1958 [40], who proposed an integrator which was reset to zero when its input is zero.

During the last years, the research on the stability analysis and switching stabilization for reset systems has been attracting the attention of many academics and engineers (see, for instance, [41], [42], [43]). However, this research has been mainly focused on control issues. According to the author's knowledge the first and unique attempt of applying reset elements within state observer framework is [44]. There, the authors developed a state estimator for tracking control of linear motors. They proposed to reset the state of the estimator to reject the quantification noise caused by the optical encoder which measures the current position. However, its design lacks generality and it can only be applied to this specific problem, because its reset condition relies on the idea that the actual position is known exactly at the mid-point of two consecutive quantizer levels when the quantized measurement changes the quantization level. This work points out the potential benefits of using reset elements for estimation problems, but also the need of a more formal and general definition of reset observes.

1.4 Objectives of this Thesis

In the context of the domestic induction hobs and considering their relevance for researchers, users and home appliance manufacturers, we consider as the main objective of this research the development of a pot temperature control for domestic induction hobs.

As said above, there exist a large number of different pots with different sort of constructions, thermal and physical properties. Due to the fact that the heat transmission is highly dependent on these parameters, the problem of designing a cooking pot temperature control for induction hobs can be regarded as the development of a control-observation strategy for a highly uncertain system. As it has been underlined above, the three main topics to be studied in these kinds of systems consists in developing new temperature sensors, using robust control techniques and using adaptive observers.

Therefore, these three topics will be the cornerstone of this research. Let us outline the more important aspects to be developed in each approach.

- Regarding the methods based on improving the temperature sensors, the research will be focused on decreasing the uncertainty of the sensing devices. Different possibilities that could be studied are: modifying the hob surface in order to remove the uncertainty caused by the concavity of the pot, combining several sensors based on different technologies (for instance, contact and non-contact sensors) and/or modifying the current layout of the sensors situated inside the hob.

- Additionally, an important effort will be made on the research on observers. This approach seems to be the best suited to cope with systems whose parameters are highly uncertain. Some modifications of the adaptive observer algorithm will be studied to improve its performance. In particular, the reset element theory will be applied to the adaptive laws in order to decrease the convergence time. However, these new proposals should be formulated in such a way that a robust behavior against disturbances is guaranteed.

- Finally, robust control techniques will be used as a benchmark to compare with. As a matter of fact, throughout this Thesis most of the results obtained with other approaches will be compared with the ones obtained by some sort of robust controller in order to demonstrate the effectiveness of our proposals.

1.5 Thesis Outline

The contents of this Thesis are organized as commented in the following.

In Chapter 1, the importance from the academic and industrial point of view of temperature control in home appliances has been shown. Due to the growing popularity of induction hobs and their relevance in the domestic cooker market, they will be used as a benchmark in which designed control-estimation algorithms will be implemented.

In Chapter 2, an in-depth study of the state of the art literature in topics of interest for this work is carried out. Due to the deterministic nature of the system under study, we will put more emphasis on the evolution over the years of the deterministic observers, analyzing the purposes they are designed for and their close relation to different control techniques. Moreover, an additional effort will be made on exploring the most cutting-edge works within the hybrid system framework, paying special attention to reset systems. Finally, this chapter also explores the different strengths and weakness of existing temperature sensors that can be used for cooking pot temperature control.

In Chapter 3, we will explore the applicability of the reset control theory, which is one of the most promising recent control techniques, to the observer framework. The contributions presented in this chapter include its formulation for linear systems, which was presented in [45], the effect of the reset condition chosen (i.e. sector reset condition, zero reset condition), which was partially presented in [46], and different stability analysis approaches depending on whether the reset instants are known a priori (reset-time dependent) or not (reset-time independent), which was presented in [47].

These results are extended in Chapter 4, wherein different extensions that could be done for different specific sorts of systems are studied. In particular, this chapter includes the formulation of reset observers for time delay systems, which was proposed in [46], and for systems affected by unknown disturbances, resulting in a reset observer that jointly estimates state and external disturbances.

Furthermore, the generalization of the reset observer for a class of nonlinear systems, which has been presented in [48], is outlined in Chapter 5. This chapter also includes a method to automatically determine the optimal reset observer's tuning parameters for the two most popular reset conditions within the reset time independent framework, which was presented in [49]. This proposal tackles and solves the main drawback of the reset elements which can decrease the observer performance or even destabilize the estimation process if the reset observer parameters are not properly chosen.

In Chapter 6, novel temperature sensor and modifications on their distribution that result in better sensing elements will be proposed as a contribution. In particular, this chapter includes a modification of the cooking surface that minimizes the dependence on the cooking pot bottom concavity, and results in a much more accurate and robust temperature sensor, which was presented in [50]. Moreover, based on the fact that there always exists a point along the inductor radius where the effect of the cooking pot concavity is minimum, this chapter also includes a different lay-out for the current thermistors, which was proposed in [51]. The additional thermistors intelligently distributed forming a straight line along the inductor's radius guarantee that at least one would be located below the point where the air gap is minimum, independently of the cooking pot position, which reduces the sensing time constant and increases the robustness of the sensing system. The last contribution of this chapter is a novel temperature sensor based on measuring the variation of the impedance of the inductor itself when the temperature of the cooking pot changes, and hence, it does not require any additional devices or modifications. This idea was presented in [52], [53].

Implementation details of the developed control-estimation algorithms for cooking pot temperature control will be given in Chapter 7. They will fall into two groups, depending on the sensor used and the type of cooking process they are designed for. On the one hand, regarding cooking temperature control in processes with high load, which will rely on a retractable

infrared sensor, an adaptive simmering control for induction cookers, whose parameters are updated on-line depending on the estimates provided by a Multiple-Model Reset Observer (MMReO), will be presented. Furthermore, we will also design a fixed robust QFT-based controller for comparison purposes, which is a control technique widely applied to industrial applications. These results have already been presented in [54], [55]. On the other hand, regarding cooking temperature control in processes with low load, which will be based on a thermistor-based approach, an adaptive MMReO-based controller, will be presented. In a similar way, a PI controller with a non-adaptive observer will be also designed for comparison purposes. In this case, related results were published in [56].

Exhaustive experimental results of the control-estimation algorithms proposed in Chapter 7 will be presented in Chapter 8. An actual induction hob will be used as a benchmark, where our proposals will be implemented, tested and compared so that the excellent features of reset observers applied to process control could be better understood. In particular, laboratory tests as well as application tests with different kinds of foods will be considered.

Concluding remarks obtained from this Thesis will be drawn in Chapter 9. Moreover, promising new research lines that emerge from this work will be outlined as well. Additionally, this Thesis includes some appendixes that will be helpful to better understand and clarify some parts of this work. Specifically, in Appendix A, we generalize the method to choose a fixed reset time interval for ReO presented in Chapter 3, to any sort of reset systems, which includes not only reset observers but also reset controllers. In Appendix B, a state space model for the system induction hob-cooking pot is presented. It considers all the heat fluxes that might take place in a cooking process, and it is characterized for the temperature sensors used.

1.6 Project Framework, Contributions and Publications

The work of this Thesis has been developed within the Computer Science and Systems Engineering Department of the University of Zaragoza, in the framework of the collaborative agreement between the University of Zaragoza and Bosch-Siemens Household Appliances's center of competence for induction hobs. Despite the fact that most part of this research has been done in the University of Zaragoza and the Research and Development Laboratory of this company, some contributions of this Thesis have been resulted from the stays at the University of Murcia in Spain, the University of Eindhoven in the Netherlands, and the University of Manchester in United Kingdom.

Contributions of this Thesis can be ordered in two groups, depending on their theoretical or practical interest.

On the one hand, due to the key role that observers can play in the cooking pot temperature control for induction hobs, an important effort has been made on developing a formal definition for a novel sort of observer, the reset observer, which could outperform existing solutions:

- Specifically, in this work we explore whether the promising features of reset controllers, (i.e. quick transient response without overshooting) can be extended to the observer framework. Regarding this topic, this work contributes with a formal definition for reset observers, which can easily consider all the existing reset conditions presented in the literature. Moreover, an in-depth study and comparison of the different reset conditions is carried out as well, in order to determine what reset condition is more suitable for the reset observer structure. Another contribution of this work is the generalization of our proposed observer for a wider class of systems such as time-delay or nonlinear. In all the cases, stability and convergence analysis is addressed.

- Unlike most of the works within the reset system framework, which only consider stability analysis, this thesis contributes with both stability analysis and observer parameter synthesis. Thus, due to the potential dangerous effect of external disturbances, which can deteriorate the behavior of reset systems, and the importance of the tuning parameters, which can decrease the performance or even destabilize the system if they are not properly chosen, this Thesis also contributes with a method to automatically determine the optimal reset observer tuning parameters by minimizing the effect of the external disturbances on the estimation error. According to the author's knowledge, this contribution can be regarded as the first result about optimal synthesis within the time independent reset system framework.

On the other hand, an analogue effort has been made to guarantee the applicability of our theoretical work to its final application: the cooking pot temperature control for induction hobs:

- Regarding this topic, this work contributes with several novel sensing methods, which outperform the current thermistor-based solution used in induction hobs. Specifically, three new proposals have been presented: the contact spots, which minimizes the effect of the air gap between the cooking pot bottom and the thermistors by introducing at least three concave deformations over the glass-ceramic, resulting in significantly better heat transmission; the sensor line, which reduces the influence of the relative position between the cooking pot and the thermistors by distributing additional thermistors forming a straight line along the inductor radius, resulting in a considerably more robust sensing system; and the magnetic sensors, which estimates the changes

of the temperature of the cooking pot by analyzing the changes of the magnetic and electrical properties of the cooking pot measured by the inductor itself, resulting in an almost instantaneous temperature sensor.

- The last contribution of this work is the application of our theoretical results to a real industrial application. As a matter of fact, the design, tuning, implementation and testing of the proposed control-estimation algorithms is a challenging task and it is an important contribution by itself. Specifically, this Thesis finally contributes with the development of a temperature cooking pot control for induction hobs that is suitable for high and low load cooking processes, and shows by exhaustive experiments the superior performance of our theoretical contributions, and their applicability to the cooking pot temperature control for induction hobs.

Finally, in order to support the results and contributions obtained during this Thesis, most of the work has been submitted for publication to prestigious journals [56], [57], [55], [49], [48] and international peer reviewed conferences [45], [58], [54], [59], [47], [46] in the field of automatic control and system engineering. Additionally, some new ideas have been patented when it has been convenient [18], [50], [60], [51], [61], [52]. Finally, it is also worth mentioning that most of the results presented in this Thesis were included in [62], the proposal that was awarded with the first prize in the category *2009 Innovation in the Industry Award for Research Groups* from the University of Zaragoza and Bosch-Siemens Household Appliances.

In particular, the following results have been obtained from this Thesis.

Journals

D. Paesa, C. Franco, S. Llorente, G. Lopez-Nicolas, and C. Sagues. Reset Adaptive Observer for a Class of Nonlinear Systems. *IEEE Trans. on Automatic Control*, (Accepted, doi 10.1109/TAC.2011.2164819).

D. Paesa, A. Baños, and C. Sagues. Optimal Reset Adaptive Observer Design. *Systems and Control Letters*, 60(10):877–883, 2011.

D. Paesa, C. Franco, S. Llorente, G. Lopez-Nicolas, and C. Sagues. Adaptive Simmering Control for Domestic Induction Cookers. *IEEE Trans. on Industry Applications*, 47(5):2257–2267, 2011.

D. Paesa, C. Franco, S. Llorente, G. Lopez-Nicolas, and C. Sagues. Reset Observers Applied to MIMO Systems. *Journal of Process Control*, 21(4):613–619, 2011.

D. Paesa, S. Llorente, C. Sagues, and O. Aldana. Adaptive Observers

Applied to Pan Temperature Control of Induction Hobs. *IEEE Trans. on Industry Applications*, 45(3):1116–1125, 2009.

International Peer Reviewed Conferences

D. Paesa, A. Baños, and C. Sagues. Reset Observers for Linear Time-Delay Systems. A Delay-Independent Approach. *In Proc. of the IEEE Conference on Decision and Control*, 2011, (Accepted).

D. Paesa, J. Carrasco, and C. Sagues. On the Design of Reset Systems With Unstable Base: a Fixed Reset-Time Approach. *In Proc. of the 37th Annual Conference of the IEEE Industrial Electronics Society*, 2011, (Accepted).

D. Paesa, C. Franco, S. Llorente, G. Lopez-Nicolas, and C. Sagues. QFT-based robust simmering control for domestic induction cookers using an infrared sensor. *In Proc. of the 45th IEEE Industry Applications Society Annual Meeting*, pages 1–6, 2010.

D. Paesa, C. Franco, S. Llorente, G. Lopez-Nicolas, and C. Sagues. On robust PI adaptive observers for nonlinear uncertain systems with bounded disturbances. *In Proc. of the IEEE Mediterranean Control Conference*, pages 1031–1036, 2010.

D. Paesa, C. Franco, S. Llorente, G. Lopez-Nicolas, and C. Sagues. *Reset adaptive observers and stability properties*. In Proc. of the IEEE Mediterranean Control Conference, pages 1435–1440, 2010.

C. Franco, D. Paesa, C. Sagues, and S. Llorente. *Analytical modeling of a saucepan in an induction hob*. In Proc. of the IEEE Mediterranean Control Conference, pages 298–303, 2010.

Patents (Authors in alphabetic order)

C. Franco, S. Llorente, D. Paesa, and C. Sagues. *Cooking device*. EP2339893. 2011.

M. Almolda, C. Franco, S. Llorente, D. Paesa, and C. Sagues. *Heating zone for a domestic appliance for preparing food*. EP2328383. 2011.

J. Acero, R. Alonso, J. I. Artigas, C. Carretero, C. Franco, S. Llorente, D. Paesa, and C. Sagues. *Cook top comprising at least one temperature sensor*. WO2011055279. 2011.

O. Aldana, S. Llorente, D. Paesa, and C. Sagues. *Hob having a temperature sensor*. WO2010139598. 2010.

O. Aldana, S. Llorente, D. Paesa, and C. Sagues. *Hob with a cover plate*. WO2010081637. 2010.

O. Aldana, R. Braulio, J. R. Garcia, S. Llorente, F. Monterde, D. Paesa, and C. Sagues. *Induction cooking hob with at least one induction heating element and at least one temperature sensor*. EP2094059. 2009.

Chapter 2

State of the Art

This chapter presents a survey of the state of the art most related to the issues addressed in this work: observers, reset systems and temperature sensors. This chapter begins exploring the deterministic observers' formulation, analyzing design concerns as well as their close relation to different control techniques. Afterwards, the attention is focused on a special sort of hybrid system, the reset system, whose formulation will be used throughout this Thesis as a basis to develop a novel sort of observer, the reset observer. This chapter ends analyzing the advantages and drawbacks of the existing temperature sensors, which justify the need of novel sensing methods that allow the development of accurate cooking pot temperature control.

2.1 Deterministic Observers

2.1.1 Observers: Purpose-Based Survey

Back in the late 50s, engineers and mathematicians found out that relevant unknown information of a system could be recovered on-line from input output data and plant dynamics. The algorithm developed for this purpose is known as an observer. Observers, also known as estimators or filters in other contexts, have proved to be an essential tool for system engineering, and in particular, for control of dynamical systems. Assuming that the system under study can be characterized by a model and its corresponding states, parameters and/or disturbances, an observer is simply a recursive algorithm that reconstructs missing information of that system from the available measurements (see Fig. 2.1). Depending on the purpose of the reconstructed information, observers fall into three different classifications. In particular, state estimation for control purposes, parameter estimation for system identification and/or adaptive control, and disturbance estimation for fault monitoring and detection.

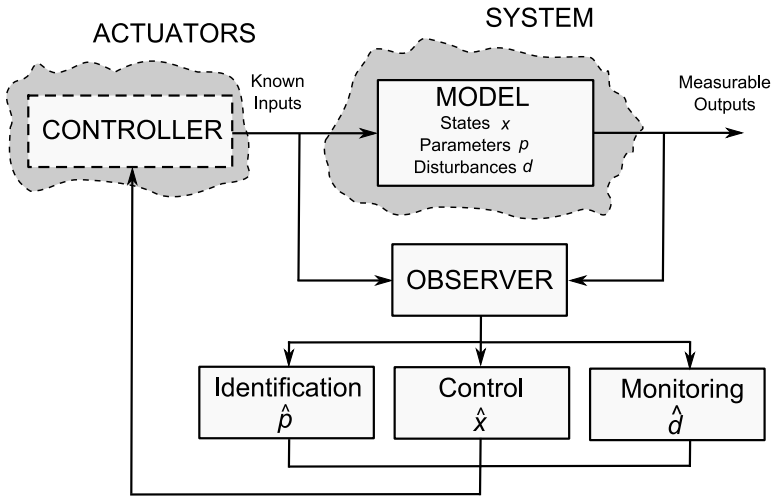

Figure 2.1: Interrelation between observers and control systems.

It is worth mentioning that feedback control systems assume initially that the entire state vector of the system to be controlled is measurable. Thus for the linear time-invariant system governed by

$$\begin{aligned} \dot{x}(t) &= Ax(t) + Bu(t) \\ y(t) &= Cx(t) \end{aligned} \tag{2.1}$$

where $x(t) \in \mathbb{R}^n$ is the system state, $u(t) \in \mathbb{R}^l$ is the system input, $y(t) \in \mathbb{R}^m$ is the system output, and A, B and C are constant matrices of appropriate

dimensions, with a cost function defined as

$$J(t) = \int_0^\infty (x^T(t)Qx(t) + u^T(t)Ru(t))dt, \tag{2.2}$$

the optimal feedback control law that minimizes the value of the cost function is $u(t) = -Kx(t)$, where $K = R^{-1}B^TP$ and P is the solution of the continuous time algebraic Riccati equation. However, the entire state $x(t)$ of (2.1) is generally not measurable, and then, the optimal feedback gain cannot be computed. This issue highlights the need of an algorithm capable of recovering the unknown states from the available measurements (i.e. $y(t)$ and $u(t)$). These sorts of algorithms are known as state observers. The simplest state observer can be obtained by using an open loop observer whose dynamics are as follows

$$\dot{\hat{x}}(t) = A\hat{x}(t) + Bu(t) \tag{2.3}$$

where the estimate $\hat{x}(t) \in \mathbb{R}^n$ of the state $x(t)$ does not include any feedback term. As a consequence, if the matrix A is known only approximately, an error will exist between $\hat{x}(t)$ and $x(t)$ even as $t \to \infty$. Furthermore, even though when A is known, $\hat{x}(t)$ tends to $x(t)$ as $t \to \infty$ only if A is asymptotically stable.

To overcome these drawbacks, a closed loop observer that feeds back the estimated state along with measured data was proposed in the early 70s in [31]. This state observer, also known as the Luenberger observer, quickly became standard, establishing the structure in which most deterministic estimators are based today due to its excellent trade-off between simplicity and performance [63]. Specifically Luenberger observer dynamics are given by

$$\dot{\hat{x}}(t) = A\hat{x}(t) + Bu(t) + L(y(t) - C\hat{x}(t)) \tag{2.4}$$

where L is a proportional gain. If the pair (A, C) is observable, it is possible to choose L so that $(A - LC)$ is asymptotically stable, guaranteeing that $\hat{x}(t)$ tends to $x(t)$ as $t \to \infty$ even if the original system matrix A is unstable.

Once the state estimation problem is solved, the next step is to jointly estimate the state as well as the unknown parameters of a system from the system input and output measurements. This problem is far from trivial, since the system parameters are unknown, and hence, the observer cannot be directly constructed. In this case, the approach relies on selecting some nominal values of the unknown system parameters and developing an algorithm that adaptively updates the estimates of the system parameters. This sort of observer is known as adaptive observer (AO), and represents a useful tool in order to cope with problems that may appear in any industrial application. For instance, they can be used to deal with systems whose parameters

are initially unknown due to modeling uncertainties and also to handle systems whose parameters are time variant. Additionally, they have important applications in adaptive control wherein some controller gains are updated on-line depending on the previously identified system parameters [35].

Typically, AOs address the problem of jointly estimate the state and unknown parameters of a linear (or nonlinear) system whose dynamics are as follows

$$\begin{aligned} \dot{x}(t) &= Ax(t) + Bu(t) + \phi(t, y, u)\theta \\ y(t) &= Cx(t) \end{aligned} \tag{2.5}$$

where $\theta \in \mathbb{R}^p$ is the unknown constant parameter vector, which can be used to represent modeling uncertainties, and the term $\phi(t, y, u)$ is a time-varying matrix which depends on the input $u(t)$ and/or the output $y(t)$ that balances the effect of the unknown parameters in the system dynamics. The resultant AO for systems (2.5) is then given by

$$\begin{aligned} \dot{\hat{x}}(t) &= A\hat{x}(t) + Bu(t) + K_P(y(t) - C\hat{x}(t)) \\ \dot{\hat{\theta}}(t) &= \Gamma\phi^T(t)C^T(y(t) - \hat{y}(t)) \end{aligned} \tag{2.6}$$

where $K_P \in \mathbb{R}^{n\times m}$ can be regarded as the proportional observer gain and $\Gamma \in \mathbb{R}^{p\times p}$ is the adaptive gain.

The first contributions on AO were applied to linear time invariant systems. Some relevant early works are [64], [65], which established the first definitions of the adaptive laws and studied the influence of the parameter estimate in the convergence and stability analysis of the overall estimation process. Afterwards, AO researches focused their attention on the nonlinear time variant systems [66]. AOs for nonlinear systems are characterized by making some assumptions on the class of the nonlinear system. Typically, they can only be applied to nonlinear systems that can be transformed into a canonical form that has the property of being linear in some way. For instance, [67], [68] and [69] can only be applied to nonlinear systems which are linear with respect to unknown parameter vector. Assuming persistent excitation, these AOs guarantee that the parameter estimation asymptotically converge to true parameter values and, moreover, asymptotic convergence is exponential both for parameter and state errors.

However, those adaptive observers do not allow obtaining an arbitrary rate of exponential convergence. This was overcome in [70], ensuring an arbitrary rate of exponential convergence both for the state and parameter errors provided that persistent excitation condition is satisfied. Another relevant works related to nonlinear AO are [71], [72]. There, the authors proposed a new approach to the design of adaptive observers which is conceptually simple, numerically efficient and well suited to cope with MIMO nonlinear systems. It ensured global convergence for joint state and parameter estimation, provided that some persistent excitation condition is

satisfied. Additionally, some authors have proposed to use an adaptive gain rather than a constant gain in the parameter adaptive law, in order to have a better tracking ability and to increase the robustness against uncertain parameters [73].

All those works were characterized by having only a proportional feedback term of the output observation error in both state observer and parameter adaptation law. Consequently, this kind of AO are called proportional adaptive observer (PAO). An interesting review about PAOs can be found in [36]. Nevertheless, all these adaptive observers can be unstable in the presence of disturbances. As it is shown in [74], a bounded disturbance might drive to infinity the parameter estimation of an adaptive observer even if the state estimation error remains bounded. This limitation motivated the design of the so-called Robust Adaptive Observers (RAO) [75]. A RAO is an adaptive observer that modifies its adaptive law for updating unknown parameters in order to overcome this drawback. Although different solutions for this limitation have been proposed [75], [76], [77], they are generally based on including a projection operator that constrains the parameter estimation inside a bounded set [78]. The definition of this bounded set is based on the maximum difference between the parameter estimation and the nominal value of the parameter. Therefore, prior knowledge of the system is required in order to define a proper nominal parameter value. One of the few papers devoted to observer synthesis of RAO for nonlinear systems is [79], wherein the robust observer gains are optimally chosen by minimizing the H_∞ norm between the disturbances and the estimation errors, where stability conditions are transformed into linear matrix inequalities, and hence can be easily computed.

From the process control point of view wherein the operation points, and hence, the system parameters are generally well defined, it could be more interesting to estimate any disturbance that might appear on the process rather than the process parameters themselves. These disturbances are likely caused by failures on the process. For instance, degradation on the system sensors, decalibration of the existing instruments, or a sudden change on the operating conditions [80]. Observers used for these purposes are known as disturbance observers (DO) [81]. Similarly to AOs, DOs address the problem of jointly estimate the state and unknown disturbances of a linear (nonlinear) system

$$\begin{aligned} \dot{x}(t) &= Ax(t) + Bu(t) + B_w w(t) \\ y(t) &= Cx(t) \end{aligned} \tag{2.7}$$

where $w(t) \in \mathbb{R}^w$ is any exogenous unknown input whose effect on the state is regulated through the matrix $B_w \in \mathbb{R}^{n \times w}$.

A common approach models the unknown input $w(t)$ as the output of a linear system and incorporates the input dynamics with the plant dynamics. Thus, the problem of state and disturbance estimation becomes a pure state

estimation problem when one considers the extended system $[\hat{x}^T(t), \hat{w}^T(t)]^T$, and then, the resultant DO dynamics is as follows

$$\begin{aligned}\begin{bmatrix} \dot{\hat{x}}(t) \\ \dot{\hat{w}}(t) \end{bmatrix} &= \begin{bmatrix} A & B \\ 0 & A_w \end{bmatrix} \begin{bmatrix} \hat{x}(t) \\ \hat{w}(t) \end{bmatrix} + \begin{bmatrix} B \\ 0 \end{bmatrix} u(t) \\ &+ \begin{bmatrix} K_p \\ K_w \end{bmatrix} (y(t) - C\hat{x}(t))\end{aligned} \tag{2.8}$$

However, this approach is limited to specific types of unknown inputs, for this reason, DOs usually define assumptions about the rate of disturbance changes. As a matter of fact, DO were initially restricted to constant disturbances, what highly decreased their applicability in practice. Another approach relies on estimating the unknown input by differentiating the system output [82]. In this case, the resultant observer is a combination of a reduced-order DO and an algebraic equation that relates the unknown disturbance to the system output and its derivatives and can be applied to a wider class of systems [83]. In a similar way as AOs, DOs originally focused on unknown external inputs for linear systems, and afterwards they were extended to nonlinear plants [84], [85], [80] and eventually to fault estimation and monitoring.

In particular, this latter framework has been subject of an extensive research, mainly motivated by a growing interest in safer and more reliable process control (see the surveys [86], [87] and references therein). Research on fault monitoring and detection began in the late 80s [88], [89], loosely speaking, the use of observers for fault detection relies on computing a residual signal by weighting output estimate errors. This residual signal is afterwards examined for the likelihood of faults by using a predefined threshold. Finally, some decision rules are applied to determine if a fault has actually occurred. Generally, decision process is simply based on analyzing whether the instantaneous values or the moving averages of the residual signal have exceeded the previously defined threshold. The problem gets harder when the system under consideration is subject to unknown disturbance or unknown inputs. In this case, the effect of the disturbance has to be de-coupled from the residual signal to avoid false positives and to achieve effective fault detection.

Summing up, there has been always a close interrelation between controllers and observers. It is widely known that observers can be used to improve the performance of the control loop by estimating unknown system states, identifying changes on relevant system parameters, monitoring external disturbances and detecting dangerous faults. However, sometimes the relation between both is even closer, since several promising new observers have emerged from novel sort of controllers. Further details about this relation are given in the following section.

2.1.2 Observers: Control-Techniques-Based Survey

Deterministic observer design has been very influenced by control theory since its first developments. As a matter of fact, the cornerstone among deterministic observers, the Luenberger observer, simply includes a proportional feedback term, in a similar way as proportional feedback controllers do, in order to adjust the convergence rate of the estimation process by modifying the eigenvalues of the closed-loop state matrix. In the course of time, observers have been modifying their structure following the steps of the most popular control techniques, trying to extend their improvements obtained in the system control framework to the estimation process. From the conceptually simple PI controller to the more complicated H_∞ compensator, many control techniques have been successfully applied to the observer framework. In this section, we outline some of the most relevant results obtained in the last decades. In particular, we will focus on proportional integral observers, and multiple model observers because of their close relation to the results that will be presented in following chapters of this Thesis.

It is well known that a steady state estimation error might appear dealing with noise corrupted systems. For this reason, some authors have proposed adding an additional integral term in the state estimation law in order to improve the steady state accuracy and to increase the robustness against modeling errors and disturbances. Such observers are known as Proportional Integral Observers (PIO). These observers aim at overcoming some performance limitations of traditional proportional observers by including an additional integral feedback loop, that increases robustness of the estimation process against disturbances, and modeling errors. They were initially introduced by Shafai and his co-workers for loop transfer recovery and robustness improvement in some publications (see [90], [91] and the references therein). Following this definition, PIO dynamics are given by

$$\begin{aligned} \dot{\hat{x}}(t) &= A\hat{x}(t) + Bu(t) + K_p(y(t) - C\hat{x}(t)) + K_i z(t) \\ \dot{z}(t) &= A_z(y(t) - C\hat{x}(t)) \end{aligned} \tag{2.9}$$

where $z(t)$ is the integral of the output estimation error whose time response can be modified through $A_z \in \mathbb{R}^{m\times m}$, which is a diagonal exponentially stable matrix, and $K_i \in \mathbb{R}^{n\times m}$ which is the integral observer gain.

The main advantage of this structure is that it is easily extended and generalized to a wide variety of systems. In particular, the adaptive version of this observer (PIAO) for linear systems was reported in [92] and [39], and recently, it has been also extended to time-delay systems in [93]. A different structure for PIOs was reported in [94] and its extended version [95]. Unlike the classical approach to PIO design (2.9), in this case the integral gain is used to stabilize the noise free error dynamics while the proportional gain is used to decouple the disturbance. This novel structure allows minimizing the effect of sensor noise or errors while increasing the accuracy of detection.

However, it is more difficult to extend, and so far it has only be applied to SISO systems.

It is worth mentioning that most papers published on this framework are only focused on stability analysis rather than on observer synthesis. As a matter of fact, there is not a general criterion to tune the PIO parameters, and hence, they have to be adjusted by simulations trials. One of the few works related to PIAO designing can be found in [38]. There, the authors propose to choose the proportional and integral gain by solving the $\mathcal{L}_2$ gain minimization problem, which leads to an optimal gain that minimizes the effect of disturbances on the estimation error.

Another sort of observer that emerged from a well established system control technique is the multiple model observer. The rationale behind this approach is that the estimation process might show a poor performance dealing with systems with different parameters than the nominal ones. In order to increase the robustness of the estimation process, an adaptive observer strategy based on the multiple model theory can be used. The idea of multiple models was introduced for control purposes first [96], in close relation to the adaptive control framework. It is commonly accepted that the convergence time of an adaptive scheme will be large if the initial parameter of the observer are not close enough to the plant parameters. This transient behavior can be improved using multiple discrete models [97]. Assuming that the plant parameters belong to a compact set S, multiple model observers use N discrete identification models with different parameters but uniformly distributed in S. So, the proposed strategy is to determine the best model for the real system at every instant which is used as the starting parameters of an additional state observer. This process is known as the reinitialization of the state observer. Since the reinitialized parameters of the state observer are closer to the real ones, the convergence time of the estimation process is decreased [98]. Typically, multiple model observer dynamics are as follows

$$\dot{\hat{x}}(t) = A_i\hat{x}(t) + B_iu(t) + K_{p_i}(y(t) - C\hat{x}(t)), \quad i = 1, \ldots, N \tag{2.10}$$

where A_i, B_i, and K_{p_i} are the plant matrices and the proportional gain respectively, which are associated with the best model identified every time instant. In order to determe the best model, an optimization algorithm that minimizes a cost function is used in practice. A standard cost function is

$$J_i(t) = \epsilon_i^2(t) + \int_{t=0}^{t=\infty} \epsilon_i^2(t)dt \tag{2.11}$$

where $\epsilon(t) = y(t) - C\hat{x}(t)$ is the estimation error.

Another approach of multiple model observers relies on combining the estimates of each individual observer balanced through a weighting function rather than just selecting the one that minimizes the cost function. This

approach has recently been proved to be useful for robust control purposes [99] and nonlinear system estimation [100], [101]. In this case multiple model observer dynamics are given by

$$\begin{array}{ll} \dot{\hat{x}}_i(t) & = A_i\hat{x}_i(t) + B_iu(t) + K_{p_i}(y(t) - C\hat{x}_i(t)), \quad i = 1, \ldots, N \\ \hat{x}(t) & = \sum_{i=1}^{N} p_i\hat{x}_i(t) \end{array} \tag{2.12}$$

where $\hat{x}_i(t)$ the estimate of each model, p_i is its corresponding weighting factor and $\hat{x}(t)$ is the resultant estimate of the multiple model observer.

This new approach is specially well-suited to deal with nonlinear systems. To see this, note that the structure of an observer is based on a mathematical model of the considered system. Therefore, the more accurate the used mathematical model is, the more accurate the estimation process will be. Moreover, dynamic behavior of most real systems is nonlinear and consequently a linear model is generally not able to provide a good characterization of the system for all its operating conditions. Moreover, the observer design process for general nonlinear models is far from trivial. For this reason, a multiple model observer (2.12) can also be used for identifying and estimating complex systems. Following this approach, the idea consists in dividing the operating space of the system into a finite number of operating zones. Hence, the dynamic behavior of the system inside each operating zone can be modeled using a simple submodel, for example a linear model. The relative contribution of each submodel is balanced with the help of a weighting function. Finally, the system estimate is carried out by combining the estimate of each submodel and by taking into consideration their respective contributions. Generally, each contribution is a probabilistically weighted combination of the estimation error of each submodel. An interesting survey of this approach has been recently published in [102].

This section has shown they key role that different control techniques have played in the development of new sort of observers. However, there are novel control techniques with attractive features that have not been applied to the observer framework yet. Among them, reset controllers stand out because their excellent balance between performance and simplicity. In the next section, a general description of hybrid and switching systems will be presented as starting point to give a detailed survey about reset systems.

2.2 Hybrid, Switching and Reset Systems

2.2.1 Hybrid Systems

Many dynamical systems combine both continuous-time and discrete-time dynamics. For instance, in a switched electrical circuit, voltages and currents change continuously according to classical electrical network laws but they also change discontinuously due to switches from relays and transistors. In

automotive transmission systems, torque transmission from the engine to the wheels has a certain continuous dynamics which depends on the current gear. Similarly, a bouncing ball exhibits continuous dynamics between each bounce but its velocity undergoes a discrete change as soon as the ball impacts the ground (see Fig. 2.2). This sort of systems fits into the class of hybrid systems.

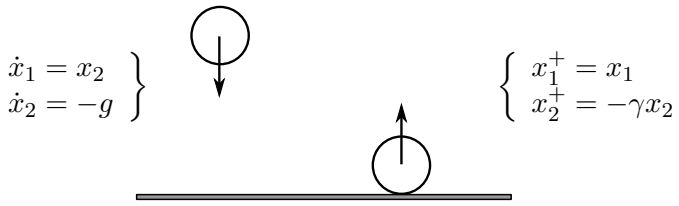

Figure 2.2: A bouncing ball behaves as a hybrid system. When the ball is above ground, it is being drawn to the ground by gravity according to the equations on the left side. Once the height of the ball is zero, that is, it has impacted the ground, its velocity is reversed and decreased by a factor of γ (inelastic collision) according to the equations on the right side.

Main reasons for using hybrid models would be to reduce complexity, since hybrid systems can incorporate models of dynamic processes at different levels of abstraction, and to avoid dealing directly with nonlinearities, since hybrid systems allow to work with sets of simpler linear equations and switch among these simpler models which is rather common approach in system modeling [103]. As a matter of fact, almost every complex system can be modeled as a hybrid system and they have applied to a wide variety of systems. For instance, robotics [104], air traffic management [105], process control [106], mechanical systems [107], biological systems such as fireflies [108] and heart muscle cells [109], and hybrid automata [110].

We now present some background leading up to the model of hybrid systems used throughout this work. The notation proposed in [111] will be partially used. Let us begin considering the following model for continuous-time dynamical system

$$\dot{x}(t) = \mathbf{f}(x(t)), \tag{2.13}$$

where $x(t) \in \mathbb{R}^n$, and the mapping $\mathbf{f} : \mathbb{R}^n \to \mathbb{R}^n$ represents how the states change in time. Sometimes, continuous-time dynamics are constrained in a subset of $\mathbf{F} \in \mathbb{R}^n$, and then $x \in \mathbf{F}$. For instance, regarding the bouncing ball example, the set $\mathbf{F}$ might indicate that the force of gravity cannot push the ball through the floor.

Similarly, we consider also discrete-time dynamics given by

$$x(t_k^+) = \mathbf{j}(x(t_k)), \tag{2.14}$$

with $x(t_k^+)$ the value of the state variable after the *k-th* jump, that is, the value of $x(t_k + \delta)$ with $\delta \to 0^+$, and the mapping $\mathbf{j} : \mathbb{R}^n \to \mathbb{R}^n$ represents how the states change after the jump. As before, discrete-time dynamics can be either applied to all the n-dimensional Euclidean space $\mathbb{R}^n$ or to a constrained subset $\mathbf{J} \in \mathbb{R}^n$, so that $x \in \mathbf{J}$.

Since a model of a hybrid dynamical system requires a description of the continuous-time dynamics, the discrete-time dynamics, and the regions on which these dynamics apply, both (2.13), (2.14) can be combined in a general model for a hybrid system as follows

$$\begin{array}{lll} \dot{x}(t) & = \mathbf{f}(x(t)) & x(t) \in \mathbf{F} \\ x(t_k^+) & = \mathbf{j}(x(t_k)) & x(t) \in \mathbf{J} \end{array} \tag{2.15}$$

where the value of the mappings $\mathbf{f}$ and $\mathbf{j}$, as well as the constrained sets $\mathbf{F}$ and $\mathbf{J}$, will all depend on the sort of hybrid system to be modeled.

The interaction of both continuous and discrete dynamics in a hybrid system (2.15) results in a rich dynamical behavior and phenomena not encountered in purely continuous-time systems. For this reason, some issues such as existence and uniqueness of solutions, robustness and well-posedness are still open problems for some sort of hybrid systems. In the following pages, we will focus on two sorts of hybrid systems that are of considerable relevance in the development of this Thesis: switching systems and reset systems.

2.2.2 Switching Systems

A switched system is a sort of hybrid system that consists of a finite number of subsystems and a logical rule that orchestrates switching between them. They have been subject of an extensive research for the past decades (see the surveys, [112] and [113] and references therein). The primary motivation for studying switched systems results from their wide variety of applications in control systems. For instance, mechanical systems, process control, automotive industry, power systems, aircraft and traffic control, and many other fields [114]. Switched systems have also revealed to be useful within nonlinear system framework, since there exists a large class of nonlinear systems which can be stabilized by switching control schemes, but cannot be stabilized by any continuous static state feedback control law [115].

Mathematically, a switched system can be modeled as

$$\dot{x}(t) = \mathbf{f}_i(x(t)), \quad i \in \mathcal{I} = [1, 2, \ldots, N], \tag{2.16}$$

where $x(t) \in \mathbb{R}^n$, the finite set $\mathcal{I}$ is an index set and stands for the collection of discrete subsystems, N is the number of subsystems, and the mapping $\mathbf{f}_i : \mathbb{R}^n \to \mathbb{R}^n$ is parametrized by the index $i = \sigma(t)$ which is called the active mode at the time instant t. Moreover, $\sigma : \mathbb{R}^+ \to \mathcal{I}$ is the switching signal

that orchestrates switching between these subsystems and it is generated by some predefined switching logic.

In particular, since we are mainly interested in the case where all the individual subsystems are linear, (2.16) can be simply rewritten as follows

$$\dot{x}(t) = A_i(x(t)), \quad i \in \mathcal{I} = [1, 2, \ldots, N]. \tag{2.17}$$

Stability of switched linear systems has been of increasing interest in the past decade [116], [117]. Switched systems include some interesting phenomena that highlight the key role played by both subsystem dynamics and switching signals in the switched system stability. On the one hand, even when all the subsystems are exponentially stable, the resultant switched system might be unstable for certain switching signals. To see this, let us consider the following simple switching system

$$\Sigma_a : \begin{cases} \dot{x}(t) = A_1 x(t) = \begin{bmatrix} -0.1 & 1 \\ -10 & -0.1 \end{bmatrix} x(t) & \text{if } \sigma(t) = 1, \\ \dot{x}(t) = A_2 x(t) = \begin{bmatrix} -0.1 & 10 \\ -1 & -0.1 \end{bmatrix} x(t) & \text{if } \sigma(t) = 2. \end{cases} \tag{2.18}$$

In this case both subsystems are stable since their eigenvalues are in both cases $\lambda = -0.1 \pm 3.16i$. However, stability of the resultant switching system depends on how the switching signal $\sigma(t)$ is defined. In particular, if $\sigma(t)$ is given by

$$\sigma(t) = \begin{cases} 1 & \text{if } x_1(t) \cdot x_2(t) \geq 0, \\ 2 & \text{if } x_1(t) \cdot x_2(t) \leq 0, \end{cases} \tag{2.19}$$

the switching system (2.18) is stable as it is shown in the left picture of Fig. 2.3, but if $\sigma(t)$ is as follows

$$\sigma(t) = \begin{cases} 1 & \text{if } x_1(t) \cdot x_2(t) \leq 0, \\ 2 & \text{if } x_1(t) \cdot x_2(t) \geq 0, \end{cases} \tag{2.20}$$

then the switching system (2.18) is unstable as it is depicted in the right picture of Fig. 2.3.

On the other hand, even when all the subsystems are unstable, a stabilizing switching signal might exist to make the resultant switched system exponentially stable. In similar way, let us consider the following switching system

$$\Sigma_b : \begin{cases} \dot{x}(t) = A_1 x(t) = \begin{bmatrix} 0.1 & -1 \\ 10 & 0.1 \end{bmatrix} x(t) & \text{if } \sigma(t) = 1, \\ \dot{x}(t) = A_2 x(t) = \begin{bmatrix} 0.1 & -10 \\ 1 & 0.1 \end{bmatrix} x(t) & \text{if } \sigma(t) = 2. \end{cases} \tag{2.21}$$

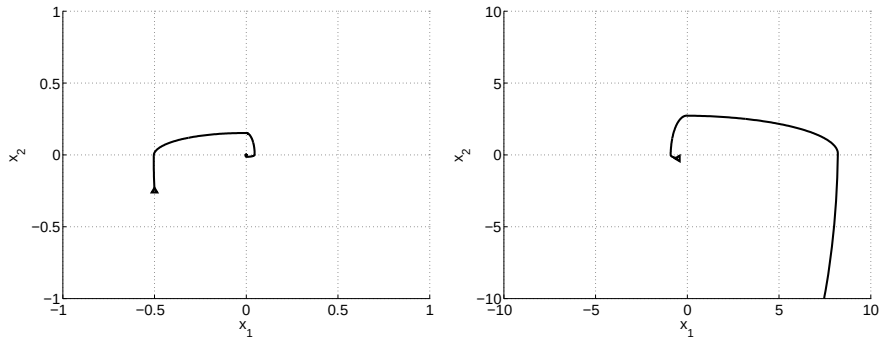

Figure 2.3: Influence of switching signals on system stability for stable subsystems. Simulation results for example (2.18).

whose both subsystems are unstable since their eigenvalues are in both cases $\lambda = 0.1 \pm 3.16i$. In this case, the resultant switching system is stable for a switching signal given by

$$\sigma(t) = \begin{cases} 1 & \text{if } x_1(t) \cdot x_2(t) \leq 0, \\ 2 & \text{if } x_1(t) \cdot x_2(t) \geq 0, \end{cases} \tag{2.22}$$

as it is shown in the left picture of Fig. 2.4, whereas it is unstable if $\sigma(t)$ is as follows

$$\sigma(t) = \begin{cases} 1 & \text{if } x_1(t) \cdot x_2(t) \geq 0, \\ 2 & \text{if } x_1(t) \cdot x_2(t) \leq 0, \end{cases} \tag{2.23}$$

as it can be seen in the right picture of Fig. 2.4.

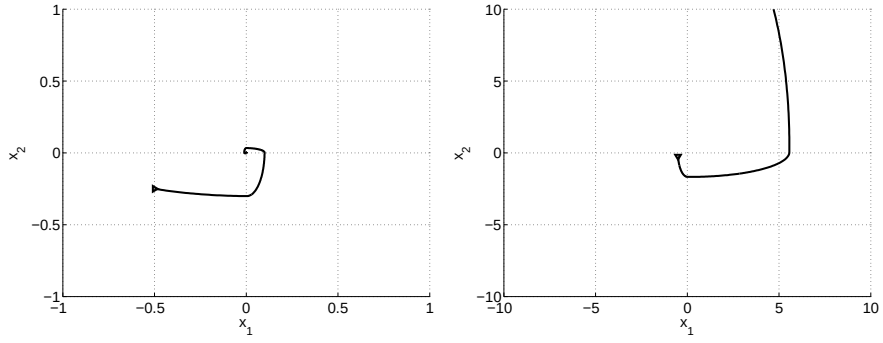

Figure 2.4: Influence of switching signals on system stability for unstable subsystems. Simulation results for example (2.21).

Motivated by the behavior shown in these examples, stability study of switched systems generally falls into two sorts of problems. One is the stability analysis of switched systems under any sort of switching signal. The other is the synthesis of stabilizing switching signals for a given collection of

dynamical systems. Finally, we outline here some of most relevant results within both approaches.

Finding conditions that guarantee that the switched system (2.17) is asymptotically stable for any switching signal is a problem that usually appears in adaptive control based on multiple models [98], [99]. Assuming that the plant parameters belong to a compact set S, this approach relies on using N identification models with different parameters but uniformly distributed in S. A controller for each model is also calculated and tuned. Therefore, the proposed strategy is to determine the best model for the real system at every instant, and using the corresponding controller to control the plant. Fig. 2.5 shows the main elements of the multiple model control scheme. A high-level decision maker, which is generally denoted by supervisor, determines which controller has to be connected in closed loop with the plant at each instant.

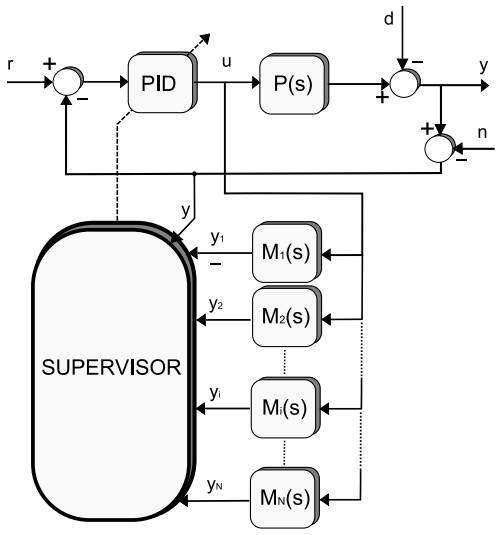

Figure 2.5: Block diagram of a PID adaptive control based on multiple models.

At first, stability of these sorts of systems was simply guaranteed by keeping each controller in the loop for a long enough time, in such a manner that transient effect due to switchings vanishes. The simplest way to specify this slow switching is to introduce a number $\rho > 0$ and restrict the class of admissible switching signals to signals with the property that the interval between any two consecutive switching times is not smaller than ρ, which is generally called dwell time. Following this approach, a method to compute a bound on ρ so that the switching system is asymptotically stable was proposed in [118]. This result was extended in [119] where the concept of average dwell time is presented. As far as asymptotic stability is concerned, it actually does not matter if the difference between two con-

secutive switches is greater than the dwell time, provided that this does not occur too frequently. Roughly speaking, the dwell time requirement has to be satisfied on average rather than continuously. However, this approach is no longer valid for quick switchings, a situation that generally appears in practice, and consequently, it highlights the need of a more sophisticated criterion to check stability of the switched system for arbitrary switching signals.

This problem is usually called stability analysis under arbitrary switching. In particular, it is necessary to require that all the subsystems are asymptotically stable. Note that this is a very natural assumption, since each controller is generally designed in such a manner that the resultant closed loop with the plant is stable. In particular, quadratic stability of the switched system under arbitrary switching is generally proven by ensuring the existence of a common quadratic Lyapunov function (CQLF) for all its subsystems. Quadratic stability implies asymptotic stability, and has become significantly popular because the conditions for the existence of a CQLF can be expressed as a linear matrix inequality problem (LMIP), which is easily computable [113], [120].

Nonetheless, it is worth mentioning that the existence of a CQLF is not necessary for the stability of arbitrary switching systems but sufficient. As matter of fact there exist switching systems that do not have a CQLF, but are exponentially stable under arbitrary switching, which points out the conservatism associated with CQLF [117]. For this reason, an important effort seeking for a less conservative class of Lyapunov functions has been made. A result that stands out among others is [121], where a switched quadratic Lyapunov functions is proposed. It consists of multiple Lyapunov functions associated with every subsystem, which are patched together based on the switching signal $\sigma(t)$ to construct a global Lyapunov function. Although the existence of a switched Lyapunov function is also a sufficient condition, it results in a less conservative method to test the stability of the switching system [122].

As it has been pointed out previously, the other relevant problem for switched systems is the switching stabilization problem. It consists in seeking a stabilizing switching signal for a given set of subsystems. Initially, research on this field was constrained to the simple case of switching between two linear systems. In this case, [123], [124] gave a necessary and sufficient condition for quadratical stability, which was based on existence of a stable convex combination of both subsystem dynamics. The problem gets harder when the number of subsystems is greater than two, in which the existence of a stable convex combination is not a sufficient condition. As a matter of fact, there are examples for which no stable convex combination state matrix exists, despite the fact that the system can be stabilizable by using certain switching signals [125]. Recently, a necessary condition for the existence of a switching signal among a finite number of LTI systems has

been given in [126]. Although this condition can be easily checked, it is only a necessary condition rather than sufficient. A necessary and sufficient condition for asymptotic stabilizability of switched LTI systems appears in [127], unfortunately it can only be applied to second-order systems, and it is not clear how to generalize this results to higher orders yet.

2.2.3 Reset Systems

A reset system is a sort of hybrid system [111] in which some of its states are reset as long as a certain condition is satisfied. The simplest reset system is the Clegg Integrator originally presented in 1958 [40]. It consists of an integrator and a reset law that resets the output of the integrator as long as the reset condition holds. It has a describing function similar to the frequency response of a linear integrator but with only 38.1° phase lag instead of the normal 90°, which results in an improvement of the closed-loop transient response. In particular, they were initially proposed for control purposes to overcome the inherent limitation of linear feedback controllers which generally require a balance between settling time and overshoot. To see this, let us begin introducing the Clegg integrator dynamics that can be described with the following differential equation

$$CI: \begin{cases} \dot{x}_k(t) = e(t) & e(t) \neq 0, \\ x_k(t^+) = 0 & e(t) = 0, \\ u(t) = x_k \end{cases} \tag{2.24}$$

where $x_k(t)$ is its state, $u(t)$ is its output, and $e(t)$ is the closed-loop error. Fig. 2.6 shows the closed-loop transient response of both a Clegg integrator and a linear integrator controlling the following plant $P(s) = \frac{s+1}{s^2+0.9s}$. It is evident how by resetting its integral term, the Clegg integrator significantly improves its transient behavior. Fig. 2.6 also highlights another advantage of reset systems. It can be used to stabilize control closed-loops which would be unstable otherwise.

It is worth mentioning that despite Clegg integrators might be very useful, there are some systems in which using a reset element could be ill-advised. Moreover, its use is not straightforward as its overall behavior is hard to analyze. As a matter of fact, it is also well-known that reset elements can deteriorate the transient response of a system, and ever worse, they can destabilize a stable system if they are not properly tuned. All these properties make reset systems an interesting and challenging area for research which has attracted the attention of theoretical and practical control engineers since the late 50s.

The main difference between reset control works relies on the definition of the reset condition which plays a key role in the stability analysis. Originally, reset condition was only dependent on the value of certain states of the systems (e.g. its input and/or output) rather than on the reset intervals

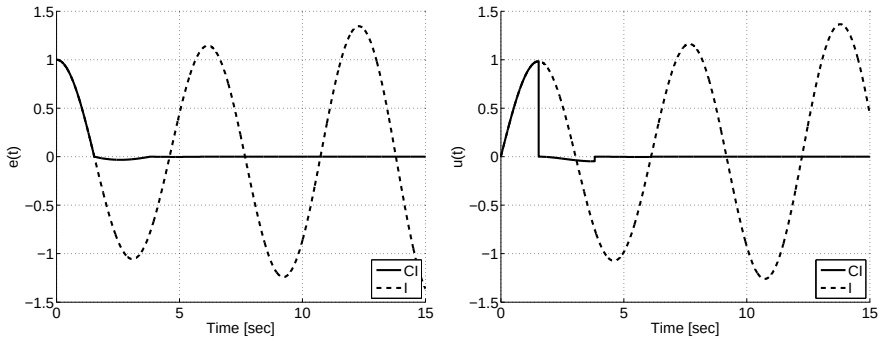

Figure 2.6: Behavior of a Clegg integrator (solid) vs a linear integrator (dashed).

themselves. As it has been previously commented, the seminal work of this reset-time-independent approach is the Clegg integrator [40]. Clegg proposed an integrator which was reset to zero when its input is zero which results in the first formal definition of a reset condition, and that was called zero crossing reset condition.

The study of reset control does not reappear until the mid-70s with the works by Horowitz et al. in [128], [129]. Influenced by his own work in the Quantitative Feedback Theory framework, Horowitz was seeking for new compensators that could overcome the feedback limitations of linear controllers. On the one hand, good reference tracking is achieved if the sensitivity function $S = \frac{1}{1+L}$ is small, where L is the open loop transfer function. On the other hand, noise rejection requires the complementary sensitivity function T to be small. Note that both functions are complementary mappings, meaning that they satisfy the constraint $T + S = 1$. Therefore, it implies that both S and T cannot be small at the same time (i.e. at the same frequencies). In theory, it should not be a problem, since tracking (low-frequency) and noise rejection (high-frequency) requirements are generally concentrated in different frequency regions. For instance, controllers with good tracking properties and noise rejection could be obtained by making S small at low frequencies and making T small at high frequencies. However, unstable poles and non-minimum phase zeros limit the achievable shape of the sensitivity and complementary sensitivity functions. Therefore, a trade-off between both requirements is usually needed in practice.

Since linear compensators cannot modify the magnitude of the closed-loop system without modifying its phase margin, Horowitz and his coworkers sought for new nonlinear controllers that could help to increase the phase margin of a system. Among others, Clegg Integrators clearly fit into this description. In [128] the authors incorporated Clegg integrators into feedback control design, and gave tuning guidelines for Clegg integrators based on their descriptive function. In 1975, Horowitz generalized his previous re-

sults by substituting the Clegg integrator by a more general structure called the first order reset element (FORE) [129]. Note that an FORE specifically behaves like a low-pass filter whose integral term can be reset according to the reset condition. In particular, its dynamics are given by the following state space representation

$$FORE: \begin{cases} \dot{x}_k(t) = A_k x_k(t) + B_k e(t) & e(t) \neq 0, \\ x_k(t^+) = A_r & e(t) = 0, \\ u(t) = C_k x_k(t) + D_k e(t) \end{cases} \tag{2.25}$$

where A_k, B_k, C_k,and D_k are tuning matrices of appropriate dimension. A_r is the reset map and indicates the value of the controller state after the reset, specifically if $A_r = 0$ it will be referred as full-reset, whereas if $A_r \neq 0$ it will be referred as partial-reset. Generally, B_k is the unity whereas D_k is set to zero, so that the effect of the FORE on the closed-loop response can be modified by choosing a proper FORE's pole A_k, and its corresponding gain C_k. To this end, the authors also gave insights into the relation between the FORE parameters and the resultant closed-loop behavior, which result in easily understandable criterion to choose the FORE's parameters [129].

An interesting survey on Horowitz's contributions on reset systems was given some years later in [130]. These contributions served as a starting point for a renewed research on reset systems in the late 90s, in which the problem of closed-loop stability for the reset system was finally addressed. In [131], stability criteria for zero-input closed-loops with a second order plant and a Clegg integrator were given. This work was extended some years later to FOREs in [132]. However, these results required the explicit computation of the reset times and their corresponding closed-loop solutions, and thus, they could not be directly applied to higher order systems. This fact also motivated the research on new stability conditions that could be easily extended to a wider variety of systems.

It took a few years more until Beker et al. proposed in [133] the first testable Lyapunov-based stability condition for reset systems. That condition was called the H_β condition, and it could be applied to test stability of systems of any order. This result was extended in [134] to bounded-input bounded-output (BIBO) stability of FOREs. Other relevant works of this group are [135], where the stability of MIMO reset systems is analyzed, and [136] where the authors studied the response of reset control systems to sinusoidal inputs. This latter work is extended to the local stability of limit-cycles induced under the same sort of excitation in [137]. Lastly, an in-depth survey of this line of work can be found in [41].

Recently, stability analysis of reset control systems has been also extended to time-delay systems for the case of zero crossing reset condition. In particular, there are two main approaches to study the stability of time-delay systems, which depend on whether the time-delay is included in the

stability analysis or not [138]. Regarding the stability of reset control systems, the delay-dependent approach was addressed in [139], whereas the delay-independent stability analysis was given in [140]. In both cases, stability conditions were given using a set of LMI, which made them easily computable.

All stability results associated with the zero crossing reset condition rely on the H_β condition. Its main advantage is that it can be expressed as a linear matrix inequality problem (LMIP), and thus, it can be easily solved. Unfortunately, the H_β condition also requires that the Lyapunov function must be decreasing over all the state space along the system trajectories and non-increasing on the reset jumps, which implies that it can only be applied to reset systems with stable base system, that is, it can only guarantee the reset actions do not destroy the stability of a stable base system. As a matter of fact, this is a significant drawback, since it is well known that there exist unstable base systems that can be stabilized by resetting the integral term. To overcome this restriction, the reset condition was modified by Zaccarian el al. in [141] as follows

$$FORE: \begin{cases} \dot{x}_k(t) = A_k x_k(t) + B_k e(t) & e(t)\cdot u(t) \geq 0, \\ x_k(t^+) = 0 & e(t)\cdot u(t) \leq 0, \\ u(t) = C_k x_k(t) + D_k e(t) & \end{cases} \tag{2.26}$$

In this case, stability conditions are obtained when the reset is performed at those instants in which the input and output of the reset element have different signs. The so-called sector reset condition significantly narrows the flow region $\mathcal{F}$, which results in a relaxation of the Lyapunov function, since it only has to be decreasing on a smaller region of state space rather than the whole state space (see Fig. 2.7).

This novel reset condition has been widely adopted by several authors. In [142] the authors analyzed the stability of a nonlinear system resulting from an FORE and a saturation in the input. Since unstable FOREs improve the transient behavior at the expense of large action values, action saturation is an issue that usually appears in practice. [143] generalizes the $\mathcal{L}_2$-gain analysis to general reset control systems fitting into the common H_∞ framework using augmented plants, and thus, higher order reset controllers can be handled instead of only CI and FOREs. Performance analysis of reset systems have been also studied in [42], where a $\mathcal{L}_2$-gain minimization algorithm is proposed, and in [143], where the performance comparison is carried out by computing the H_2 norm.

Recently, some authors have proposed to include the reset intervals in the stability analysis. This results in the third sort of reset condition available in the literature. These proposals are based on checking the stability of the induced discrete time system, which is obtained representing the dynamics of the reset system between two consecutive after-reset instants. Therefore, they can guarantee the stability of the original reset control system checking

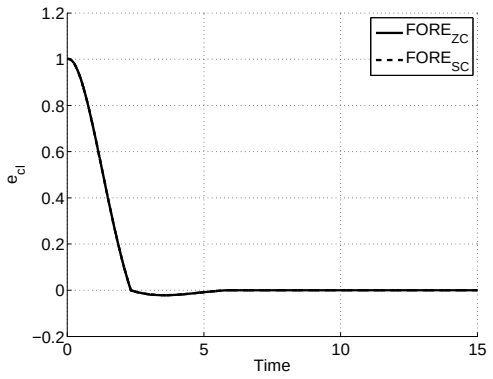

(a) Closed-loop response of both approaches controlling the aforementioned plant $P(s) = \frac{s+1}{s^2+0.9s}$. Note that both approaches give exactly the same result.

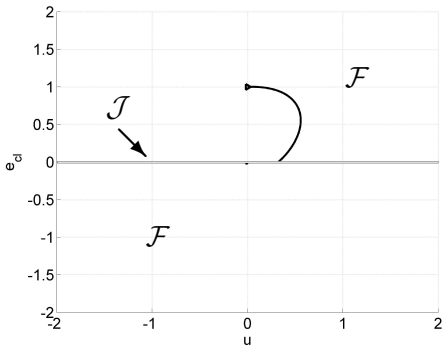

(b) State evolution within flow and reset region for the zero-crossing reset condition ($FORE_{ZC}$).

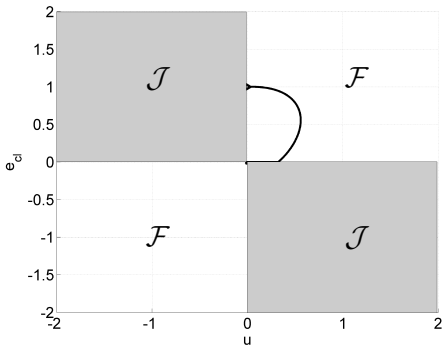

(c) State evolution within flow and reset region for the sector reset condition ($FORE_{SC}$).

Figure 2.7: Effect of the reset condition on the flow and reset region. For full-reset CI and FOREs, both reset conditions give the same results, but their corresponding flow and reset regions are completely different.

only the stability of the induced discrete system, thus it is expected to obtain less conservative stability results. Relevant works related to this approach are [144], which addresses the stability at fixed reset time instants, [145], which provides a method to determine the minimal reset time intervals guaranteeing the stability of the induced discrete time system for stable base system, and [146] where unstable base systems are also considered.

As far as performance comparison is concerned, it was proved that reset systems can achieve performance specifications that cannot be satisfied by linear controllers in [147]. After that promising result, superior performance of reset controllers compared with traditional linear controllers has already been proved in a wide variety of industrial applications. For instance, teleoperation of time delay passive systems [148], [149], temperature control of heat exchangers [150], and robust control of uncertain systems such as solar collector fields [151]. In all these examples, a significant improvement of the transient behavior has been achieved. However, regarding the steady state behavior, it is worth mentioning that since the state of the reset element (either CI or an FORE) is eventually reset, it does not have the characteristic of eliminating the steady state error in response to step disturbances by itself, thus a steady state error is expected for all systems without an integrator. For this reason, lots of efforts have been made to improve the steady state performance of reset compensators. One of these approaches is the PI+CI controller that was proposed in [152]. It consists of a PI controller that guarantees zero steady state error, and a CI controller that improves the transient response of the system. A different approach has been proposed in [153], where the authors presented a generalization of the standard FORE which guarantees asymptotic tracking of constant references. This approach relies on a feed forward interconnection of the reference, and requires that the static plant gain is perfectly known, which can be a drawback in practice. A more general study on reset controller stability tracking nonzero references is given in [154], where constant and slow time-varying references are considered.

Although the research on reset elements is still an open and challenging topic, this research has been mainly focused on control issues. According to the author's knowledge the first and unique attempt of applying reset elements within state observer framework is [44]. There, the authors developed a state estimator for tracking control of linear motors. They proposed to reset the state of the estimator to reject the quantification noise caused by the optical encoder which measures the current position. However, its design lacks generality and it can only be applied to this specific problem, because its reset condition relies on the idea that the actual position is known exactly at the mid-point of two consecutive quantizer levels when the quantized measurement changes the quantization level. This work points out the potential benefits of using reset elements for estimation problems, but also the need of a more formal and general definition of reset observes. This

challenging task will be faced in the following chapter.

2.3 Temperature Sensors

Temperature sensors are widely used in many industrial applications. The particular design and selection of the sensing element will depend on the application itself, and the required accuracy, sensitivity, and robustness. To justify the temperature sensors finally used in the induction hob, we explore in this section the strengths and weaknesses of each sort of sensor.

As it is shown in Fig. 2.8 temperature sensors generally fall into two main categories: contact sensors and non-contact sensors. As its own name suggests, a contact sensor must be as close as possible to the element to be measured. Strictly speaking, contact temperature sensors measure their own temperature, and hence, to guarantee that the obtained measurements are accurate, both the contact temperature sensor and the element to be measured should be in thermal equilibrium, that is, there is no heat flow between them. Unfortunately, this is not true in our application in which the element to be measured (i.e. the cooking pot) is separated from the contact temperature sensors by the glass-ceramic. This results in an increase of the uncertainty of the process, justifying the need of some modifications on the existing sensors and/or the glass-ceramic itself. On the other hand, non-contact sensors directly measure the temperature of the element under study. Most of them measure the infrared radiation emitted by the element to be measured, and from this value and its emissivity, it is possible to compute its actual temperature. However, the emissivity of the cooking pot is generally unknown, and consequently, it should be estimated and/or its variation should be limited somehow. These and another issues related to contact and non-contact temperature sensors will be further analyzed throughout this chapter.

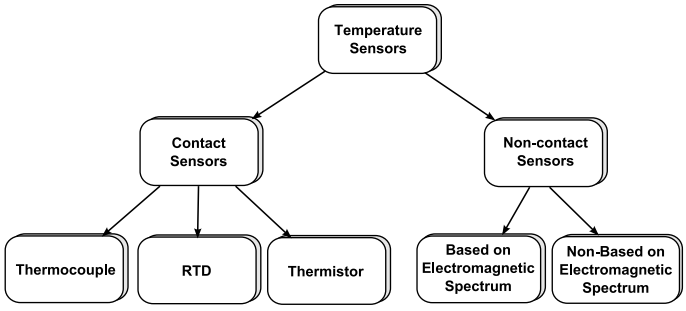

Figure 2.8: Temperature Sensor Classification.

2.3.1 Contact Sensors

When any conductor (e.g. a metal) is subjected to a thermal gradient, it will generate a voltage. This phenomenon is known as the thermoelectric effect or Seebeck effect [155]. Based on it, a thermocouple is a junction between two different metals that produces a voltage related to a temperature difference between those different metals. Specifically, thermocouples measure the temperature difference between two points, not absolute temperature. In particular, a thermocouple senses the temperature difference between its hot and cold junctions. Therefore, to know the hot junction temperature, you must already know the cold junction temperature somehow. If the temperature at the cold junction is uncertain, then this results in a more uncertain hot junction temperature. To overcome this issue, the cold junction is either maintained at a known reference temperature, or its temperature is directly measured by an additional thermistor. Consequently, the voltage corresponding to the cold junction can be estimated, and hence, the appropriate correction applied [156]. Thermocouples are the smallest, simplest, and most enduring of the three non-contact temperature sensor types. Because of their relative small size, they are fast reacting and the sensing junction can often be placed very close to the desired point of measurement.

Resistance thermometers, also called resistance temperature detectors or resistive thermal devices (RTDs), are temperature sensors that exploit the predictable change in electrical resistance of some materials when its own temperature changes [157]. They are generally made of platinum because of its quasi-linear response and repeatability, rather than nickel, whose response is more non-linear, or copper, which is more prone to oxidation, and hence, they are often called platinum resistance thermometers (PRTs). Compared to other temperature sensors, RTDs stand out because of its high sensitivity to small temperature changes, wide operating range and linear response. However, RTDs are generally more expensive than thermocouples and thermistors.

Thermistors consist of a semiconductor whose resistance is sensitive to temperature [158]. Thermistors differ from resistance temperature detectors (RTD) in that the material used in a thermistor is generally a ceramic or polymer, while RTDs are pure metals. Thermistors also differ in their temperature: RTDs are useful over larger temperature ranges whereas thermistors typically achieve a higher precision but within a narrower temperature range. Its maximum sensitivity point is generally near room temperature, however, the maximum sensitivity point can be tuned to other temperatures through a properly designed voltage divider. It is worth mentioning that when the thermistor is working near its maximum sensitivity point, small changes in temperature produce relatively high changes in resistance. On the other hand, working away from the maximum sensitivity point results

in that considerably higher changes in temperature are needed to produce significant changes in resistance [159].

A relevant drawback that affects both thermistors and RTDs is that their thermal responses depend on the size and mass of the sensors and their encasements. Typically, thermistors and RTDs are larger and more massive than thermocouples which result in higher response times. Moreover, both thermistors and RTDs tend to be affected by the averaging effect, which depends on how concentrated and big the sensor encasement is. Note that the total resistance change of these sorts of sensors actually indicates that the obtained temperature lies somewhere between the highest and lowest temperatures that exist within the sensor encasement. Therefore, the smaller the sensors are, the more accurate the resultant temperature measurement will be.

Summing up, the thermocouple is the smallest, fastest, and most durable temperature measurement solution and the closest to a point sensor, but it is also the sensor type most subject to noise, and precision errors. An RTD is recommended where extreme stability and precision are needed and where accuracy over a prolonged time is important. The thermistor is the recommended choice where high sensitivity is required over a relatively narrow range of temperatures (below $350°C$. that is the expected range for pot temperature control). Thermistors are less subject to the different types of error. Despite the fact that signal conditioning is needed to tune its maximum sensitivity point, its associated electronics are simple and cheap. Averaging effect and slow thermal response can be minimized by means of proper location and encasement selection. For this reason, thermistors are the most suitable non-contact temperature sensors for the pot temperature control in induction hobs.

2.3.2 Non-Contact Sensors

It is worth noting that is almost impossible for a contact temperature sensor to measure the temperature exactly where you need it. There exist always size constraints, interfering elements, or limitations associated with the application itself that impede you from measuring where you intended. Even in the unlikely case that the contact-senor could be placed where you need it, the sensor itself has a finite size that displaces the sensing element from the element to be measured. Therefore, there will be always an error resulting from the fact that the sensor is placed at a different location than the desired measurement location. This error can be significant in applications in which its different elements are not in thermal equilibrium, and hence, there exits a heat flow from the element to be measured and the point where the contact sensor is actually sensing. In this case, using non-contact temperature sensors, which are almost immune to location errors, would be recommended.

As it has been explained previously non-contact methods fall into two main categories depending on whether they measure the temperature under study from the electromagnetic spectrum or not. The electromagnetic spectrum is the range of all possible frequencies of electromagnetic radiation. Furthermore, the electromagnetic spectrum of a certain object is the characteristic distribution of electromagnetic radiation emitted or absorbed by that object (see Fig. 2.9).

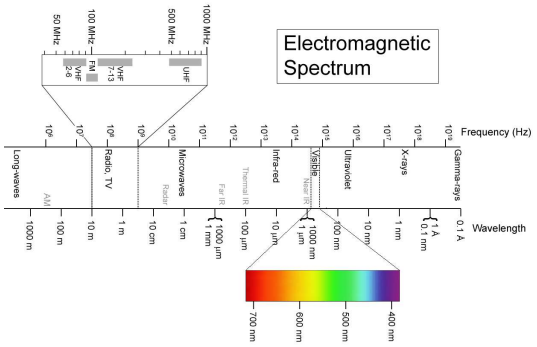

Figure 2.9: Electromagnetic spectrum.

Most non-contact sensors measure temperature from the electromagnetic spectrum (e.g. infrared or optical devices). One remarkable exception is acoustic thermography or simply acoustic temperature measurement, which relies on the measurement of the speed of sound [160]. Traditionally, this method is only applied to measure the temperature of liquids or gases. It is based on the fact that the speed of the sounds varies depending on the absolute temperature of the medium (i.e. liquid or gas) in which the sound wave is propagating, hence, the medium temperatures can be determined by the measurement of the transit time of a sound signal between a pair of acoustic transducers which are located at a known separation distance [161].

Optical techniques such as absorption and emission spectroscopy, scattering and luminescence, are sensitive in the visible region mostly because lasers are used as part of the system [162]. However, these techniques generally require highly cost instrumental and equipments that make them unfeasible for our application. On the other hand, infrared detectors are significantly more cost-attractive, and there already exist different attempts of using these sorts of devices for home appliances such as ovens [163], radiant hobs [164], and gas hobs [165].

As its name suggests, infrared devices are sensitive to that part of the spectrum due to the fact that hot objects strongly radiate in this range. An infrared measurement system consists of the source to be measured, the environment, the medium through which the radiant energy is transmitted, and the measurement device, which might also include an optical system, a detector, and an amplifier if necessary. Infrared detectors provide a signal

that is directly proportional to all radiation incident upon it, and that highly depends on the absolute temperature of the radiating element, as it is shown in Fig. 2.10. Temperature sensors based on measuring thermal radiation in the infrared spectrum are useful for sensing temperatures above $60°C$. Below this point, the emitted radiation would be insufficient to generate an output signal that would be detectable.

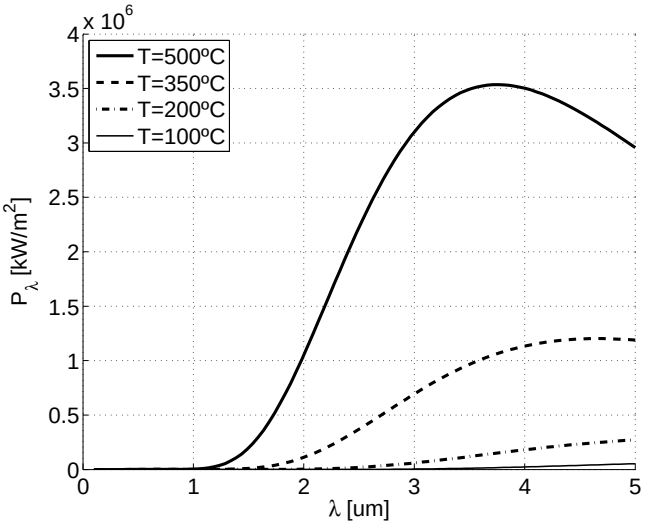

Figure 2.10: Irradiance as a function of the wavelength λ.

2.3.3 Current Status in Induction Hobs

As it has been explained previously, the key point to develop an accurate pot temperature control for domestic cookers is how to determine the actual temperature of the pot. Ideally, this issue could be easily overcome by using an external thermal sensor that would be in contact with the surface of the cooking pot, and thus, it would measure the actual temperature of the pot. Then, to guarantee a perfect contact between the pot and that external sensor, it would be attached to the pot by means of magnets, since the induction heating requires that the cooking pot is ferromagnetic, and finally, that external thermal sensor could send the relevant data to the power electronics somehow, for instance, by means of radio frequency signals.

A precursor work related to this approach is [166]. That work was based on a temperature sensor that had to be put into the food to ensure a proper control. In this case, the actual temperature of the pot was directly measured and consequently the uncertainty of the system was completely removed. That approach made the pot temperature control straightforward, however, since the sensor and its wires were situated inside the pot rather than underneath the cooking surface, it was regarded as quite intrusive for

the user. Some of the restrictions that any suitable pan temperate control solution has to take into account is that the complete control scheme has to be simple, safe, robust, and the most important, very user friendly. For this reason, throughout this Thesis we restrict ourselves to sensors that are already integrated into the hob, or that could be relatively easy to integrate into the actual induction hob structure.

Currently, induction hobs have both non-contact and contact temperature sensors which are used for different purposes. In particular, induction hobs have two NTC (Negative Temperature Coefficient) thermistors for each inductor underneath the glass ceramic, which are used to estimate the temperature of the cooking pot bottom, and an infrared sensor located at both left and right corners of the glass-ceramic. The layout of both temperature sensors is depicted in Fig. 2.11.

Figure 2.11: Layout of temperature sensors currently used in induction hobs.

This specific distribution requires further comment. On the one hand, due to the fact that the surface of many cooking pots become convex when they are heated up, resulting in an increase of the gap of air above the center of the induction coil, one of the NTC sensors is shifted from the center, in order to reduce the influence of the gap of air in the temperature measurements. On the other hand, there exist size constraints that make impossible to include a different infrared sensor for each inductor directly beneath the glass-ceramic. For this reason, infrared sensors are not located below the glass-ceramic but inside a retractable device so that it can be raised above the cooking surface and measure the temperature of the cooking pot wall.

As it has been commented previously, NTC thermistors currently integrated into the hob generally provide a quite uncertain measurement of the temperature of the cooking pot that is being used. As a matter of fact, these measurements are highly dependent on the used cooking pot and on its relative position with respect to the NTC thermistors. Since there exist a vast variety of cooking pots, each of them with a different construction and convexity, it might be possible that the NTC thermistors measure almost

the same temperature for different cooking pots at substantially different temperatures, as it is shown in Fig. 2.12.

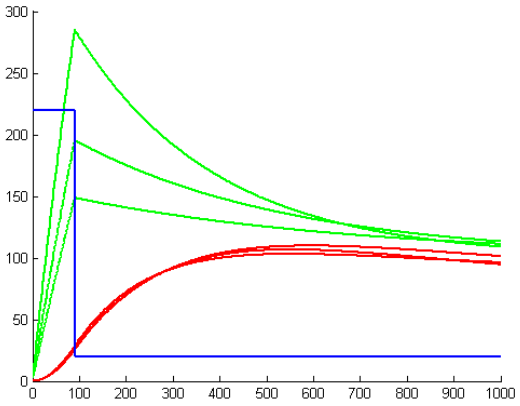

Figure 2.12: Influence of the cooking pot construction on the temperature evolution. Green lines are the actual cooking pot temperature ($^{\circ}C$) for different pots. Red lines are the NTC thermistor temperatures for each case. Blue line is the power supplied to each pot ($watts/10$). Despite that the same power is supplied to each pot and that almost the same temperature is measured by the NTC thermistors, each cooking pot reaches a substantially different temperature.

The influence of the relative position of the cooking pot with respect to the temperature sensors can be better understood analyzing Fig. 2.13. Due to its fabrication process, the cooking pot bottoms are not completely flat but convex. That results in an air gap between the cooking pot bottom and the glass-ceramic.

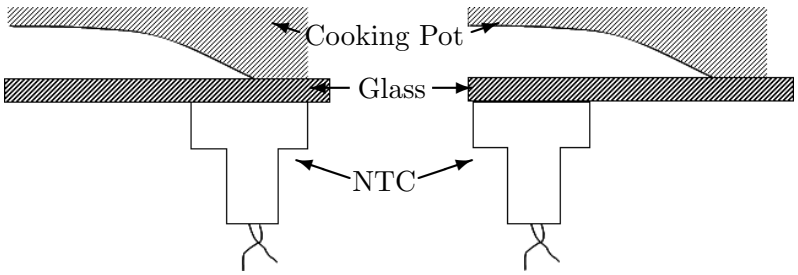

Figure 2.13: Different relative positions of the same cooking pot with respect to the NTC thermistors. The air gap is different in each situation, and consequently, the heat transmission from the cooking pot bottom to the NTC thermistor will be different as well.

Furthermore, that air gap generally varies along the cooking pot radius,

and it is maximum at the center and minimum at some points near the periphery. Consequently, a heat flow analysis in involving conductive, convective and radiative energy exchange has to be performed, in such a manner that uncertainty caused by location error could be modeled, and afterward minimized. The same process was performed when considering an infrared sensor as the sensing unit to estimate the temperature of the cooking pot instead of NTC thermistors. Obtained results are described in Appendix B. From them, it can be concluded that it is possible to develop an analytical model to estimate and control the actual temperature of the cooking pot from the available temperature sensors.

Part II

Reset Observers

Chapter 3

Reset Observers for SISO Linear Systems

Motivated by the promising features of reset controllers, that is, quick time response and lack of overshooting, this chapter studies the applicability of the reset system formulation to the state observer framework. This task will be performed in two steps. First, the three existing reset conditions (zero crossing [41], sector condition [42] and fixed intervals [43]) will be presented and included in the observer's formulation to obtain three novel reset observers, each of them with different dynamics, which result in different stability analysis. Second, exhaustive simulation will be carried out to determine what reset condition is more suitable, and to highlight the performance improvement that reset observers can obtain compared to traditional observers.

3.1 Introduction and Preliminaries

The main characteristic of all deterministic Luenberger-like observers presented so far is that they are based on estimation laws which are linear, that is, their feedback terms are simply a gain multiplied by the proportional (integral) error. Consequently, they have the inherent limitations of linear feedback control. Namely, they cannot decrease the settling time and the overshoot of the estimation process simultaneously. Therefore, a trade-off between both requirements is generally needed. As it has been explained in the previous chapter, this limitation could be solved by adding a reset element to the estimation laws. They have been successfully used for control purposes, although they have not been applied to the adaptive observer framework yet.

The main goal of this chapter is to find out whether reset elements could be applied to adaptive observers in order to improve the performance of the estimation process. Inspired by the promising results obtained by reset controllers, we propose a novel sort of observer called reset observer (ReO) and its corresponding adaptive version (i.e. reset adaptive observer ReAO). An ReO is an observer consisting of an integrator and a reset law that resets the output of the integrator depending on a predefined condition. The main advantage of an ReO compared with other Luenberger-like observers is that although its adaptive laws is linear, it basically behaves in a nonlinear way because of its resets, and hence, it results in a potentially much richer feedback signals which can improve the estimation process.

It is well known that the reset condition plays a key role in the behavior of reset systems, due to the fact that in reset systems, resets occur as a result of interrelation of the reset condition and system dynamics, which are generally known a priori, and the effect of external factors such as disturbances or delays, which might not be known. For this reason, reset systems can be characterized depending on whether reset instants are known a priori or not, and consequently, on whether the resultant stability analysis can be explicitly dependent on the reset times. As its name suggests, a Reset-Time Dependent (RTD) ReO would be characterized by the fact that its reset instants are initially well defined, and hence, its resultant stability analysis explicitly depends on how its reset intervals are chosen. Alternatively, when reset intervals are unknown, they cannot be directly used in the stability analysis, and results in a Reset-Time Independent (RTI) ReO.

The applicability of the reset element theory to the observer framework, which is the main contribution of this chapter, will be carried out in two steps. First, the three existing reset conditions, which consider both RTD and RTI formulations, will be presented to obtain three novel ReOs, each of them with different dynamics, which result in different stability analysis. Second, exhaustive simulation results will be carried out to determine what reset condition is more suitable, and to highlight the performance improve-

ment that ReOs can obtain.

It is worth noting that the concept of reset has already been used in the adaptive observer framework [167], however that approach relies on directly resetting the unknown parameter estimate rather than some observer states (i.e. its integral term) that is the approach that most fits the current reset control system framework, being this the reason why it will be used through this Thesis.

In the following, we use the notation $(x, y) = \begin{bmatrix} x^T & y^T \end{bmatrix}^T$. Given a state variable $x(t)$ of an ReO with resets, we will denote its time derivative with respect to the time by $\dot{x}(t)$, and the value of the state variable after the resets, that is, the value of $x(t + \delta)$ with $\delta \to 0^+$ by $x(t^+)$. Additionally, we assume at this stage that given an ReO defined according to (2.15) with a flow set $\mathbf{F}$, a jump or reset set $\mathbf{J}$, and a reset mapping $\mathbf{j} : \mathbb{R}^n \to \mathbb{R}^n$, the following assumptions are satisfied.

Assumption 1. *The ReO state $x(t)$ is such that $x(t) \in \mathbf{J} \Rightarrow \mathbf{j}(x(t)) \in \mathbf{F}$.*

Assumption 2. *The ReO is such that the reset times $t_{i+1} - t_i \geq \rho \; \forall i \in \mathbb{N}$, $\rho > 0$.*

Since these assumptions might be regarded as conservative, it is worth to note that both are quite natural to assume, and consequently, these conditions are widely used in the reset system formulations available in literature. On the one hand, Assumption 1 guarantees that after each reset, the solution will be mapped to the flow set $\mathbf{F}$ and, as a consequence, it is possible flowing after resets. Some selected references that adopt this assumption are, for instance, [141], [142], [42], [168]. On the other hand, Assumption 2 ensures that the ReO uses time regularization to avoid Zeno solutions. It guarantees that the time interval between any two consecutive resets is not smaller than $\rho \in \mathbb{R}$ which is a positive constant. This sort of assumption is still used in recent reset-based works [154], [143], [168], [58], although other authors prefer to remove this assumption by including a temporal regularization on the reset term. Readers interested in this approach are referred to [142], [42].

3.2 Reset-Time Independent ReO

In this section, the two most popular RTI formulations are presented to obtain two novel reset observers. Specifically, used reset conditions differ by the reset condition preferred. Namely, zero crossing reset condition [41] and sector reset condition [42].

3.2.1 Zero Crossing Reset Condition

Initially, we address the problem of the state estimation of single-input single-output (SISO) linear time invariant systems which are described by

$$\begin{array}{ll} \dot{x}(t) & = Ax(t) + Bu(t) + B_w w(t) \\ y(t) & = Cx(t) \end{array} \tag{3.1}$$

where $x(t) \in \mathbb{R}^n$ is the state vector, $u(t) \in \mathbb{R}$ is the input vector, $w(t) \in \mathbb{R}^n$ is the disturbance vector, $y(t) \in \mathbb{R}$ is the output vector, $A \in \mathbb{R}^{n\times n}$, $B \in \mathbb{R}^{n\times 1}$, $B_w \in \mathbb{R}^{n\times 1}$ and $C \in \mathbb{R}^{1\times n}$ are known constant matrices. At this stage, we consider SISO systems only, since a suitable formulation of reset elements for multiple-input multiple-output (MIMO) systems is still an open research topic.

The structure of our proposed ReO applied to an LTI system (3.1) is given in Fig. 3.1, and its dynamics is given by

$$\left.\begin{array}{ll} \dot{\hat{x}}(t) & = A\hat{x}(t) + Bu(t) + K_P\tilde{y}(t) + K_I\zeta(t) \\ \dot{\zeta}(t) & = A_\zeta\zeta(t) + B_\zeta\tilde{y}(t) \\ \hat{y}(t) & = C\hat{x}(t) \end{array}\right\} \quad \text{if } \eta(t) \notin \mathcal{M},$$
$$\left.\begin{array}{ll} \hat{x}(t^+) & = \hat{x}(t) \\ \hat{\zeta}(t^+) & = A_r\zeta(t) \\ \hat{y}(t^+) & = \hat{y}(t) \end{array}\right\} \quad \text{if } \eta(t) \in \mathcal{M}, \tag{3.2}$$

where $\eta(t) = [\tilde{x}(t)\ \ \zeta(t)]^T$ is the ReO augmented state error, $\hat{x}(t)$ is the estimated state, $\tilde{x}(t) = x(t) - \hat{x}(t)$ is the state error, K_I and K_P represent the integral and proportional gain respectively and $\tilde{y}(t) = y(t) - \hat{y}(t)$ is the output estimation error, $\zeta(t) \in \mathbb{R}$ is the reset integral term, $A_\zeta \in \mathbb{R}$ and $B_\zeta \in \mathbb{R}$ are two tuning scalars which regulate the transient response of $\zeta(t)$, and A_r is the reset matrix. Unless otherwise stated, we consider full-reset ReOs, and hence, $A_r = 0$.

Therefore, to complete closed-loop system equations, the set $\mathcal{M}$ that will be referred to as the reset surface, needs to be defined. Another set, the after-reset surface $\mathcal{M}_\mathcal{R}$, also plays an important role in the definition of closed-loop system solutions. Note that reset actions occur when the augmented state error $\eta(t)$ contacts the reset surface $\mathcal{M}$ at some instant t, that is $\eta(t) \in \mathcal{M}$, and then the reset term jumps to $A_r\eta(t) \in \mathcal{M}_\mathcal{R}$. In general, the set $\mathcal{M}_\mathcal{R}$ will be defined as $\mathcal{M}_\mathcal{R} = \mathcal{R}(A_r) \cap \mathcal{N}(C)$ where $\mathcal{R}(X)$ and $\mathcal{N}(X)$ stands for the image and null subspace of the linear operator given by the matrix X, respectively. Thus, $\mathcal{M}_\mathcal{R}$ is the set of states $\eta(t)$ that belong both to the null space of C (and then the output $C\eta(t) = 0$), and to the image space of A_r (they are after reset states). In addition, the set $\mathcal{M}$ is defined as $\mathcal{M} = \mathcal{N}(C)\backslash\mathcal{M}_\mathcal{R}$.

The next step consists in analyzing the asymptotic stability of (3.2). To this end, let us begin defining again the state estimation error as $\tilde{x}(t) =$

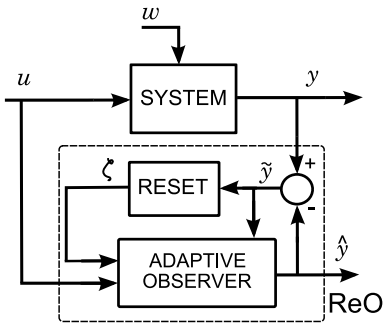

Figure 3.1: Reset adaptive observer applied to an LTI system.

$x(t)-\hat{x}(t)$, and by using the previously defined augmented state error $\eta(t) = [\tilde{x}(t)\ \ \zeta(t)]^T$, we can analyze the error ReO dynamics which can be obtained subtracting (3.1) from (3.2) as follows

$$\left.\begin{array}{ll} \dot{\eta}(t) & = A_\eta\,\eta(t) + B_\eta\,w(t) \\ \tilde{y}(t) & = C_\eta\,\eta(t) \end{array}\right\} \quad \text{if } \eta(t) \notin \mathcal{M}, \\ \left.\begin{array}{ll} \eta(t^+) & = A_R\,\eta(t) \\ \tilde{y}(t^+) & = \tilde{y}(t) \end{array}\right\} \quad \text{if } \eta(t) \in \mathcal{M}, \tag{3.3}$$

where

$$A_\eta = \left[\begin{array}{cc} A - K_P C & -K_I \\ B_\zeta C & A_\zeta \end{array}\right],\ B_\eta = \left[\begin{array}{c} B_w \\ 0 \end{array}\right], \tag{3.4}$$

and

$$C_\eta = \left[\begin{array}{cc} C & 0 \end{array}\right],\ A_R = \left[\begin{array}{cc} I & 0 \\ 0 & A_r \end{array}\right]. \tag{3.5}$$

Let us now state a sufficient condition for the existence of a quadratically stable ReO based on an LMI approach.

Proposition 1. *For given A_η, B_η and A_R the augmented error dynamic shown in (3.3) with $B_w = 0$ is quadratically stable, if for any matrix Θ with $Im\,\Theta = Ker\,C$ there exist a matrix $P = P^T > 0$ subject to*

$$A_\eta^T P + P A_\eta < 0, \tag{3.6}$$

$$\Theta^T \left[A_R^T P A_R - P\right] \Theta \leq 0, \tag{3.7}$$

which is a linear matrix inequality problem in the variable P.

Proof. It is quite similar to the proof shown in Proposition 3 in [140] for time-delay systems, simply by substituting the Lyapunov-Krasovskii functional [138], by a standard quadratic Lyapunov function. To this end, let us begin considering the following quadratic Lyapunov function for the augmented error dynamics described by (3.3):

$$V(\eta(t)) = \eta^T(t)\, P\, \eta(t). \tag{3.8}$$

Then, to prove the quadratic stability of our proposed ReOs based on the zero crossing reset condition, we have to check that there exists a common Lyapunov function that decreases when the reset system is flowing, and does not grow when the reset system is within the reset region. This is the standard stability requirements for reset systems and it can be formalized trough the following inequalities,

$$\begin{array}{ll} \frac{d}{dt}V(\eta(t)) < 0 & \eta(t) \notin \mathcal{M}, \\ V(\eta(t^+)) - V(\eta(t)) \leq 0 & \eta(t) \in \mathcal{M}. \end{array} \tag{3.9}$$

To prove the first term of (3.9), let us compute the time derivative of (3.8), which is given by

$$\dot{V}(\eta(t)) = \dot{\eta}^T(t)P\eta(t) + \eta^T(t)P\dot{\eta}(t) = \eta^T(t)(A_\eta^T P + PA_\eta)\eta(t), \tag{3.10}$$

which can be rearranged as an equivalent LMI problem in the variables $P > 0$

$$A_\eta^T P + PA_\eta < 0, \tag{3.11}$$

which is the first inequality of Proposition 1.

It remains to prove the second term of (3.9). Since the reset action is only active when $\eta(t) \in \mathcal{M}$, it directly results in that

$$V(\eta(t^+)) - V(\eta(t)) = \Theta^T(A_R^T P A_R - P)\Theta \leq 0, \tag{3.12}$$

for every $\eta(t) \in \mathcal{M} = \operatorname{Ker} C$, which is the second inequality of Proposition 1 and completes the proof. □

3.2.2 Sector Reset Condition

In a similar way to (3.2), an ReO based on the sector reset condition applied to an LTI system (3.1) has the following dynamics

$$\left.\begin{array}{ll} \dot{\hat{x}}(t) & = A\hat{x}(t) + Bu(t) + K_P\tilde{y}(t) + K_I\zeta(t) \\ \dot{\zeta}(t) & = A_\zeta\zeta(t) + B_\zeta\tilde{y}(t) \\ \hat{y}(t) & = C\hat{x}(t) \end{array}\right\} \quad \text{if } \eta(t) \in \mathcal{F},$$
$$\left.\begin{array}{ll} \hat{x}(t^+) & = \hat{x}(t) \\ \hat{\zeta}(t^+) & = A_r\zeta(t) \\ \hat{y}(t^+) & = \hat{y}(t) \end{array}\right\} \quad \text{if } \eta(t) \in \mathcal{J}, \tag{3.13}$$

Evidently, it can be regarded as a hybrid system with a *flow set* $\mathcal{F}$ and a *jump or reset set* $\mathcal{J}$. Regarding (3.13), the two conditions at the right side are the *flow* and the *jump* condition respectively. On the one hand, as long as $(\tilde{y}, \zeta) \in \mathcal{F}$ the observer behaves as a proportional integral observer. On the other hand, if the pair $(\tilde{y}, \zeta)$ satisfies the *jump* condition, the integral term is reset according to the reset map A_r.

Thus, the observer flows whenever $\tilde{y} \cdot \zeta \geq 0$, that is, if $\tilde{y}$ and ζ have the same sign, whereas the observer jumps whenever $\tilde{y} \cdot \zeta \leq 0$, that is, if $\tilde{y}$ and ζ have different sign. According to this statement and since $\tilde{y} = C\tilde{x}$, we can formalize the definition of both sets by using the following representation:

$$\begin{aligned} \mathcal{F} &:= \left\{ (\tilde{x}, \zeta) : \begin{bmatrix} \tilde{x} \\ \zeta \end{bmatrix}^T M \begin{bmatrix} \tilde{x} \\ \zeta \end{bmatrix} \geq 0 \right\}, \\ \mathcal{J} &:= \left\{ (\tilde{x}, \zeta) : \begin{bmatrix} \tilde{x} \\ \zeta \end{bmatrix}^T M \begin{bmatrix} \tilde{x} \\ \zeta \end{bmatrix} \leq 0 \right\}, \end{aligned} \tag{3.14}$$

where M is defined as

$$M = \begin{bmatrix} 0 & C^T \\ C & 0 \end{bmatrix}. \tag{3.15}$$

In this case, its error dynamics are given by

$$\begin{array}{ll} \dot{\eta}(t) = A_\eta\, \eta(t) + B_\eta\, w(t) \\ \tilde{y}(t) = C_\eta\, \eta(t) \end{array} \Bigg\} \quad \text{if } \eta(t) \in \mathcal{F}, \\ \begin{array}{ll} \eta(t^+) = A_R\, \eta(t) \\ \tilde{y}(t^+) = \tilde{y}(t) \end{array} \Bigg\} \quad \text{if } \eta(t) \in \mathcal{J}, \tag{3.16}$$

where A_η, B_η, C_η and A_R are defined according to (3.4)-(3.5).

Let us now state a sufficient condition for the existence of a quadratically stable ReO based on an LMI approach.

Proposition 2. *For given A_η, B_η and A_R the augmented error dynamic shown in (3.16) with $B_w = 0$ is quadratically stable, if there exist a matrix $P = P^T > 0$ and scalars $\tau_F \geq 0$ and $\tau_J \geq 0$ subject to*

$$A_\eta^T P + P A_\eta + \tau_F M < 0, \tag{3.17}$$

$$A_R^T P A_R - P - \tau_J M \leq 0, \tag{3.18}$$

which is a linear matrix inequality problem in the variables P, τ_F and τ_J.

Proof. Let us begin considering the previously presented Lyapunov function (3.8) and its time derivative (3.10). Similarly, to prove the quadratically

stability of an ReO based on the sector reset condition, we have to check that:

$$\begin{array}{ll} \dot{V}(\eta(t)) < 0 & \eta(t) \in \mathcal{F}, \\ V(\eta(t^+)) \leq V(\eta(t)) & \eta(t) \in \mathcal{J}. \end{array} \tag{3.19}$$

According to (3.14), since $\mathcal{F} := \left\{\eta : \eta^T M \eta \geq 0\right\}$ and employing the S-procedure [120], the first term of (3.19) is equivalent to the existence of $\tau_F \geq 0$ such that

$$\dot{V}(\eta(t)) < -\eta^T(t)\tau_F M\eta(t). \tag{3.20}$$

Rearranging terms of (3.10) and (3.20), the first term of (3.19) holds if the following inequality is satisfied

$$\eta^T(A_\eta^T P + PA_\eta)\eta + \eta^T\tau_F M\eta < 0, \tag{3.21}$$

which can be rearranged as an equivalent LMI problem in the variables $P > 0$ and $\tau_F \geq 0$

$$A_\eta^T P + PA_\eta + \tau_F M < 0, \tag{3.22}$$

which is analogous to (3.17) and consequently, proves the first equation of (3.19).

Similarly, employing again the S-procedure, the second term of (3.19) holds if there exists $\tau_J \geq 0$ such that

$$V(\eta(t^+)) \leq V(\eta)(t) + \eta^T(t)\tau_J M\eta(t), \tag{3.23}$$

which is equivalent to

$$\eta^T(t)A_R^T PA_R\eta(t) - \eta^T(t)P\eta(t) - \eta(t)^T\tau_J M\eta(t) \leq 0. \tag{3.24}$$

Rearranging terms, (3.24) can be also rewritten as an equivalent LMI problem in the variables $P > 0$ and $\tau_J \geq 0$ as follows

$$A_R^T PA_R - P - \tau_J M \leq 0, \tag{3.25}$$

which is analogous to (3.18) and proves the second equation of (3.19) and, as a consequence, completes the proof of the Proposition. □

3.2.3 RTI ReO - Tuning Guidelines

Both proposed ReOs mainly rely on four tuning gains. Namely, the proportional gain K_P and the integral gain K_I, which modify the convergence speed of the state estimation error, and the reset term gains A_ζ and B_ζ, which regulate the transient response of the reset term.

Before tuning the algorithm on a real system, it is strongly recommended to first perform some simulations, and tune the observer gains following the next guidelines. Firstly, the gains of the reset term A_ζ and B_ζ have to be chosen. Analyzing (3.2)-(3.13), it is evident that the reset term $\zeta(t)$ stands for a low-pass filter whose cutoff frequency relies on A_ζ and whose gain depends on B_ζ. Typically, it is selected $B_\zeta = 1$, because the effect of the integral term can be increased by tuning the integral gain K_I, therefore the transient response of the integral term only relies on A_ζ. Intuitively, to guarantee a proper integration of the error dynamics, A_ζ should be chosen to be Hurwitz with $|A_\zeta|$ at least 5 times lower than the minimum absolute value of the eigenvalues of A.

The second step is to find suitable K_P and K_I in such a way that the response of the state estimation error is fast enough but without overshooting. Since the pair (A_η, C_η) is constant, it can be done by using any pole placement method. Once both gains have been computed, it is time to exploit the potential benefit of the reset element. The aim is to increase the integral gain in order to obtain a quicker and oscillating response due to the fact that most of the overshoots will be removed by resetting the integral term. Consequently, we will obtain a state estimation error response quicker than before but without overshooting. This fact underlines the benefit of the reset observers, which are mainly nonlinear and, as a consequence, it can achieve some specifications that cannot be achieved by pure linear observers.

3.3 Reset-Time Dependent ReO

Although an RTI approach is more popular, some authors have included the reset time intervals in the stability analysis recently. In [144], [169], a feedback was introduced in reset law so that the state of the controller was reset to nonzero values to minimize some performance index. Nonetheless, the authors focused only on improving the temporal behavior of the system when it is reset every sample time, thus, the authors did not give any procedure to choose the reset time interval. In [43], the authors give new sufficient stability conditions that explicitly depend on the reset times. As it was explained in [146], a faster temporal response could be obtained by tuning the reset controller parameters so that the resultant closed-loop system without resets is unstable (denoted by unstable base system), and afterwards, by stabilizing the system through the reset actions. In particular, for the case of unstable base system, the optimal reset time interval has to be in a bounded set of $\mathbb{R}^+$. However, it is not clear how to select the best time interval within this bounded set $[\Delta_{min}, \Delta_{max}]$.

Among every $\Delta \in [\Delta_{min}, \Delta_{max}]$ we focus on determining a constant reset interval Δ that improves the transient closed-loop response. Thus,

ReO open-loop dynamics are modified as follows

$$\left.\begin{array}{ll}\dot{\hat{x}}(t) & = A\hat{x}(t) + Bu(t) + K_P\tilde{y}(t) + K_I\zeta(t)\\ \dot{\zeta}(t) & = A_\zeta\zeta(t) + B_\zeta\tilde{y}(t)\\ \hat{y}(t) & = C\hat{x}(t)\\ \dot{\varphi}(t) & = 1\end{array}\right\} \text{ if } \varphi \in [0, \Delta),$$
$$\left.\begin{array}{ll}\hat{x}(t^+) & = \hat{x}(t)\\ \hat{\zeta}(t^+) & = A_r\zeta(t)\\ \hat{y}(t^+) & = \hat{y}(t)\\ \varphi(t^+) & = 0\end{array}\right\} \text{ if } \varphi = \Delta. \tag{3.26}$$

where $\varphi(t)$ is an auxiliary temporal variable that guarantees that the ReO is reset every Δ, and its resultant closed-loop dynamics are given by

$$\left.\begin{array}{ll}\dot{\eta}(t) & = A_\eta\eta(t) + B_\eta w(t)\\ \hat{y}(t) & = C_\eta\eta(t)\\ \dot{\varphi}(t) & = 1\end{array}\right\} \text{ if } \varphi \in [0, \Delta),$$
$$\left.\begin{array}{ll}\eta(t^+) & = A_R\eta(t)\\ \hat{y}(t^+) & = \hat{y}(t)\\ \varphi(t^+) & = 0\end{array}\right\} \text{ if } \varphi = \Delta. \tag{3.27}$$

where A_η, B_η, C_η and A_R are again defined according to (3.4)-(3.5).

3.3.1 Asymptotic Stability Analysis

Before the main results are given, the following well known results on asymptotic stability of discrete and reset systems are needed.

A discrete system $x(k+1) = \Phi x(k)$ with a transition matrix Φ and initial condition $x(k_0) = x_0$ is *asymptotically stable*, if for every k_0 and $x(k_0) = x_0$, there exist some $\gamma > 0$ and $0 < \lambda < 1$ such that the corresponding solution satisfies $\|x(k)\| \leq \gamma\lambda^{k-k_0}\|x(k_0)\|$ [170]. On the other hand, the equilibrium point x_e of the reset system (3.27) is *asymptotically stable*, if for any $\epsilon > 0$ there exists a $\delta(\epsilon)$ such that if $\|x_0\| < \delta$ then $\|x(t, x_0)\| < \epsilon$ for all $t \geq 0$, where $x(t, x_0)$ is the solution of the system (3.27) at instant t, and for the initial condition $x_0 = x(0)$, and additionally, there exists some positive real η such that if $\|x_0\| < \eta$ then $x(t, x_0) \to 0$ as $t \to \infty$.

Considering that there exists a sequence of reset times $\tau_0, \tau_1, \ldots, \tau_k$, or equivalently $\Delta_0 = \tau_0 - t_0$, $\Delta_1 = \tau_1 - \tau_0, \ldots, \Delta_k = \tau_k - \tau_{k-1}$, where each Δ_k is referred to as reset interval. It has been shown in [43] that the stability of the reset system (3.27) can be checked from stability of the discrete system the following, which is obtained by sampling the reset control system at the after-reset instants τ_k^+, $k = 0, 1, \ldots$,

$$x(\tau_{k+1}^+, x_0) = A_R e^{A_\eta(\tau_{k+1}(x_0) - \tau_k(x_0))} x(\tau_k^+, x_0). \tag{3.28}$$

Proposition 3. *Assuming that the reset intervals are upper bounded, that is for $k = 0, 1, \ldots$ and some Δ_{max}, $\Delta_k \leq \Delta_{max}$, then the equilibrium point $x_e = 0$ of the reset system (3.27) is asymptotically stable if and only if the equivalent time varying discrete system*

$$x(k+1) = A_R e^{A_\eta \Delta_k} x(k), \tag{3.29}$$

is asymptotically stable [43].

The above Proposition gives necessary and sufficient conditions for stability based on the knowledge of reset intervals Δ_k, which generally are not constant, and thus, resultant equivalent discrete system is time-varying. It is worth mentioning that for reset systems with stable base system (i.e. A_η is Hurwitz), any large enough Δ_k guarantees stability of the closed-loop reset system. Nonetheless, it is not true for reset systems with unstable base system (i.e. A_η is not Hurwitz). In this case, it is needed that reset intervals are upper bounded for ensuring the stability, since the reset interval cannot be chosen to be too large because the reset actions would not be capable of stabilizing the system. As it is pointed out in [43], [146], an appropriate reset interval has to be within a bounded interval $[\Delta_{min}, \Delta_{max}]$. However, it is not clear which one would give a better performance.

As it has been commented previously, we restrict ourselves to constant reset intervals, and hence, $\Delta = \tau_k - \tau_{k-1}, k = 1, 2, \ldots$ is constant. For this reason, the equivalent time-varying discrete system (3.29) becomes time-unvarying, and consequently, its stability analysis is highly simplified. The following proposition formalizes this result.

Proposition 4. *Given $\Delta > 0$, the reset system (3.27) is asymptotically stable if and only if the spectral radius of $A_R e^{A_\eta \Delta} < 1$.*

Proof. It follows directly from Proposition 3.1 in [43] by substituting $\Delta_k = \Delta, k = 1, 2, \ldots$ in (3.29), and applying the classical result for stability of time unvarying discrete system (Theorem 22.11 in [170]). Since both results are necessary and sufficient, the obtained result is also necessary and sufficient. □

3.3.2 RTD ReO Tuning Guidelines

Unlike in the tuning guidelines presented in Chapter 3.2.3, in this case the integral gain K_I has to be designed so that the closed-loop system is unstable. In spite of that, the resultant behavior will be stable if a proper bound of the reset intervals is designed. To this end, in this section we propose a novel procedure to choose a fixed reset time interval. Our motivation is to use this change in the definition of the system in order to simplify stability conditions and optimize the performance. However, it is worth mentioning that if the resultant reset time interval is too large, the

corresponding transient response might be worse than the obtained with a reset time-independent approach. For this reason, a criterion to avoid this situation has also to be given.

The spectrum radius of the transition matrix $\rho(A_R e^{A_\eta \Delta})$, or equivalently maximum absolute value of its eigenvalues, gives information about the expected response of the equivalent discrete system. Specifically, the lower $\rho(A_R e^{A_\eta \Delta})$ is, the faster the convergence of the closed-loop system is [170]. For this reason, a reasonable criterion to optimize the performance of the closed-loop response would be to choose the reset interval Δ so that the spectrum radius of the transition matrix $\rho(A_R e^{A_\eta \Delta})$ is minimized.

Then, the proposed search procedure is as follows. Let us begin defining a discrete set $\mathcal{D} = \{a \cdot \Delta_s \,:\, a \in \mathbb{N} \backslash \{0\}\}$, with an arbitrary resolution, Δ_s. For each element $\Delta_i \in \mathcal{D}$, the spectrum radius of the transition matrix $\rho(A_R e^{A_\eta \Delta_i})$ is computed. Then, we find some couple $(\Delta_i, \rho(A_R e^{A_\eta \Delta_i}))$ that characterize the response of the equivalent discrete system. Since a lower $\rho(\cdot)$ implies a better closed-loop response, the best reset interval Δ is finally chosen as the Δ_i whose corresponding spectrum radius $\rho(A_R e^{A_\eta \Delta_i})$ is minimum.

The resultant sub-optimal Δ can also be used to determine whether the fixed reset-time closed-loop response will be worse than the one that could have been obtained by following a zero crossing reset condition, that is, resetting the same closed-loop system when its output reaches the reset surface according to (3.27). To see this, note that reset systems with unstable base systems are designed in such a manner that the closed loop matrix A_η has a pair of unstable poles in the form $p_u = -\xi\omega_n \pm j\omega_n\sqrt{1-\xi^2}$ where $\xi < 0$ is its damping ratio and w_n is its natural frequency [146]. The remaining closed loop poles are stable, so their contribution to the transient response of the closed loop disappears quickly. In this way the trajectories in the state-space will tend to the trajectories of the unstable modes, which are spirals diverging from the origin and with a period $T = 2\pi/\omega_n$.

In the absence of resets, each of these spirals would reach its first maximum value at $t_{peak} = \pi/w_n$ as it is shown in Fig. 3.2. Since the aim of reset is to reduce the overshoot, the closed-loop system has to be reset for the first time before $t = t_{peak}$. Otherwise the resultant transient response would be deteriorated, since the system would have already overshot its equilibrium point. Therefore, if the obtained reset interval $\Delta \geq t_{peak}$, using a zero crossing reset condition is strongly recommend. This fact results in an intuitive criterion to determine when a fixed reset-time approach is not advised.

Both proposed criteria can be combined and formally stated as follows. Given a reset system with unstable base system (3.27) whose state matrix is A_η and whose unstable conjugate dominant poles are $p_u = -\xi\omega_n \pm j\omega_n\sqrt{1-\xi^2}$, the following simple procedure gives a sub-optimal constant reset interval Δ that maximizes the performance of the closed-loop response,

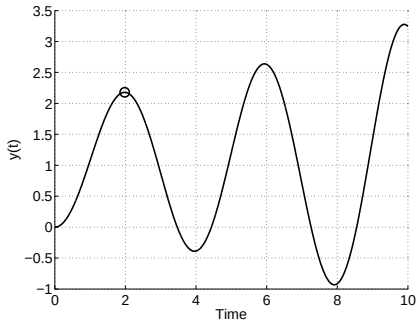

Figure 3.2: Solid line is the transient response of an unstable base system whose dominant unstable poles have a damping ratio $\xi = -0.052$ and a natural frequency $\omega_n = 1.59$. Then, $t_{peak} = \pi/1.59 \approx 1.98$ and is represented by a circle.

and determines whether by resetting the system periodically every Δ, the transient response would be worse than by resetting the system when its output reaches the reset surface (i.e. $x(t) \in \mathcal{M}$, $x(t) \in \mathcal{J}$).

Search procedure:

- Tune K_P, K_I, A_ζ, and B_ζ so that A_η has a pair of unstable conjugate dominant poles.
- Define a discrete set $\mathcal{D} = \{a \cdot \Delta_s : a \in \mathbb{N} \backslash \{0\}\}$, with an arbitrary resolution Δ_s.
- Compute the spectrum radius of the transition matrix $\rho(A_R e^{A_\eta \Delta_i})$ for every $\Delta_i \in \mathcal{D}$.
- Determine the couple $(\Delta, \rho(A_R e^{A_\eta \Delta}))$ such that $\rho(A_R e^{A_\eta \Delta})$ is minimum.
- Compute $t_{peak} = \pi / w_n$.
- If $\Delta \geq t_{peak}$, using a fixed reset-time approach is ill-advised.
- If $\Delta < t_{peak}$, resetting the system every Δ will maximize the performance of the transient response.

3.4 Simulation Results

In this section, extensive simulations are presented in order to show the effectiveness of our proposed ReOs, and the effect of each reset condition on the estimation process. Our first aim is to determine which of the previously presented reset conditions is more suitable for the ReO structure. To this end, we compare the simulation results obtained by an ReO based on the

zero crossing reset condition, an ReO based on the sector reset condition, and an ReO that is reset at fixed times, which in the following will be denoted by ReO_{ZC}, ReO_{SC}, ReO_{FT} respectively. These simulation results have been obtained by using Simulink with the ode3 solver.

Initially, let us consider the following third-order noise-free LTI system:

$$\begin{array}{rl} \dot{x}_1(t) & = -4.5x_1(t) - 4x_2(t) + 0.5x_3(t) + 0.1u(t) \\ \dot{x}_2(t) & = 0.5x_1(t) - 2x_2(t) - 1.1u(t) \\ \dot{x}_3(t) & = -0.5x_1(t) - 3x_3(t) - 0.5u(t) \\ y(t) & = x_1(t) \end{array} \tag{3.30}$$

with $x(t=0) = [-2.3; 1.5; 1.8]^T$, and $u(t) = sin(5t)$. According to (3.1), (3.30) has the following parameters:

$$A = \begin{bmatrix} -4.5 & -4 & 0.5 \\ 0.5 & -2 & 0 \\ -0.5 & 0 & -3 \end{bmatrix}, \quad B = \begin{bmatrix} 0.1 \\ -1.1 \\ -0.5 \end{bmatrix}, \quad C = \begin{bmatrix} 1 \\ 0 \\ 0 \end{bmatrix}^T. \tag{3.31}$$

Initially, we choose the same tuning parameters for all ReO as it is shown in Table 3.1. These parameters have been obtained following the tuning rules explained in section 3.3.2. For this reason K_P, K_I, A_ζ, and B_ζ have been tuned so that A_η is not Hurwitz. Following the previously presented search procedure and with the tuning parameters shown in Table 3.1, the Fig. 3.3 is obtained. In this case, the minimum spectral radius results from $\Delta = 0.26$. The unstable poles of the Example (3.30) have a damping ratio $\xi = -0.4236$ and a natural frequency $\omega_n = 0.8045$, and then $t_{peak} = \pi/1.59 \approx 4.3110$. Since $\Delta < t_{peak}$, resetting the system every $\Delta = 0.26$ maximizes the performance of the transient response as it is shown in Fig. 3.4. In this case, despite the fact that the closed-loop estimation process is unstable, the ReO_{FT} is not only capable of stabilizing it but also achieves an excellent performance. However, this comparison is not totally fair since neither ReO_{ZC} nor ReO_{SC} have been tuned according to their corresponding guidelines. In fact, to our best knowledge, there generally exist some tuning matrices obtained following the guidelines shown in section 3.2.3 such that an ReO based on an RTI condition (either zero crossing or sector condition) performs significantly better that an ReO based on an RTD condition.

To see this, let us readjust both RTI observers following the guidelines shown in section 3.2.3. Specifically, these new tuning parameters of each ReO are now shown in Table 3.2. Notice that when it is possible, the tuning parameters are equal in order to make the results more comparable. Consequently, the only tuning parameter that is different is the integral gain K_I of the ReO_{FT}. As it is shown in Fig. 3.5, both ReO_{ZC} and ReO_{SC} behave considerably better than the ReO_{FT} in this case. This superior performance

Table 3.1: Tuning parameters of each ReO for Example (3.30)

AO	K_P	K_I	A_ζ	B_ζ
ReO_{ZC}	$[2.5, -1.75, -2.5]^T$	$[-20, -35, 5]^T$	-0.1	1
ReO_{SC}	$[2.5, -1.75, -2.5]^T$	$[-20, -35, 5]^T$	-0.1	1
ReO_{FT}	$[2.5, -1.75, -2.5]^T$	$[-20, -35, 5]^T$	-0.1	1

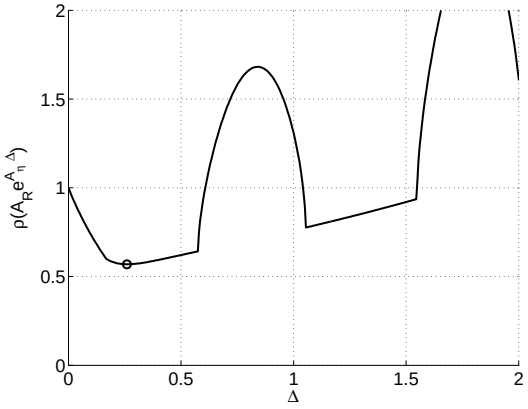

Figure 3.3: $\rho(A_R e^{A_\eta \Delta})$ vs Δ for Example (3.30). Minimum value is represented by a circle and is obtained with $\Delta = 0.26$.

can be easily checked by computing and comparing their corresponding Integral of Absolute Error (IAE) and Integral of Time multiplied by Absolute Error (ITAE). These performance indexes are defined as follows:

$$\begin{array}{ll} IAE_\alpha & = \int_0^\infty (|\alpha(t) - \hat{\alpha}(t)|)dt, \\ ITAE_\alpha & = \int_0^\infty (|\alpha(t) - \hat{\alpha}(t)| \cdot t)dt, \end{array} \tag{3.32}$$

where α can be either $x_1(t)$, $x_2(t)$, or $x_3(t)$. Obtained results are summarized in Table 3.3.

It is worth mentioning that in all the simulation results presented so far both ReO_{ZC} and ReO_{SC} behave exactly in the same way. This is because for some structures of reset systems (like low-pass filters) the two reset conditions are equivalent, and the resultant system behaves in the same way except under some special initial conditions [168]. That is the sort of structure used for both ReOs, as it can be seen analyzing (3.2) and (3.13).

Fig. 3.6 shows how slight differences on the estimation error appear when the initial reset state $\zeta(t)$ is modified. To understand this, it is worth remembering that the ReO_{SC} is reset depending on the sign of multiplying the output estimation error $\tilde{y}(t)$ by the reset integral term $\zeta(t)$, and hence, additional resets might take place through a proper selection of the initial value $\zeta(t = 0)$, which results in a somewhat faster estimation process, as it is shown in Fig. 3.6.

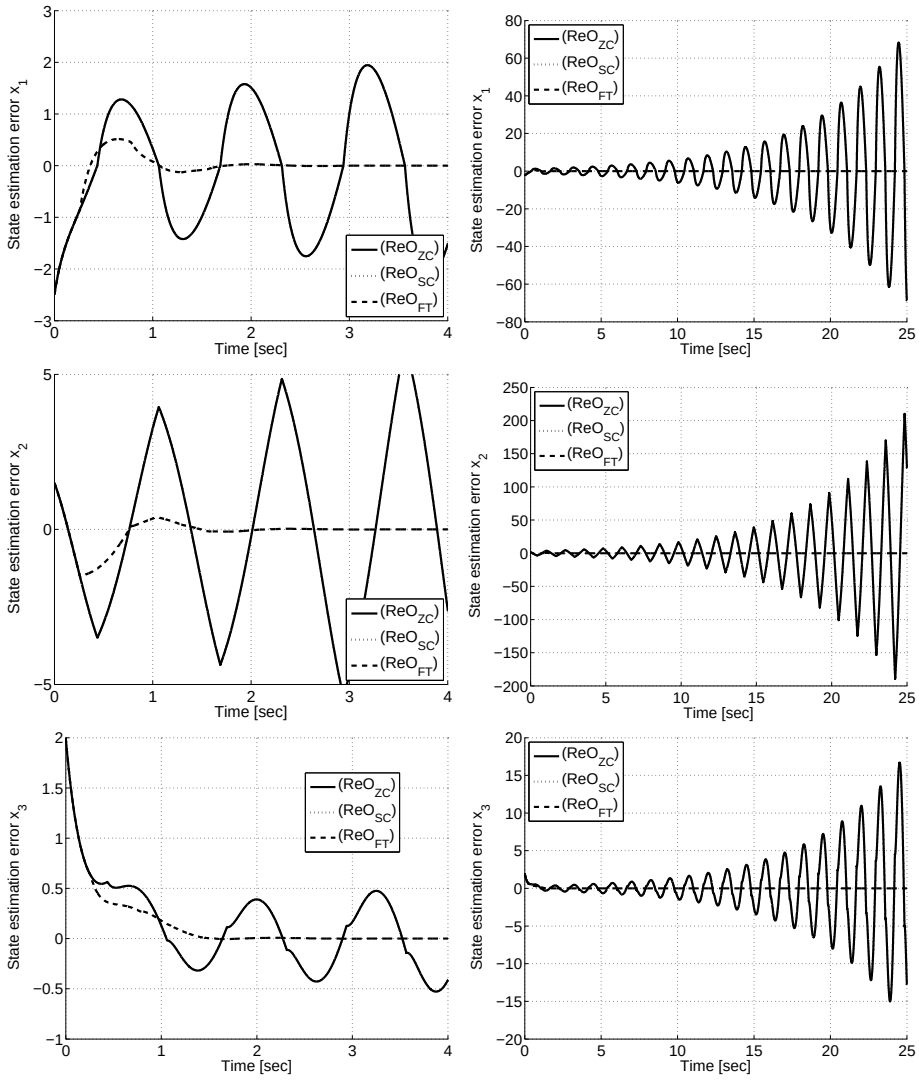

Figure 3.4: State estimation error $\tilde{x}(t)$ for each adaptive observer for Example (3.30). Solid lines have been obtained by using the ReO_{ZC}. Dotted lines have been obtained by using the ReO_{SC}. Dashed lines have been obtained by using the ReO_{FT}. Note that both ReO_{ZC} and ReO_{SC} behave exactly in the same way.

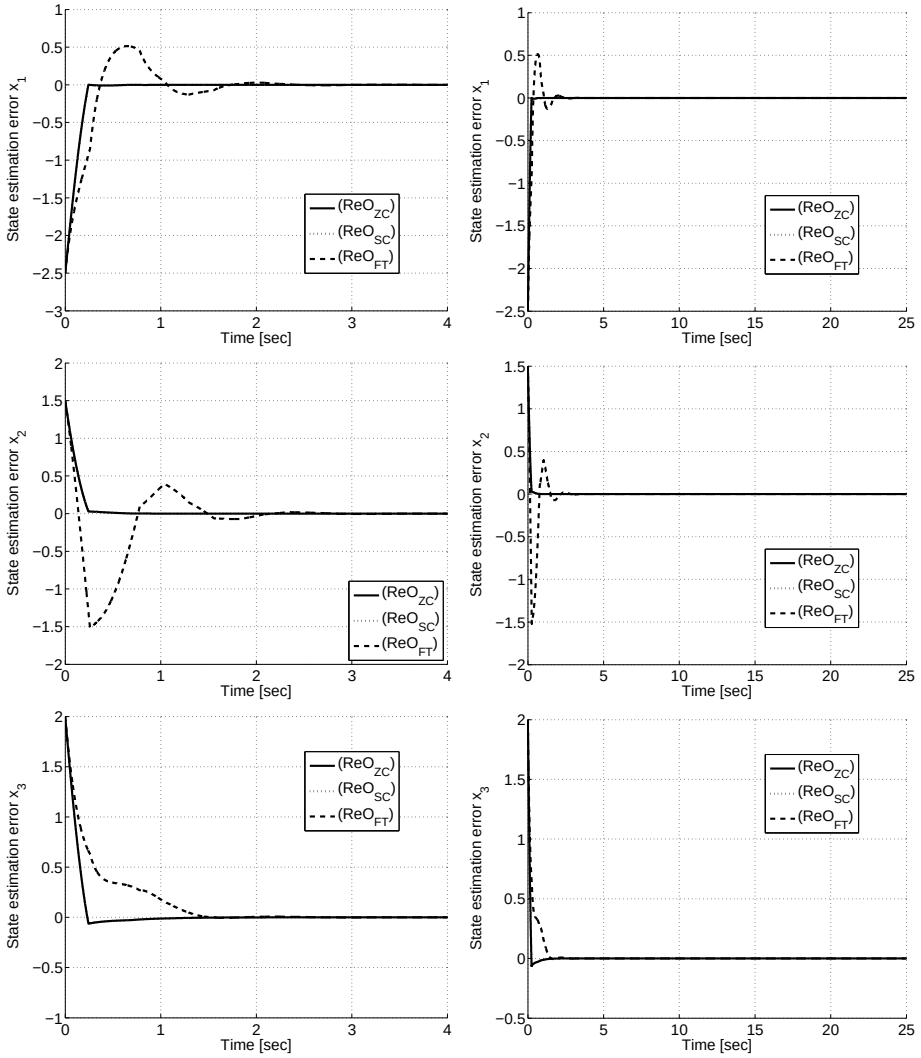

Figure 3.5: State estimation error $\tilde{x}(t)$ for each adaptive observer for Example (3.30). Solid lines have been obtained by using the ReO_{ZC}. Dotted lines have been obtained by using the ReO_{SC}. Dashed lines have been obtained by using the ReO_{FT}. Note that both ReO_{ZC} and ReO_{SC} behave exactly in the same way.

Table 3.2: Tuning parameters of each ReO for example 3.30

AO	K_P	K_I	A_ζ	B_ζ
ReO_{ZC}	$[2.5, -1.75, -2.5]^T$	$[25, -12, -20]^T$	-0.1	1
ReO_{SC}	$[2.5, -1.75, -2.5]^T$	$[25, -12, -20]^T$	-0.1	1
ReO_{FT}	$[2.5, -1.75, -2.5]^T$	$[-20, -35, 5]^T$	-0.1	1

Table 3.3: AO Performance Indexes for example (3.30).

AO	$\text{IAE}_{\tilde{x}_1}$	$\text{IAE}_{\tilde{x}_2}$	$\text{IAE}_{\tilde{x}_3}$	$\text{ITAE}_{\tilde{x}_1}$	$\text{ITAE}_{\tilde{x}_2}$	$\text{ITAE}_{\tilde{x}_3}$
ReO_{ZC}	0.275	0.166	0.234	0.022	0.015	0.033
ReO_{SC}	0.275	0.166	0.234	0.022	0.015	0.033
ReO_{FT}	0.728	0.890	0.577	0.310	0.498	0.224

Analyzing the results obtained until now, it is possible to draw the first conclusions. It has been shown than an ReO_{FT} can behave better than either an ReO_{ZC} or an ReO_{SC} with the same parameters, providing that these parameters were designed following the RTD guidelines. However, once both RTI ReOs are designed according their own tuning rules, they substantially outperform any ReO reset at fixed time instants. Further results about this point are shown in Appendix A. Once the reset condition based on fixed reset intervals has been discarded, we can just focus on analyzing both RTI ReOs, that is, ReO_{ZC} and ReO_{SC}. It has been shown that both give exactly the same estimation response except for some initial conditions of the reset integral term $\zeta(t)$. However, how to select that initial value in order to improve performance is far from trivial, since it depends on the interrelation between system and observer dynamics, their initial conditions, and the likely presence of unknown disturbances. Moreover, it is worth remarking that most observers initialize all their states to zero by default, when no information about the real system is available. For these reasons, we will consider in the following simulations, that all the ReO initial states are set to zero, and therefore, both ReO_{ZC} and ReO_{SC} will behave exactly in the same way. Consequently, and to increase the readability of the figures, we will show only the response of an ReO_{SC} that in the following will be simply denoted by ReO.

Once a suitable reset condition for our ReO structure has been founded, the next step consists in comparing its performance with the one obtained with other existing observers, in order to truly determine its potential. To this end, we compare the simulation results obtained by an ReO with a proportional integral observer PIO, (2.9) and a disturbance observer DO (2.7). As a benchmark, we extend the previously presented example (3.30) with different sort of disturbances so it could be understood whether performance

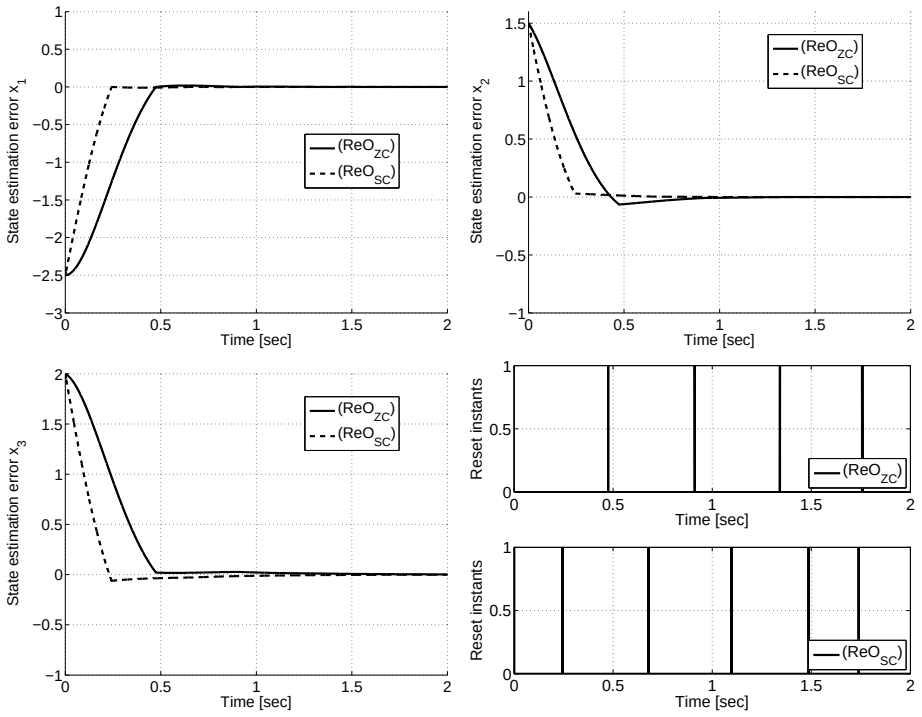

Figure 3.6: Effect of the initial reset state $\zeta(t)$ on the state estimation error $\tilde{x}(t)$ with $\zeta(t=0)=0.5$. Solid lines have been obtained by using the ReO_{ZC}. Dashed lines have been obtained by using the ReO_{SC}.

will consistently improve for all possible disturbances.

Let us begin considering the following third-order noise-corrupted LTI system:

$$\begin{array}{rl} \dot{x}_1(t) & = -4.5x_1(t) - 4x_2(t) + 0.5x_3(t) + 0.1u(t) + 0.1w(t) \\ \dot{x}_2(t) & = 0.5x_1(t) - 2x_2(t) - 1.1u(t) - 1.1w(t) \\ \dot{x}_3(t) & = -0.5x_1(t) - 3x_3(t) - 0.5u(t) - 0.5w(t) \\ y(t) & = x_1(t) \end{array} \tag{3.33}$$

with $x(t=0) = [-2.3; 1.5; 1.8]^T$, and $u(t) = sin(5t)$, which has the parameters shown in (3.31), apart from the disturbance input matrix B_w which is now given by $B_w = B$.

In the following, we will consider three different sorts of disturbances $w(t) = \{w_1(t), w_2(t), w_3(t)\}$. The idea is to cover most of the typical situations that could be found in practice, including high frequency noise, slowly varying perturbation, and constant disturbance. To this end, we will define $w_1(t)$ as a zero-mean high frequency noise, whose dynamics are given by $w_1(t) = sin(25t)$. Additionally, $w_2(t)$ and $w_3(t)$ are a time-varying perturbation and a constant disturbance respectively, whose dynamics are

Table 3.4: Tuning parameters of each observer for example 3.33. NR stands for non required

AO	K_P	K_I	A_ζ	B_ζ	A_z	B_z	A_w
ReO	$[2.5, -1.75, -2.5]^T$	$[25, -12, -20]^T$	-0.1	1	NR	NR	NR
PIO	$[2.5, -1.75, -2.5]^T$	$[25, -12, -20]^T$	NR	NR	-0.1	1	NR
DO	$[2.5, -1.75, -2.5]^T$	NR	NR	NR	NR	NR	0

governed by the following state space representation

$$\begin{aligned} \dot{w}_2(t) &= -0.2w_2(t) \\ \dot{w}_3(t) &= 0 \end{aligned} \tag{3.34}$$

with $w_2(t=0) = 1$ and $w_3(t=0) = 1$.

The tuning parameters of each observer are given in Table 3.4, where the notation corresponding to each observer has been used. As previously, tuning parameters have been set to the same values when it has been possible, in order to guarantee a fair comparison.

Fig. 3.7 shows the state estimation error $\tilde{x}(t)$ for each observer when $w(t) = w_1(t)$. It is worth mentioning that two different time spans are considered (i.e. $t = [0, 4]$ and $t = [0, 25]$) in order to stress on the different behavior of each algorithm not only in their transient stage but also in steady state. In this case, both ReO and PIO behave substantially better than the DO. The rationale behind this is that the integral gains of both observers (i.e. K_I, A_ζ and A_z), can be used to increase the convergence speed of the estimation process. In general, these additional degrees of freedom have to be tuned carefully, since an oscillating behavior can be obtained if K_I is chosen to be too large. However, this drawback can be minimized by resetting the integral term, being that the reason why the ReO has a response as quick as the PIO but without overshooting. This superior performance can be better compared by computing their corresponding IAE and ITAE, which are given in Table 3.5. Analyzing the obtained results, it is evident that the ReO clearly outperforms other observers when the system to be observed is affected by zero-mean disturbances, since it obtains a significantly lower IAE and ITAE for all involved state variables.

A different behavior can be found when the system is affected with non-zero mean disturbances. To see this, the state estimation error $\tilde{x}(t)$ for each observer when $w(t) = w_2(t)$ and $w(t) = w_3(t)$ are depicted in Figs. 3.8 and 3.9 respectively, whereas both IAE and ITAE for both sort of disturbances are shown in Table 3.5. In this case, the ReO still behaves better than the PIO in general, however it is beaten by the DO in some cases. Analyzing the results given in Table 3.5 when $w(t) = w_3(t)$, it can be seen that the ReO obtains the lowest $\text{IAE}_{\tilde{x}_1}$ and $\text{ITAE}_{\tilde{x}_1}$, which implies that the ReO is the

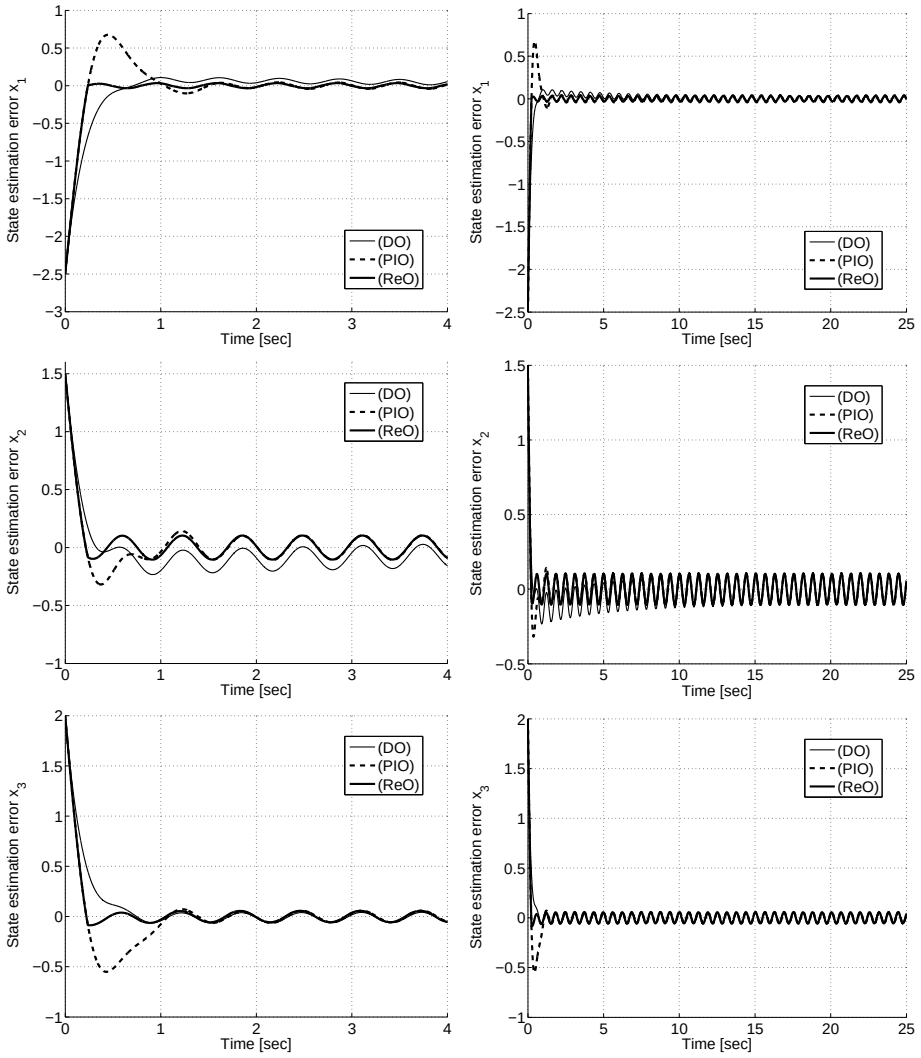

Figure 3.7: State estimation error $\tilde{x}(t)$ for each adaptive observer for Example (3.33) with $w(t) = w_1(t)$. (A) Thin solid lines have been obtained by using a disturbance observer (DO). (B) Dashed lines have been obtained by using a proportional integral adaptive observer (PIO). (C) Thick solid lines have been obtained by using the reset observer (ReO).

Table 3.5: AO Performance Indexes for Example (3.33).

AO	w(t)	$\text{IAE}_{\tilde{x}_1}$	$\text{IAE}_{\tilde{x}_2}$	$\text{IAE}_{\tilde{x}_3}$	$\text{ITAE}_{\tilde{x}_1}$	$\text{ITAE}_{\tilde{x}_2}$	$\text{ITAE}_{\tilde{x}_3}$
ReO	$w_1(t)$	0.275	0.166	0.234	0.022	0.015	0.033
PIO	$w_1(t)$	0.584	0.278	0.492	0.214	0.089	0.189
DO	$w_1(t)$	0.881	0.947	0.422	2.577	4.060	0.559
ReO	$w_2(t)$	0.582	1.388	0.573	1.669	6.451	2.017
PIO	$w_2(t)$	0.627	1.374	1.083	0.335	5.900	3.831
DO	$w_2(t)$	1.214	1.539	0.459	4.623	7.385	1.023
ReO	$w_3(t)$	0.414	5.986	3.186	1.392	73.911	38.564
PIO	$w_3(t)$	0.713	6.074	3.412	1.569	73.945	38.678
DO	$w_3(t)$	1.791	2.488	0.599	7.833	12.509	1.635

best choice to accurately estimate the system output despite the presence of disturbances. On the other hand, the DO obtains significantly lower $\text{IAE}_{\tilde{x}_2}$, $\text{IAE}_{\tilde{x}_3}$, $\text{ITAE}_{\tilde{x}_2}$, and $\text{ITAE}_{\tilde{x}_3}$, which implies that it is the only algorithm that effectively rejects the presence of non-zero mean disturbances. The rationale behind this is that a DO considers in its formulation the structure of the disturbance itself, since it includes a correction term that explicitly depends on B_w, which is considered to be known. Consequently, it results in a faster disturbance rejection. On the other hand, unlike other integral observers, an ReO eventually resets its integral term, which decreases its performance dealing with this sort of non-zero mean disturbances. Following that reasoning, the PIO should behave better than the ReO when estimating the non-measurable states, since its integral term is never reset. However, it behaves even slightly worse that the ReO as it is shown in Table 3.5. This result could be somewhat surprising, however, it is justified by the fact that this PIO has the same integral gain K_P than the ReO. It is worth remembering, that the integral gain was obtained following the ReO's tuning guidelines, and hence, it might not be suitable for a PIO. This point would be further studied in the next chapter, where an optimally designed ReO will be compared with an also optimally designed PIO.

3.5 Discussion

Summing up, this chapter has thrown light on relevant topics for completely defining a formal and suitable structure for ReOs.

First, regarding what is the most suitable reset condition for ReOs, simulation results have shown that once both RTI ReOs are designed according to their own tuning rules, they substantially outperform any ReO reset at fixed time instants, being this the reason for discarding the RTD formulation. With regard to RTI formulations, both have strengths and weaknesses.

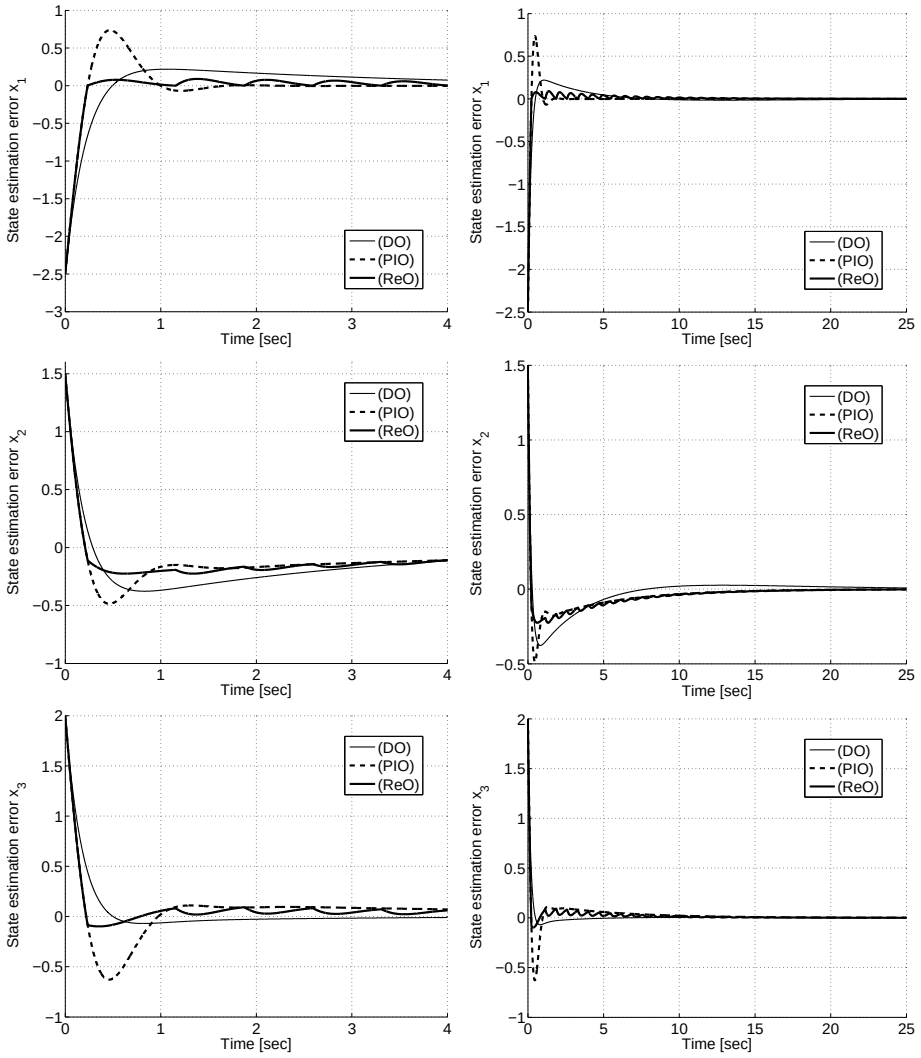

Figure 3.8: State estimation error $\tilde{x}(t)$ for each adaptive observer for Example (3.33) with $w(t) = w_2(t)$. (A) Thin solid lines have been obtained by using a disturbance observer (DO). (B) Dashed lines have been obtained by using a proportional integral adaptive observer (PIO). (C) Thick solid lines have been obtained by using the reset observer (ReO).

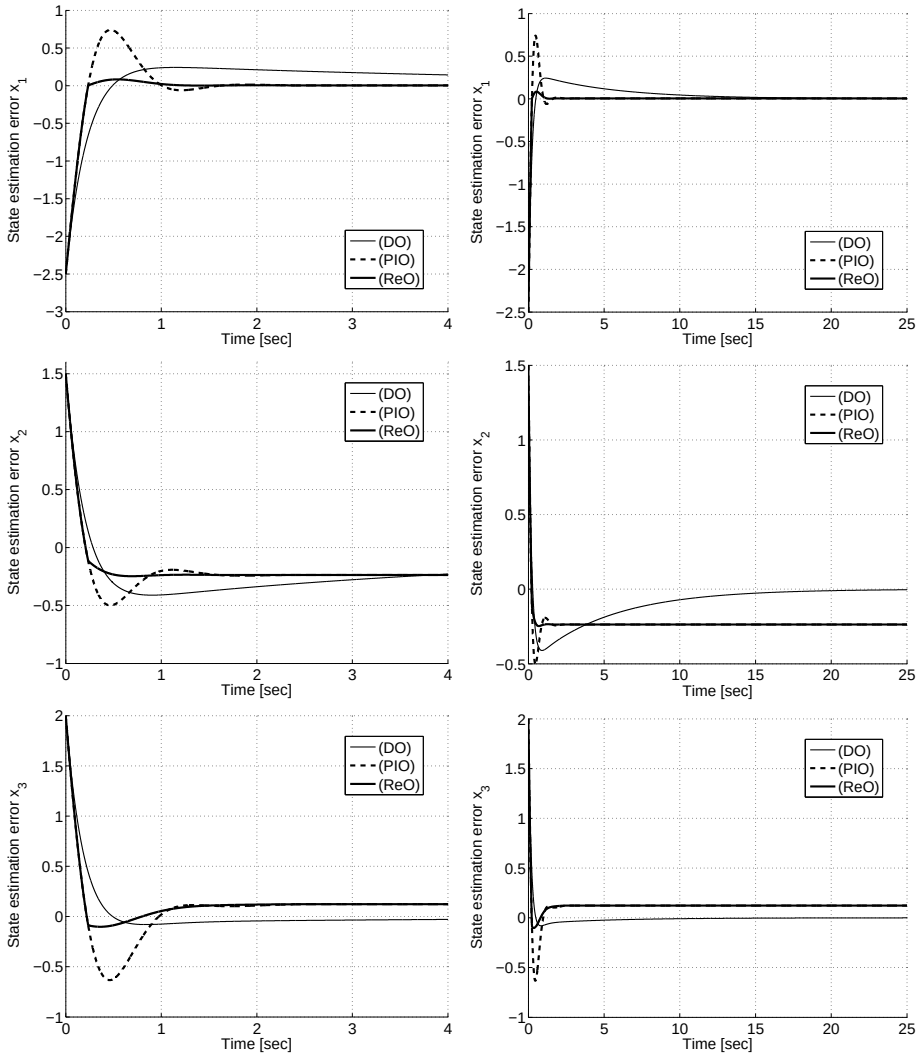

Figure 3.9: State estimation error $\tilde{x}(t)$ for each adaptive observer for Example (3.33) with $w(t) = w_3(t)$. (A) Thin solid lines have been obtained by using a disturbance observer (DO). (B) Dashed lines have been obtained by using a proportional integral adaptive observer (PIO). (C) Thick solid lines have been obtained by using the reset observer (ReO).

It is well known that although the stability analysis based on the sector condition is generally less conservative than the one based on the zero crossing condition, the latter is considerably easier to implement. Therefore, a definitive criterion to choose one could be based on the performance obtained with each one. However, it has been shown that ReO's reset condition based on zero crossing and sector condition give exactly the same estimation response for the initial conditions generally used in practice (i.e. all the ReO initial states are set to zero). For this reason, both reset conditions are equally suitable and will be considered in the following chapters.

Second, regarding the ReO's achievable performance and their behavior dealing with noise corrupted systems, obtained results have shown that a properly designed ReO generally achieves a better performance than other existing alternatives such as PIO and DO. An exception would be when the system is affected by disturbances with a steady-state offset, since the ReO might need more time to reject the effect of the disturbance on the unknown variables. These results justify the need of a modification in the current structure of the ReO in order to obtain an observer that combines the excellent transient performance of ReOs with the quick disturbance rejection of DOs. However, there are also different modifications that could be done for different specific sorts of systems, such as time-delay systems or nonlinear systems. These and other modifications will be studied in the next chapter.

Chapter 4

On Time Delay and Disturbance Reset Observers

Once the reset observer's structure for linear systems has been formally defined, several extensions to different systems are presented. In particular, this chapter explores the achievable performance of reset observers dealing with time delay systems and systems affected by external disturbances. In both cases, stability issues are addressed considering both RTI reset conditions (i.e. zero crossing and sector condition). Simulation results will show that our proposed reset observer can outperform other existing estimation algorithms once it is properly tuned.

4.1 Introduction and Preliminaries

As it has been explained in Chapter 2, observers fall into three different categories depending on the purpose of the reconstructed information. In particular, state estimation for control purposes, parameter estimation for system identification and/or adaptive control, and disturbance estimation for fault monitoring and detection. In the previous Chapter, potential of ReO has only been analyzed in the case of state estimation. Moreover, it has been pointed out that the structure presented in Chapter 2 must be modified to improve its performance dealing with some sorts of disturbances. For this reason, different formulations of ReOs will be presented depending on the specific nature of the system to deal with. In particular, two different sorts of ReOs will be presented. An ReO for time-delay systems, and an ReO for disturbance estimation, due to the fact that time-delays as well as external disturbances are issues that usually appear in industry applications, in which we are specially interested. Since RTD ReOs have been proved to be inferior to both sorts of RTI ReOs (i.e. zero crossing reset condition and sector reset condition), only these latter ReOs will be considered.

Throughout this chapter, it is worth noting that any ReO formulation will include temporal regularization in order to avoid Zeno Solution, and hence, Assumption 2 is no longer needed. We use the notation proposed by [42], based on including an auxiliary variable τ which guarantees that the time interval between any two consecutive resets is not smaller than $\rho \in \mathbb{R}^+$, which is a small enough positive number. Temporal regularization generally does not cause any practical issue since ρ can be chosen to be arbitraryly small so that its effect on the ReO behavior is negligible. From the theoretical point of view, the main consequence of using temporal regularization is that the flow region becomes slightly enlarged, which will require some modifications in the stability analysis when the ReO based on sector condition is considered.

Finally, the following standard definition within the adaptive observer framework is introduced for future reference.

Definition 1. *A signal $u(t)$ is persistently exciting if there exists three positive reals k_1, k_2, T such that $k_1 \leq \int_t^{t+T} u^T(\tau)u(\tau)d\tau \leq k_2$ for all $t \geq 0$.*

4.2 ReO for Time-Delay Systems

The design of state observers for time-delay systems has attracted the attention of many researchers and practitioners, since time-delays often appear in many control applications [150]. It is worth mentioning that stability analysis of reset control systems has been recently extended to time-delay systems only for the case of zero crossing reset law. There are two main approaches to study the stability of time-delay systems, which depend on

whether the time-delay is included in the stability analysis or not [138]. Regarding the stability of reset control systems based on zero reset condition, the delay-dependent approach was addressed in [139], whereas the delay-independent stability analysis was given in [140]. Based on those results, we extend the results presented in the previous chapter to the time-delay system framework.

In this case, we address the problem of the state estimation of linear time-delay systems [171], which are described by:

$$\begin{aligned} \dot{x}(t) &= Ax(t) + A_d x(t-h) + Bu(t) + B_w w(t), \ t \geq 0 \\ x(t) &= \phi(t), \ t \in [-h, 0) \\ y(t) &= Cx(t) \end{aligned} \tag{4.1}$$

where $\phi(t)$ is the continuous initial function, $x(t) \in \mathbb{R}^n$ is the state vector, $u(t) \in \mathbb{R}$ is the input vector, $w(t) \in \mathbb{R}^n$ is the disturbance vector, $y(t) \in \mathbb{R}$ is the output vector, h is the constant known time delay in the range of $(0, h_{max}]$ where $h_{max} > 0$, $A \in \mathbb{R}^{n\times n}$, $A_d \in \mathbb{R}^{n\times n}$, $B \in \mathbb{R}^{n\times 1}$, $B_w \in \mathbb{R}^{n\times 1}$, and $C \in \mathbb{R}^{1\times n}$ are known constant matrices. We consider single-input single-output (SISO) systems only, since a suitable formulation of reset elements for multiple-input multiple-output (MIMO) systems is still an open research topic. Moreover, $u(t)$ is assumed persistently exciting, and the pair (A, C) is assumed observable.

4.2.1 Zero Crossing Reset Condition

In this case, ReO dynamics are given by:

$$\left.\begin{aligned} \dot{\hat{x}}(t) &= A\hat{x}(t) + A_d\hat{x}(t-h) + Bu(t) \\ &+ K_P\tilde{y}(t) + K_I\zeta(t) \\ \dot{\zeta}(t) &= A_\zeta\zeta(t) + B_\zeta\tilde{y}(t) \\ \hat{y}(t) &= C\hat{x}(t) \\ \dot{\tau}(t) &= 1 \end{aligned}\right\} \text{if } \eta(t) \notin \mathcal{M} \ \vee \ \tau \leq \rho, \tag{4.2}$$

$$\left.\begin{aligned} \hat{x}(t^+) &= \hat{x}(t) \\ \hat{\zeta}(t^+) &= A_r\zeta(t) \\ \hat{y}(t^+) &= \hat{y}(t) \\ \dot{\tau}(t^+) &= 0 \end{aligned}\right\} \text{if } \eta(t) \in \mathcal{M} \ \wedge \ \tau \leq \rho, \tag{4.3}$$

where $\eta(t) = [\tilde{x}(t) \ \zeta(t)]^T$, $\hat{x}(t)$ is the estimated state, $\tilde{x}(t) = x(t) - \hat{x}(t)$ is the state error, K_I and K_P represent the integral and proportional gain respectively. $\tilde{y}(t) = y(t) - \hat{y}(t)$ is the output estimation error, $\zeta(t)$ is the reset integral term, $A_\zeta \in \mathbb{R}$ and $B_\zeta \in \mathbb{R}$ are two tuning scalars which regulate the transient response of ζ, and A_r is the reset matrix. Specifically, we define $A_r = 0$, since the reset integral term $\zeta(t)$ is reset to zero when $\zeta(t) \in \mathcal{M}$. As

it has been explained previously, the reset term dynamics (4.2)-(4.3) include temporal regularization to avoid Zeno solutions.

To analyze the asymptotic stability of 4.2, 4.3, let us begin defining the state estimation error as $\tilde{x}(t) = x(t) - \hat{x}(t)$, and by using the previously defined augmented state error $\eta(t) = [\tilde{x}(t) \;\; \zeta(t)]^T$, $\eta(t-h) = [\tilde{x}(t-h) \;\; \zeta(t-h)]^T$, the error dynamics of the ReO based on the reset condition are given by

$$\left.\begin{array}{rcl} \dot{\eta}(t) & = & A_\eta\,\eta(t) + A_{\eta_d}\,\eta(t-h) + B_\eta\,w(t) \\ \tilde{y}(t) & = & C_\eta\,\eta(t) \end{array}\right\} \text{if } \eta(t) \notin \mathcal{M} \;\vee\; \tau \leq \rho, \quad (4.4)$$

$$\left.\begin{array}{rcl} \eta(t^+) & = & A_R\,\eta(t) \\ \tilde{y}(t^+) & = & \tilde{y}(t) \end{array}\right\} \text{if } \eta(t) \in \mathcal{M} \;\wedge\; \tau \leq \rho, \quad (4.5)$$

where

$$A_\eta = \left[\begin{array}{cc} A - K_P C & -K_I \\ B_\zeta C & A_\zeta \end{array}\right],\; A_{\eta_d} = \left[\begin{array}{cc} A_d & 0 \\ 0 & 0 \end{array}\right], \quad (4.6)$$

$$B_\eta = \left[\begin{array}{c} B_w \\ 0 \end{array}\right],\; C_\eta = \left[\begin{array}{cc} C & 0 \end{array}\right]. \quad (4.7)$$

In this case the stability analysis follows directly from Propositions 1-2 in [140] where quadratic stability of time-delay reset systems subject to the zero crossing reset condition is addressed. As long as the same reset condition is used, those results can be particularized for the stability of ReOs as follows.

Proposition 5. *For given A_η, A_{η_d}, B_η and A_R the augmented error dynamics shown in (4.4)-(4.5) with $B_w = 0$ is quadratically stable, if for any matrix Θ with $Im\,\Theta = Ker\,C$ there exist some matrix $P = P^T > 0$, $Q = Q^T > 0$ subject to*

$$\begin{array}{c} \left[\begin{array}{cc} A_\eta^T P + P A_\eta + Q & P A_{\eta_d} \\ A_{\eta_d}^T P & -Q \end{array}\right] \;<\; 0, \\ \Theta^T (A_R^T P A_R - P)\Theta \leq 0, \end{array} \quad (4.8)$$

which is a linear matrix inequality problem in the variables P, Q.

Proof. It is quite similar to the proof shown in Proposition 3 in [140]. Firstly, let us introduce the Lyapunov-Krasovskii functional [138] that is defined as:

$$V(\eta_t) = \eta^T(t) P \eta(t) + \int_{-h}^{0} \eta^T(t+\theta) Q \eta(t+\theta) d\theta, \quad (4.9)$$

for some symmetric and positive definite matrices P, Q with size $n \times n$. Notice that $V(\eta_t) \geq 0$, and that $V(\eta_t) = 0$ only if $\eta_t(\theta) = 0 \in \mathbb{R}^n$, for each $\theta \in [-h, 0]$.

Then, to prove the quadratic stability of our proposed ReOs based on the zero crossing reset condition, we have to check that:

$$\begin{array}{ll} \frac{d}{dt}V(\eta_t) < 0 & \eta(t) \notin \mathcal{M} \\ V(\eta_{t^+}) - V(\eta_t) \leq 0 & \eta(t) \in \mathcal{M} \end{array} \tag{4.10}$$

Note that these inequalities are the standard stability requirements for reset systems, and they guarantee that there exists a common Lyapunov function that decreases when the reset system is flowing, and does not grow when the reset system is within the reset region.

Then, let us take derivative of (4.9) to obtain

$$\begin{array}{rcl} \frac{d}{dt}V(\eta_t) & = & \dot{\eta}(t)^T P\eta(t) + \eta(t)^T P\dot{\eta}(t) \\ & & +\eta(t)^T Q\eta(t) - \eta(t-h)^T Q\eta(t-h) \\ & = & \left(\eta(t)^T A_\eta^T + \eta(t-h)^T A_{\eta_d}^T\right) P\eta(t) \\ & & +\eta(t)^T P\left(A_\eta\eta(t) + A_{\eta_d}\eta(t-h)\right) \\ & & +\eta(t)^T Q\eta(t) - \eta(t-h)^T Q\eta(t-h), \end{array} \tag{4.11}$$

and using the first term of (4.10), (4.11) can be rearranged as an equivalent LMI problem in the variables $P, Q > 0$

$$\left[\begin{array}{cc} A_\eta^T P + PA_\eta + Q & PA_{\eta_d} \\ A_{\eta_d}^T P & -Q \end{array}\right] < 0, \tag{4.12}$$

which is the first inequality of (4.8).

It remains to prove the second term of (4.10). Since the reset action is only active when $\eta(t) \in \mathcal{M}$, and thus does not affect the delay buffer $\eta(t+\theta)$ for any $\theta \in [-h, 0)$ then the integral part of the Lyapunov functional (4.11) does not contribute to the jump, thus the reset jump in second term of (4.10) results in that

$$V(\eta_{t^+}) - V(\eta_t) = \Theta^T(A_R^T P A_R - P)\Theta \leq 0 \tag{4.13}$$

for every $\eta(t) \in \mathcal{M} = \operatorname{Ker} C$, which is the second inequality of (4.8) and completes the proof. □

4.2.2 Sector Reset Condition

In this case, ReO dynamics are described as follows:

$$\left.\begin{array}{rcl} \dot{\hat{x}}(t) & = & A\hat{x}(t) + A_d\hat{x}(t-h) \\ & & +Bu(t) + K_P\tilde{y}(t) + K_I\zeta(t) \\ \dot{\zeta}(t) & = & A_\zeta\zeta(t) + B_\zeta\tilde{y}(t) \\ \hat{y}(t) & = & C\hat{x}(t) \\ \dot{\tau}(t) & = & 1 \end{array}\right\} \text{if } \eta(t) \in \mathcal{F} \vee \tau \leq \rho, \tag{4.14}$$

$$\left.\begin{array}{rcl} \hat{x}(t^+) & = & \hat{x}(t) \\ \hat{\zeta}(t^+) & = & A_r\zeta(t) \\ \hat{y}(t^+) & = & \hat{y}(t) \\ \dot{\tau}(t^+) & = & 0 \end{array}\right\} \text{if } \eta(t) \in \mathcal{J} \ \wedge \ \tau \leq \rho, \tag{4.15}$$

As it was shown in [58], as long as the sector condition is preferred the ReO can be regarded as a hybrid system with a *flow set* $\mathcal{F}$ and a *jump or reset set* $\mathcal{J}$. On the one hand, when $\eta(t) \in \mathcal{F}$, that is, if $\tilde{y}(t)$ and $\zeta(t)$ have the same sign, the ReO behaves as a proportional integral observer. On the other hand, if $\eta(t) \in \mathcal{J}$, that is, if $\tilde{y}(t)$ and $\zeta(t)$ have different sign, the integral term is reset according to the reset map A_r. According to these statements and since $\tilde{y}(t) = C\tilde{x}(t)$, the definition of both sets can be formalized by using the following augmented representation:

$$\mathcal{F} := \left\{\eta(t) : \eta^T(t)M\eta(t) \geq 0\right\}, \tag{4.16}$$

$$\mathcal{J} := \left\{\eta(t) : \eta^T(t)M\eta(t) \leq 0\right\}, \tag{4.17}$$

where $M = M^T$ is defined as

$$M = \left[\begin{array}{cc} 0 & C^T \\ C & 0 \end{array}\right]. \tag{4.18}$$

Since the ReO flows not only when $\eta^T(t)M\eta(t) \geq 0$ but also when $\tau \leq \rho$, the flow set $\mathcal{F}$ becomes slightly inflated. That inflated flow set is formally defined as $\mathcal{F}_\epsilon := \left\{\eta(t) : \eta^T(t)M\eta(t) + \epsilon\eta^T(t)\eta(t)\right\}$ where $\epsilon(\rho) \geq 0$ represents how the set is inflated [42]. Since $\epsilon \to 0$ as $\rho \to 0$, an arbitrarily small ρ can be chosen so that the effect of ϵ is small enough to be neglected [142]. Given that $\mathcal{F}_\epsilon$ slightly overflows into the jump set $\mathcal{J}$, the following assumption is needed to guarantee that the solution will be mapped to the flow set $\mathcal{F}$ after each reset and, consequently, there are no trajectories that keep flowing and jumping within $\mathcal{J}$.

In this case, error dynamics of the ReO based on the sector condition are as follows

$$\left.\begin{array}{rcl} \dot{\eta}(t) & = & A_\eta\,\eta(t) + A_{\eta_d}\,\eta(t-h) \\ & & +B_\eta\,w(t) \\ \tilde{y}(t) & = & C_\eta\,\eta(t) \end{array}\right\} \text{if } \eta(t) \in \mathcal{F} \ \vee \ \tau \leq \rho, \tag{4.19}$$

$$\left.\begin{array}{rcl} \eta(t^+) & = & A_R\,\eta(t) \\ \tilde{y}(t^+) & = & \tilde{y}(t) \end{array}\right\} \text{if } \eta(t) \in \mathcal{J} \ \wedge \ \tau \leq \rho, \tag{4.20}$$

where A_η, A_{η_d}, B_η, C_η, A_R are defined as in (4.6),(4.7).

In this case the quadratic stability is addressed in similar way than [58], although in this time the standard quadratic Lyapunov function candidate must be substituted for the previously presented Lyapunov-Krasovskii functional.

Proposition 6. *For given A_η, A_{η_d}, B_η and A_R the augmented error dynamics shown in (4.19)-(4.20) with $B_w = 0$ is quadratically stable, if there exist some matrix $P = P^T > 0$, $Q = Q^T > 0$ and scalars $\tau_F \geq 0$ and $\tau_J \geq 0$ subject to*

$$\begin{aligned} \left[\begin{array}{cc} A_\eta^T P + P A_\eta + Q + \tau_F (M + \epsilon I) & P A_{\eta_d} \\ A_{\eta_d}^T P & -Q \end{array} \right] &< 0, \\ A_R^T P A_R - P - \tau_J M \leq 0, & \end{aligned} \tag{4.21}$$

which is a linear matrix inequality problem in the variables P, Q, τ_F and τ_J.

Proof. In this case, to prove the quadratic stability of the ReO based on the sector reset condition, we have to check that:

$$\begin{array}{ll} \frac{d}{dt} V(\eta_t) < 0 & \eta(t) \in \mathcal{F}_\epsilon \\ V(\eta_{t^+}) - V(\eta_t) \leq 0 & \eta(t) \in \mathcal{J} \end{array} \tag{4.22}$$

where V is the Lyapunov-Krasovskii functional (4.9) and $\frac{d}{dt} V(\eta_t)$ is as defined in (4.11).

Since $\mathcal{F}_\epsilon := \left\{ \eta(t) : \eta^T(t)\, M\, \eta(t) + \epsilon \eta^T(t) \eta(t) \geq 0 \right\}$ and employing the S-procedure [120], the first term of (4.22) is equivalent to the existence of $\tau_F \geq 0$ such that

$$\frac{d}{dt} V(\eta_t) < -\tau_F \eta^T(t) (M + \epsilon I) \eta(t) \tag{4.23}$$

Rearranging terms of equations (4.23) and (4.11), the first term of (4.22) holds if the following inequality is satisfied

$$\begin{array}{l} \eta(t)^T \left(A_\eta^T P + P A_\eta + Q + (M + \epsilon I) \right) \eta(t) \\ + \eta(t-h)^T A_{\eta_d}^T P \eta(t) + \eta(t)^T P A_{\eta_d} \eta(t-h) \\ - \eta(t-h)^T Q \eta(t-h) < 0, \end{array} \tag{4.24}$$

which can be rearranged as an equivalent LMI problem in the variables $P, Q > 0$ and $\tau_F \geq 0$

$$\left[\begin{array}{cc} A_\eta^T P + P A_\eta + Q + (M + \epsilon I) & P A_{\eta_d} \\ A_{\eta_d}^T P & -Q \end{array} \right] < 0, \tag{4.25}$$

which is the first inequality of (4.21) and consequently, proves the first equation of (4.22).

Similarly, employing again the S-procedure, the second term of (4.22) holds if there exists $\tau_J \geq 0$ such that

$$V(\eta_{t^+}) - V(\eta_t) \leq \eta^T(t) \tau_J M \eta(t), \tag{4.26}$$

which is equivalent to

$$\eta(t)^T A_R^T P A_R \eta(t) - \eta^T(t) P \eta(t) - \eta(t)^T \tau_J M \eta(t) \leq 0. \tag{4.27}$$

Rearranging terms, (4.27) can be also rewritten as an equivalent LMI problem in the variables $P > 0$ and $\tau_J \geq 0$ as follows

$$A_R^T P A_R - P - \tau_J M \leq 0, \tag{4.28}$$

which is analogous to the second inequality of (4.21) and proves the second equation of (4.22) and, as a consequence, completes the proof of the proposition. □

Remark 1. It is worth noting that due to the effect of the temporal regularization, the first condition of (4.22) must be proved for any $\eta(t) \in \mathcal{F}_\epsilon$ rather for any $\eta(t) \in \mathcal{F}$. The rationale behind this can be better understood with the following explanation.

Let us consider all the different situations of flowing and resetting that can happen. If the ReO starts in the reset region, it would be reset as soon as $\tau \geq \rho$, and the state $\eta(t)$ would be mapped into the set $\mathcal{F}$ according to Assumption 1. Therefore, we can directly assume without loss of generality that the ReO starts flowing within the original flow set $\mathcal{F}$, that is $\eta^T(t) M \eta(t) \geq 0$. Eventually, it would hit the reset surface, i.e. $\eta^T(t) M \eta(t) \leq 0$, then due to the effect of the temporal regularization the following situations could arise.

a) Let us begin considering that the time regularization condition has already been satisfied (i.e. $\tau \geq \rho$) when the ReO hits the reset surface, and then it can be reset as usual. In this case, the flow region would be $\mathcal{F} := \{\eta(t) : \eta^T(t) M \eta(t) \geq 0\}$.

b) Let us now consider that the time regularization condition has not been satisfied yet (i.e. $\tau \leq \rho$) when the ReO hits the reset surface, and thus it cannot be reset yet. Obviously the ReO keeps flowing until $\tau \geq \rho$, but meanwhile, the state $\eta(t)$ might overflow into the adjacent reset region. Let assume in this case that it happens, and thus, the ReO has actually been flowing in the slightly inflated flow region $\mathcal{F}_\epsilon := \{\eta(t) : \eta^T(t) M \eta(t) + \epsilon \eta^T(t) \eta(t)\}$, which considers the original flow region $\mathcal{F}$ and a slight portion of the jump set adjacent to the original flow set boundary.

c) Finally, let us consider that the time regularization condition has not been satisfied yet (i.e. $\tau \leq \rho$) when the ReO hits the reset surface, and that the state $\eta(t)$ does not overflow into the adjacent reset region until $\tau \geq \rho$. In this case, the behavior of the system is the same than in the case 1), and the ReO has only been flowing in the original flow region $\mathcal{F}$.

For stability purposes, we have to prove that $\frac{d}{dt}V(\eta_t)$ is negative in any region wherein the state $\eta(t)$ can flow, and that $\Delta V(\eta_t) \leq 0$ for any region wherein the state $\eta(t)$ is reset. In particular, since $\mathcal{F} \subseteq \mathcal{F}_\epsilon$, $\frac{d}{dt}V(\eta_t)$ must be proven for all $\eta(t) \in \mathcal{F}_\epsilon$. If we only check $\frac{d}{dt}V(\eta_t)$ when $\eta(t) \in \mathcal{F}$, we cannot guarantee that the Lyapunov function is decreasing when the state $\eta(t)$ overflows into the adjacent reset region because of the temporal regularization, as it has been explained in item b). For this reason, we have to check $\frac{d}{dt}V(\eta_t)$ for all $\eta(t) \in \mathcal{F}_\epsilon$, and $\Delta V(\eta_t) \leq 0$ for all $\eta(t) \in \mathcal{J}$.

4.2.3 Generalized Reset Observer

The previously presented ReOs for time-delay systems can be extended to a more general structure that employs not only the current estimation error $\tilde{x}(t)$ but also the time-delayed estimation error $\tilde{x}(t-h)$. The dynamics of the generalized ReO based on the zero crossing reset condition are given by:

$$\left.\begin{array}{rcl} \dot{\hat{x}}(t) &=& A\hat{x}(t) + A_d\hat{x}(t-h) + Bu(t) \\ && +K_P\tilde{y}(t) + K_I\zeta(t) \\ && +K_{P_d}\tilde{y}(t-h) + K_{I_d}\zeta(t-h) \\ \dot{\zeta}(t) &=& A_\zeta\zeta(t) + B_\zeta\tilde{y}(t) \\ && +A_{\zeta_d}\zeta(t-h) + B_{\zeta_d}\tilde{y}(t-h) \\ \hat{y}(t) &=& C\hat{x}(t) \\ \dot{\tau}(t) &=& 1 \end{array}\right\} \text{if } \eta(t) \notin \mathcal{M} \vee \tau \leq \rho, \quad (4.29)$$

$$\left.\begin{array}{rcl} \hat{x}(t^+) &=& \hat{x}(t) \\ \hat{\zeta}(t^+) &=& A_r\zeta(t) \\ \hat{y}(t^+) &=& \hat{y}(t) \\ \dot{\tau}(t^+) &=& 0 \end{array}\right\} \text{if } \eta(t) \in \mathcal{M} \wedge \tau \leq \rho, \quad (4.30)$$

whereas for the sector reset condition the dynamics are

$$\left.\begin{array}{rcl} \dot{\hat{x}}(t) &=& A\hat{x}(t) + A_d\hat{x}(t-h) + Bu(t) \\ && +K_P\tilde{y}(t) + K_I\zeta(t) \\ && +K_{P_d}\tilde{y}(t-h) + K_{I_d}\zeta(t-h) \\ \dot{\zeta}(t) &=& A_\zeta\zeta(t) + B_\zeta\tilde{y}(t) \\ && +A_{\zeta_d}\zeta(t-h) + B_{\zeta_d}\tilde{y}(t-h) \\ \hat{y}(t) &=& C\hat{x}(t) \\ \dot{\tau}(t) &=& 1 \end{array}\right\} \text{if } \eta(t) \in \mathcal{F} \vee \tau \leq \rho, \quad (4.31)$$

$$\left.\begin{array}{rcl} \hat{x}(t^+) &=& \hat{x}(t) \\ \hat{\zeta}(t^+) &=& A_r\zeta(t) \\ \hat{y}(t^+) &=& \hat{y}(t) \\ \dot{\tau}(t^+) &=& 0 \end{array}\right\} \text{if } \eta(t) \in \mathcal{J} \wedge \tau \leq \rho, \quad (4.32)$$

where in both cases K_{I_d} and K_{P_d} represent the integral and proportional gains of the time-delayed estimation error respectively, $\tilde{y}(t-h) = y(t-h) - \hat{y}(t-h)$ is the time-delayed output estimation error, and $A_{\zeta_d} \in \mathbb{R}$ and $B_{\zeta_d} \in \mathbb{R}$ are additional tuning scalars that regulate the influence of time-delayed terms.

Asymptotic stability of generalized ReOs for both reset conditions can be straightforwardly checked by using the appropriate propositions previously presented and taking into account that now the matrix A_{η_d} is given by

$$A_{\eta_d} = \begin{bmatrix} A_d - K_{P_d}C & -K_{I_d} \\ B_{\zeta_d}C & A_{\zeta_d} \end{bmatrix}. \tag{4.33}$$

4.2.4 Simulation Results

In this section, an example is presented in order to show the effectiveness of our proposed ReOs. To this end, we compare the simulation results obtained by an ReO based on the zero crossing reset condition (ReO_{ZC}), and an ReO based on the sector reset condition (ReO_{SC}) with a PO and with a PIO. On the one hand, the PO will be tuned to minimize the overshooting and, as a consequence, it provides a smooth response. On the other hand, the PIO will be designed to minimize the rising time, and hence, it gives an oscillating and faster response. The next simulation example will show that our proposed ReOs can achieve both requirements (i.e. a smooth and quick response) simultaneously. These simulation results have been obtained by using Simulink with the ode3 solver.

Let us consider the following time-delay system based on Example 5.3 in [138]:

$$\begin{aligned} \begin{bmatrix} \dot{x}_1(t) \\ \dot{x}_2(t) \end{bmatrix} &= \begin{bmatrix} -2 & 0.1 \\ 0.1 & -0.9 \end{bmatrix} \begin{bmatrix} x_1(t) \\ x_2(t) \end{bmatrix} \\ &\quad + \begin{bmatrix} -0.75 & 0 \\ -0.75 & -0.75 \end{bmatrix} \begin{bmatrix} x_1(t-h) \\ x_2(t-h) \end{bmatrix} \\ &\quad + \begin{bmatrix} 0.5 \\ 2.5 \end{bmatrix} u(t) + \begin{bmatrix} 0.5 \\ 0.5 \end{bmatrix} w(t) \\ y(t) &= \begin{bmatrix} 1 & 0 \end{bmatrix} \begin{bmatrix} x_1(t) \\ x_2(t) \end{bmatrix} \end{aligned} \tag{4.34}$$

with $x(t=0) = x(t=h) = [1, -1]^T$, $u(t) = sin(5t)$, and $h = 0.2\, sec.$ The aim is to develop a state observer for the system described by (4.34) which satisfies that the state estimation error tends to zero without overshooting as fast as possible.

Additionally, let us outline the tuning parameter for each observer (i.e. PO, PIO, and ReO). Notice that when it is possible, the tuning parameters are equal for each observer in order to make the results more comparable.

Since the tuning process of each observer involves several parameters, let us outline how all these tuning parameters have been determined. Firstly, we have designed the PO in such a manner that its rising time is around 1.5 seconds without overshooting. After that, to design the oscillating PIO we have increased the K_I gain until its rising time is roughly equal to 0.5 seconds, which implies an oscillating estimation process. Finally, to make the results more comparable, the ReOs have the same K_I and K_P than the oscillating PIO.

Specifically, the parameters of the PO are $\hat{x}(t=0) = \hat{x}(t=h) = [0,0]^T$, $K_P = [0.05, -1]^T$, whereas the tuning parameters of the oscillating PIO are $\hat{x}(t=0) = \hat{x}(t=h) = [0,0]^T$, $z(t=0) = z(t=h) = 0$, $A_z = -0.5$, $B_z = 1$, $K_P = [0.05, -1]^T$, and $K_I = [16, -20]^T$. For a further discussion on the structure of POs and PIOs the reader is referred to [38] and [58].

On the other hand, both ReOs for the system (4.34) have the same tuning parameters. Namely, $\hat{x}(t=0) = \hat{x}(t=h) = [0,0]^T$, $\zeta(t=0) = \zeta(t=h) = 0$, $A_\zeta = -0.5$, $B_\zeta = 1$, $K_P = [0.05, -1]^T$, $K_I = [16, -20]^T$, $A_r = 0$, $\epsilon = 0$. Notice that the K_P and K_I gains of the ReOs are equal to the gains of the oscillating PIO.

The stability of both ReOs can be checked with the propositions given in Chapters 4.2.1, 4.2.2. According to Proposition 5, it is possible to guarantee the asymptotic stability of the ReO$_{ZC}$, since there exist some matrices $P, Q > 0$ that solve the LMI problem (4.8). In particular, a possible choice is:

$$\begin{aligned} P &= \begin{bmatrix} 6.977 & 3.037 & 0.360 \\ 3.037 & 2.434 & 0 \\ 0.360 & 0 & 49.436 \end{bmatrix}, \\ Q &= \begin{bmatrix} 14.207 & 3.207 & 0.929 \\ 3.207 & 1.624 & -0.078 \\ 0.929 & -0.078 & 11.232 \end{bmatrix}. \end{aligned} \tag{4.35}$$

Moreover, as stated in Proposition 6, it is also possible to guarantee the asymptotic stability of the ReO$_{SC}$, since there exist some matrices $P, Q > 0$ and scalars $\tau_F, \tau_J > 0$ that solve the LMI problem (4.21). Specifically, a possible choice is:

$$\begin{aligned} P &= \begin{bmatrix} 169.077 & 77.628 & -1.261 \\ 77.628 & 62.168 & -0.023 \\ -1.261 & -0.023 & 735.759 \end{bmatrix}, \\ Q &= \begin{bmatrix} 324.475 & 83.905 & 6.553 \\ 83.905 & 43.656 & -0.618 \\ 6.553 & -0.618 & 70.490 \end{bmatrix}, \\ \tau_F &= 403.039,\ \tau_J = 1.271. \end{aligned} \tag{4.36}$$

To analyze the effect of the disturbance $w(t)$ on the performance of our proposal, let us begin considering that the system (4.34) is noise-free, and

thus, $w(t) = 0$. In this case, the state estimation error $\tilde{x}(t) = [\tilde{x}_1(t), \tilde{x}_2(t)]^T$ of all the observers is shown in the left pictures of Fig. 4.1. It is evident that our proposed ReOs obtain a better performance compared with traditional PIOs, since it has a response as quick as the oscillating PIO but without overshooting. Notice that if we decrease the integral gain K_I of the oscillating PIO to avoid overshooting it will behave as the conservative PIO and, thus, its rising time will be higher than the obtained by ReOs. On the other hand, if we increase the integral gain K_I of the conservative PIO to reduce its rising time, it will behave as the oscillating PIO and, as a consequence, its response will be oscillating.

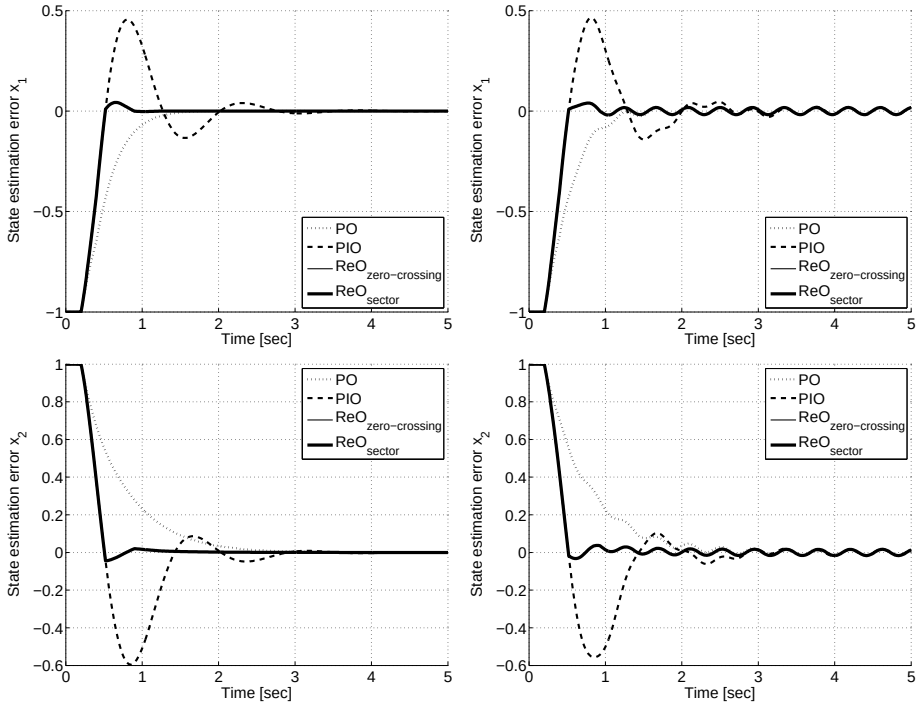

Figure 4.1: State estimation error $\tilde{x}(t)$ obtained for each observer when the system is noise-free (left) and affected by time-varying disturbance $w(t) = sin(15t)$ (right). Dotted lines have been obtained by using the proportional observer. Dashed lines have been obtained by using the oscillating proportional integral observer. Thin solid lines have been obtained by using the ReO_{ZC}. Thick solid lines have been obtained by using the ReO_{SC}. Note that the behavior of both ReOs is exactly the same.

Let us now consider that the system (4.34) is affected by time-varying disturbance $w(t) = sin(15t)$. Note that, a slow-time-varying disturbance $w(t)$ is preferred rather than white noise in order to represent changes on the operating point or gradual decalibration of the system which are issues that usually arise in the state observer framework [80]. The state estimation error

$\tilde{x}(t) = [\tilde{x}_1(t), \tilde{x}_2(t)]$ obtained in this case for all the observers is shown in the right pictures of Fig. 4.1. Despite the system is affected by an unknown disturbance, the state estimation error remains bounded around zero for all the observers. Nonetheless, ReOs still obtain a superior performance compared with linear observers.

4.3 ReDO: ReO for Disturbance Estimation

As it has been suggested previously, a modification in the ReO's structure would be needed in order to improve its performance providing that the system were affected by disturbances with a steady-state offset. The solution proposed is depicted in Fig. 4.2. It consists in including an additional non-reset integral feedback loop, which can be used to reject the effect of non-zero mean disturbances in the estimation process. The influence of the reset integral feedback loop (i.e. a pure ReO), and of the non-reset integral term (i.e. a standard DO) can be balanced through the reset ratio β. It is worth mentioning that this configuration is clearly influenced by recent results in the control reset system framework, where authors have been focused on improving the steady state performance of Clegg Integrators (CI). Since the state of the CI is eventually reset, it does not have the characteristic of eliminating the steady state error in response to step disturbances by itself, thus a steady state error is expected for all systems without an integrator. To overcome this drawback, a PI+CI controller was proposed in [152]. It consists of a PI controller that guarantees zero steady state error, and a CI controller that improves the transient response of the system.

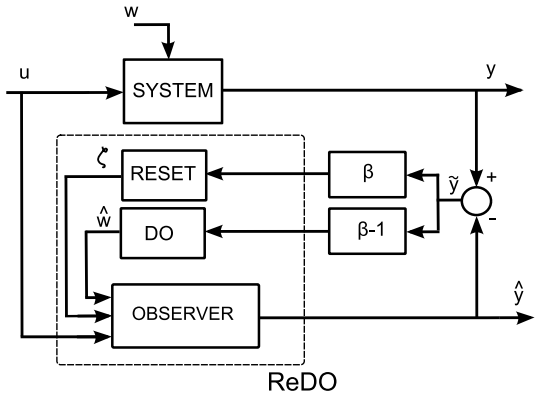

Figure 4.2: ReDO structure including its reset and non-reset feedback loops.

Obtained results showed that a properly designed ReO generally achieves a better performance than other existing alternatives such as PIO and DO. An exception would be when the system is affected by disturbances with a

steady-state offset, since the ReO might need more time to reject the effect of the disturbance on the unknown variables. These results justify the need of a modification in the current structure of the ReO in order to obtain an observer that combines the excellent transient performance of ReOs with the quick disturbance rejection of DOs, resulting in an observer that jointly estimates system states and external disturbances.

For this reason, we address in this section the problem of joint state and disturbance estimation for LTI systems which are described by

$$\begin{aligned} \dot{x}(t) &= Ax(t) + Bu(t) + B_w w(t) \\ \dot{w}(t) &= A_w w(t) \\ y(t) &= Cx(t) \end{aligned} \tag{4.37}$$

where $x \in \mathbb{R}^n$ is the state vector, $u \in \mathbb{R}^l$ is the input vector, $y \in \mathbb{R}^m$ is the output vector, $w \in \mathbb{R}^w$ is the disturbance vector, $A \in \mathbb{R}^{n\times n}$, $B \in \mathbb{R}^{n\times l}$, $C \in \mathbb{R}^{m\times n}$, $A_w \in \mathbb{R}^{w\times w}$ and $B_w \in \mathbb{R}^{n\times w}$ are known constant matrices.

4.3.1 ReDO Based on Zero Crossing Reset Condition

Similarly, ReDO dynamics for systems (4.37) are as follows:

$$\left.\begin{aligned} \dot{\hat{x}}(t) &= A\hat{x}(t) + Bu(t) + K_P\tilde{y}(t) \\ &\quad + K_I\zeta(t) + B_w\hat{w}(t) \\ \dot{\zeta}(t) &= A_\zeta\zeta(t) + \beta B_\zeta\tilde{y}(t) \\ \dot{\hat{w}}(t) &= A_w\zeta(t) + (1-\beta)\tilde{y}(t) \\ \hat{y}(t) &= C\hat{x}(t) \\ \dot{\tau}(t) &= 1 \end{aligned}\right\} \text{if } \eta \notin \mathcal{M} \vee \tau \leq \rho,$$

$$\left.\begin{aligned} \hat{x}(t^+) &= \hat{x}(t) \\ \zeta(t^+) &= A_r\zeta(t) \\ \hat{w}(t^+) &= \hat{w}(t) \\ \hat{y}(t^+) &= \hat{y}(t) \\ \tau(t^+) &= 0 \end{aligned}\right\} \text{if } \eta(t) \in \mathcal{M} \wedge \tau > \rho, \tag{4.38}$$

where $\eta(t) = \left[\tilde{x}^T(t) \;\; \hat{w}^T(t) \;\; \zeta^T(t)\right]^T$, $\hat{x}(t)$ is the estimated augmented state, which now includes the state error $\tilde{x}(t) = x(t) - \hat{x}(t)$, the disturbance error $\tilde{w}(t) = w(t) - \hat{w}(t)$, and the reset term $\zeta(t)$. Additionally, K_I and K_P are the integral and proportional gains respectively and $\tilde{y}(t) = y(t) - \hat{y}(t)$ is the output estimation error, $A_w \in \mathbb{R}$ is a tuning scalar that regulates the transient response of $\hat{w}(t)$. The reset surface $\mathcal{M}$ and the reset map A_r, are defined as in (3.2). As before, the reset term dynamics (4.38) includes temporal regularization to avoid Zeno solutions.

To analyze its asymptotic stability we firstly present its error dynamics,

which are simply given by

$$\left.\begin{array}{ll}\dot{\eta}(t) & = A_\eta\,\eta(t)\\ \tilde{y}(t) & = C_\eta\,\eta(t)\end{array}\right\}\ \text{if } \eta(t)\notin\mathcal{M}\ \vee\ \tau\le\rho,$$
$$\left.\begin{array}{ll}\eta(t^+) & = A_R\,\eta(t)\\ \tilde{y}(t^+) & = \tilde{y}(t)\end{array}\right\}\ \text{if } \eta(t)\in\mathcal{M}\ \wedge\ \tau>\rho, \tag{4.39}$$

where the augmented matrices are now given by

$$A_\eta=\left[\begin{array}{ccc} A-K_PC & B_w & -K_I\\ -(1-\beta)C & A_w & 0\\ \beta B_\zeta C & 0 & A_\zeta\end{array}\right], \tag{4.40}$$

and

$$C_\eta=\left[\begin{array}{ccc} C & 0 & 0\end{array}\right],\ A_R=\left[\begin{array}{ccc} I & 0 & 0\\ 0 & 1 & 0\\ 0 & 0 & A_r\end{array}\right]. \tag{4.41}$$

The following proposition states a sufficient condition for the existence of a quadratically stable ReDO based on the zero crossing reset condition.

Proposition 7. *For given A_η, C_η, and A_R according to (4.40)-4.41), the augmented error dynamics 4.39 is quadratically stable, if for any matrix Θ with $Im\,\Theta = Ker\,C$ there exists some matrix $P=P^T>0$ subject to*

$$\begin{array}{rcl} A_\eta^TP+PA_\eta & < & 0,\\ \Theta^T(A_R^TPA_R-P)\Theta & \le & 0,\end{array} \tag{4.42}$$

which is a linear matrix inequality problem in the variable P.

Proof. This proof directly follows from the proof of Proposition 1 in Chapter 3, and then it is omitted for brevity. □

4.3.2 ReDO Based on Sector Reset Condition

In an analogous way, ReAO based on sector reset condition dynamics for systems (4.37) are described as follows:

$$\left.\begin{array}{rcl}\dot{\hat{x}}(t) & = & A\hat{x}(t)+Bu(t)\\ & + & K_P\tilde{y}(t)+K_I\zeta(t)+B_w\hat{w}(t)\\ \dot{\zeta}(t) & = & A_\zeta\zeta(t)+\beta B_\zeta\tilde{y}(t)\\ \hat{w}(t) & = & A_w\zeta(t)+(1-\beta)\tilde{y}(t)\\ \hat{y}(t) & = & C\hat{x}(t)\\ \dot{\tau}(t) & = & 1\end{array}\right\}\ \text{if } \eta(t)\in\mathcal{F}\ \vee\ \tau\le\rho,$$
$$\left.\begin{array}{rcl}\hat{x}(t^+) & = & \hat{x}(t)\\ \zeta(t^+) & = & A_r\zeta(t)\\ \hat{w}(t^+) & = & \hat{w}(t)\\ \hat{y}(t^+) & = & \hat{y}(t)\\ \tau(t^+) & = & 0\end{array}\right\}\ \text{if } \eta(t)\in\mathcal{J}\ \wedge\ \tau>\rho, \tag{4.43}$$

where the *flow set* $\mathcal{F}$ and the *jump or reset set* $\mathcal{J}$ are defined as in (3.14), and the remaining parameters are defined as in 4.38. Additionally, it is worth mentioning that despite the fact that both regions are defined as usual: $\mathcal{F} := \{\eta : \eta^T M \eta \geq 0\}$, and $\mathcal{J} := \{\eta : \eta^T M \eta \leq 0\}$, the matrix M is no longer a $(n+m \times n+m)$ matrix but a $(n+w+m \times n+w+m)$ matrix given by

$$M = \begin{bmatrix} 0_{n,n} & 0_{m,w} & C^T \\ 0_{w,n} & 0_{w,w} & 0_{w,m} \\ C_{m,n} & 0_{m,w} & 0_{m,m} \end{bmatrix}. \tag{4.44}$$

In this case, its error dynamics are simply given by

$$\left.\begin{array}{ll} \dot{\eta}(t) & = A_\eta \, \eta(t) \\ \tilde{y}(t) & = C_\eta \, \eta(t) \end{array}\right\} \quad \text{if } \eta(t) \in \mathcal{F} \ \vee \ \tau \leq \rho,$$
$$\left.\begin{array}{ll} \eta(t^+) & = A_R \, \eta(t) \\ \tilde{y}(t^+) & = \tilde{y}(t) \end{array}\right\} \quad \text{if } \eta(t) \in \mathcal{F} \ \wedge \ \tau > \rho, \tag{4.45}$$

where the augmented matrices A_η, C_η, and A_R are defined as in (4.40)-(4.41).

Proposition 8. *For given A_η, C_η, and A_R the augmented error dynamic shown in (4.45) is quadratically stable, if there exist a matrix $P = P^T > 0$ and scalars $\tau_F \geq 0$ and $\tau_J \geq 0$ subject to*

$$\begin{array}{rcl} A_\eta^T P + P A_\eta + \tau_F (M + \epsilon I) & < & 0, \\ A_R^T P A_R - P - \tau_J M & \leq & 0, \end{array} \tag{4.46}$$

which is a linear matrix inequality problem in the variables P, τ_F and τ_J.

Proof. This proof trivially follows from the proof of Proposition 2 in Chapter 3, taking now into account that the ReDO is actually flowing in the augmented flow region $\mathcal{F}_\epsilon$ rather than in the standard flow region $\mathcal{F}$. Since $\mathcal{F}_\epsilon := \{\eta(t) : \eta^T(t) \, M \, \eta(t) + \epsilon \eta^T(t)\eta(t) \geq 0\}$ and employing the S-procedure [120], the first term of (3.19) is equivalent to the existence of $\tau_F \geq 0$ such that

$$\frac{d}{dt} V(\eta(t)) = \eta^T(t)(A_\eta^T P + P A_\eta)\eta(t) < -\tau_F \eta^T(t)(M + \epsilon I)\eta(t) \tag{4.47}$$

which results in the first term of 4.46.

On the other hand, the second term of 4.46 has already been proved in the proof of Proposition 2, and therefore, its proof is omitted. □

4.3.3 Simulation Results

In this section, additional simulations are presented in order to show the effectiveness of our proposed ReDO. To this end, we compare the simulation

Table 4.1: Tuning parameters of each observer for example 4.48. NR stands for non required

AO	K_P	K_I	A_ζ	B_ζ	A_w	β
ReO	$[2.5, -1.75, -2.5]^T$	$[0.5, -5, -2.5]^T$	-0.001	1	NR	0.5
ReDO	$[2.5, -1.75, -2.5]^T$	$[0.5, -5, -2.5]^T$	-0.001	1	0	NR
DO	$[2.5, -1.75, -2.5]^T$	NR	NR	NR	0	NR

results obtained by an ReDO with an ReO and a standard DO. As it has been explained in Chapter 3, ReOs as well as ReDOs will behave exactly in the same way independently of the reset condition chosen (i.e. zero crossing or reset condition) providing that their initial states are set to zero, which is the initial condition used for our proposals. For this reason, we only show in the following the results obtained with an ReO and ReDO based on the sector reset condition. All the simulation results have been obtained by using Simulink with the ode3 solver.

Let us consider again the third-order noise-corrupted LTI system (3.33) introduced in Chapter 3. In this case, we only consider non-zero mean noises whose dynamics are given by

$$\dot{w}(t) \quad = 0 \tag{4.48}$$

with $w(t = 0) = 1$.

The tuning parameters of each observer are given in Table 4.1. It is worth mentioning that we have modified the integral gain K_I of both the ReO and the ReDO compared to the reset observer used in the previous chapter, whose parameters were shown in Table 3.4. As it was explained in Chapter 3, DO achieved a faster disturbance rejection of non-zero mean disturbances due to the fact that it considers in its formulation the structure of the disturbance itself, by including a correction term that explicitly depends on B_w. Inspired by this fact, the steady-state performance of the ReO dealing with non-zero mean disturbances could be improved by selecting an integral gain K_I that would depend on B_w, (e.g. $K_I = \nu B_w$ where ν is an arbitrary positive number). According to our simulations, a reasonable trade-off between transient and steady state performance is achieved with $\nu = 5$. The effectiveness of this simple tuning criterion is shown in Fig. 4.3, where the state estimation error $\tilde{x}(t)$ for each observer are depicted. As previously, two different time spans are considered (i.e. $t = [0, 4]$ and $t = [0, 25]$) in order to highlight the different behavior of each algorithm in the transient stage as well as in the steady state.

It is evident that thank to this new criterion to tune the integral gain K_I, both reset observers completely reject the effect of the disturbance in the steady state, unlike the ReO observers designed in the previous chapter,

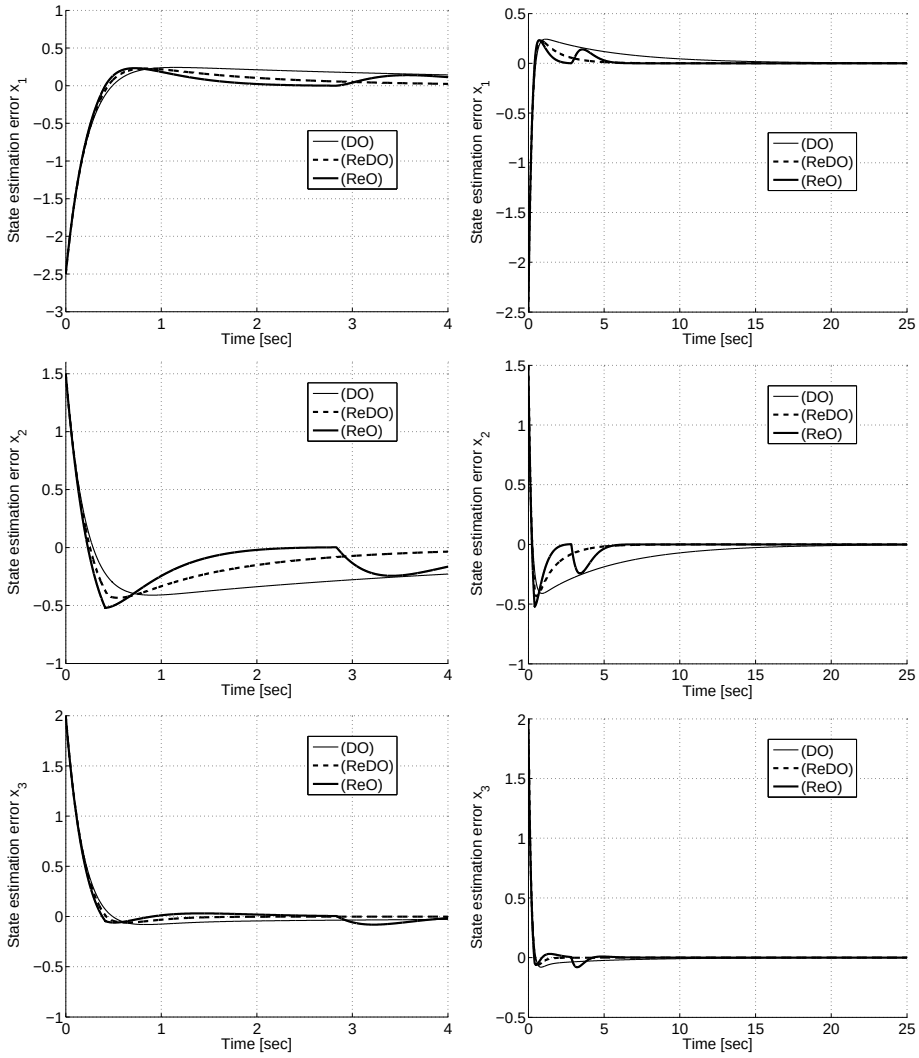

Figure 4.3: State estimation error $\tilde{x}(t)$ for each adaptive observer for example (4.48). (A) Thin solid lines have been obtained by using a disturbance observer (DO). (B) Dashed lines have been obtained by using a reset disturbance observer (ReDO). (C) Thick solid lines have been obtained by using the reset observer (ReO).

Table 4.2: AO Performance Indexes for example (4.48).

AO	$\text{IAE}_{\tilde{x}_1}$	$\text{IAE}_{\tilde{x}_2}$	$\text{IAE}_{\tilde{x}_3}$	$\text{ITAE}_{\tilde{x}_1}$	$\text{ITAE}_{\tilde{x}_2}$	$\text{ITAE}_{\tilde{x}_3}$
ReO	0.785	0.874	0.399	1.102	1.675	0.394
DO	1.791	2.488	0.599	7.832	12.509	1.635
ReDO	0.794	0.871	0.321	0.922	1.374	0.101

which obtained a poor performance dealing with non-zero mean disturbances (see Table 3.5). However, an even better performance can be obtained with the ReDO by properly tuning the reset ratio β. In particular, Fig. 4.3 shows how an ReDO with $\beta = 0.5$ combines the quick transient response of ReOs with the smooth disturbance rejection of DOs. This superior performance can be better compared by computing their corresponding IAE and ITAE, which are given in Table 4.2. Analyzing the obtained results, it is evident that the ReDO clearly outperforms other observers when the system to be observed is affected by non-zero mean disturbances, since it obtains a significantly lower IAE and ITAE for all involved state variables.

4.4 Discussion

Throughout this chapter we have shown how reset observers can be extended to different sorts of systems and/or specific purposes. On the one hand, regarding the different sorts of systems, we have shown the effectiveness of reset observers dealing with time-delay systems and noise corrupted systems. On the other hand, with regard to the modification of the reset observer structure for specific purposes, we have shown how reset observers can be extended for joint state and disturbance estimation (ReDO). The stability analysis for all these proposed extensions considering both reset-time independent formulations has been given. This approach was based on linear matrix inequalities, and consequently, it is easily computable. Additionally, extensive simulations have been given to underline the potential benefits of including a reset term in the observer's formulation independently of the system under study.

One of the relevant conclusions obtained from these results is the fact that the performance of reset observers dealing with non-zero mean disturbances not only depends on the eventual reset of the integral term ζ (as it was suggested in Chapter 3), but also on the value of the integral gain K_I (as it has been shown in this chapter). As the integral gain K_I is chosen as a function of the disturbance input matrix B_w, ReOs reject reasonably fast the effect of non-zero mean disturbances. This performance can be improved by including an additional non-reset integral feedback loop, resulting in an observer that jointly estimates system states and external disturbances

(ReDO). The influence of the reset integral feedback loop (i.e. a pure ReO), and of the non-reset integral term (i.e. a standard DO) can be balanced through the reset ratio β. The need of a different tuning criterion depending on the observer's structure and/or the external disturbances suggests that it would be interesting to develop a method to automatically determine the observer's tuning parameters in an optimal way.

Chapter 5

Reset Adaptive Observer and Optimal Design

In this chapter, the reset observer formulation is first extended to a class of nonlinear systems. This novel formulation will be the starting point for developing the adaptive version of our reset observer, which will jointly consider state and parameter estimation. Additionally, motivated by the negative effect of external disturbances on the reset observer's behavior, and the importance of properly tuning its parameters, a method to automatically determine the optimal reset observer's parameters by minimizing the effect of the external disturbances on the estimation error, is presented. Simulation results will show the effectiveness of an optimal designed reset observer compared to other optimal design methods for conventional observers.

5.1 Introduction

Here, some modifications on the ReO formulation are proposed so that the ReO can also be applied to a class of nonlinear systems. It is worth mentioning the importance of this contribution because most industry applications, in which we are considerably interested, exhibit complex dynamics that generally can be better represented with a nonlinear model.

In particular, we will focus on the special class of nonlinear systems presented in [70]. One of the main advantages of this especial structure is that it can easily be adapted to consider jointly state and parameter estimation (see, for instance [72]). Therefore, this structure will be the starting point for developing the adaptive version of our proposed ReO, which in the following will be denoted by ReAO, that jointly estimates system states and unknown constant parameters. It is worth mentioning the relevance of formally extending the reset observer to its adaptive formulation, because as it was explained in Chapter 2, parameter estimation plays a key role in system identification and adaptive control.

Finally, based on this modified formulation, a method to optimally determine the tuning parameters and the gains of the ReAO is presented. The effectiveness of the proposed ReAO will be illustrated through different simulation examples by comparison with an optimally designed PIAO. As previously, we will consider both RTI formulations. Namely, ReAO based on zero crossing reset condition as well as ReAO based on sector reset condition. Note that although this tunning method is only formulated for a class of nonlinear systems, it can be easily extended to other sort of systems such as time-delay and/or linear systems.

5.2 ReAO for a Class of Nonlinear Systems

Specifically, we address in this section the problem of joint state and unknown parameter estimation for a class of uncertain nonlinear systems which are described by

$$\begin{aligned} \dot{x}(t) &= Ax(t) + Bu(t) + \Lambda\phi(t)\theta + B_w w(t), \\ y(t) &= Cx(t), \end{aligned} \tag{5.1}$$

where $x \in \mathbb{R}^n$ is the state vector, $u \in \mathbb{R}^l$ is the input vector, $y \in \mathbb{R}^m$ is the output vector, $\theta \in \mathbb{R}^p$ is the unknown constant parameter vector which can be used to represent modeling uncertainties, $w \in \mathbb{R}^w$ is the disturbance vector, $A \in \mathbb{R}^{n\times n}$, $B \in \mathbb{R}^{n\times l}$, $C \in \mathbb{R}^{m\times n}$, $\Lambda \in \mathbb{R}^{n\times m}$, and $B_w \in \mathbb{R}^{n\times w}$ are known constant matrices. The nonlinearity $\phi(t) \in \mathbb{R}^{m\times p}$ is a time-varying matrix which depends on the input $u(t)$ and/or the output $y(t)$. In addition, $u(t)$ and $\phi(t)$ are assumed persistently exciting, and the pair (A, C) is assumed observable. As it is shown in [70], a class of nonlinear

systems can be formulated as a system described by (5.1) through a change of coordinates.

5.2.1 ReAO Based on Zero Crossing Reset Condition

In this case, ReAO dynamics are given by:

$$\left.\begin{array}{rcl} \dot{\hat{x}}(t) & = & A\hat{x}(t) + Bu + \Lambda\phi(t)\hat{\theta}(t) \\ & & +K_P\tilde{y}(t) + K_I\zeta(t) \\ \dot{\zeta}(t) & = & A_\zeta\zeta(t) + \tilde{y}(t) \\ \dot{\hat{\theta}}(t) & = & \Gamma\phi^T(t)\tilde{y}(t) - \Gamma\sigma_s\hat{\theta}(t) \\ \hat{y}(t) & = & C\hat{x}(t) \\ \dot{\tau}(t) & = & 1 \end{array}\right\} \text{if } \eta \notin \mathcal{M} \vee \tau \leq \rho, \qquad (5.2)$$

$$\left.\begin{array}{rcl} \hat{x}(t^+) & = & \hat{x}(t) \\ \zeta(t^+) & = & A_r\zeta(t) \\ \hat{\theta}(t^+) & = & \hat{\theta}(t) \\ \hat{y}(t^+) & = & \hat{y}(t) \\ \tau(t^+) & = & 0 \end{array}\right\} \text{if } \eta(t) \in \mathcal{M} \wedge \tau > \rho,$$

where $\eta(t) = \left[\tilde{x}^T(t) \;\; \zeta^T(t)\right]^T$, $\hat{x}(t)$ is the estimated state, $\tilde{x}(t) = x(t) - \hat{x}(t)$ is the state error, K_I and K_P are the integral and proportional gains respectively and $\tilde{y}(t) = y(t) - \hat{y}(t)$ is the output estimation error, $\zeta(t) \in \mathbb{R}$ is the reset integral term, $A_\zeta \in \mathbb{R}$ is a tuning scalar which regulates the transient response of $\zeta(t)$, A_r is the reset matrix, and the reset surface $\mathcal{M}$ and the reset map A_r, are defined as in (3.2). As before, the reset term dynamics (5.2) includes temporal regularization to avoid Zeno solutions.

Moreover, $\Gamma \in \mathbb{R}^{p\times p}$ is a positive definite matrix, and σ_s is a switching leakage term defined as [172]

$$\sigma_s = \left\{ \begin{array}{ll} 0 & \text{if } \|\hat{\theta}\| < T \\ \sigma & \text{if } \|\hat{\theta}\| \geq T \end{array} \right\}, \qquad (5.3)$$

which guarantees that the estimated parameter $\hat{\theta}$ is bounded and remains within a predefined threshold T, which is chosen to be large enough in such a manner that $T > \|\theta\|$, and where σ is a small positive constant. Although the discontinuity of σ_s may cause small oscillations on the switching surface $\|\hat{\theta}\| = T$, these oscillations never appear working on nominal conditions. In particular, they only appear in case of a failure affects the real system (5.1), and then the parameter estimate will drift until it reaches the switching surface. These failures include a degradation on the system sensors, an unexpected decalibration of the existing instruments, or a sudden change on the operating conditions. The switching leakage term (5.3) is an effective method to be robust to those failures by eliminating parameter drift and keeping the parameter estimates bounded.

As previously, to analyze the stability of this proposal we initially preset its error dynamics, which are as follows

$$\left.\begin{array}{ll}\dot{\eta}(t) & = A_\eta\,\eta(t) + B_\Lambda\phi(t)\tilde{\theta}(t) + B_\eta\,w(t)\\ \tilde{y}(t) & = C_\eta\,\eta(t)\\ \dot{\tilde{\theta}}(t) & = -\Gamma\phi^T(t)\tilde{y}(t) + \Gamma\sigma_s\hat{\theta}(t)\end{array}\right\} \quad \text{if } \eta(t)\notin\mathcal{M}\ \vee\ \tau\leq\rho,$$
$$\left.\begin{array}{ll}\eta(t^+) & = A_R\,\eta(t)\\ \tilde{y}(t^+) & = \tilde{y}(t)\\ \tilde{\theta}(t^+) & = \tilde{\theta}(t)\end{array}\right\} \quad \text{if } \eta(t)\in\mathcal{M}\ \wedge\ \tau>\rho, \tag{5.4}$$

where A_η, B_η, C_η and A_R are defined according to (3.4)-(3.5), and $B_\Lambda = [\Lambda\ 0]^T$.

Moreover, it is worth mentioning that the parameter error dynamic does not change after resets, that is, $\tilde{\theta}(t^+) = \tilde{\theta}(t)$. Only the reset term ζ of the augmented state error dynamic η is modified through A_R after resets, since $\eta(t^+) = A_R\,\eta(t)$. It is also worth pointing out that the output of the augmented error dynamic (5.4) is equal to the output of the ReAO observer (5.2), that is, $\tilde{y}(t) = C\tilde{x}(t) = C_\eta\,\eta(t)$.

Here, we state a sufficient condition for the existence of a quadratically stable ReAO assuming absence of disturbances, that is, $w(t) = 0$. This analysis is based on an LMI approach.

Proposition 9. *For given A_η, B_η, C_η, B_Λ and A_R the augmented error dynamic shown in (5.4) with $w = 0$ is quadratically stable, if for any matrix Θ with $Im\,\Theta = Ker\,C$ there exist some matrix $P = P^T > 0$ subject to*

$$\begin{array}{rcl} A_\eta^T P + P A_\eta & < & 0,\\ \Theta^T(A_R^T P A_R - P)\Theta & \leq & 0,\\ P B_\Lambda & = & C_\eta^T, \end{array} \tag{5.5}$$

which is a linear matrix inequality problem in the variables P, τ_F and τ_J.

Remark 2. For implementation purposes, it is worth noting that the equality constraint $PB_\Lambda = C^T$ can be replaced by the following LMI

$$\left[\begin{array}{cc} \delta I & PB_\Lambda - C^T\\ B_\Lambda^T P - C & \delta I \end{array}\right] \geq 0.$$

If this inequality is feasible for $\delta = 0$, the resulting P will satisfy the equality constraint $PB_\Lambda = C^T$ [84].

Proof. Let us begin considering the following quadratic Lyapunov function for the error dynamics described by (5.4):

$$V(\eta(t),\tilde{\theta}(t)) = \eta^T(t)\,P\,\eta(t) + \tilde{\theta}^T(t)\,\Gamma^{-1}\,\tilde{\theta}(t), \tag{5.6}$$

where $P = P^T > 0$ and $\Gamma = \Gamma^T > 0$.

To prove the stability of our proposed ReAO based on zero crossing reset condition we have to check that:

$$\begin{array}{ll} \dot{V}(\eta(t),\tilde{\theta}(t)) < 0 & \eta(t) \notin \mathcal{M}, \\ V(\eta(t^+),\tilde{\theta}(t^+)) - V(\eta(t),\tilde{\theta}(t)) \leq 0 & \eta(t) \in \mathcal{M}, \end{array} \tag{5.7}$$

these inequalities guarantee that there exists a common Lyapunov function $V(\eta(t),\tilde{\theta}(t))$ that decreases when the reset system is flowing, and does not grow when the reset system is within the reset region, which are the standard stability requirements for reset systems.

Firstly, let us take derivative of (5.6) to obtain

$$\begin{array}{rcl} \dot{V}(\eta(t),\tilde{\theta}(t)) & = & \dot{\eta}^T(t)P\eta(t) + \eta^T(t)P\dot{\eta}(t) \\ & & +\dot{\tilde{\theta}}^T(t)\,\Gamma^{-1}\,\tilde{\theta}(t) + \tilde{\theta}^T(t)\,\Gamma^{-1}\,\dot{\tilde{\theta}}(t) \\ & = & \eta^T(t)(A_\eta^T P + PA_\eta)\eta(t) \\ & & +\eta^T(t)\left(PB_\Lambda\phi(t) - C_\eta^T\phi(t)\right)\tilde{\theta}(t) \\ & & +\tilde{\theta}^T(t)\left(\phi^T(t)B_\Lambda^T P - \phi^T(t)C_\eta\right)\eta(t) + \varphi(t), \end{array} \tag{5.8}$$

where $\varphi(t) = 2\sigma_s\hat{\theta}^T(t)\tilde{\theta}(t)$. Notice that σ_s should be designed in such a manner that $\varphi(t)$ becomes non-positive in the space of the parameter estimates. Thus, let us prove that $\varphi(t)$ has an upper non-positive bound by using the Cauchy-Schwarz inequality and $T > \|\theta(t)\|$:

$$\begin{array}{rcl} \varphi(t) & = & \hat{\theta}^T(t)\sigma_s^T\left(\theta(t) - \hat{\theta}(t)\right) + \left(\theta(t) - \hat{\theta}(t)\right)^T\sigma_s\hat{\theta}(t) \\ & = & \sigma_s(\hat{\theta}^T(t)\theta(t) + \theta^T(t)\hat{\theta}(t) - 2\hat{\theta}^T(t)\hat{\theta})(t) \\ & \leq & \sigma_s\left(\|\hat{\theta}(t)\|T + T\|\hat{\theta}(t)\| - 2\|\hat{\theta}(t)\|^2\right) \\ & = & 2\sigma_s\left(\|\hat{\theta}(t)\|\left(T - \|\hat{\theta}(t)\|\right)\right). \end{array} \tag{5.9}$$

According to the first term of (5.3), as long as $\|\hat{\theta}(t)\| < T$, $\varphi(t) = 0$ since $\sigma_s = 0$. On the other hand, when $\|\hat{\theta}(t)\| \geq T$, $\varphi(t) < 0$ since $T - \|\hat{\theta}(t)\| \leq 0$. Consequently, $\varphi(t) \leq 0$ is proved.

Rearranging terms of equations (5.8), and by using $PB_\Lambda = C_\eta^T$, the first term of (5.7) holds if the following inequality is satisfied

$$\eta^T(t)(A_\eta^T P + PA_\eta)\eta(t) + \varphi(t) \leq \eta^T(t)(A_\eta^T P + PA_\eta)\eta(t) < 0, \tag{5.10}$$

which can be rearranged as an equivalent LMI problem in $P > 0$

$$A_\eta^T P + PA_\eta + \tau_F M < 0, \tag{5.11}$$

which is the first term of (5.5) and consequently, proves the first equation of (5.7).

It remains to prove the second term of (5.7). Since the reset action is only active when $\eta(t) \in \mathcal{M}$, thus the reset jump in the second term of (5.16) results in that

$$V(\eta(t^+)) - V(\eta(t)) = \Theta^T(A_R^T P A_R - P)\Theta \leq 0, \tag{5.12}$$

for every $\eta(t) \in \mathcal{M} = \operatorname{Ker} C$, which is the second inequality of (5.5) and completes the proof.

□

5.2.2 ReAO Based on Sector Reset Condition

In this case, ReAO dynamics are described as follows:

$$\left.\begin{array}{rcl} \dot{\hat{x}}(t) &=& A\hat{x}(t) + Bu(t) + \Lambda\phi(t)\hat{\theta}(t) \\ & & +K_P\tilde{y}(t) + K_I\zeta(t) \\ \dot{\zeta}(t) &=& A_\zeta\zeta(t) + \tilde{y}(t) \\ \dot{\hat{\theta}}(t) &=& \Gamma\phi^T(t)\tilde{y}(t) - \Gamma\sigma_s\hat{\theta}(t) \\ \hat{y}(t) &=& C\hat{x}(t) \\ \dot{\tau}(t) &=& 1 \end{array}\right\} \text{ if } \eta(t) \in \mathcal{F} \ \vee \ \tau \leq \rho,$$

$$\left.\begin{array}{rcl} \hat{x}(t^+) &=& \hat{x}(t) \\ \zeta(t^+) &=& A_r\zeta(t) \\ \hat{\theta}(t^+) &=& \hat{\theta}(t) \\ \hat{y}(t^+) &=& \hat{y}(t) \\ \tau(t^+) &=& 0 \end{array}\right\} \text{ if } \eta(t) \in \mathcal{J} \ \wedge \ \tau > \rho, \tag{5.13}$$

where the *flow set* $\mathcal{F}$ and the *jump or reset set* $\mathcal{J}$ are defined as in (3.14).

Similarly, its error dynamics for the ReAO based on sector reset condition are given by

$$\left.\begin{array}{rl} \dot{\eta}(t) &= A_\eta\,\eta(t) + B_\Lambda\phi(t)\tilde{\theta}(t) + B_\eta\,w(t) \\ \tilde{y}(t) &= C_\eta\,\eta(t) \\ \dot{\tilde{\theta}}(t) &= -\Gamma\phi^T(t)\tilde{y}(t) + \Gamma\sigma_s\hat{\theta}(t) \end{array}\right\} \quad \text{if } \eta \in \mathcal{F} \ \vee \ \tau \leq \rho,$$

$$\left.\begin{array}{rl} \eta(t^+) &= A_R\,\eta(t) \\ \tilde{y}(t^+) &= \tilde{y}(t) \\ \tilde{\theta}(t^+) &= \tilde{\theta}(t) \end{array}\right\} \quad \text{if } \eta \in \mathcal{J} \ \wedge \ \tau > \rho, \tag{5.14}$$

where A_η, B_η, C_η, A_R, and B_Λ are defined as previously.

Here, we state a sufficient condition for the existence of a quadratically stable ReAO assuming absence of disturbances, that is, $w(t) = 0$. This analysis is based on an LMI approach.

Proposition 10. *For given A_η, B_η, C_η, B_Λ and A_R the augmented error dynamic shown in (5.14) with $w = 0$ is quadratically stable, if there exist a matrix $P = P^T > 0$ and scalars $\tau_F \geq 0$ and $\tau_J \geq 0$ subject to*

$$\begin{array}{rcl} A_\eta^T P + PA_\eta + \tau_F(M + \epsilon I) &<& 0, \\ A_R^T P A_R - P - \tau_J M &\leq& 0, \\ PB_\Lambda &=& C_\eta^T, \end{array} \tag{5.15}$$

which is a linear matrix inequality problem in the variables P, τ_F and τ_J.

Proof. Let us begin considering the previously presented quadratic Lyapunov function (5.6) for the error dynamics described by (5.14), whose time derivative is (5.8). Similarly, to prove the quadratically stability of (5.14), we have to check that:

$$\begin{array}{ll} \dot{V}(\eta(t), \tilde{\theta}(t)) < 0 & \eta(t) \in \mathcal{F}_\epsilon, \\ V(\eta(t^+), \tilde{\theta}(t^+)) \leq V(\eta(t), \tilde{\theta}(t)) & \eta(t) \in \mathcal{J}. \end{array} \tag{5.16}$$

Since $\mathcal{F}_\epsilon := \left\{\eta(t) : \eta^T(t) M \eta(t) + \epsilon \eta^T(t)\eta(t)\right\}$, employing the S-procedure [120], the first term of (5.16) is equivalent to the existence of $\tau_F \geq 0$ such that

$$\dot{V}(\eta(t), \tilde{\theta}(t)) < -\eta^T(t)\tau_F(M + \epsilon I)\eta(t). \tag{5.17}$$

Rearranging terms of equations (5.8) and (5.17), and by using $PB_\Lambda = C_\eta^T$ and $\varphi(t) \leq 0$, the first term of (5.16) holds if the following inequality is satisfied

$$\begin{aligned} &\eta^T(t)(A_\eta^T P + P A_\eta)\eta(t) + \eta^T(t)\tau_F(M + \epsilon I)\eta(t) + \varphi(t) \\ &\leq \eta^T(t)(A_\eta^T P + P A_\eta)\eta(t) + \eta^T(t)\tau_F(M + \epsilon I)\eta(t) < 0, \end{aligned} \tag{5.18}$$

which can be rearranged as an equivalent LMI problem in the variables $P > 0$ and $\tau_F \geq 0$

$$A_\eta^T P + P A_\eta + \tau_F(M + \epsilon I) < 0, \tag{5.19}$$

which is the first term of (5.15) and consequently, proves the first equation of (5.16).

Similarly, employing again the S-procedure, the second term of (5.16) holds if there exists $\tau_J \geq 0$ such that

$$V(\eta(t^+), \tilde{\theta}(t^+)) \leq V(\eta(t), \tilde{\theta}(t)) + \eta^T(t)\tau_J M \eta(t), \tag{5.20}$$

which is equivalent to

$$\eta^T(t) A_R^T P A_R \eta(t) - \eta^T(t) P \eta(t) - \eta^T(t)\tau_J M \eta(t) \leq 0. \tag{5.21}$$

Rearranging terms, (5.21) can be also rewritten as an equivalent LMI problem in the variables $P > 0$ and $\tau_J \geq 0$ as follows

$$A_R^T P A_R - P - \tau_J M \leq 0, \tag{5.22}$$

which is the second term of (5.15) and proves the second equation of (5.16) and, as a consequence, completes the proof of the proposition. □

5.2.3 Tuning and Design

According to (5.4) and (5.14), there are several tuning gains which play a key role in the performance of our proposed reset adaptive observer for nonlinear systems. Specifically, there are five tuning gains: the proportional gain K_P, the integral gain K_I, the reset term gains A_ζ and B_ζ, and the parameter gain Γ. Since we have already explained how to select K_P, K_I, A_ζ, and B_ζ in Chapter 3.2.3, we can focus on designing an appropriate parameter gain Γ. Typically, Γ is chosen to be a positive diagonal matrix in such a manner that the convergence speeds of each estimated parameter can be tuned separately. Although some authors have proposed to use time varying $\Gamma(t)$ matrix [35], [73], we consider only constant parameter gain Γ due to the fact that a constant Γ highly simplifies the Lyapunov stability analysis.

After tuning the ReAO in nominal conditions, the last step is to guarantee a bounded estimate in presence of unmodeled disturbances by choosing the threshold T and the leakage term σ. T should be chosen large enough so that $T > \|\theta(t)\|$ based on prior knowledge of the system. Finally, σ is chosen to be any small positive scalar.

5.2.4 Simulation Results

In this section, the performance of the ReAO applied to an uncertain high-order nonlinear plant is shown. It can achieve a zero steady-state estimation error for all the state variables as well as for the uncertain parameter. After that, the results obtained by the ReAO are compared with a PIAO with the same tuning parameters than the ReAO, which is denoted by Std-PIAO, and with an optimal PIAO designed according to [38], which is denoted by J-PIAO. Notice that all these simulation results have been obtained by using Matlab-Simulink with the ode3 solver and a variable step.

Let us consider the following third-order noise-corrupted nonlinear system according to (5.1):

$$\begin{array}{ll} \dot{x}_1(t) & = -2x_1(t) + x_2(t) - 2x_3(t) + u(t) + 0.2w(t) \\ \dot{x}_2(t) & = -x_2(t) - 2x_3(t) - 0.5u(t) + 0.2w(t) \\ \dot{x}_3(t) & = x_2(t) - x_3(t) + 0.2(y^3(t) + u(t))\theta + 0.5u(t) + 0.2w(t) \\ y(t) & = x_3(t) \end{array} \tag{5.23}$$

with $x(t=0) = [1.5; 0.5; 1]^T$, $u(t) = sin(t)$, $w(t) = sin(10t)$ and an uncertain parameter $\theta = 1$.

A low-time-varying disturbance $w(t)$ is preferred rather than white noise in order to represent changes on the operating point or gradual decalibration of the system which are issues that usually arise in the adaptive observer framework [80].

Then, the aim is to develop an adaptive observer for the system described by (5.23) which estimates all the state variables as well as the uncertain parameter without overshooting as fast as possible.

Let us begin showing the potential benefit of using a reset element in the state adaptive law. For this reason, we compare an ReAO with the Std-PIAO, which is designed with the same tuning parameters than the ReAO. Both observers are applied to the nonlinear system (5.23). Generally, PIAO for nonlinear systems are described by:

$$\begin{aligned} \dot{\hat{x}}(t) &= A\hat{x}(t) + Bu(t) + K_I z(t) + K_P \tilde{y}(t), \quad \hat{y}(t) = C\hat{x}(t), \\ \dot{\hat{\theta}}(t) &= \Gamma \phi^T(t)\tilde{y}(t) - \Gamma \sigma_s \hat{\theta}(t), \qquad\qquad \dot{z}(t) = A_z z(t) + B_z \tilde{y}(t), \end{aligned} \tag{5.24}$$

where $A_z \in \mathbb{R}$ and $B_z \in \mathbb{R}$ are two tuning scalars which regulate the transient response of the integral term $z(t)$, and σ_s is defined as in (5.3).

Fig. 5.1 shows how the reset element can be used to minimize the rise time without overshooting. It is evident that the ReAO obtains a much better performance compared with the Std-PIAO, since it obtains a response as quick as Std-PIAO but without overshooting. The integral gain is too high for the Std-PIAO and, as consequence, it causes an oscillating estimation process. If we decrease the integral gain of the Std-PIAO to avoid overshooting it will give a slower response. However, the overshoots associated with the high integral gain are almost removed by resetting the integral term of the ReAO. That result underlines the potential benefit of the reset element, due to the fact that we can decrease the settling time as long as we increase the integral gain, while we can remove the overshoots resetting the integral term.

We also present a different tuning maximizing the performance of the observers in order to compare the ReAO with an optimal PIAO designed according to [38]. Now, the ReAO for the nonlinear system (5.23) has been tuned following the guidelines given in Section 5.2.3, while the parameters of the J-PIAO are obtained by solving the minimization problem that appears in [38]. These tuning parameters as well as the state estimation error $\tilde{x}(t) = x(t) - \hat{x}(t) = [\tilde{x}_1(t); \tilde{x}_2(t); \tilde{x}_3(t)]^T$ of both adaptive observers are shown in Fig. 5.2.

Comparing the results of the ReAO with the J-PIAO, it can be seen that both observers achieve a fast estimation of the measured variable x_3. Nevertheless, there are significant differences in how the observers estimate the non-accessible variables $x_1(t), x_2(t)$. As before, the ReAO exploits the reset element properties to estimate $x_1(t), x_2(t)$ as fast as the J-PIAO but without overshooting. Fig. 5.2 also points out that both observers could achieve zero steady-state error once they have been properly tuned.

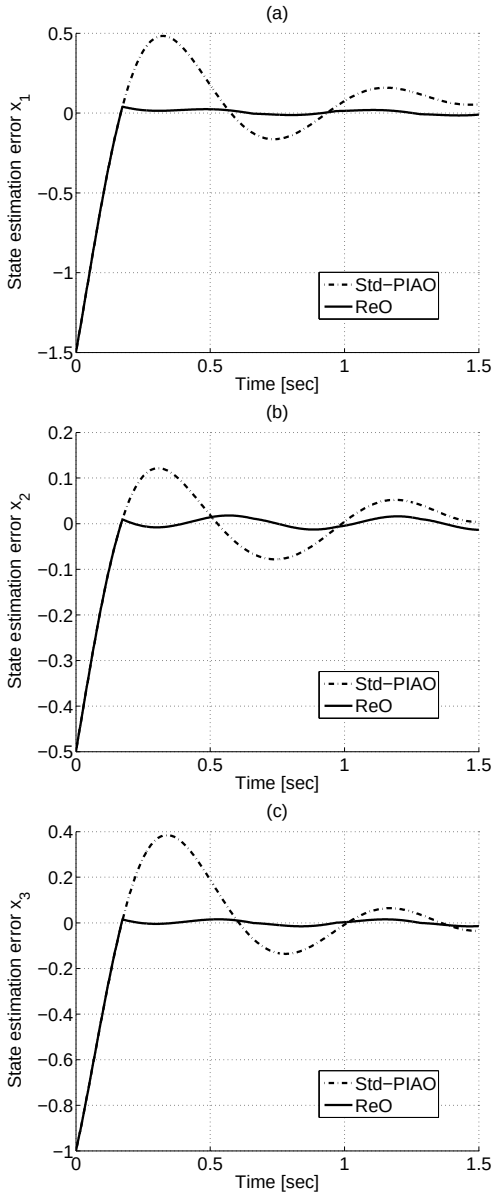

Figure 5.1: Estimation results for example (5.23). (a), (b), and (c) show the state estimation error $\tilde{x}_1$, $\tilde{x}_2$, and $\tilde{x}_3$ respectively. Dash-dot lines have been obtained by using the Std-PIAO with $\hat{x}(t=0) = [0;0;0]^T$, $z(t=0) = 0$, $A_z = -0.1$, $B_z = 1$, $K_P = [5;1;5]^T$, $K_I = [80;25;60]^T$, $\Gamma = 12$, $T = 3.5$, and $\sigma = 10$. Solid lines have been obtained by using the ReAO with $\hat{x}(t=0) = [0;0;0]^T$, $\zeta(t=0) = 0$, $A_\zeta = -0.1$, $B_\zeta = 1$, $K_P = [5;1;5]^T$, $K_I = [80;25;60]^T$, $A_r = 0$, $\Gamma = 12$, $T = 3.5$, and $\sigma = 10$. Note that the system is perturbed by a periodic disturbance, being this the reason of the oscillatory behavior in the steady state.

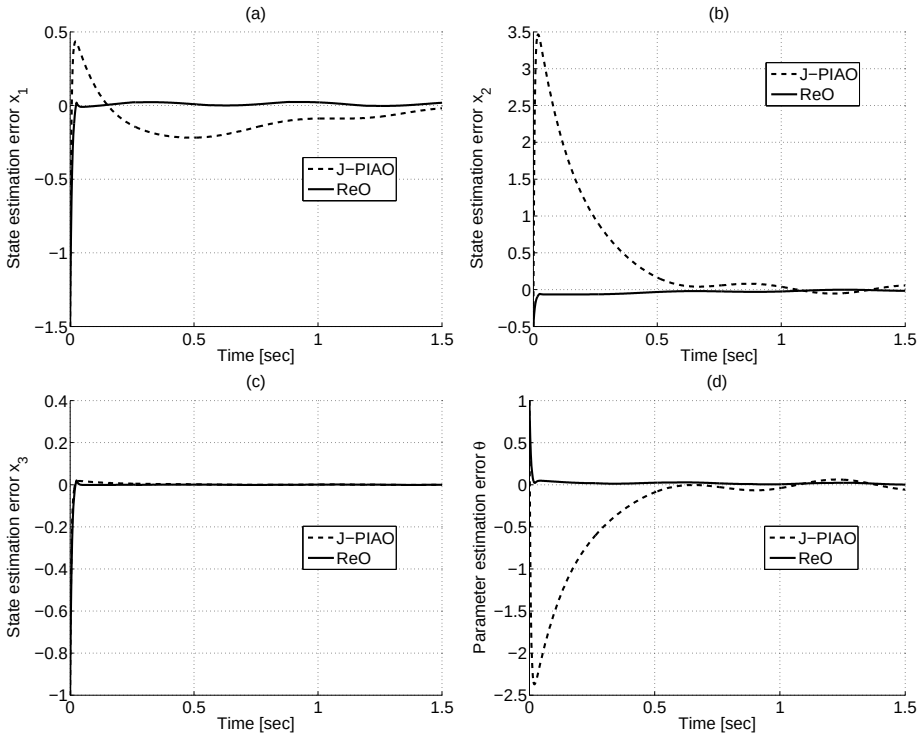

Figure 5.2: Estimation results for example (5.23). (a), (b), and (c) show the state estimation error $\tilde{x}_1$, $\tilde{x}_2$, and $\tilde{x}_3$ respectively. (d) shows the parameter estimation error $\tilde{\theta}$. Dashed lines have been obtained by using the J-PIAO with $\hat{x}(t=0) = [0;0;0]^T$, $z(t=0) = 0$, $A_z = -0.1$, $B_z = 1$, $K_P = [400;856;200]^T$, $K_I = [-0.0007;0.0006;1.14]^T$, $\Gamma = 720$, $T = 3.5$, and $\sigma = 10$. Solid lines have been obtained by using the ReAO with $\hat{x}(t=0) = [0;0;0]^T$, $\zeta(t=0) = 0$, $A_\zeta = -0.1$, $B_\zeta = 1$, $K_P = [210;60;150]^T$, $K_I = [2100;600;1125]^T$, $A_r = 0$, $\Gamma = 165$, $T = 3.5$, $\sigma = 10$.

5.3 Optimal ReAO Design

So far, we have been only focused on the stability and performance analysis of the ReAO, nonetheless another important issue to solve is the reset element synthesis. Although reset element might seem very advantageous, their parameter tuning is far from straightforward. It is well known that a reset controller can cause performance degradation or even destroy the stability of the system if it is not properly tuned [144]. A precursor work that deals with the optimal design of reset controllers is [169]. However, since it is based on a time dependent approach, i.e. the reset intervals are known a priori, it cannot be applied to our ReAO formulation.

In this section, we present a different approach for optimal ReAO design. According to the author's knowledge, this contribution can be regarded as the first result about optimal synthesis within the time independent reset system framework. The observer gains as well as the reset element parameters are optimally chosen by solving the $\mathcal{L}_2$ gain minimization problem, which can be rewritten as an equivalent LMI problem.

Here, we present only the results of optimal ReAO design for a class of nonlinear systems described by (5.1), since the application to SISO linear systems (3.1) follows in a straightforward manner. Let us begin redefining the reset integral term $\zeta(t)$. Since B_ζ is typically selected $B_\zeta = 1$ because the effect of the integral term can be increased by tuning the integral gain K_I, we can rewrite the integral term $\zeta(t)$ as follows

$$\begin{array}{lll} \dot{\zeta}(t) & = A_\zeta \zeta(t) + \tilde{y}(t) & \tilde{y}(t)\cdot\zeta(t) \geq 0, \\ \zeta(t^+) & = A_r \zeta(t) & \tilde{y}(t)\cdot\zeta(t) \leq 0. \end{array} \tag{5.25}$$

Then, let us redefine the error system dynamics for both RTI ReAO, taking into account that now $B_\zeta = 1$. Defining the state estimation error as $\tilde{x}(t) = x(t) - \hat{x}(t)$, and the parameter error as $\tilde{\theta}(t) = \theta(t) - \hat{\theta}(t)$, the error dynamics of the ReAO based on the reset condition are given by

$$\left.\begin{array}{rcl} \dot{\tilde{x}}(t) & = & (A - K_P C)\tilde{x}(t) + \Lambda\phi(t)\tilde{\theta}(t) \\ & & -K_I\zeta(t) + B_w w(t) \\ \dot{\zeta}(t) & = & A_\zeta\zeta(t) + \tilde{y}(t) \\ \dot{\tilde{\theta}}(t) & = & -\Gamma\phi^T(t)\tilde{y}(t) + \Gamma\sigma_s\hat{\theta}(t) \end{array}\right\} \text{if } \eta(t) \notin \mathcal{M} \ \vee \ \tau \leq \rho,$$
$$\left.\begin{array}{rcl} \tilde{x}(t^+) & = & \tilde{x}(t) \\ \zeta(t^+) & = & A_r\zeta(t) \\ \tilde{\theta}^+ & = & \tilde{\theta}(t) \end{array}\right\} \text{if } \eta(t) \in \mathcal{M} \ \wedge \ \tau > \rho, \tag{5.26}$$

and the error dynamics of the ReAO based on the sector condition are as

follows

$$\left.\begin{array}{rcl}\dot{\tilde{x}}(t) &=& (A-K_PC)\tilde{x}(t)+\Lambda\phi(t)\tilde{\theta}(t)\\ && -K_I\zeta(t)+B_ww(t)\\ \dot{\zeta}(t) &=& A_\zeta\zeta(t)+\tilde{y}(t)\\ \dot{\tilde{\theta}}(t) &=& -\Gamma\phi^T(t)\tilde{y}(t)+\Gamma\sigma_s\hat{\theta}(t)\end{array}\right\}\text{if } \eta(t)\in\mathcal{F}\ \vee\ \tau\leq\rho,$$
$$\left.\begin{array}{rcl}\tilde{x}(t^+) &=& \tilde{x}(t)\\ \zeta(t^+) &=& A_r\zeta(t)\\ \tilde{\theta}(t^+) &=& \tilde{\theta}(t)\end{array}\right\}\text{if } \eta(t)\in\mathcal{J}\ \wedge\ \tau>\rho. \tag{5.27}$$

According to (5.26), (5.27) the performance of the ReAO mainly relies on three tuning parameters. Namely, K_P, K_I, and A_ζ, which are the proportional gain, the gain of the reset element and the pole of the reset element respectively. For this reason, we present now our results about how to optimally choose these parameters by solving the $\mathcal{L}_2$ gain minimization problem for both formulations given in the previous section. Note that, most works devoted to reset systems consider only noise-free plants [43], [41], [140], since the reset controller performance might be deteriorated because of the disturbances. This justifies the need of a designing criterion that minimizes the effect of the disturbances in the observer behavior.

For latter reference, we also introduce the following definition of the matrix M

$$M=\left[\begin{array}{cc}M_{\tilde{x}\tilde{x}} & M_{\tilde{x}\zeta}\\ M_{\zeta\tilde{x}} & M_{\zeta\zeta}\end{array}\right]=\left[\begin{array}{cc}0 & C^T\\ C & 0\end{array}\right]. \tag{5.28}$$

5.3.1 ReAOs Based on Zero Crossing Reset Condition

Proposition 11. *For given A, B, C, Λ, and A_r the error dynamic shown in (5.26) is quadratically stable and has a $\mathcal{L}_2$ gain from w to $\tilde{y}$ which is smaller than γ, if for any matrix Θ with $Im\,\Theta = Ker\,C_\eta$ there exist the matrices $P=P^T>0$, $Q=Q^T>0$, R, S, U and $\gamma>0$ subject to*

$$\begin{array}{rcl}\left[\begin{array}{ccc}A^TP+PA-R^TC-C^TR+C^TC & C^TQ-S & PB_w\\ QC-S^T & U^T+U & 0\\ B_w^TP & 0 & -\gamma^2I\end{array}\right] &<& 0,\\ \Theta^T\left[\begin{array}{cc}0_{n,n} & 0\\ 0 & A_r^TQA_r-Q\end{array}\right]\Theta &\leq& 0,\\ P\Delta &=& C^T,\end{array}$$

which is a linear matrix inequality problem in the variables P, Q, R, S, U, and γ. Once the minimum $\mathcal{L}_2$ has been obtained, the optimal ReAO gains can be computed as $K_P=P^{-1}R^T$, $K_I=P^{-1}S$, $A_\zeta=Q^{-1}U$.

Proof. To prove the stability of our proposed ReAO based on zero crossing reset condition and that its $\mathcal{L}_2$ gain from $w(t)$ to $\tilde{y}(t)$ is smaller than γ, we have to check that:

$$\begin{array}{ll} \dot{V}(\tilde{x}(t),\zeta(t),\tilde{\theta}(t)) < \gamma^2 w^T(t)w(t) - \tilde{x}^T(t)C^TC\tilde{x}(t) & \eta(t) \notin \mathcal{M}, \\ V(\tilde{x}(t^+),\zeta(t^+),\tilde{\theta}(t+)) - V(\tilde{x}(t),\zeta(t),\tilde{\theta}(t)) \leq 0 & \eta(t) \in \mathcal{M}. \end{array} \tag{5.29}$$

Note that these inequalities are the standard stability requirements for reset systems, and they guarantee that there exists a common Lyapunov function $V(\tilde{x}(t),\zeta(t),\tilde{\theta}(t))$ that is a disturbance attenuation Lyapunov function for the input $w(t)$ and the output $\tilde{y}(t)$ when the reset system is flowing, and does not grow when the reset system is within the reset region.

Let us now consider the following quadratic Lyapunov function for the error dynamics described by (5.26):

$$V(\tilde{x}(t),\zeta(t),\tilde{\theta}(t)) = \tilde{x}^T(t)\, P\, \tilde{x}(t) + \zeta^T(t)\, Q\, \zeta(t) + \tilde{\theta}^T(t)\, \Gamma^{-1}\, \tilde{\theta}(t), \tag{5.30}$$

where $P = P^T > 0$, $Q = Q^T > 0$ and $\Gamma = \Gamma^T > 0$. Then, let us take derivative of (5.30) to obtain

$$\begin{array}{rcl} \dot{V}(\tilde{x}(t),\zeta(t),\tilde{\theta}(t)) & = & \dot{\tilde{x}}^T(t)P\tilde{x}(t) + \tilde{x}^T(t)P\dot{\tilde{x}}(t) + \dot{\zeta}^T(t)Q\zeta(t) \\ & & +\zeta^T(t)Q\dot{\zeta}(t) + \dot{\tilde{\theta}}^T(t)\,\Gamma^{-1}\,\tilde{\theta}(t) + \tilde{\theta}^T(t)\,\Gamma^{-1}\,\dot{\tilde{\theta}}(t) \\ & = & \tilde{x}^T(t)((A-K_PC)^TP + P(A-K_PC))\tilde{x}(t) \\ & & +\tilde{x}^T(t)\left(P\Lambda\phi - C^T\phi\right)\tilde{\theta}(t) \\ & & +\zeta^T(t)(QC - PK_I)\tilde{x}(t) + w^T(t)B_w^TP\tilde{x}(t) \\ & & +\zeta^T(t)(A_\zeta^TQ + QA_\zeta)\zeta(t) \\ & & +\tilde{x}^T(t)(C^TQ - K_I^TP)\zeta(t) + \tilde{x}^T(t)PB_ww(t) \\ & & +\tilde{\theta}^T(t)\left(\phi^T\Lambda^TP - \phi^TC\right)\tilde{x}(t) + \varphi(t). \end{array} \tag{5.31}$$

Now, by using $P\Delta = C^T$ and $\varphi(t) \leq 0$ as it was shown in (5.9), and by introducing the new variables $R = K_P^TP$, $S = PK_I$, $U = QA_\zeta$, (5.31) can be written as follows:

$$\begin{array}{rcl} \dot{V}(\tilde{x}(t),\zeta(t),\tilde{\theta}(t)) & \leq & \tilde{x}^T(t)(A^TP + PA - R^TC - C^TR)\tilde{x}(t) \\ & & +w^T(t)B_w^TP\tilde{x}(t) + \tilde{x}^T(t)PB_ww(t) \\ & & +\tilde{x}^T(t)(C^TQ - S)\zeta(t) + \zeta^T(t)(QC - S^T)\tilde{x}(t) \\ & & +\zeta^T(t)(U^T + U)\zeta(t). \end{array} \tag{5.32}$$

Rearranging terms of equation (5.32), the first term of (5.29) holds if the following inequality is satisfied

$$\begin{array}{l} \tilde{x}^T(t)(A^TP + PA - R^TC - C^TR)\tilde{x}(t) + w^T(t)B_w^TP\tilde{x}(t) \\ +\tilde{x}^T(t)PB_ww(t) + \tilde{x}^T(t)(C^TQ - S)\zeta(t) \\ +\zeta^T(t)(QC - S^T)\tilde{x}(t) + \zeta^T(t)(U^T + U)\zeta(t) \\ -\gamma^2w^T(t)w(t) + \tilde{x}^T(t)C^TC\tilde{x}(t) < 0, \end{array} \tag{5.33}$$

which can be rearranged as the following equivalent LMI problem

$$\begin{bmatrix} A^TP + PA - R^TC - C^TR + C^TC & C^TQ - S & PB_w \\ QC - S^T & U^T + U & 0 \\ B_w^TP & 0 & -\gamma^2 I \end{bmatrix} < 0, \tag{5.34}$$

which is the first term of Proposition 11 and consequently, proves the first equation of (5.29).

It remains to prove the second term of (5.29). Since both state error $\tilde{x}$ and parameter error $\tilde{\theta}$ do not change after resets, their dynamics do not contribute to the jump, thus the reset jump in second term of (5.29) directly results in

$$\begin{aligned} &V(\tilde{x}(t^+), \zeta(t^+), \tilde{\theta}(t^+)) - V(\tilde{x}(t), \zeta(t), \tilde{\theta}(t)) \\ &\quad = \Theta^T \begin{bmatrix} 0_{n,n} & 0 \\ 0 & A_r^TQA_r - Q \end{bmatrix} \Theta \leq 0, \end{aligned} \tag{5.35}$$

for every $\eta \in \mathcal{M} = \operatorname{Ker} C_\eta$, which is the second term of Proposition 11 and proves the second equation of (5.29) and, as a consequence, completes the proof. □

5.3.2 ReAOs Based on Sector Reset Condition

Proposition 12. *For given A, B, C, Λ, M and A_r the error dynamic shown in (5.27) is quadratically stable and has a $\mathcal{L}_2$ gain from w to $\tilde{y}$ which is smaller than γ, if there exist the matrices $P = P^T > 0$, $Q = Q^T > 0$, R, S, U and scalars $\tau_F \geq 0$, $\tau_J \geq 0$ and $\gamma > 0$ subject to*

$$\begin{bmatrix} A^TP + PA - R^TC - C^TR + C^TC + \epsilon I_{n,n} & C^TQ - S + \tau_F M_{\tilde{x}\zeta} & PB_w \\ QC - S^T + \tau_F M_{\zeta\tilde{x}} & U^T + U + \epsilon & 0 \\ B_w^TP & 0 & -\gamma^2 I \end{bmatrix} < 0,$$

$$\begin{bmatrix} 0_{n,n} & -\tau_J M_{\tilde{x}\zeta} \\ -\tau_J M_{\zeta\tilde{x}} & A_r^TQA_r - Q \end{bmatrix} \leq 0,$$

$$P\Delta = C^T,$$

which is a linear matrix inequality problem in the variables P, Q, R, S, U, τ_F, τ_J and γ. Once the minimum $\mathcal{L}_2$ has been obtained, the optimal ReAO gains can be computed as $K_P = P^{-1}R^T$, $K_I = P^{-1}S$, $A_\zeta = Q^{-1}U$.

Proof. In a similar way, to prove the stability of our proposed ReAO based on sector reset condition and that its $\mathcal{L}_2$ gain from w to $\tilde{y}$ is smaller than γ, we have to check that:

$$\begin{aligned} &\dot{V}(\tilde{x}(t), \zeta(t), \tilde{\theta}(t)) < \gamma^2 w^T(t)w(t) - \tilde{x}^T(t)C^TC\tilde{x}(t) && \eta(t) \in \mathcal{F}_\epsilon, \\ &V(\tilde{x}(t^+), \zeta(t^+), \tilde{\theta}(t^+)) - V(\tilde{x}(t), \zeta(t), \tilde{\theta}(t)) \leq 0 && \eta(t) \in \mathcal{J}. \end{aligned} \tag{5.36}$$

Let us consider the previously defined quadratic Lyapunov function (5.31) whose time derivative is upper-bounded as in (5.32) for the error dynamics described by (5.27).

According to the previous definition of $\mathcal{F}_\epsilon$, and employing the S-procedure [120], the first term of (5.36) is equivalent to the existence of $\tau_F \geq 0$ such that

$$\begin{aligned}\dot{V}(\tilde{x}(t),\zeta(t),\tilde{\theta}(t)) \quad < \quad & \gamma^2 w^T(t)w(t) - \tilde{x}^T(t)C^TC\tilde{x}(t) \\ & -\tau_F\left(\tilde{x}^T(t)M_{\tilde{x}\zeta}\zeta(t) + \zeta^T(t)M_{\zeta\tilde{x}}\tilde{x}(t)\right) \\ & -\epsilon I_{n,n}\tilde{x}^T(t)\tilde{x}(t) - \epsilon\zeta^T(t)\zeta(t).\end{aligned} \tag{5.37}$$

Rearranging terms of equations (5.37) and (5.32), the first term of (5.36) holds if the following inequality is satisfied

$$\begin{aligned}&\tilde{x}^T(t)(A^TP + PA - R^TC - C^TR)\tilde{x}(t) + w^T(t)B_w^TP\tilde{x}(t) \\ &+\tilde{x}^T(t)PB_ww(t) + \tilde{x}^T(t)(C^TQ - S)\zeta(t) \\ &+\zeta^T(t)(QC - S^T)\tilde{x}(t) + \zeta^T(t)(U^T + U)\zeta(t) - \gamma^2 w^T(t)w(t) \\ &+\tilde{x}^T(t)C^TC\tilde{x}(t) + \tau_F\left(\tilde{x}^T(t)M_{\tilde{x}\zeta}\zeta(t) + \zeta^T(t)M_{\zeta\tilde{x}}\tilde{x}(t)\right) \\ &+\epsilon I_{n,n}\tilde{x}^T(t)\tilde{x}(t) + \epsilon\zeta^T(t)\zeta(t) < 0,\end{aligned} \tag{5.38}$$

which can be rearranged as the following equivalent LMI problem

$$\begin{aligned}&\begin{bmatrix} A^TP + PA - R^TC - C^TR + C^TC + \epsilon I_{n,n} & C^TQ - S + \tau_F M_{\tilde{x}\zeta} & PB_w \\ QC - S^T + \tau_F M_{\zeta\tilde{x}} & U^T + U + \epsilon & 0 \\ B_w^TP & 0 & -\gamma^2 I \end{bmatrix} \\ &\qquad\qquad < 0,\end{aligned} \tag{5.39}$$

which is the first term of Proposition 12 and consequently, proves the first equation of (5.36).

Similarly, employing again the S-procedure, the second term of (5.36) holds if there exists $\tau_J \geq 0$ such that

$$\begin{aligned}&V(\tilde{x}(t^+),\zeta(t^+),\tilde{\theta}(t^+)) - V(\tilde{x}(t),\zeta(t),\tilde{\theta}(t)) \\ &\leq \tau_J\left(\tilde{x}^T(t)M_{\tilde{x}\zeta}\zeta(t) + \zeta^T(t)M_{\zeta\tilde{x}}\tilde{x}(t)\right),\end{aligned} \tag{5.40}$$

which is equivalent to

$$\begin{aligned}&\zeta^T(t)A_r^TQA_r\zeta(t) - \zeta^T(t)Q\zeta(t) \\ &-\tau_J\left(\tilde{x}^T(t)M_{\tilde{x}\zeta}\zeta(t) + \zeta^T(t)M_{\zeta\tilde{x}}\tilde{x}(t)\right) \leq 0.\end{aligned} \tag{5.41}$$

Rearranging terms, (5.41) can be also rewritten as an equivalent LMI problem as follows

$$\begin{bmatrix} 0_{n,n} & -\tau_J M_{\tilde{x}\zeta} \\ -\tau_J M_{\zeta\tilde{x}} & A_r^TQA_r - Q \end{bmatrix} \leq 0, \tag{5.42}$$

which is the second term of Proposition 12 and proves the second equation of (5.36) and, as a consequence, completes the proof of the proposition. □

Remark 3. Both Propositions are formulated as a convex optimization problem, being the $\mathcal{L}_2$ gain (i.e. γ) the variable to be minimized. Then, the resultant ReAO gains (namely K_P, K_I and A_ζ) not only guarantee the quadratic stability of the error dynamics but also that the $\mathcal{L}_2$ gain between disturbance and state estimation errors is minimum. Since they are obtained by solving an optimization problem, the resultant conditions are optimal. Additionally, note that some conservatism might arise from using quadratic Lyapunov function rather than piece-wise quadratic Lyapunov functions as in [42]. Unfortunately, since the tuning gains rely on the Lyapunov function structure, a piece-wise quadratic Lyapunov function would result in piece-wise tuning gains, which would highly increase the complexity of the resultant observer. Since we are concerned about the final implementation of our proposal in real applications, we have to balance complexity and conservativeness. This is the reason because a simple quadratic Lyapunov function is preferred. However, the proposed method provides excellent results as it can be seen it the next section.

5.3.3 Simulation Results

In this section, an example is presented in order to show the effectiveness of the proposed methods to determine the ReAO parameters. We have used the example proposed in [38] as a benchmark, and we have compared the results obtained by our optimal ReAO considering both reset conditions with the optimal PIAO proposed by [38], which will be denoted by J-PIAO throughout the simulation section. Although in that example the system is only affected by a high-frequency disturbance, we have considered here two different types of inputs $u(t) = \{0,\ 10sin(0.05t)\}$ and four different types of disturbances $w(t) = \{0,\ sin(0.5t),\ sin(0.001t) - 1,\ 1\}$ that results in seven different simulation scenarios (note that the case $(u(t) = 0,\ w(t) = 0)$) is not considered). All these simulation results have been obtained by using Matlab-Simulink with the ode3 solver.

Let us take the following example from [38],

$$\begin{array}{rl} \dot{x}_1(t) & = -x_2(t) + y^3(t)\theta + 0.1w(t) \\ \dot{x}_2(t) & = -x_1(t) - 2x_2(t) + 0.1w(t) \\ y(t) & = x_1(t) \end{array} \tag{5.43}$$

with $x(t=0) = [-0.5, 0.2]$, $\theta = 1.1$.

On the one hand, the J-PIAO tuning parameters are $\hat{x}(t=0) = [0,0]^T$, $z(t=0) = 0$, $A_z = -10$, $B_z = 1$, $K_P = [3.18, 5]^T$, $K_I = [0.93, 0]^T$, $\Gamma = 50$, $T = 1.5$, and $\sigma = 10$ which have been taken from [38]. On the other hand, the optimal ReAO tuning parameters have been obtained according to Propositions 11-12 depending on the reset condition chosen. In this particular example (5.43) both ReAOs obtain the same tuning parameters which are $A_\zeta = -1.123$, $K_P = [12.2877, 12.336]^T$, $K_I = [4.4745, 0.5349]^T$.

Table 5.1: AO Performance Indexes. S(·) stands for sin(·).

AO	u(t)	w(t)	$IAE_{\tilde{x}_1}$	$IAE_{\tilde{x}_2}$	$IAE_{\tilde{\theta}}$	$ITAE_{\tilde{x}_1}$	$ITAE_{\tilde{x}_2}$	$ITAE_{\tilde{\theta}}$
ReAO	0	S(0.5t)	0.05	0.21	15.28	0.04	0.11	53.32
JPIAO	0	S(0.5t)	0.15	0.29	15.81	0.17	0.23	54.65
ReAO	0	$S(10^{-3}t)$-1	0.07	0.30	16.33	0.12	0.51	57.95
JPIAO	0	$S(10^{-3}t)$-1	0.20	0.28	17.06	0.42	0.14	61.39
ReAO	0	1	0.09	0.30	15.32	0.13	0.46	54.03
JPIAO	0	1	0.24	0.33	17.38	0.43	0.26	61.87
ReAO	10S(0.05t)	0	0.06	0.32	4.39	0.04	0.32	4.30
JPIAO	10S(0.05t)	0	0.15	0.34	4.76	0.11	0.27	4.72
ReAO	10S(0.05t)	S(0.5t)	0.06	0.37	4.44	0.04	0.57	4.59
JPIAO	10S(0.05t)	S(0.5t)	0.15	0.39	4.80	0.12	0.52	4.91
ReAO	10S(0.05t)	$S(10^{-3}t)$-1	0.06	0.44	5.07	0.05	1.13	6.23
JPIAO	10S(0.05t)	$S(10^{-3}t)$-1	0.15	0.51	5.23	0.13	1.18	6.23
ReAO	10S(0.05t)	1	0.06	0.57	4.40	0.03	1.42	5.16
JPIAO	10S(0.05t)	1	0.16	0.57	4.80	0.12	1.35	5.42

Note that in general, tuning gains obtained from Propositions 11-12 might be different, since the LMIs in each case are different. Remaining ReAO tuning parameters are $\hat{x}(t=0) = [0,0]^T$, $\zeta(t=0) = 0$, $A_r = 0$, $\rho = 10^{-2}$, $\Gamma = 50$, $T = 1.5$, and $\sigma = 10$, which have the same value than the J-PIAO to guarantee a fair comparison. Note that since both ReAOs have obtained the same optimal tuning gains, both will perform exactly in the same way for the previously selected initial conditions. For this reason and to increase the readability of the figures, we only show the response of the ReAO based on zero crossing condition that in the following will be simply denoted by ReAO.

An analysis of the state and parameter estimation errors of both observers for each simulation scenario is given in Table 5.1. To this end, we have computed the Integral of Absolute Error (IAE) and Integral of Time multiplied by Absolute Error (ITAE), which were defined in (3.32), and now α can be either $x_1(t)$, $x_2(t)$, or $\theta(t)$. Analyzing the results given in Table 5.1, it can be seen that the ReAO generally outperforms the J-PIAO, since the ReAO obtains a significantly lower IAE and ITAE index in most simulation scenarios. Note that when the system is affected by disturbances with a steady-state offset (e.g. $w(t) = 1$), the ReAO needs more time to reject the effect of the disturbance on the unknown variable x_2, which results in a similar $IAE_{\tilde{x}_2}$ but a slightly higher $ITAE_{\tilde{x}_2}$. However even in this case, its other performance indexes are considerably better than the ones obtained by the J-PIAO.

To see this, Fig. 5.3 shows actual state variables and their respective estimates by J-PIAO and ReAO when $u(t) = 0$ and $w(t) = sin(0.5t)$. It is evident that our proposed ReAO achieves a better performance than the J-PIAO comparing the estimation process of both observers. In particular,

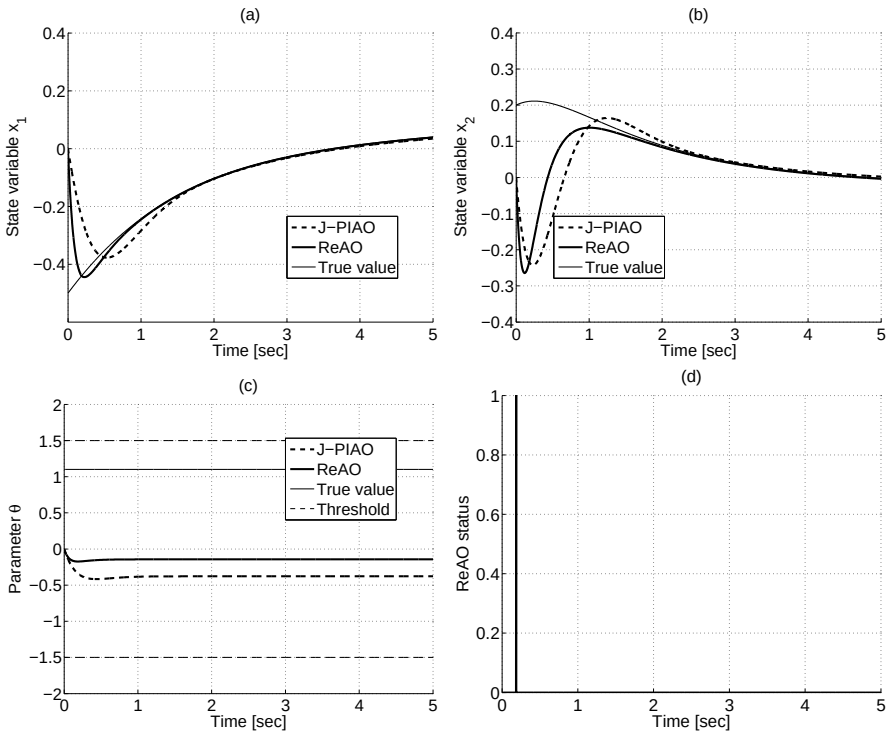

Figure 5.3: Estimation results with $u(t) = 0$, $w(t) = sin(0.5t)$. (a) shows real state x_1 and the estimated state $\hat{x}_1$. (b) shows real state x_2 and the estimated state $\hat{x}_2$. (c) shows the actual parameter θ and the estimated parameter $\hat{\theta}$ at different time spans. Thick dashed lines are the estimate obtained by using the J-PIAO. Thick solid lines are the estimate obtained by using the ReAO. Thin solid lines are the true values of the states and parameter. Thin dashed lines are the threshold of the estimated parameter. (d) shows the status of the ReAO (i.e. 0: the ReAO is in the flow set, 1: the ReAO is in the jump set).

the ReAO has a lower steady state error as well as a faster estimation process as it can be deduced from Table 5.1. Actual uncertain parameter and its parameter estimate of both adaptive observers are shown in Fig. 5.3. In this case, the behavior of both observers is similar. The two observers are not able to estimate the unknown parameter because the system (5.43) is not persistently excited since $u(t) = 0$. Nonetheless the estimation error of the unknown parameter computed by each observer remains bounded since the estimated parameter is within the threshold T.

Additionally, we can also compare the bound of the $\mathcal{L}_2$ of all observers. Minimizing the value of γ^2 according to Proposition 11-12, both ReAOs obtain a $\mathcal{L}_2 = 0.3162$ whereas the J-PIAO obtained a $\mathcal{L}_2 = 0.5$.

Fig. 5.4 shows the actual state variables and the respective estimates

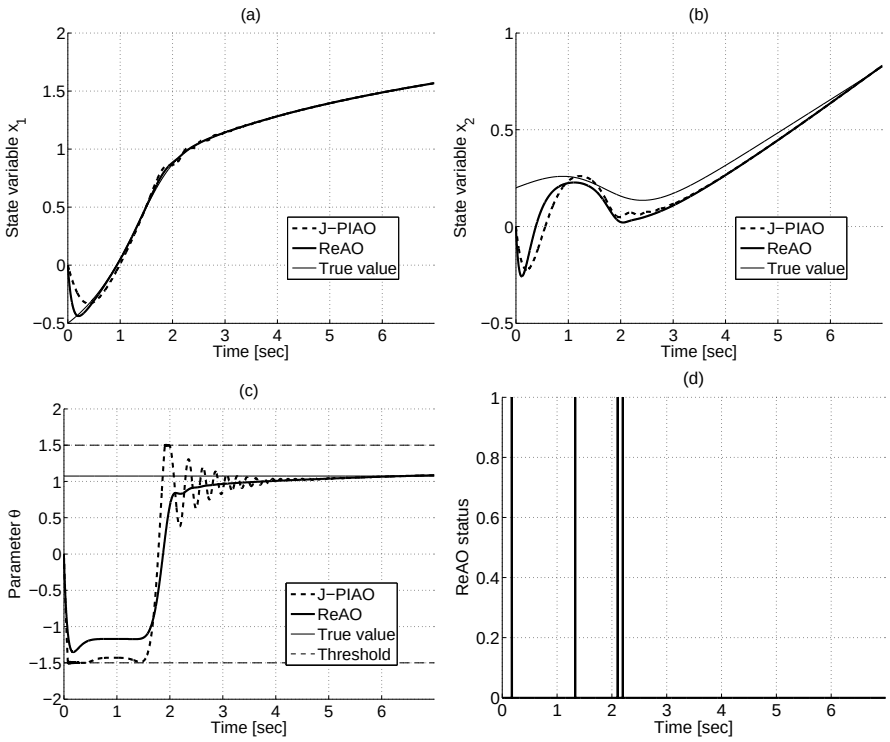

Figure 5.4: Estimation results with $u(t) = 10sin(0.05t)$, $w(t) = sin(0.5t)$ and $\Gamma = 400$. (a) shows real state x_1 and the estimated state $\hat{x}_1$. (b) shows real state x_2 and the estimated state $\hat{x}_2$. (c) shows the actual parameter θ and the estimated parameter $\hat{\theta}$ at different time spans. Thick dashed lines are the estimate obtained by using the J-PIAO. Thick solid lines are the estimate obtained by using the ReAO. Thin solid lines are the true values of the states and parameter. Thin dashed lines are the threshold of the estimated parameter. (d) shows the status of the ReAO (i.e. 0: the ReAO is in the flow set, 1: the ReAO is in the jump set).

of both adaptive observers with $u(t) = 10sin(0.05t)$, $w(t) = sin(0.5t)$ and $\Gamma = 400$, and hence, the system is persistently excited. Note that Γ has been chosen to be considerably larger than in the previous simulation to highlight the influence of the reset element on the evolution of the estimated parameter $\hat{\theta}$. Analyzing Fig. 5.4, we can see how by resetting the integral term, the ReAO achieves a slightly faster convergence of the state error $\tilde{x} = x - \hat{x}$, and a much less oscillating response of the estimated parameter $\hat{\theta}$.

5.4 Discussion

Throughout this chapter we have extended our reset observer formulation for joint parameter and state estimation for a class of nonlinear systems.

Motivated by the results presented in Chapter 4, where the need of a different tuning criterion depending on the observer's structure was highlighted, we have proposed in this chapter a method to automatically determine the optimal ReAO tuning parameters for the two most popular reset conditions within the reset time independent framework. Our proposal tackles and solves the main drawback of the reset elements which can decrease the observer performance or even destabilize the estimation process if the ReAO parameters are not properly chosen. Since the method is based on minimizing the $\mathcal{L}_2$ gain of the ReAO, the stability and convergence of the estimation process are guaranteed. Despite the fact that this method is originally formulated for a class of nonlinear systems, another advantage of this method is that it can be easily extended to other sort of systems such as time-delay and/or linear systems.

A question that might arise is why the $\mathcal{L}_2$ gain is a suitable criterion for observer performance. Nowadays, there exists a considerable interest in real applications affected by unknown disturbances and in fault detection, mainly motivated by a growing interest in safer and more reliable process control. Moreover, most works devoted to reset systems consider only noise-free plants, since the reset controller performance might be deteriorated because of the disturbances. Both reasons justify the need of a designing criterion that minimizes the effect of the disturbances in the observer behavior.

It is also worth mentioning that there are other criteria that could be used to optimize the observer performance. For instance, in the H_∞ observer framework, a cost function that directly minimizes the estimation error is proposed. However, since several states are generally non-accessible, only the measurable variables can be used in the cost function. Hence, this approach generally results in an observer that gives an excellent performance (i.e. considerable fast settling time) for the measurable states, whereas the unknown state estimates behave worse. According to our experience and simulations, $\mathcal{L}_2$ norm criterion is the most robust to this issue, which also justifies its selection.

Part III

Application to Induction Hobs

Chapter 6

Novel Temperature Sensors

Before designing a temperature control strategy that relies on the previously presented reset observer formulation, further research has been made on determining what temperature sensors are more suitable for developing an accurate temperature control. In particular, this chapter details three novel sensing methods that outperform existing thermistor-based strategies for controlling low load cooking processes. However, this better performance is at expense of a higher cost. Taking this into consideration, this chapter ends concluding what temperature sensor best balances performance and cost.

6.1 Introduction

As it has been explained in Chapter 2, induction hobs currently have both non-contact and contact temperature sensors. Specifically, induction hobs have two NTC thermistors for each inductor underneath the glass ceramic, and an infrared sensor located at both left and right corners of the glass-ceramic.

Each sort of sensor is more suitable for some specific cooking processes. For instance, the cooking pot bottom temperature is the variable to be controlled in dry heat cooking processes such as roasting or grilling, in which food is not submerged in large amount of hot liquid (e.g. water, oil, fat). In this case, using the NTC thermistors would be more appropriate, because they sense the heat directly transmitted from the bottom of the cooking pot through the glass-ceramic. This is no longer true when the food needs to be submerged in large amount of liquid to obtain properly cooked food. This situation arises in a wide variety of cooking processes such as simmering, boiling, or deep frying. In those cases, the temperature of the liquid itself is the variable to be controlled. This temperature is generally quite different from the cooking pot bottom temperature, due to the fact that the heat is firstly generated at the cooking pot bottom, and then, transmitted upwards to the liquid. As a matter of fact, the larger the amount of liquid, the larger the difference will be. For this reason, the infrared sensor, which measures the temperature of the cooking pot wall, is a much better choice providing that the liquid used in the cooking process is as high as the infrared sensor itself. To be robust to the possible variations of emissivity, because it varies depending on the cooking pot used, a high-emissivity sticker with known properties is provided so that the effective emissivity of the measuring point is under control (see Fig. 6.1). Undoubtedly, the temperature provided by the infrared sensor is much more precise than the temperature measured by the NTC thermistor beneath the glass-ceramic. However, it cannot be applied to cooking processes that do not require large amount of liquid.

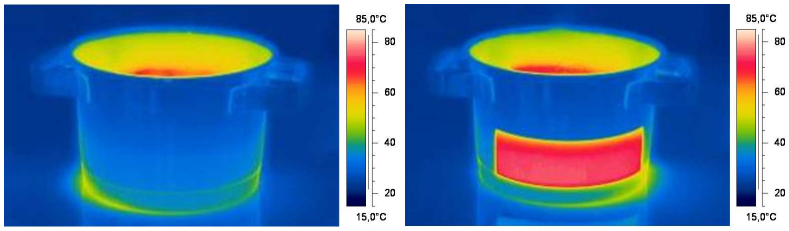

Figure 6.1: Temperature of a cooking pot with a thermal infrared camera in a simmering process. By using a high-emissivity sticker, it is possible to measure the temperature of the cooking pot wall, which is almost equal to the liquid temperature.

For this reason, it would be interesting to develop new temperature sensors or to improve the existing ones, so that the resultant solution could outperform the current NTC thermistors for these sorts of processes. An important effort towards this direction will be made throughout section. In particular, three different novel sensing devices will be presented: the contact spots, which minimizes the dependence on the cooking pot bottom concavity by modifying the cooking surface; the sensor line, which consists in a novel distribution of additional thermistor along the inductor's radius that reduces the effect of the cooking pot bottom concavity as well; and the magnetic sensor, which is an almost instantaneous temperature sensor based on measuring the variation of the impedance of the inductor itself when the temperature of the cooking pot changes.

6.2 Contact Spots

Good thermal contact between the cooking pot bottom and the glass-ceramic surface must exist in order to guarantee precise temperature measurements. However, as it has been commented previously, cooking pot bottoms are not flat but convex, which results in a higher contact thermal resistor due to the presence of an air gap. A recent attempt to minimize this influence are the so-called contact spots [50]. A contact spot is a concave deformation over the glass-ceramic surface. According to our experiments, with at least three contact spots for each cooking zone is possible to guarantee that the cooking pot bottom is always standing on them. Therefore, this proposal guarantees a perfect contact between the cooking pot bottom and the glass-ceramic, and consequently, the uncertainty of the heat transmission dependent on the cooking pot concavity is completely removed.

Two different sorts of contact spots are depicted in Fig. 6.2. In the left picture, the contact spot consists in a small sphere of glass-ceramic that is directly welded to the hob surface (e.g. by using a laser), and a NTC thermistor located just beneath it. The central picture shows the final appearance of this proposal. A different approach is shown in the right picture. In this case, a small hole is drilled into the hob surface and a NTC thermistor is directly located there. To guarantee a perfect contact between the cooking pot bottom and the NTC thermistor, its encasement must be processed until its head is completely rounded.

The benefit of contact spots can be better understood analyzing Fig. 6.3, wherein the temperature of the cooking surface measured with a thermal infrared camera is shown. There exists a clear difference between the temperature of the cooking pot surface (left picture) and the temperature of the glass-ceramic (central picture). As it has been commented previously, this difference varies along the radius and is caused by the convexity of the cooking pot. This difference is minimized when the cooking surface includes

(a) (b) (c)

Figure 6.2: Contact spots construction. (a) Option 1: NTC thermistor beneath a welded contact spot. (b) Final appearance of Option 1. (c) Option 2: Rounded-head NTC sensor used directly as a contact spot.

at least three contact spots (right picture). By locating a contact temperature sensor just beneath the contact spots is possible to guarantee that at least one of them would be located where the difference between the cooking pot temperature and the glass-ceramic temperature is minimum.

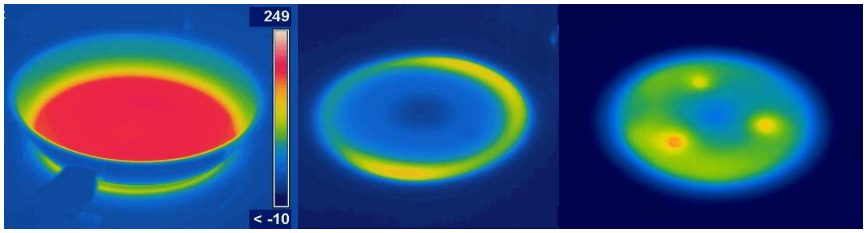

Figure 6.3: Temperature of the cooking surface measured with a thermal infrared camera.

Another advantage of the contact spots is that the area of contact between the cooking pot bottom and the glass-ceramic surface is minimized, and hence, the amount of heat dissipated through the glass-ceramic is minimized as well. It is worth mentioning that during any cooking process, a part of the heat generated in the cooking pot is dissipated upwards through the air and downwards through the glass-ceramic. These heat losses depend on the surface contact, that is, the larger the surface, the greater the losses. Evidently, for the same surface, the heat losses through the glass-ceramic by means of conduction are greater than the heat losses through the air by means of natural convection. Therefore, from the thermal point of view, it would be desirable to decrease the contact surface between the cooking pot and the glass-ceramic, as the contact spots do. This results in a considerable improvement of the efficiency of the cooking process itself. To see this, the same power step is provided to the same cooking pot in an induction hob with and without contact spots. Obtained results are depicted in Fig 6.4. When the cooking zone includes contact spots, the cooking pot reaches higher temperatures, which means that the overall

efficiency is higher (specifically 5% higher), because the power supplied is constant. Moreover, the maximum temperature measured by the NTC thermistor beneath the contact spots is significantly higher than the maximum temperature measured by the NTC thermistors when no contact spots are used.

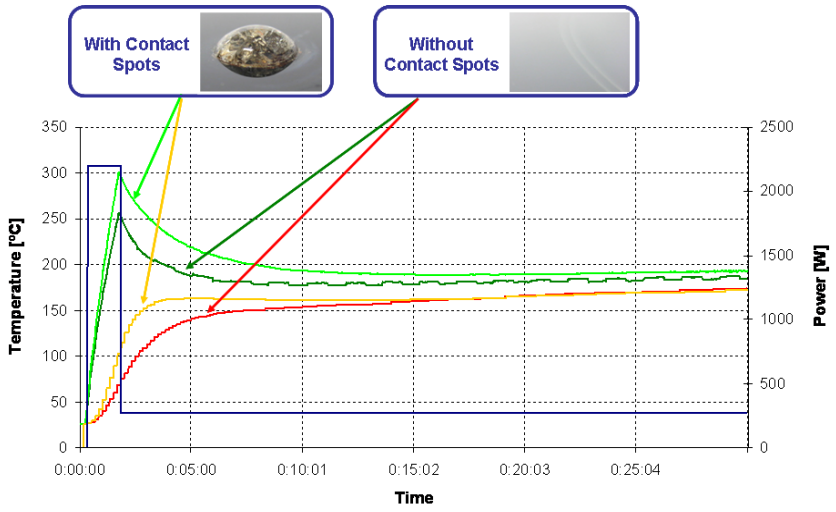

Figure 6.4: Effect of the contact spots. Blue line is the supplied power. Light and dark green lines are the cooking pot temperatures with and without contact spots respectively. Yellow and red lines are the temperature measured by the NTC-thermistors with and without contact spots respectively.

Despite all these advantages, contact spots have not been included in a commercial induction hob but only in prototypes. The main reason for this is that contact spots modify the evenness of the hob surface, and consequently, it might decrease the cleanness of the induction hob, which is one of its strong points from the marketing point of view. This justify the need of a different approach to minimized the influence of the cooking pot concavity and of the relative position between the contact sensors and the cooking pot, in which no modifications of the cooking surface were needed.

6.3 Sensor Line

Based on these requirements, a different lay-out for the NTC thermistors were proposed: the sensor line [62], [51]. Its behavior is based on the fact that there always exists a point where the gap of air is minimum, that is, the thermal contact resistor between the cooking pot bottom and the glass-ceramic is minimum. Providing that a non-contact sensor were located

just beneath that point, the difference between the actual temperature of the cooking pot and the temperature measured by that non-contact sensor would be minimum as well. As it has been commented previously, the uncertainty associated with the cooking pot concavity varies along its radius. This suggest a new lay-out for the NTC thermistors in which them are not located at few discrete positions (see Fig. 2.11), but in a straight line along the inductor radius separated by 10 millimeters (see Fig. 6.5).

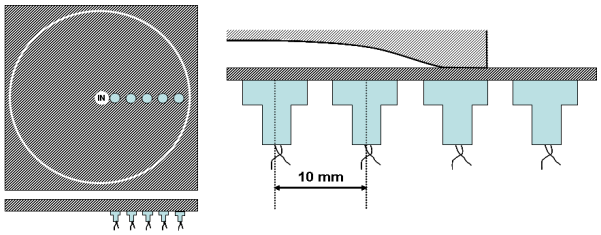

Figure 6.5: Sensor Line.

Unfortunately, due to the current design of the inductor, there exist considerable size constraints, and consequently, it is not possible to locate all the required NTC thermistors with the lay-out proposed in Fig. 6.5. For this reason, wire-thermocouples, which are thinner and more flexible, have been used instead so that the feasibility and effectiveness of this proposal could be checked. Resultant prototype is shown in Fig. 6.6, where the radial distribution of the contact sensors is shown.

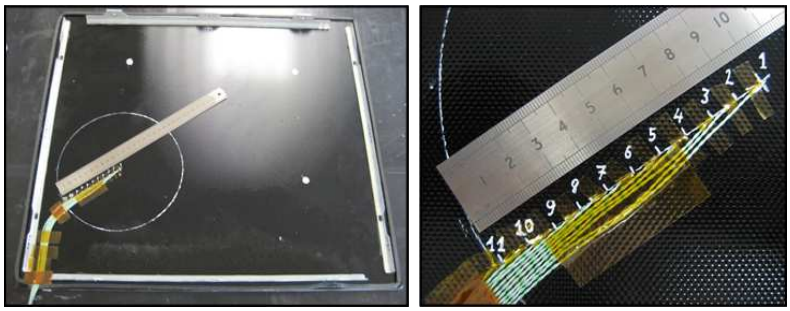

Figure 6.6: Radial distribution of the wire-thermocouple.

To show the superior performance of this prototype, the temperature measured by each wire-thermocouple was monitored while heating up several different cooking pots. One of these tests is shown in Fig. 6.7. Black line is the actual temperature of the cooking pot; green line is the maximum temperature measured with the sensor line, which is obtained where the air gap is minimum; red line is the temperature measured by the thermocouple located at the center of the inductor; green line is the temperature measured by a thermocouple located at a distance of 60 millimeters from the center

of the inductor. It is worth mentioning that both the green line and the red line actually show the temperature that the two NTC thermistors currently used in induction hobs would measure, due to the fact that they are located at the same positions that the current NTC thermistors (see Fig. 2.11), and hence, these results can also be used to compare the performance of the sensor line with the present solution.

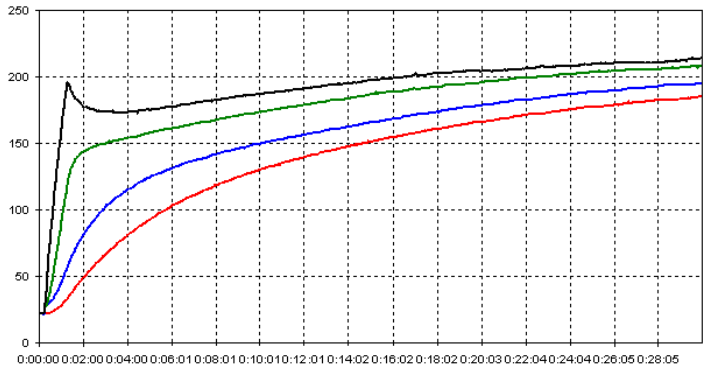

Figure 6.7: Influence of the radial distribution on the resultant temperature measurement.

Analyzing Fig. 6.7, it can be seen how the heat transmission from the cooking pot bottom though the glass-ceramic is better depending on the radial distance of each thermocouple. Moreover, it is also evident how the sensor line outperforms the current discrete NTC thermistors. To quantify this improvement, Fig. 6.8 shows the evolution of $\frac{-1}{a_{22}}$ as a function of the distance to the center for several cooking pots. These cooking pots have been selected because of their different characteristics (i.e. bottom convexity, weight, construction), which cover almost all the possible cooking pots available on the market. As it is shown in Appendix B, $\frac{-1}{a_{22}}$ represents how much the heat is filtered before being sensed by the NTC thermistors, due to the effect of the gap of air, and the glass ceramic itself, and hence, the lower $\frac{-1}{a_{22}}$, the faster the heat transmission will be.

Specifically, the uncertainty associated with $\frac{-1}{a_{22}}$ is decreased up to 40% (from $[50, 330]$ to $[50, 170]$). As it is pointed out in [62], decreasing the uncertainty of the system not only makes easier the pot temperature control but also would open a wide range of possibilities. For instance, it would be possible to substitute the current glass-ceramic for simpler materials such as toughened glass, cordierite, or borosilicate glass, which would result in a significant cost reduction. It is worth mentioning that despite the fact that these materials have worse mechanical and thermal properties, they would be still valid for cooking purposes, providing that the maximum achievable temperature were kept under control.

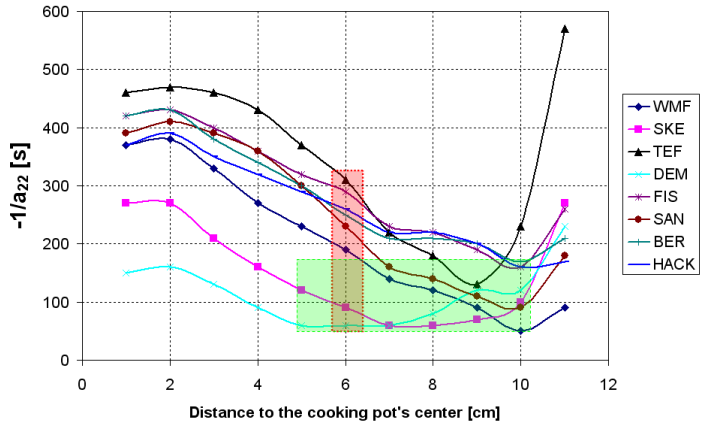

Figure 6.8: Variation of $\frac{-1}{a_{22}}$ as a function of the radius for several cooking pots. Red area represents the current $\frac{-1}{a_{22}}$ uncertainty. Green area represents the $\frac{-1}{a_{22}}$ uncertainty obtained with the sensor line.

6.4 Magnetic Sensor

All the approaches presented so far are based on modifying the current surface of the glass-ceramic and/or including additional temperature sensors, and consequently, increase the cost of the product. Ideally, we would prefer an alternative that could be performed with the elements currently integrated in a induction hob. To this end, a different approach for measuring the cooking pot temperature in induction hobs was presented in [53]. This novel temperature sensor consists of a coil and an oscillator [173]. It measures the variation of the impedance of the coil placed below a ferromagnetic pot when its temperature changes. This sensing method has promising applicability in induction hobs because it is cheap, contactless, and has instantaneous response. The main advantage of this approach is that the sensing coil is the same that heats up the cooking pot on induction hobs and consequently no additional investment is needed.

The sensing method is based on the dependence of the electrical conductivity of the material of the pot with respect to its temperature. Nowadays, iron is the most common material used to manufacture suitable pots for induction cookers. Although the magnetic permeability of iron also depends on the temperature, this dependence is not determinant unless the Curie temperature of the material is reached [174]. Thus, for the considered temperature span ($20°C - 300°C$), the magnetic permeability of the iron is considered constant, whereas the electrical conductivity $\sigma_{Fe}(T)$ is as

follows [175]:

$$\sigma_{Fe}(T) = \frac{1.003 \cdot 10^7}{1 + 0.00536(T - 300) + 7.67 \cdot 10^{-6} \cdot (T - 300)^2} \tag{6.1}$$

where T is the temperature of the cooking pot in Kelvin, whose value is required. The value of the numerator is also called the electrical conductivity at ambient temperature σ_0. Given the arrangement of induction cookers, a sensor shape similar to that of the main heating coil (i.e. planar and spiral shape) is the most plausible because this shape makes its integration into the hob easier and no additional elements are needed.

The change in the electrical conductivity of the material leads to a change in the electrical equivalent impedance of the coupled sensor-vessel system. As is known, the equivalent impedance Z_{eq} of an induction system consists of the series connection of equivalent resistance and inductance [7], i.e.

$$Z_{eq} = R_{eq} + jwL_{eq} \tag{6.2}$$

Therefore, the measurement of the temperature consists in detecting the variation of the equivalent inductance with respect to the reference value corresponding to the ambient temperature. The variation of L_{eq} is the origin of the change of the oscillator frequency, which can be easily measured by either analog or digital methods, and is given by

$$f(T) = \frac{1}{2\pi}\sqrt{\frac{1}{L_{eq}C_{res}} - \left(\frac{R_{eq}(T)}{L_{eq}(T)}\right)^2} \tag{6.3}$$

where C_{res} is the resonant capacitor and is a design parameter to tune the frequency range. Due to the fact that the inductance span grows as the frequency decreases, to obtain the most accurate measurement we must select the resonant capacitor that allows the oscillator to work at as low a frequency as possible.

As a calibration process is needed, some laboratory tests were carried out to obtain the different gains of the sensor depending on the materials of the base of the pot. We selected four typical pots to train the microcontroller of the hob. As the kinds of alloys used to make ferromagnetic pots are quite similar to those of the four pots used for calibration, it is unnecessary to train the hob with all the pots on the market. To calibrate the hob, each characteristic pot is placed over the induction hob at room temperature and its impedance values R_{eq}, L_{eq} are obtained. Afterwards, a heating-up test is done registering the temperature of the pot and the frequency of the marginal oscillator throughout the cooking range. The initial inductance of each pot is then related to its temperature-frequency curve and logged into the memory of the control unit of the hob. In the real application, the hob, having been previously calibrated in the laboratory, measures the

Table 6.1: Calibration results for cooking pots shown in Fig. 6.9

Cooking Pot	$\beta_i[K/Hz]$
1	3427.9
2	2272.9
3	3468.9
4	12066

initial inductance at room temperature and assigns the pot a temperature-frequency curve so that the real temperature can be obtained.

Calibration results are shown in Fig. 6.9. From these measurements it is possible to establish the relation between the percentage of frequency variation and the temperature of the pot for each type of cooking pot $T_i = \beta_i \Delta f_i$. The results are summarized in Table 6.1. As mentioned above, the memory of the control unit of the hob stores the initial impedance value and β_i for each kind of pot. When the user places a pot over the cooking zone, the hob measures the initial inductance value identifying the kind of cooking pot that the user is going to use, and converts the frequency measurements to temperature by means of β_i.

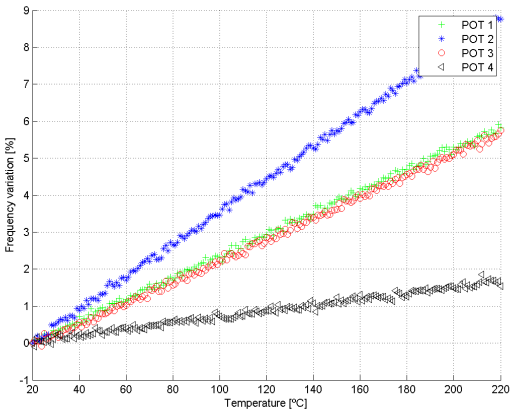

Figure 6.9: Temperature of the cooking surface measured with a thermal camera.

The sensor has been implemented in an induction hob to test its behavior in a real environment, previous to serial manufacturing. Obtained results in a real induction hob are presented in Fig. 6.10. The graph shows the behavior of the cooking pot POT1 and POT4. The measurement of the temperature with the proposed inductive sensor shows a good fitting with the real temperature registered. In spite of the noise that appears in the measurements (smaller than $6°C$), the precision is regarded to be good

enough.

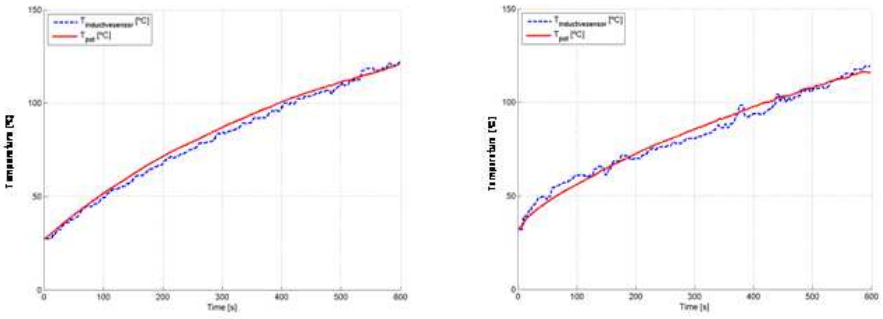

Figure 6.10: Application results over POT1 (left) and POT4 (right).

Some critical issues in the use of the sensor at household conditions require further comment. First of all, we focus on the starting condition. As the initial state is used to determine the properties of the pot and a gain is assigned to relate frequency and temperature, for a correct measurement it is important that the pot is identified at the same state at which the microcontroller has been trained, that is to say, at room temperature with the pot totally covering the sensing coil. Secondly, there is the cooking process itself. The pot is not fixed to the cooking zone, and it is therefore possible that the pot is misaligned from the center. Moreover, users generally move the cooking pot while they are cooking generating misalignments as well. Small misalignments have slight influence on the variation of frequency and are not critical, but larger displacements that uncover the sensing coil may cause an abrupt change in the frequency causing a wrong measurement. A way to solve this issue would be to assume that any abrupt change in the temperature measurement is caused by misalignments, and then as a safety measure, the hob would reduce the power to a safe range, and would alert the user through acoustic signals that the cooking pot is not centered.

6.5 Discussion

Summing up, since sensing the pot temperature for cooking processes with high load is solved by using a retractable infrared sensor, most of the effort has been focused on developing new temperature sensors that were feasible for temperature control in cooking processes with low load, and that outperformed the existing solution, which is based on two NTC thermistors. Despite the fact that NTC thermistors suffer from robustness issues, because their sensed temperature depends on the relative position between the cooking pot and themselves, and that their sensing time constant is generally high, due to the fact that the heat has to be transmitted downwards from the cooking pot bottom through both air gap and glass-ceramic, they

have been used in induction cookers mostly because of their very low cost and their simplicity, since no modification on either the glass-ceramic surface or the inductor construction is needed.

Contact spots succeed where NTC thermistors fail. The dependence on the relative position between the cooking pot and the sensors is completely removed, because the special distribution of the contact spots (i.e. forming a triangle) force the cooking pot to be in a fixed location just like happens in traditional gas stoves. Moreover, the effect of the air gap is also minimized, due to their rounded head, which guarantees a reduced thermal contact resistor between the sensor located beneath each contact spot and the cooking pot bottom, regardless its concavity. However, these excellent features result at the expense of a substantial cost increment, due to the fact that additional thermistors for each contact spot are needed and that the glass-ceramic surface has to be modified.

Similar performance can also be obtained by using a sensor line. The additional thermistors intelligently distributed forming a straight line along the inductor radius guarantee that at least one would be located below the point where the air gap is minimum, independently of the position of the cooking pot, which reduces the sensing time constant and increases the robustness of the sensing system. Moreover, no modifications on the glass-ceramic surface are needed, and consequently, final hob's cleanness is not affected. Main drawbacks of this approach are that it requires additional thermistors (even more than contact spots), and more important, the fact that these additional thermistors cannot be included in the current inductor because of size constraints, which would result in a new redesign for the inductor, and hence, in a significant cost increment.

Unlike previous proposals, magnetic sensor does not require any additional modification, because its operation only requires a simple oscillator and the induction coil that is currently used to heat up the cooking pot. Another strong point is the fact that it measures the temperature of the cooking pot in an instantaneous way, because it is not based on the heat transmitted downwards but on changes in the electrical properties of the cooking pot itself. However, these changes are highly dependent on the relative position between the cooking pot and the induction coil, which reduce the robustness of the resultant system working in household conditions.

In conclusion, main strengths and weaknesses of each proposed sensor are summarized in Table 6.2. All the proposed novel approaches have promising features and generally outperform the existing NTC thermistor-based solution in terms of robustness, accuracy, or response time. Unfortunately, most of them require additional elements and some modifications on the inductor structure and/or the glass-ceramic surface that make them unfeasible from the marketing point of view, because they would sensibly increase the cost of the final product. An exception would be the magnetic sensor, which almost does not increase the cost. However, its lack of robustness in household

Table 6.2: Temperature sensor comparison

Sensor	Cooking Load Required	Robustness	Sensing Time Constant	Surface Modification Required	Cost
Infrared Sensor	High	Very High	Instantaneous	Yes	High
NTC Thermistor	Low	Medium	Medium	No	Very Low
Contact Spots	Low	High	Low	Yes	Medium
Sensor Line	Low	High	Low	No	Medium
Magnetic Sensor	Low	Low	Instantaneous	No	Very Low

conditions decreases its applicability at its current status.

For all these reasons, the current NTC thermistor-based solution is the one that best balances the two most important features of a temperature sensor: performance and cost. However, as it has been commented previously, this solution provides a quite uncertain measurement of the temperature of the cooking pot that is being used. For this reason, an estimation algorithm is needed to estimate the temperature of the cooking pot bottom from the measurements of the NTC thermistors, so that the effect of this uncertainty on the temperature control could be minimized. How it can be carried out is outlined in the next chapters.

Chapter 7

Implementation

Once the most suitable temperature sensors for high and low load cooking processes have been determined, the next step consists in designing an effective control-estimation algorithm to guarantee a robust temperature control. To this end, some of the theoretical proposals previously presented have been implemented and compared with alternative solutions. First, an adaptive controller based on Multiple-Model Reset Observers is presented, including its design and tuning, which depends on the temperature sensor used. For comparison purposes, a QFT-robust controller and a PI-like non-adaptive controller are also tuned and designed. Simulation results show that our proposed adaptive controller based on Multiple-Model Reset Observers is able to achieve a robust temperature control for both high and low load cooking processes, outperforming other alternatives. This comparison will be extended in the next chapter, in which real experiments are considered.

7.1 Introduction

In the previous chapters, the feasibility of the retractable infrared sensor and the NTC thermistors, for cooking pot temperature control in processes with high and low load respectively, has been proved. Based on these sensors, the next step consists in developing a control-estimation algorithm to guarantee an accurate temperature control in household conditions. These algorithms will be mostly based on the reset observer formulation previously presented in Chapters 3-5. For this reason, the goal of this chapter is twofold. Firstly, we aim at investigating the potentials of the proposed reset observers applied to process control. Secondly, we aim to overcome the existing performance limitations of the temperature control in domestic cookers. In addition, our proposals exploit the potential benefits of using an accurate model of the system, which is explained in detail in Appendix B. Consequently, controller-observer tuning processes are highly simplified because our control strategies are based on an analytical model of the system rather than on multiple experimental tests.

7.2 Temperature Control by Using a Retractable Infrared Sensor

Regarding cooking temperature control in processes with high load, and hence, by using a retractable infrared sensors, an adaptive simmering control for induction cookers, whose parameters are updated on-line depending on the estimates provided by a Multiple-Model Reset Observer (MMReO), is presented. This new observer results of extending the idea of multiple models to the state observer framework. MMReO consists of a reinitialized reset observer, and of multiple fixed identification models. The resultant control scheme satisfies the user requirements such as quick heating up, accurate temperature control, and fast disturbance rejection, outperforming previous results. Moreover, the proposed control scheme reduces energy consumption and, consequently, it can increase the efficiency of the whole cooking process. Additionally, for comparison purposes, we have designed a fixed robust QFT-based controller, which is a control technique widely applied to industrial applications. To highlight the performance of our proposal, both control schemes have been implemented in a real induction hob, and several verification tests will be shown in the next chapter.

7.2.1 System Model

State space model can be used to represent the relation between the power supplied by the induction coil and the temperatures of the system. Gener-

Table 7.1: Nominal model parameters and their ranges

Parameter	Nominal Value	Variations
a_{11}	-0.0197	[-0.0461 -0.0048]
a_{12}	0.0097	[0.00230 0.02291]
a_{21}	0.0018	[0.00030 0.00540]
a_{22}	-0.0010	[-0.0029 -0.0002]
b_{11}	0.0018	[0.00120 0.00290]
b_{22}	0.0001	[0.00010 0.00040]

ally, state space models are described by the following equation:

$$\begin{array}{rcl} \dot{x}_p(t) & = & A_p \cdot x_p(t) + B_p \cdot u(t) \\ y_p(t) & = & C_p \cdot x_p(t) \end{array} \tag{7.1}$$

where $x_p(t) \in \mathbb{R}^n$ is the state vector, $u(t) \in \mathbb{R}^l$ is the input vector, $y_p(t) \in \mathbb{R}^m$ is the system output vector and A_p, B_p, C_p are constant $(n \times n), (n \times l), (m \times n)$ matrices.

The model used in this section is the same that the analytical pot model proposed by [59], and, how that system is obtained is described in Appendix B.2. To sum it up, by using an electrical equivalent model that represents the different heat transmissions which appear in our system, and applying the Laplace transform, it is possible to obtain the following state space model:

$$\begin{array}{rcl} \begin{bmatrix} \dot{\theta}_B \\ \dot{\theta}_W \end{bmatrix} & = & \begin{bmatrix} a_{11} & a_{12} \\ a_{21} & a_{22} \end{bmatrix} \begin{bmatrix} \theta_B \\ \theta_W \end{bmatrix} + \begin{bmatrix} b_{11} & 0 \\ 0 & b_{22} \end{bmatrix} \begin{bmatrix} P \\ Q_E \end{bmatrix} \\ \theta_W & = & \begin{bmatrix} 0 & 1 \end{bmatrix} \begin{bmatrix} \theta_B \\ \theta_W \end{bmatrix} \end{array} \tag{7.2}$$

where $\theta_B = T_B - T_0$ is the difference between the pot bottom temperature T_B and the ambient temperature, $\theta_W = T_W - T_0$ is the difference between the pot wall temperature T_B and the ambient temperature, P is the power supplied by the inductor coil which takes into account the efficiency of the electronics and of the inductor and Q_E is the latent heat. Additionally, a_{11}, a_{12}, a_{21}, a_{22}, b_{11} and b_{22} are uncertain parameters that depend on the pot and glass thermal properties as well as on the different thermal losses of the system. Namely, convention losses, radiant losses and conduction losses.

Since the pot which is being used during the simmering process is unknown, these uncertain parameters are initially unknown. However, according to our results obtained during simulation the value of each uncertain parameter is inside a known variation range. Table 7.1 summarizes the nominal values of all model parameters and their variations.

Notice that most of cooking processes are carried out using a lid, because it highly decreases the thermal losses of the system, and consequently,

improves the efficiency. Therefore, we consider that the simmering cooking process is done in a pot with lid which implies that $Q_E = 0$.

7.2.2 QFT Control Scheme

Quantitative Feedback Theory (QFT) is a robust control technique developed by Isaac Horowitz [21]. It has been widely used in industrial applications for the last three decades [176], [177], because it takes into account the system parameter uncertainty in the design of the controller.

The first step in QFT design is to translate the system uncertainty to frequency domain. For this purpose, the frequency responses of all possible combinations of system parameters are represented in a Nichols chart. Each point plotted represents a possible plant or sensor for a given frequency. Therefore all these points define a region of the uncertainty of the system at the different working frequencies. These regions are known as templates. In particular, the templates obtained for the uncertain system described in Table 7.1 for the working frequencies $w = [0.002, 0.005, 0.02, 0.1, 1]$ rad/s are shown in Fig. 7.1.

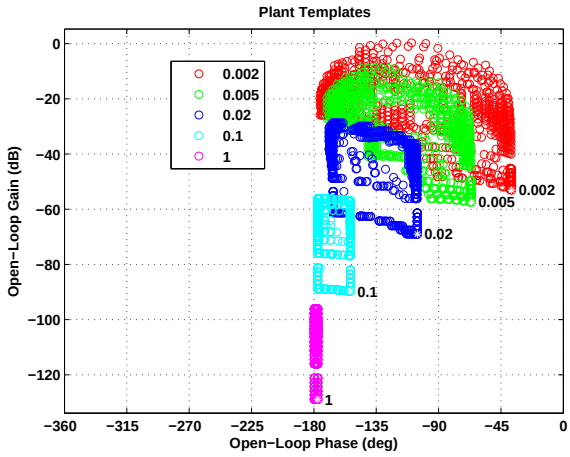

Figure 7.1: Plant Templates.

In the next step, control requirements have to be translated into boundaries in a Nichols chart. In QFT, each closed-loop specification, such as robust stability, tracking ability and disturbance rejection, generates a boundary. If the nominal open loop gain avoids the boundaries, it is guaranteed that the closed loop specifications are satisfied for all the plants considered in the template.

For our system, we have selected the following closed-loop performance specifications:

a) *Robust Stability:* To ensure robust stability of the closed-loop system,

the following constraint on the peak magnitude of the closed loop frequency response is set:

$$\left| \frac{P(s)G(s)}{1+P(s)G(s)} \right| \leq \gamma, \tag{7.3}$$

where $P(s)$ is the plant and $G(s)$ is the controller. Moreover, γ is the maximum peak magnitude which corresponds to a minimum gain margin (GM) and phase margin (PM), [178] as follows:

$$GM = 20log\left(\frac{\gamma+1}{\gamma}\right)[dB], \tag{7.4}$$

$$PM = 2sin^{-1}\left(\frac{1}{2\gamma}\right)[deg], \tag{7.5}$$

in particular, we have chosen $\gamma = 1.5$ which gives $GM = 4.43$ and $PM = 39^\circ$.

b) *Reference Tracking:* Due to system uncertainty, we define an acceptable range of variations in the closed loop tracking responses. According to [22], [24], we define an upper $T_{UP}(s)$ and lower $T_{DW}(s)$ bounds for the closed-loop response of our system as follows:

$$|T_{UP}(s)| \leq \left| \frac{P(s)G(s)}{1+P(s)G(s)} \right| \leq |T_{DW}(s)|. \tag{7.6}$$

Specifically, Fig. 7.2 shows the upper and lower tracking bounds selected which have the following transfer functions:

$$T_{UP}(s) = \frac{1.02}{(20s+1)(5s+1)}, \tag{7.7}$$

$$T_{DW}(s) = \frac{0.98}{(80s+1)(70s+1)(1s+1)(0.1s+1)}. \tag{7.8}$$

c) *Plant input noise rejection:* According to (7.2), the power supplied by the inductor is the input of our system which is measured with a Sigma-Delta analog-to-digital converter implemented in the ASIC of the induction hob [179]. Since this converter has a measurement error about a 5%, we have designed a controller able to reject this kind of disturbances. In particular, we have chosen the following input noise rejection specification:

$$\left| \frac{P(s)}{1+P(s)G(s)} \right| \leq 0.01. \tag{7.9}$$

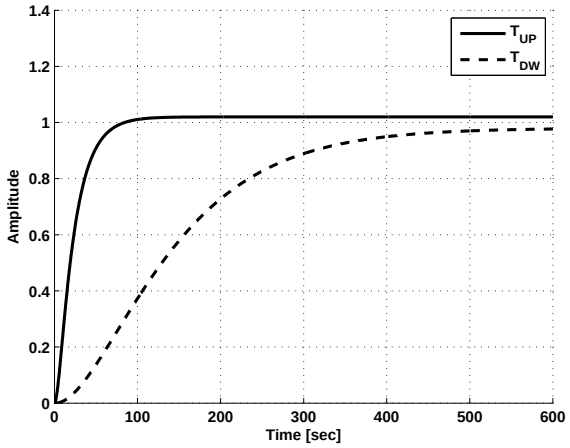

Figure 7.2: Step response of the upper and lower tracking bounds.

Fig. 7.3 shows the intersection of these three performance specifications at the design frequencies used during the template generation. To satisfy the performance specifications, the open-loop response has to be above the corresponding boundary as long as it is drawn in solid line, whereas if the boundary is drawn in dashed line the open-loop response has to be below the boundary.

It is easy to see, that the system does not meet the performance specifications since the open-loop frequency response is below the performance specification bounds at each frequency. Therefore, we have to modify the system response adding poles and zeros until the nominal loop lies near its bounds and results in nominal closed-loop stability. This process is known as loop-shaping and generates directly the robust feedback compensator.

Fig. 7.3 also points out that an appropriate control gain should be introduced to push the open-loop frequency response upwards. Additionally, a dynamic compensator is required in order to change the shape of the open-loop frequency response too. Following this approach, the resulting controller is:

$$G(s) = 9\frac{\left(\frac{1}{0.0028}s+1\right)\left(\frac{1}{0.035}s+1\right)}{s\left(\frac{1}{0.9}s+1\right)}, \tag{7.10}$$

whose frequency response with the plant is illustrated in Fig. 7.4. It is clearly seen that the open-loop frequency response meets now all performance requirements, since it is above all bounds at the corresponding frequency. Therefore, we can state that the designed controller ensures robust stability and an appropriate noise rejection for all of the family of plants

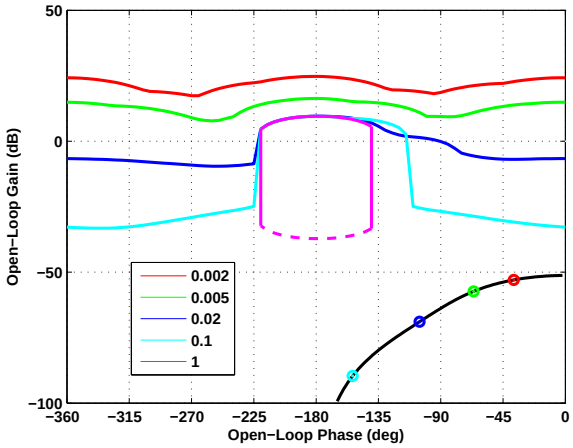

Figure 7.3: Open-loop frequency response and performance specification bounds.

defined under the uncertainty shown in Table 7.1.

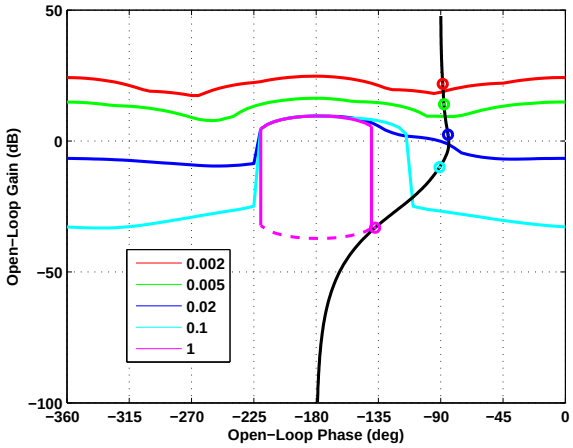

Figure 7.4: Open-loop frequency response with the controller.

Nevertheless, the controller is not able to satisfy the tracking specification as it shown in Fig. 7.5. Therefore, a dynamic pre-filter is required to shape the frequency response to be within the required envelope and attenuate high frequency peaking. Specifically, we have designed the following

pre-filter:

$$F(s) = 1\frac{\left(\frac{1}{0.3}s+1\right)}{\left(\frac{1}{0.017}s+1\right)\left(\frac{1}{0.1}s+1\right)}, \tag{7.11}$$

which allows to meet now the tracking specification as it is shown in Fig. 7.6.

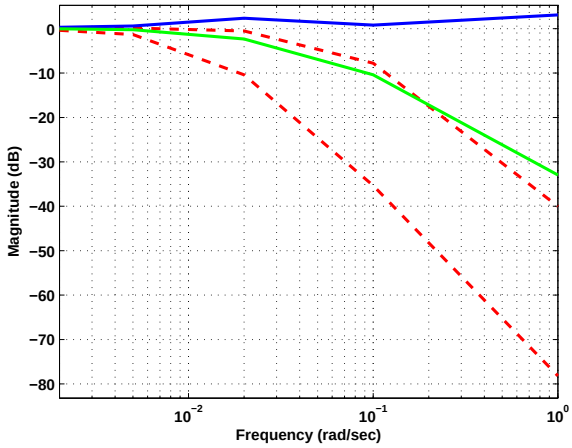

Figure 7.5: Closed-loop frequency response with the controller.

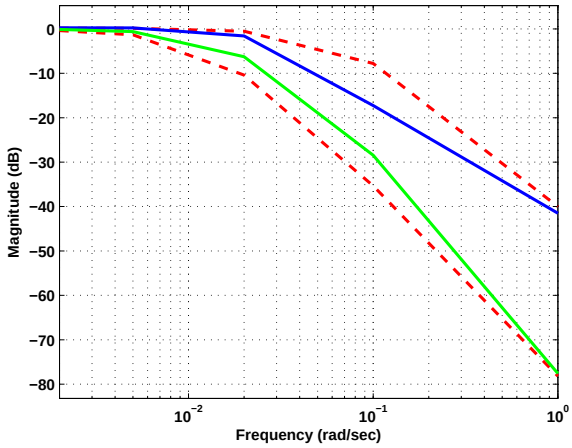

Figure 7.6: Closed-loop frequency response with the controller and the pre-filter.

So far, we have only ensured that the proposed controller meets the performance requirements at some discrete frequencies. Consequently, an

additional checking step at all frequencies inside the working range is needed. For this reason, we show in Figs. 7.7, 7.8 and 7.9 the closed-loop response of the system with the designed controller and per-filter for the robust stability, reference tracking and noise rejection specifications respectively.

Concluding, the proposed controller and pre-filter meet the robust stability and noise rejection specifications at all frequencies, since the closed-loop response is below the corresponding boundary in both cases (see Fig. 7.7 and Fig. 7.9). Additionally, the proposed controller and pre-filter satisfy also the reference tracking specification, since the maximum and minimum closed-loop response are inside the tracking range defined in (7.8).

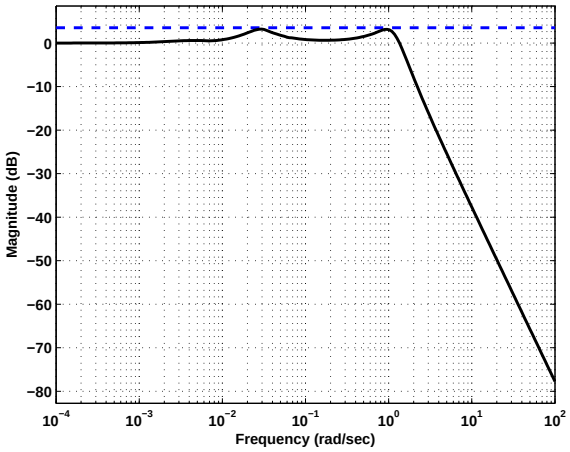

Figure 7.7: Closed-loop stability margins.

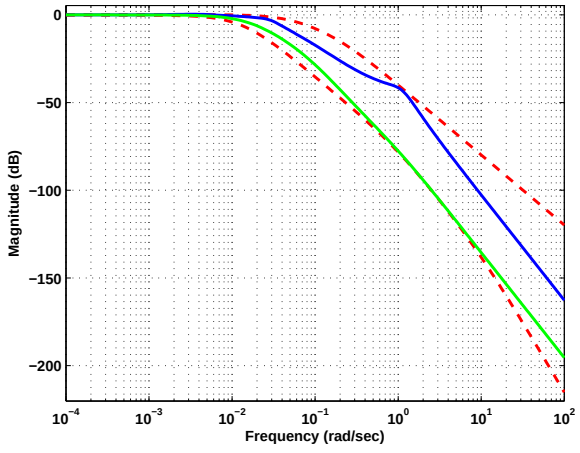

Figure 7.8: Closed-loop reference tracking margins.

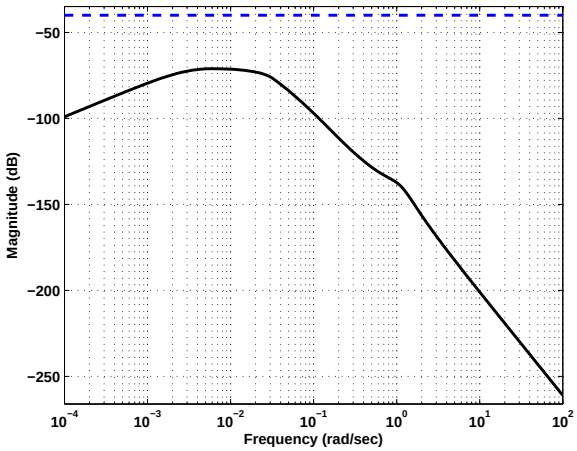

Figure 7.9: Closed-loop noise rejection margins.

7.2.3 Adaptive MMReO-Based Controller

Robust control techniques commented above can be regarded as conservative, due to the fact that the resultant controller has to be designed to meet control requirements for the worst-case behavior between all the considered operation points (i.e. for all the uncertainty of the system). Therefore we could obtain a better performance, if we were able to reduce the uncertainty of the parameters of the cooking process somehow.

Adaptive observers can play a key role in this approach, since they have been widely used to estimate the unknown parameters of a system from the available information (e.g. system input and output measurements) [35]. Therefore, these algorithms represent a useful tool in order to cope with problems that may appear in any industrial application. For instance, they can be used to deal with systems whose parameters are initially unknown due to modeling uncertainties, and also to handle systems whose parameters are time variant. Additionally, they have important applications not only in adaptive control but also in fault detection and isolation [180].

Among the different sort of adaptive observers, we present an estimation strategy that relies on multiple models of the system, in order to increase the robustness of the estimation process. The idea of multiple models was firstly introduced for control purposes [96]. It is commonly accepted that the convergence time of an adaptive control scheme will be large if the initial parameters of the controller are not close enough to the plant parameters. This transient behavior can be improved using multiple models [98], [99]. Assuming that the plant parameters belong to a compact set S, this approach relies on using N identification models with different parameters but uniformly distributed in S. A controller for each model is also calculated

and tuned. Therefore, the proposed strategy is to determine the best model for the real system at every instant, and using the corresponding controller to control the plant.

Building on [98], we extended the idea of multiple models to the state observer framework. The resultant observer scheme is denoted as Multiple Model Observer (MMO). In a similar way, N identification models with different parameters but uniformly distributed in S are used to estimate the best model for the real system. At every instant, the parameters of the best identified model are used as the starting parameters of an additional state observer. This process is known as the reinitialization of the state observer. Since the reinitialized parameters of the state observer are closer to the real ones, the convergence time of the estimation process is decreased. Afterwards, the state estimated by the reinitialized observer can be used in the control law. Furthermore, the parameters corresponding to the best identified model can also be used to adapt the control law, to improve even more the closed-loop response of the system.

Observer Scheme

Based on this approach, we present in this paper an adaptive controller whose parameters are updated on-line depending on the estimates provided by a Multiple-Model Reset Observer (MMReO). MMReO scheme is depicted in Fig. 7.10. It consists of a reinitialized reset observer, and of multiple fixed identification models. Each fixed identification model has the structure shown in (7.2) with different parameters a_{11}, a_{12}, a_{21}, a_{22}, b_{11}, and b_{22} defined according to Table 7.1, which actually define the convex set S for our system. The behavior of the MMReO scheme is as follows. It selects the identification model that best represents the cooking process depending on the output of the system y (i.e. the temperature measured with the infrared sensor), and the input of the system u (i.e. the power supplied with the induction coil). Specifically, the algorithm uses the following cost function J_i to find out the best model $i \in [1, N]$

$$J_i = \epsilon_i^2 + \int_{t=0}^{t=\infty} \epsilon_i^2 dt, \tag{7.12}$$

where $\epsilon_i = y - y_i$ is the identification error of the model i defined as the difference between the output of the system y and the output of the identification model y_i. The algorithm also generates a switching signal σ that is used to update the parameters of the reinitialized reset observer. Since the observer parameters are closer to the real system parameters, it is expected to decrease the transient behavior of the observer and, as a consequence, to improve the control performance which relies on the estimated state.

As it is shown in Fig. 7.10, we use a reset observer (ReO) based on the sector reset condition whose matrices A_i, B_i are reinitialized according to

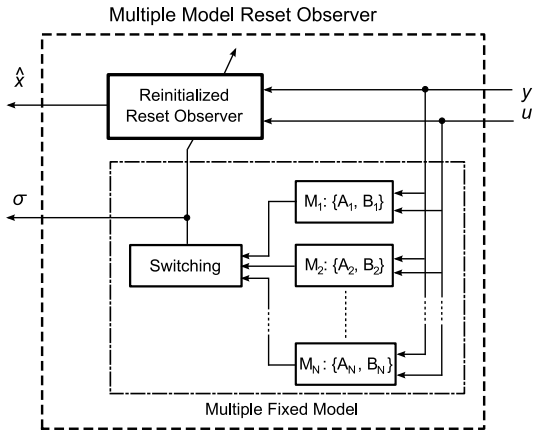

Figure 7.10: Multiple Model Reset Observer Scheme.

the matrices of the best model chosen. The aim of the ReO is to estimate the system state variables (i.e. $\hat{x} = [\hat{\theta}_B, \hat{\theta}_W]^T$), which will be used afterwards in the control law. The ReO dynamics based on the sector reset condition are given by

$$\begin{aligned} \dot{\hat{x}} &= A_i\hat{x} + B_i u + K_I\zeta + K_P\tilde{y} \\ \hat{y} &= C_p\hat{x} \end{aligned} \tag{7.13}$$

where A_i and B_i are the system matrices associated with the best model previously identified in such a manner that $A_i \approx A_p$ and $B_i \approx B_p$. In addition, the remaining terms are defined as in Chapter 3.

Control Scheme

Once the estimation process is done (i.e. when $\hat{x}$ has been computed), the parameters of the adaptive controller are updated depending on the identified model. An adaptive PI-like controller is selected because of its simplicity and easy auto-tuning [181]. Fig. 7.11 shows the proposed adaptive control scheme. It has a term that depends on the integral error as usual, but the proportional term affects directly the system state rather than the control error. The corresponding control law is given by

$$\begin{aligned} u &= L_{I_i}x_I - L_{S_i}\hat{x} \\ \dot{x}_I &= r - y \end{aligned} \tag{7.14}$$

where r is the target temperature, x_I is the integral error, L_{I_i} and L_{S_i} are the integral gain of the controller and the state gain of the controller respectively, which are computed off-line with pole placement methods, and afterwards, are updated on-line through a look-up table depending on the i-model identified with the MMReO scheme.

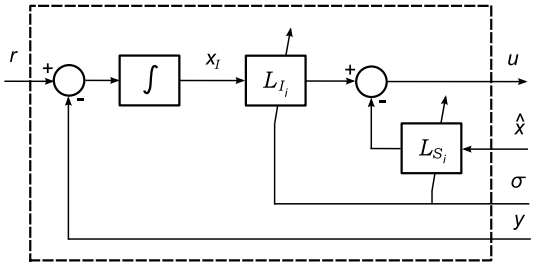

Figure 7.11: Adaptive Control Scheme.

It is worth mentioning that since we have implemented $N = 60$ fixed identification models, we do not include here for brevity all the values of the parameters involved in this control scheme that depend on the identified model (e.g. A_i, and B_i in the MMReO scheme; L_{I_i}, and L_{S_i} in the adaptive control scheme).

Quadratic stability analysis

The proposed adaptive MMReO-Based Controller can be regarded as a dynamical system that consists of a finite number of subsystems and a logical rule that defines switching between these subsystems. Since there exists no restriction on the switching signals, the stability of our proposal has to be checked under arbitrary switching.

Quadratic stability of the switched system under arbitrary switching is generally proven by ensuring the existence of a common quadratic Lyapunov function (CQLF) for all its subsystems. Quadratic stability implies asymptotic stability, and has become significantly popular because the conditions for the existence of a CQLF can be expressed as a linear matrix inequality problem (LMIP), which is easily computable [113], [120].

Since the control law of the MMReO-Based Controller relies on the estimate provided by the multiple model reset observer scheme, we have to prove first the asymptotic convergence of the estimation process (i.e. the estimation error $\tilde{x}(t) \to 0$ as $t \to \infty$), and after that, the asymptotic stability of the closed-loop system.

Let us begin analyzing the corresponding error system dynamics of the multiple model reset observer scheme. According to (7.13), it consists of N different reset observers whose matrices A_i and B_i change depending on the best chosen model, and whose matrices K_P, K_I,A_ζ, B_ζ and A_r remain constant independently of the chosen model. Since the state estimation error is $\tilde{x} = x - \hat{x}$, and by defining the augmented state estimation error $\eta = \begin{bmatrix}\tilde{x}^T & \zeta^T\end{bmatrix}^T$, the error dynamics of the estimation process of each of the

$i = 1, \ldots, N$ reset observers are given by

$$\left.\begin{array}{rcl} \dot{\eta} & = & A_{\eta_i}\,\eta \\ \tilde{y} & = & C_\eta\,\eta \end{array}\right\} \text{if } \eta \in \mathcal{F}, \quad i = 1, \ldots, N \tag{7.15}$$

$$\left.\begin{array}{rcl} \eta^+ & = & A_{R_i}\,\eta \\ \tilde{y}^+ & = & \tilde{y} \end{array}\right\} \text{if } \eta \in \mathcal{J}, \quad i = 1, \ldots, N \tag{7.16}$$

where

$$\begin{aligned} A_{\eta_i} &= \left[\begin{array}{cc} A_i - K_P C_p & -K_I \\ B_\zeta C_p & A_\zeta \end{array}\right], \quad C_\eta = \left[\begin{array}{cc} C_p & 0 \end{array}\right], \\ A_{R_i} &= \left[\begin{array}{cc} I & 0 \\ 0 & A_r \end{array}\right]. \end{aligned} \tag{7.17}$$

Then, the following proposition gives sufficient conditions for the existence of a CQLF between all of the $i = 1, \ldots, N$ reset observers so that the asymptotic stability of the multiple model reset observer scheme is guaranteed. This proposition is a standard argument for switching system stability (see, for instance, [113], [112] and references therein), and guarantees the existence of a CQLF that decreases when any reset system flows, and does not grow when any reset system is reset.

Proposition 13. *For given A_{η_i}, A_R and M the augmented error dynamics shown in (7.15)-(7.16) are quadratically stable, if for all $i = 1, \ldots, N$ there exist a matrix $P = P^T > 0$ and scalars $\tau_F \geq 0$ and $\tau_J \geq 0$ subject to*

$$\left.\begin{array}{rcl} A_{\eta_i}^T P + P A_{\eta_i} + \tau_F M & < & 0 \\ A_{R_i}^T P A_{R_i} - P - \tau_J M & \leq & 0 \end{array}\right\} \quad i = 1, \ldots, N \tag{7.18}$$

which is a linear matrix inequality problem in the variables P, τ_F and τ_J.

Proof. Let us begin considering the standard CQLF candidate for the error dynamics (7.15)-(7.16) that is given by

$$V_i(\eta) = V(\eta) = \eta^T\,P\,\eta, \quad i = 1, \ldots, N \tag{7.19}$$

To prove the quadratically stability of our proposed reset adaptive observer, we have to check that:

$$\begin{array}{ll} \dot{V}_i(\eta) < 0 & \eta \in \mathcal{F}, \quad i = 1, \ldots, N \\ V_i(\eta^+) \leq V_i(\eta) & \eta \in \mathcal{J}, \quad i = 1, \ldots, N \end{array} \tag{7.20}$$

According to (3.14), since $\mathcal{F} := \left\{\eta : \eta^T\,M\,\eta \geq 0\right\}$ and employing the S-procedure [120], the first term of (7.20) is equivalent to the existence of $\tau_F \geq 0$ such that

$$\dot{V}_i(\eta) < -\eta^T \tau_F M \eta, \quad i = 1, \ldots, N \tag{7.21}$$

Then, let us take derivative of (7.19) to obtain

$$\begin{aligned} \dot{V}_i(\eta) &= \dot{\eta}^T P\eta + \eta^T P\dot{\eta} \\ &= \eta^T (A_{\eta_i}^T P + PA_{\eta_i})\eta, \quad i = 1, \ldots, N \end{aligned} \tag{7.22}$$

Rearranging terms of equations (7.21) and (7.22), the first term of (7.20) holds if the following inequality is satisfied

$$\eta^T (A_{\eta_i}^T P + PA_{\eta_i})\eta + \eta^T \tau_F M\eta < 0, \quad i = 1, \ldots, N \tag{7.23}$$

which can be rearranged as an equivalent LMI problem in the variables $P > 0$ and $\tau_F \geq 0$

$$A_{\eta_i}^T P + PA_{\eta_i} + \tau_F M < 0, \quad i = 1, \ldots, N \tag{7.24}$$

which is analogous to the first term of (7.18) and consequently, proves the first equation of (7.20).

Similarly, employing again the S-procedure, the second term of (7.20) holds if there exists $\tau_J \geq 0$ such that

$$V_i(\eta^+) \leq V_i(\eta) + \eta^T \tau_J M, \quad i = 1, \ldots, N \tag{7.25}$$

which is equivalent to

$$\eta^T A_{R_i}^T PA_{R_i}\eta - \eta^T P\eta - \eta^T \tau_J M\eta \leq 0, \quad i = 1, \ldots, N \tag{7.26}$$

Rearranging terms, (7.25) can be also rewritten as an equivalent LMI problem in the variables $P > 0$ and $\tau_J \geq 0$ as follows

$$A_{R_i}^T PA_{R_i} - P - \tau_J M \leq 0, \quad i = 1, \ldots, N \tag{7.27}$$

which is analogous to the second term of (7.18) and proves the second equation of (7.20) and, as a consequence, completes the proof of the proposition. Note that this proof is similar to the one given in [58], but taking into account that now there are N different reset observers rather than only one. □

Now it only remains to prove the asymptotic stability of the control scheme. Note that since the asymptotic stability of the estimation process is guaranteed, we can substitute $\hat{x}$ for x. According to (7.14), it can be regarded as N different PI-like controllers whose adaptive gains L_{S_i} and L_{I_i} change depending on the best chosen model i. Defining the augmented closed-loop state $x_{cl} = \begin{bmatrix} x^T & x_I^T \end{bmatrix}^T$, and rearranging terms of (7.1) and (7.14), it is possible to write the closed-loop system dynamics as follows

$$\left.\begin{aligned} \dot{x}_{cl} &= A_{cl_i} x_{cl} + B_{cl_i} r \\ y_{cl} &= C_{cl_i} x_{cl} \end{aligned}\right\}, \quad i = 1, \ldots, N \tag{7.28}$$

where

$$\begin{aligned} A_{cl_i} &= \begin{bmatrix} A_p - B_p L_{S_i} & B_p L_{I_i} \\ -C_p & 0 \end{bmatrix}, \; B_{cl_i} = \begin{bmatrix} 0 \\ 1 \end{bmatrix}, \\ C_{cl_i} &= \begin{bmatrix} C_p & 0 \end{bmatrix}. \end{aligned} \tag{7.29}$$

Then the following proposition gives sufficient conditions for the existence of a CQLF between all of the $i = 1, \ldots, N$ controllers so that the quadratic stability of the multiple model adaptive controller scheme is guaranteed.

Proposition 14. *For given A_{cl_i}, the unforced version of the augmented state dynamics shown in (7.28) (i.e. $r = 0$) are quadratically stable, if for all $i = 1, \ldots, N$ there exist a matrix $Q = Q^T > 0$ subject to*

$$A_{cl_i}^T Q + Q A_{cl_i} < 0 \quad i = 1, \ldots, N \tag{7.30}$$

which is a linear matrix inequality problem in the variable Q.

Proof. This proposition follows directly from the results presented in [112]. As before, let us begin considering the standard CQLF candidate for the augmented state dynamics (7.28) that is given by

$$V_i(x_{cl}) = V(x_{cl}) = x_{cl}^T \, Q \, x_{cl}, \quad i = 1, \ldots, N \tag{7.31}$$

To prove the quadratic stability of our adaptive controller, we have to check that:

$$\dot{V}_i(x_{cl}) < 0, \quad i = 1, \ldots, N \tag{7.32}$$

To this end, let us take derivative of (7.31) to obtain

$$\dot{V}_i(x_{cl}) = x_{cl}^T (A_{cl_i}^T Q + Q A_{cl_i}) x_{cl}, \quad i = 1, \ldots, N \tag{7.33}$$

Then, substituting (7.33) in (7.32), it writes

$$x_{cl}^T (A_{cl_i}^T Q + Q A_{cl_i}) x_{cl} < 0, \quad i = 1, \ldots, N \tag{7.34}$$

that can be easily rewritten as the LMI problem (7.30), completing the proof. □

Simulation Example

To give insights into the behavior of the proposed adaptive control based on MMReO, we show some simulation results obtained with the simulator developed from [59]. We aim at heating up a cooking pot filled with 1 liter

of water from ambient temperature (i.e. $25°C$) to the target temperature (i.e. $91°C$).

Fig. 7.12 shows the parameters of the best model identified minimizing the cost function (7.12) at every instant. Since the number of fixed identification models is finite there still exists a small difference between the best model and the real system. Nonetheless, identified parameters are close enough to real ones in such a manner that the convergence speed of the reinitialized reset observer is highly decreased. Fig. 7.13 shows the temperatures of the cooking process as well as the temperatures estimated by the ReO. It underlines the good performance of the MMReO, since both temperatures are properly estimated.

Additionally, Fig. 7.14 shows the action computed by using the control law (7.14), which relies on the temperatures estimated by the ReO. It is evident the good performance of the whole control scheme, since T_W reaches the target temperature without overshooting as it is shown in Fig. 7.13. Finally, Fig. 7.15 shows the reset integral term ζ, and how it is reset at $t = [200, 310, 550]$. These resets as well as the reinitializations of the state observer, cause small discontinuities in the temperature of the bottom of the pot estimated by the ReO, and thus, in the action computed by the adaptive controller, as it is shown in Fig. 7.14. However, these discontinuities allow the water temperature to reach the desired reference, minimizing rise time and overshoot.

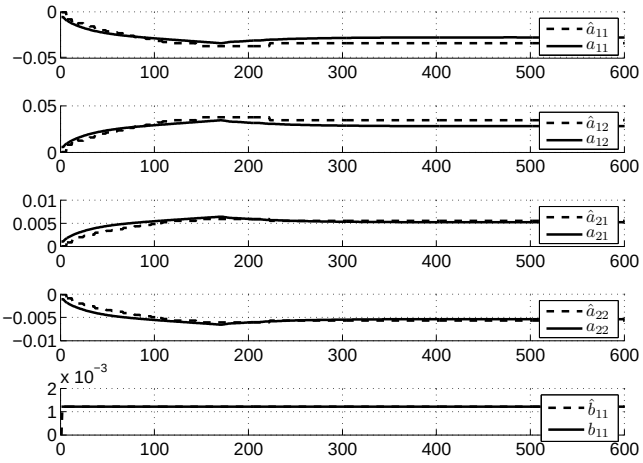

Figure 7.12: Simulation Results with the adaptive controller based on MMReO. Solid lines are the parameters a_{11}, a_{12}, a_{21}, a_{22}, b_{11}. Dashed lines are the estimated parameters $\hat{a}_{11}$, $\hat{a}_{12}$, $\hat{a}_{21}$, $\hat{a}_{22}$, $\hat{b}_{11}$. Notice that, since it is assumed $Q_E = 0$, the effect of $Q_E \cdot b_{22}$ is negligible for all b_{22}. Therefore, b_{22} is not estimated on-line but set to the nominal value during all the tests.

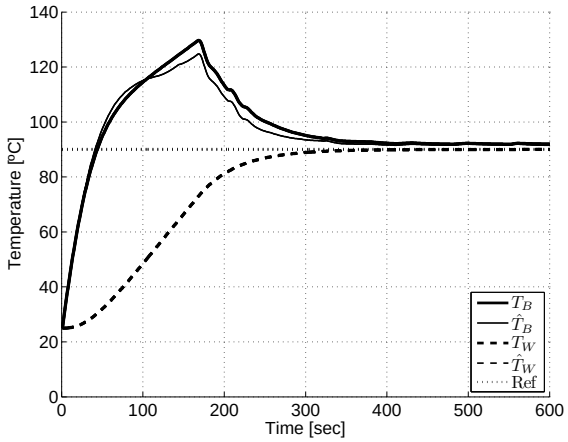

Figure 7.13: Simulation Results with the adaptive controller based on MMReO. T_B is the temperature of the bottom of the pot, $\hat{T}_B$ is the estimated temperature of the bottom of the pot, T_W is the temperature measured with the infrared sensor, $\hat{T}_W$ is the estimated temperature of the wall of the pot which is almost equal to T_W, *Ref* is the target temperature.

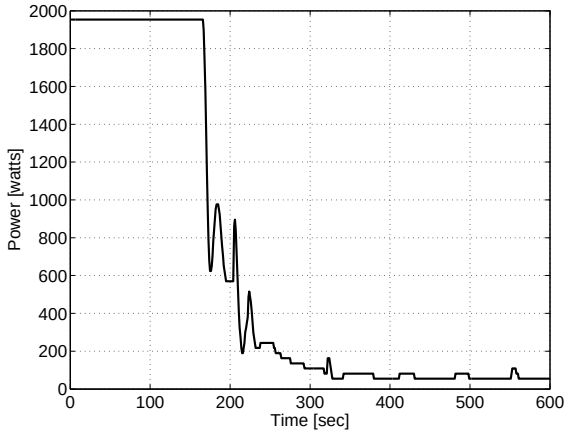

Figure 7.14: Simulation Results with the adaptive controller based on MMReO. Power computed with the control law (7.14) which depends on the state estimated with the ReO.

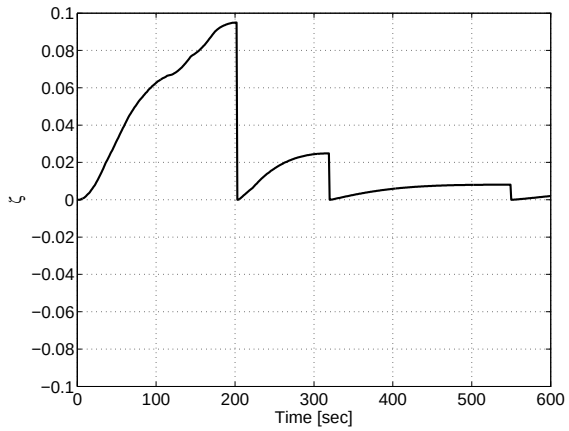

Figure 7.15: Simulation Results with the adaptive controller based on MMReO. Reset integral term ζ computed with the ReO. When ζ is reset to zero, it means that the reset condition holds.

7.3 Temperature Control by Using NTC Thermistors

One issue that arises while designing a cooking temperature control in processes with low load (i.e. by using two NTC thermistors underneath the glass ceramic) is that the cooking pot bottom temperature cannot be directly measured, consequently, an online scheme to estimate this temperature is necessary. Two different ways to address this issue are proposed. The first one consists of a simple PI-like controller with a non-adaptive observer, which simply estimates the cooking pot bottom temperature. As it will be shown, the non-adaptive observer will not be capable of accurately estimating the cooking pot bottom temperature in a robust manner. This result justifies the need of an observer scheme that modifies its parameters depending on the cooking pot, in order to successfully design a temperature control for low load cooking processes. This issue will be finally tackled by the second proposal: an adaptive MMReO-based controller similar to the one previously presented above. In this case, its identification models will be based on a slightly different system model, that better characterizes the heat transmission from the cooking pot bottom the to the NTC thermistors underneath the glass ceramic.

7.3.1 System Model

In this case, the state space model that represents the relation between the power supplied by the induction coil and the temperatures of the system is

Table 7.2: Nominal model parameters and their ranges

Parameter	Nominal Value	Variations
a_{11}	-0.005	[-0.01 -0.0025]
a_{21}	0.01	[0.003 0.02]
a_{22}	-0.001	[-0.02 -0.003]
b_1	0.002	[0.00065 0.005]

given by:

$$\begin{aligned} \dot{x}(t) &= A_p \cdot x(t) + B_p \cdot u(t) \\ y_p(t) &= C_p \cdot x_p(t) \end{aligned} \tag{7.35}$$

where $x_p(t) \in \mathbb{R}^2$ is the state vector, $u(t) \in \mathbb{R}$ is the input vector, $y(t) \in \mathbb{R}$ is the system output vector and A_p, B_p, C_p are constant $(2 \times 2), (2 \times 1), (1 \times 1)$ matrices. Specifically, the model used in this section results from the analytical pot model described in Appendix B.3. In particular, its dynamics are given by

$$\begin{aligned} \begin{bmatrix} \dot{\theta}_B \\ \dot{\theta}_G \end{bmatrix} &= \begin{bmatrix} a_{11} & 0 \\ a_{21} & a_{22} \end{bmatrix} \begin{bmatrix} \theta_B \\ \theta_G \end{bmatrix} + \begin{bmatrix} b_1 \\ 0 \end{bmatrix} P \\ \theta_G &= \begin{bmatrix} 0 & 1 \end{bmatrix} \begin{bmatrix} \theta_B \\ \theta_G \end{bmatrix} \end{aligned} \tag{7.36}$$

where $\theta_B = T_B - T_0$ is the difference between the pot bottom temperature T_B and the ambient temperature, $\theta_G = T_G - T_0$ is the difference between the glass ceramic temperature T_G and the ambient temperature, P is the power supplied by the inductor coil, which as previously, considers the efficiency of the electronics and of the inductor. Additionally, a_{11}, a_{21}, a_{22}, and b_1 are uncertain parameters that depend on the cooking pot thermal properties. Therefore, there will be one different state-space model for each pan. The modeling process was repeated for all the available pans; hence, a database with more than 150 simulation models was obtained. Table 7.2 summarizes the nominal values of all model parameters and their variations.

From all the obtained state-space models, we denoted as reference model the one that reaches the highest pan temperature for the same supplied power. Step response for the most characteristic pans is shown in Fig. 7.16. In this case, the solid line would represent the evolution of the reference model because its step response is the highest. This definition for the reference model will be useful to avoid temperature overshooting until the estimation of the cooking pot temperature finishes.

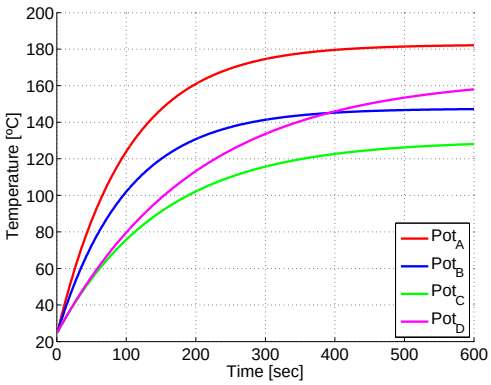

Figure 7.16: (A) Represents the reference model step response. (B-D) Represent the step responses of other different cooking pots.

7.3.2 PI-like Controller With Non-adaptive Observer

Firstly, a simple PI-like controller (C_1) with a non-adaptive observer is designed. In particular its dynamics are given by

$$C_1 : \begin{cases} u(t) &= L_I x_I(t) - L_S \hat{x}_p(t) \\ \dot{x}_I(t) &= r(t) - y_p(t) \\ \dot{\hat{x}}_p(t) &= A_p \hat{x}_p(t) + B_p u(t) + K_p C_p (x_p(t) - \hat{x}_p(t)) \end{cases} \tag{7.37}$$

where $x(t) = [T_B(t)\, T_G(t)]$, A_p, B_p, C_p are the matrices associated with the reference model, $r(t)$ is the target temperature, $x_I(t)$ is the integral error, L_I and L_S are the integral and the state gain of the controller respectively.

In this case, tuning parameters (i.e. L_I, L_S, and K_p) are designed to obtain a good close loop response when the cooking pot to control presents a similar behavior than the reference model as it is depicted in Fig. 7.17. In particular, simulation results were obtained with $L_S = [183.22,\ 52.35]^T]^T$, $L_I = 3.97$, and $K_p = [1.91,\ 0.21]^T$. However, its performance worsen when the cooking pot to control presents different thermal parameters than those expected, due to the fact that the matrices A_p and B_p are initially set to the parameters of the reference model, and cannot be updated online in order to compensate that difference. As a result, a considerable difference between the actual temperature and the estimated temperature might exist as it is shown in Fig. 7.18.

7.3.3 Adaptive MMReO-Based Controller

As it has been suggested, poor performance obtained by the PI-like controller with non-adaptive observer could be improved simply by updating the observer's parameters online. This is the approach followed in this section, in which an adaptive MMReO-based controller, which includes several identification models to guarantee an accurate estimation, is designed.

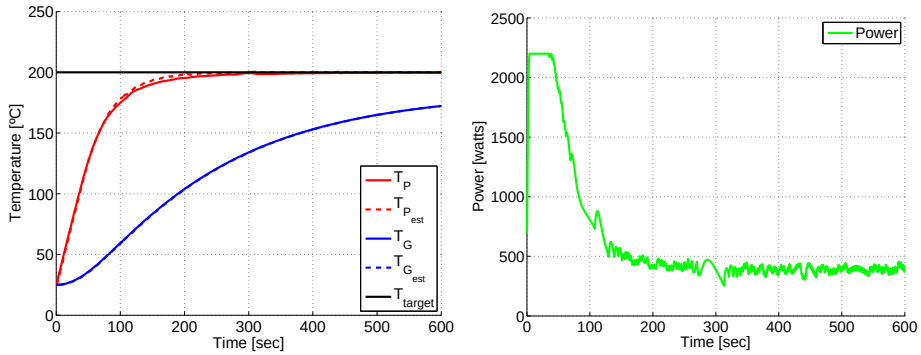

Figure 7.17: Simulations results of the PI-like Controller With a Non-adaptive Observer when the cooking pot to control is similar to the reference model. Solid blue line is the actual cooking pot bottom temperature. Solid dashed line is the estimated cooking pot bottom temperature. Solid red line is the actual NTC-thermistor temperature. Solid dashed line is the estimated NTC-thermistor temperature. Green solid line is the supplied power.

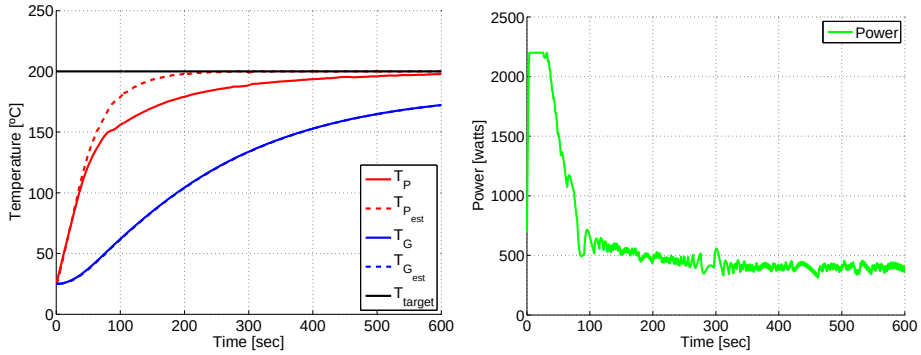

Figure 7.18: Simulations results of the PI-like Controller With a Non-adaptive Observer when the cooking pot to control is different to the reference model. Solid blue line is the actual cooking pot bottom temperature. Solid dashed line is the estimated cooking pot bottom temperature. Solid red line is the actual NTC-thermistor temperature. Solid dashed line is the estimated NTC-thermistor temperature. Green solid line is the supplied power.

As previously, its observation scheme consists of a reinitialized reset observer, and of multiple fixed identification models. In this case, each fixed identification model has the structure shown in (7.36) with different parameters a_{11}, a_{21}, a_{22}, and b_1 defined according to Table 7.2, which now define the new convex set S. It is worth mentioning that the formulation, structure, and stability analysis of the adaptive MMReO-based controller has already been proved in Chapter 7.2.3, therefore, we directly show here the simulation results obtained with this controller applied to the cooking pot temperature control of low load cooking process.

In this case, we aim at heating up an empty cooking pot from ambient temperature (i.e. $25°C$) to the target temperature (i.e. $200°C$). Fig. 7.19 shows the parameters of the best model identified minimizing the cost function (7.12) at every instant. In particular, we have implemented $N = 15$ fixed identification models, which characterize the most likely thermal behavior that it is possible to find in practice. Moreover, it is worth mentioning that fewer identification models are enough, due to the fact that cooking pots are assumed to be empty or with low load, and hence, there are fewer possible situations that have to be modeled.

As previously, there still exists a small difference between the best model and the real system caused by the fact that the number of fixed identification models is finite. However, identified parameters are close enough to real ones in such a manner the convergence speed of the reinitialized reset observer is highly decreased, and consequently, the closed-loop performance is significantly improved, even when a cooking pot with different thermal parameters is used. This is shown in Fig. 7.20, wherein the temperatures of the cooking process as well as the temperatures estimated by the ReO are depicted. It underlines the good performance of the MMReO, because the estimated cooking pot bottom temperature is considerable closer to the actual temperature.

7.4 Discussion

Summing up, this chapter has detailed the different control-estimation algorithms designed for guaranteeing a robust temperature control in household conditions. In particular, we have made an important effort in applying the theoretical results presented in previous chapters (i.e reset observers), which have resulted in a novel adaptive controller.

The special structure of our proposed adaptive controller, which is based on Multiple-Model Reset Observer rather than in the adaptive reset observer presented in Chapter 5, requires further comments. It is worth mentioning that although the estimation problem addressed in Chapter 5 is quite general, it does not totally fit our system models (7.1), (7.36), due to the fact that (5.1) requires that the unknown parameters to be estimated, that is

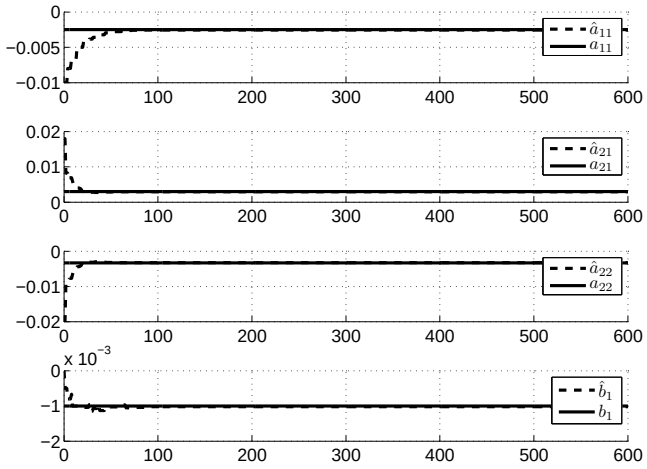

Figure 7.19: Simulations results of the adaptive MMReO-based controller when the cooking pot to control is different to the reference model. Solid lines are the parameters a_{11}, a_{21}, a_{22}, b_1. Dashed lines are the estimated parameters $\hat{a}_{11}$, $\hat{a}_{21}$, $\hat{a}_{22}$, $\hat{b}_1$.

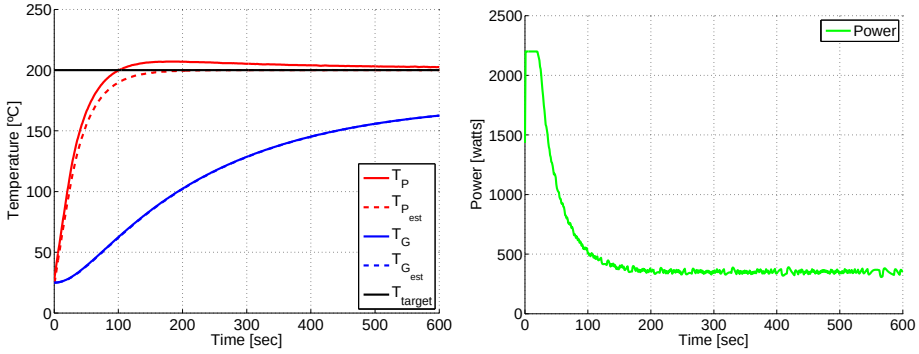

Figure 7.20: Simulations results of the adaptive MMReO-based controller when the cooking pot to control is different to the reference model. Solid blue line is the actual cooking pot bottom temperature. Solid dashed line is the estimated cooking pot bottom temperature. Solid red line is the actual NTC-thermistor temperature. Solid dashed line is the estimated NTC-thermistor temperature. Green solid line is the supplied power.

θ, must be related to the system input $u(t)$ and/or the system output $y(t)$ through the matrices Λ and $\phi(t, u, y)$, which is not the case because both (7.1) and (7.36) include unknown parameters that depend on other system states. As an example, a_{11} and a_{21} from (7.1) are related to θ_B that is neither the system input nor the system output. This justifies the development of a different adaptive strategy, being this the reason why a Multiple-Model Reset Observer scheme was used.

Finally, the superior performance of the adaptive controller based on Multiple-Model Reset Observer compared to different alternatives, and its applicability to both high and low cooking processes has been shown by simulations. Therefore, the next step will be to verify whether this better performance also is obtained in a real induction hob. This task is described in the next chapter.

Chapter 8

Experimental Results

This chapter summarizes the experimental results of all the control-estimation algorithms developed in the previous chapter. Both laboratory and application tests are considered. In particular, application tests differ from laboratory tests in the fact that actual food is used, and that their evaluation depends on the resultant food's appearance and taste. These tests will show the superior performance of the proposed adaptive controller based on Multiple-Model Reset Observers, and how it satisfactory addresses the problem of developing a cooking pot temperature control for high and low load processes.

8.1 Introduction

This chapter summarizes the experimental results of all the control-estimation algorithms developed in the previous chapter. All proposed control and estimation algorithms have been implemented in the microcontroller of actual induction hobs. Specifically, these algorithms have been programmed in C language. In order to demonstrate that the designed control schemes work properly, several verification tests on real induction hobs were carried out. Main elements of the induction hob used are shown in Fig. 8.1, in which both sorts of sensors used for temperature control are clearly identified.

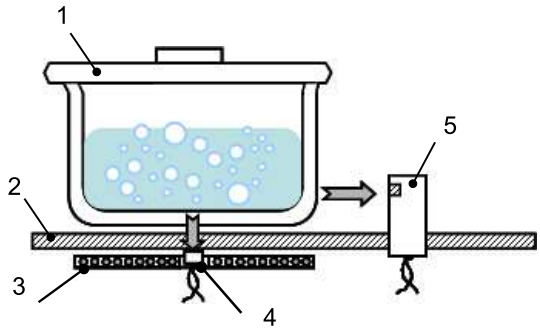

Figure 8.1: Main elements of a domestic induction hob. 1: pot. 2: ceramic glass. 3: induction coil. 4: internal NTC sensor. 5: external infrared sensor

Since the output of the developed algorithms is the power supply, the way the induction hob generates the desired power requires further comments. Specifically, the inverter topology provides to the induction coil the high-frequency current needed to heat up the cookware. Since power supply depends on it (the lesser the frequency, the higher the power), the microcontroller modifies the working frequency of the inverter to provide the desired power. The frequency control algorithm used is described in [182]. The changes of the working frequency are taken in fixed and small steps, which ensures stability and convergence of the frequency control algorithm but which causes a transient behavior before the algorithm determines the proper working frequency. Nevertheless, it has no effect in the temperature control, due to the fact that the thermal dynamics are much slower than the inverter topology dynamics (less than one second).

8.2 Temperature Control by Using a Retractable Infrared Sensor

This section summarizes the experimental results obtained with the control algorithms explained in Section 7.2. Actual hob used during the verification tests is shown in Fig. 8.2.

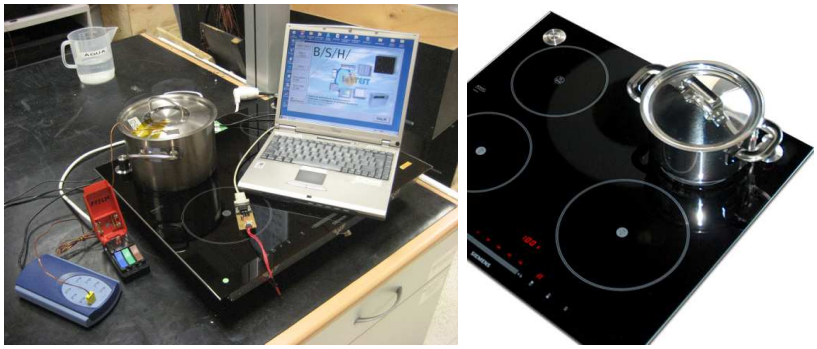

Figure 8.2: Domestic induction hob with retractable infrared sensor used during verification test (left). Final system in household conditions (right).

During these tests, the temperature evolution of the water during a simmering process is measured. It has to reach a settling temperature between $88°C$ and $94°C$. The software of the microcontroller automatically calculates how much power is needed in order to reach the set point with the minimum rise time but without overshoots. To check the system behavior, we measure the water temperature with an additional thermocouple situated inside the water during the entire test. Notice that the software does not use the temperature measured by the thermocouple. Therefore, this thermocouple is not used in household conditions.

Figs. 8.3-8.8 show some of the results obtained with both control schemes during the verification tests. We have used a 180 mm-diameter induction coil whose maximum power is 1800 watts. The objective is to heat up a predefined amount of water until the simmering temperature as fast as possible. After that, each controller has to keep the water temperature inside the simmering range.

Fig. 8.3 and Fig. 8.4 show the results obtained with the QFT-based controller when the initial amount of water is 1.5 liters and 2.5 liters respectively. On the other hand, Fig. 8.6 and Fig. 8.7 show the results obtained with the adaptive controller based on MMReO when the initial amount of water is 1.5 liters and 2.5 liters respectively. It is worth mentioning that in all these tests the pot was covered with a lid, so that $Q_E = 0$.

Analyzing those figures, it is easy to see that both proposed controllers meet control requirements because the water reaches the simmering temperature without overshooting independently of the initial amount of water. However, the adaptive controller based on MMReO has a better performance as long as we compare the rising time. Depending on the initial amount of water, up to a 30% time saving is achieved by using our proposal.

Additionally, we have tested the robustness of each controller to disturbances. Two different sort of disturbances have been considered. Firstly, we have performed these tests without a lid, and thus Q_E is not longer negli-

gible (i.e. $Q_E \neq 0$), which as a matter of fact was an assumption for the tuning of both controllers. Secondly, we have also considered typical disturbances that take place during any cooking process because of the addition of food. Specifically, they have been simulated adding 0.5 liters of water to the pot after the water temperature has reached the simmering temperature. Fig. 8.5 shows the results obtained with the QFT-based controller whereas Fig. 8.8 shows the results obtained with the adaptive controller based on MMReO. Both controllers show a good behavior since both are able to keep the water temperature within the simmering range even after more water is added to the pot. Nevertheless, the adaptive controller based on MMReO outperforms again the fixed QFT-based controller, since the disturbance rejection time is significantly decreased. Specifically, it is up to 50 seconds shorter, which represents about a 33% time reduction.

Regarding energy consumption, since both control schemes avoid overshooting, no energy is wasted to evaporate water. For comparison purposes, let us analyze energy consumption of induction cookers without temperature control, and with temperature control. Let assume that the user selects the maximum power level during all the test (i.e. 1800 watts), in order to heat up 2.5 liters of water for 20 minutes, in the induction cooker without temperature control. In this case, the energy consumption would be 600 $W \cdot h$. On the other hand, the induction cooker with the QFT-based controller would consume 265.55 $W \cdot h$ to perform the same process, whereas the induction cooker with the adaptive MMReO control would only need 260.33 $W \cdot h$. This result underlines the fact that temperature control can play a key role reducing energy consumption and, as a consequence, it can increase the efficiency of the whole cooking process.

It is worth mentioning that the verification tests were not limited to laboratory tests but also considered application test. In particular, Fig. 8.9 shows the evolution of the water temperature and the supplied power while cooking actual food, in this case, tortellini. The adaptive MMReO-based controller quickly heats up 1.5 liters of water to the simmering range in just 5 minutes, afterwards, 300 grams of tortellinis are added to the cooking pot, which cause a sudden drop of the water temperature. However, the adaptive MMReO-based controller is able to reject the effect of that disturbance and the water temperature reaches again the simmering range. As a result, the tortellinis are perfectly cooked as it is shown in Fig. 8.10.

8.3 Temperature Control by Using NTC Thermistors

Here, we summarize the verification test carried out to ensure the proper behavior of the control strategies presented in Section 7.3. During the verification tests, the system temperature evolution is measured for a set point

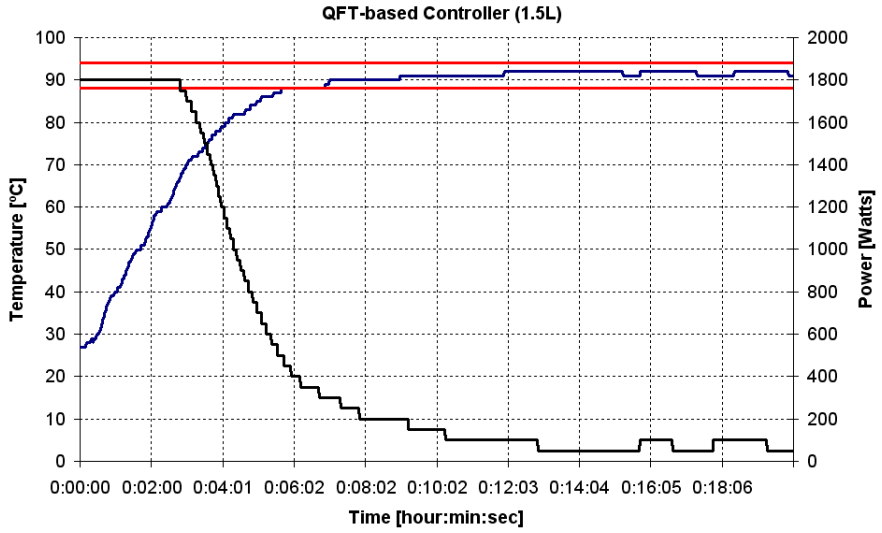

Figure 8.3: Experimental results obtained with the fixed QFT-based controller. It has to heat up 1.5 liters of water to the simmering range. The pot is covered with a lid. Black line represents the supplied power. Blue line represents the water temperature measured with a thermocouple. Area between red lines represents the simmering range.

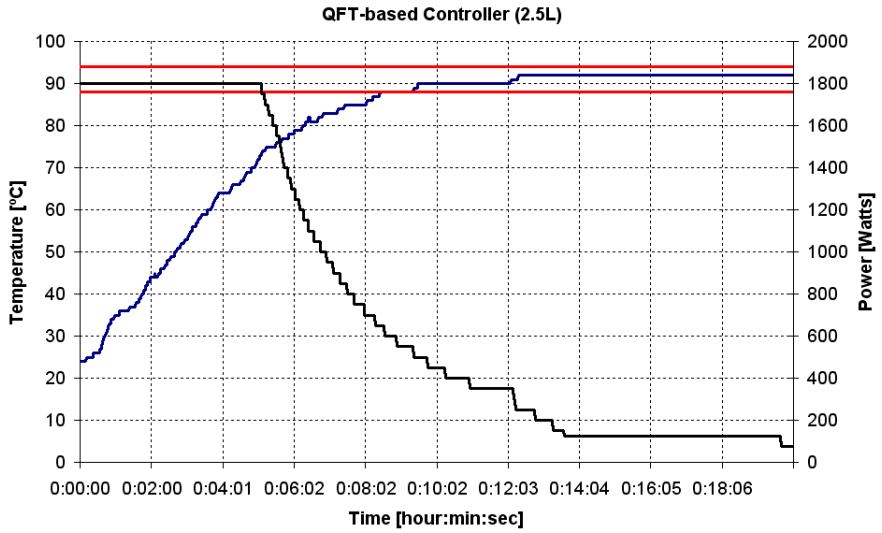

Figure 8.4: Experimental results obtained with the fixed QFT-based controller. It has to heat up 2.5 liters of water to the simmering range. The pot is covered with a lid. Blue line represents the water temperature measured with a thermocouple. Area between red lines represents the simmering range.

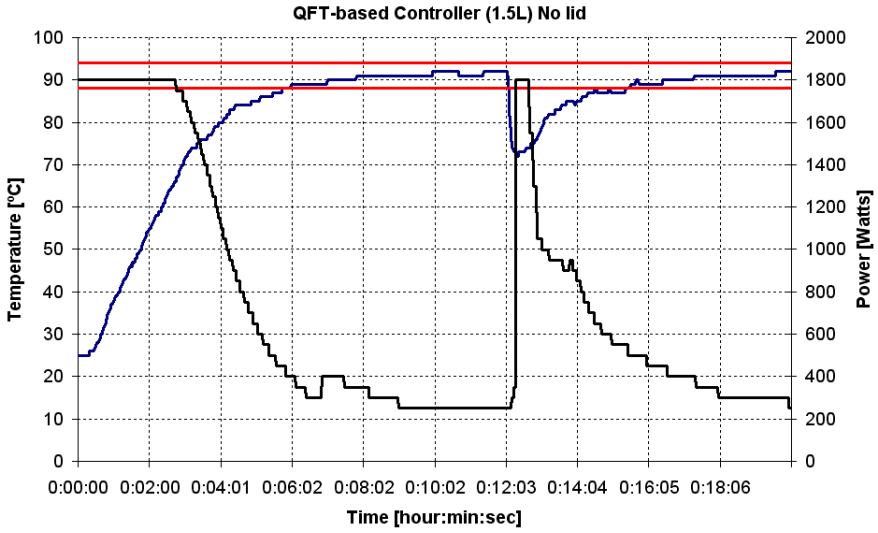

Figure 8.5: Experimental results obtained with the fixed QFT-based controller. It has to heat up 1.5 liters of water to the simmering range. Besides, 0.5 liters of water are added at t=12:15. The pot is not covered with a lid. Blue line represents the water temperature measured with a thermocouple. Area between red lines represents the simmering range.

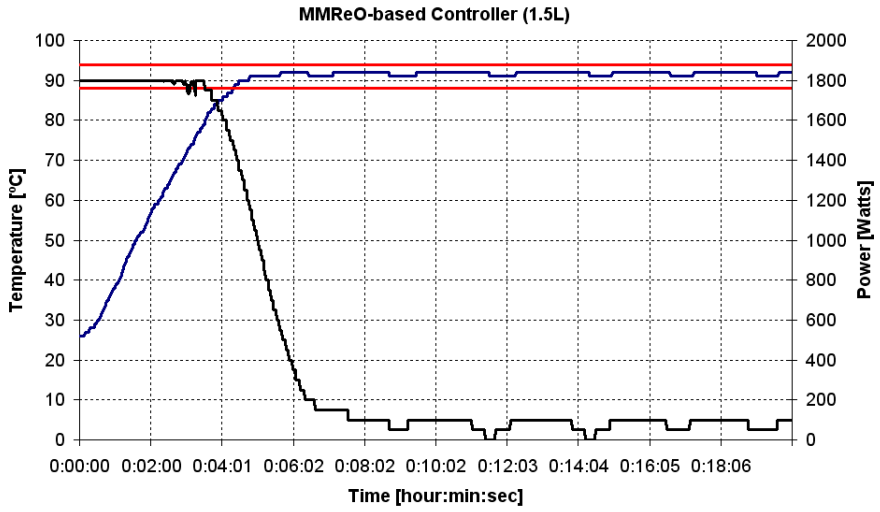

Figure 8.6: Experimental results obtained with the adaptive MMReO-based controller. It has to heat up 1.5 liters of water to the simmering range. The pot is covered with a lid. Black line represents the supplied power. Blue line represents the water temperature measured with a thermocouple. Area between red lines represents the simmering range.

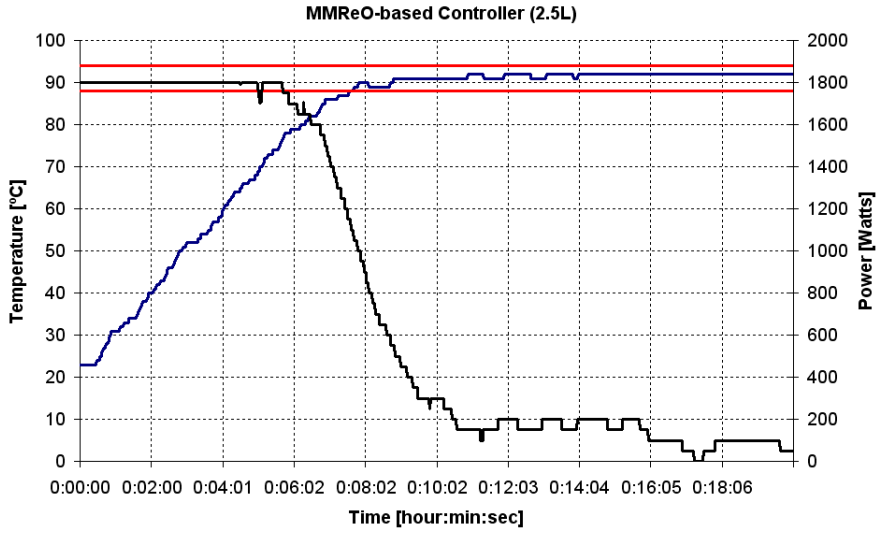

Figure 8.7: Experimental results obtained with the adaptive MMReO-based controller. It has to heat up 2.5 liters of water to the simmering range. The pot is covered with a lid. Blue line represents the water temperature measured with a thermocouple. Area between red lines represents the simmering range.

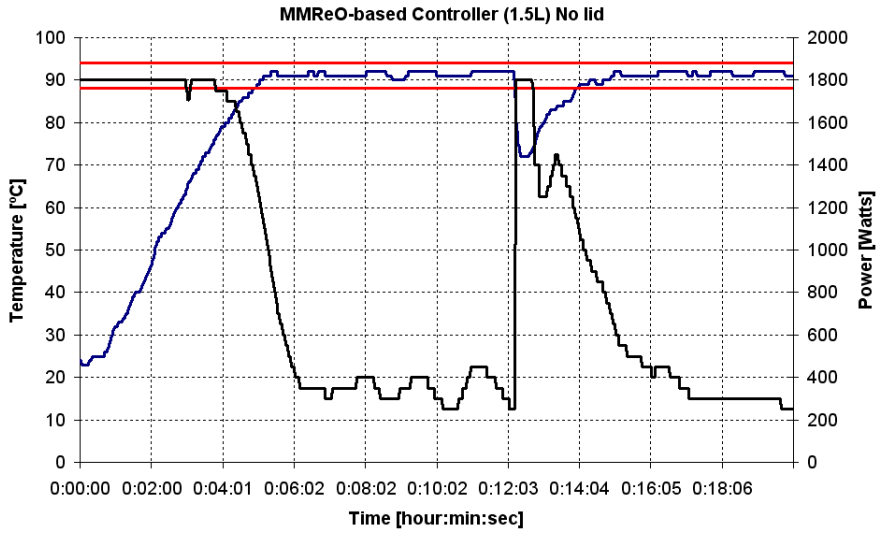

Figure 8.8: Experimental results obtained with the adaptive MMReO-based controller. It has to heat up 1.5 liters of water to the simmering range. Besides, 0.5 liters of water are added at t=12:10. The pot is not covered with a lid. Blue line represents the water temperature measured with a thermocouple. Area between red lines represents the simmering range.

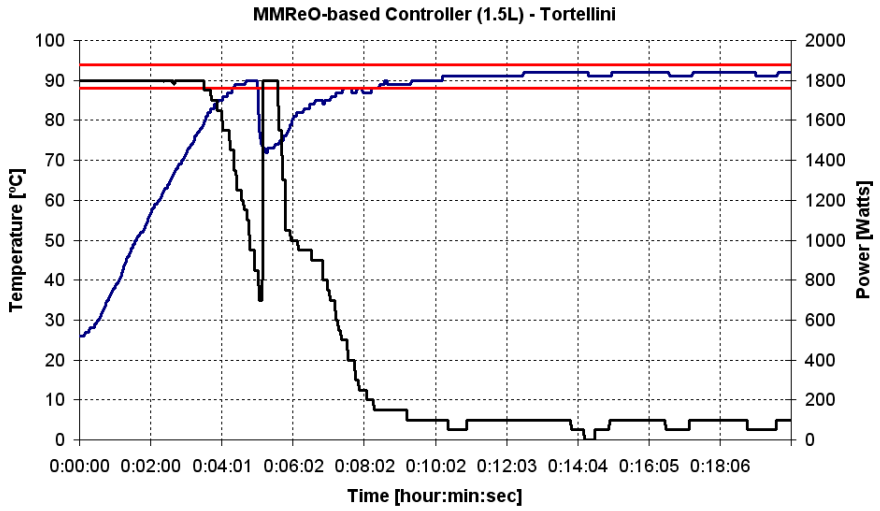

Figure 8.9: Application results obtained with the adaptive MMReO-based controller. It has to heat up 1.5 liters of water to the simmering range. 300 grams of tortellini are added when the water temperature reaches $90°C$ at t=5:00. The pot is covered with a lid. Black line represents the supplied power. Blue line represents the water temperature measured with a thermocouple. Area between red lines represents the simmering range.

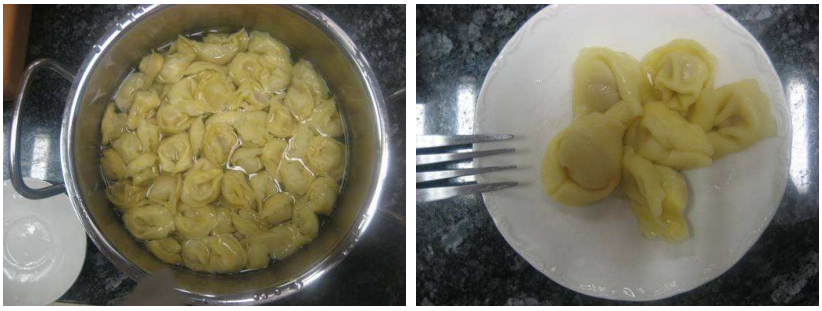

Figure 8.10: Application results obtained with the adaptive MMReO-based controller.

of 200°C. Additionally, a large disturbance has been forced adding water to the pot. Therefore, we can check the performance of each control scheme not only in usual situation but also in the presence of large disturbances. As it is shown in Fig. 8.11, the pan temperature was measured using thermocouples placed on the pan surface. Cooking pot temperature is estimated by the algorithm in the microcontroller of the induction hob from the NTC thermistor measurements. Note that the algorithms do not need the temperatures measured by the three thermocouples. We use the three thermocouples placed on the pan surface only in the laboratory to measure its temperature just to register its evolution and to check when the actual pan temperature reaches the reference. Therefore, the three thermocouples are not required in household conditions.

The evolution of the power supplied by the induction coil, the estimated temperature of the cooking pot, the actual temperature of the cooking pot, and the maximum temperature of both NTC thermistor located beneath the glass ceramic, for the different control schemes are shown in the following figures.

Figure 8.11: Domestic Induction hob used during verification tests with three thermocouples to measure the temperature of the cooking pot (left). Final system in household conditions (right).

PI-like Controller With Non-adaptive Observer

A PI-like controller was designed to ensure a good performance for a pan with the same parameters than the reference model. As the temperature of the cooking pot is not accessible, an additional observer with the parameters of the reference model was also designed. Note that the parameters of that observer remain constant independently of the pot used. Fig. 8.12 shows the performance of the PI-like controller with a non-adaptive observer testing a pot with the same parameters than the reference model. In this case, the estimated pot temperature and the real pot temperature are identical and the PI-like controller brings the pan temperature to the set point with an overshoot less than 4°C and with ± 3°C of steady state offset. Besides, pan

temperature reaches the reference in 2 min. In Fig. 8.13, the performance of the PI-like controller with a non-adaptive observer for a pot with different parameters than the reference model is shown. In this case, the estimated pot temperature and the real pot temperature are very different and the control performs badly.

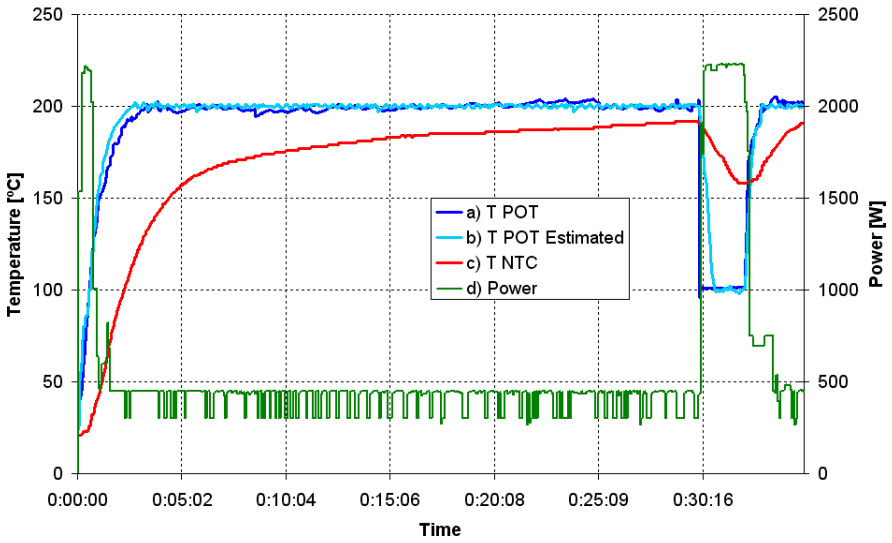

Figure 8.12: Temporal course of a real test. Pan used is the reference model. (a) Represents the real pan temperature. (b) Represents the estimated pan temperature. (c) Represents the temperature measured by the NTC thermistor. (d) Represents the power supplied by the inductor.

Adaptive MMReO-based controller

In Fig. 8.14, we use again a real pan with the same thermal and magnetic properties than the reference model. One of the identification models of the multiple model reset observer has the same parameters than the real pot, and it is denoted by M_R. As expected, the control scheme selects the model M_R as the best one. Results obtained with the reference pot are, in that case, quite similar to the obtained with the adaptive observer. Multiple model observers bring the pan temperature to the set point in less than 2 min and without overshoot and with $\pm 2°C$ of steady state offset.

In Fig. 8.15, we show the results of a real pan with different thermal and magnetic properties than every identification model available on the multiple model reset observer. As the model chosen has not the same thermal behavior, the pot temperature estimation and the real pot temperature do not match perfectly. Anyway, as is shown above, the plant has a better transient behavior than the same plant controlled by the adaptive observer.

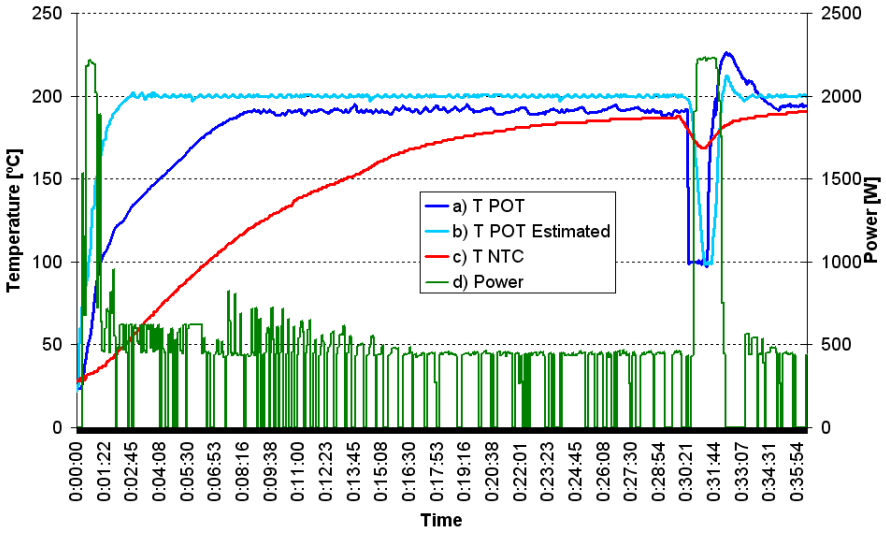

Figure 8.13: Temporal course of a real test. Pan used has different thermal properties than the reference model. (a) Represents the real pan temperature. (b) Represents the estimated pan temperature. (c) Represents the temperature measured by the NTC thermistor. (d) Represents the power supplied by the inductor.

In this case, the multiple model observer brings the pan temperature to the set point in less than 4 min, without overshoot and with $\pm 8°C$ of steady state offset.

As before, several application tests were performed so that the performance of our proposal could be tested in household conditions. One application test that is especially well suited to test the accuracy of our proposed temperature control for low load processes consists in cooking multiple pancakes one after another, and after that, analyzing the variations in color between each of them. If all of them present a homogeneous browning, it would imply that the temperature of the cooking pot has been constant, because all the pancake pastries have the same weight and are cooked for the same time span. Evidently, it is not possible to measure the actual temperature of the cooking pot while cooking the pancakes, which justify the need of an evaluation criterion that does not depend on the temperature but on the homogeneity of the obtained pancakes. Fig. 8.16 shows the appearance of the obtained pancakes in one of these tests. It can be concluded that the adaptive MMReO-based controller has been able to reject the effect of the disturbance caused when each pancake pastry is added, and could keep the cooking temperature almost constant during the entire test. As a result, all the pancakes are perfectly cooked and present an appetizing and homogeneous browning.

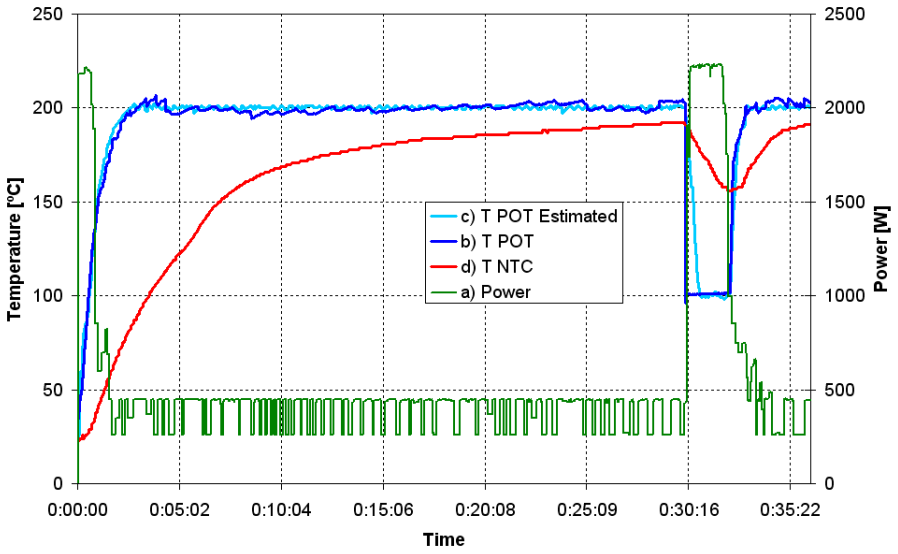

Figure 8.14: Temporal course of a real test. Pan used is the reference model and the model chosen has the same thermal properties than the reference model. (a) Represents the real pan temperature. (b) Represents the estimated pan temperature. (c) Represents the temperature measured by the NTC thermistor. (d) Represents the power supplied by the inductor.

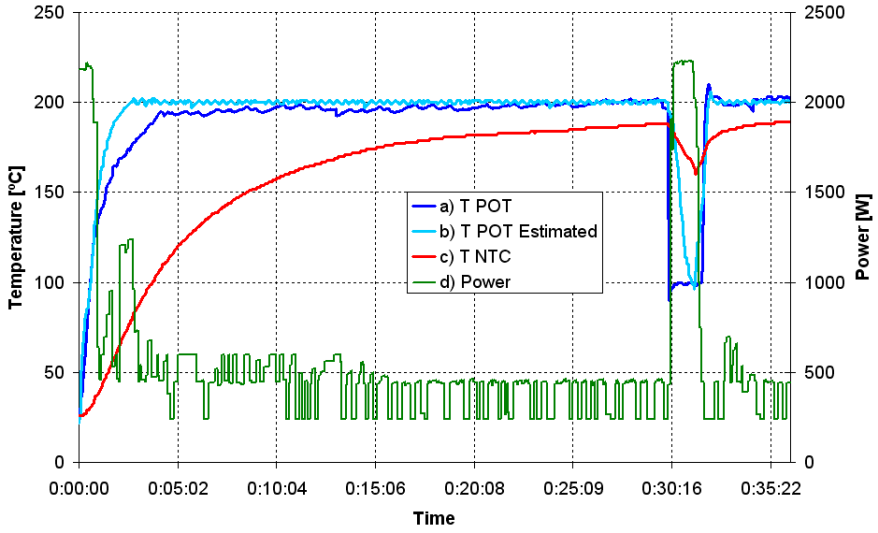

Figure 8.15: Temporal course of a real test. Pan used has different thermal properties than the model chosen. (a) Represents the real pan temperature. (b) Represents the estimated pan temperature. (c) Represents the temperature measured by the NTC thermistor. (d) Represents the power supplied by the inductor.

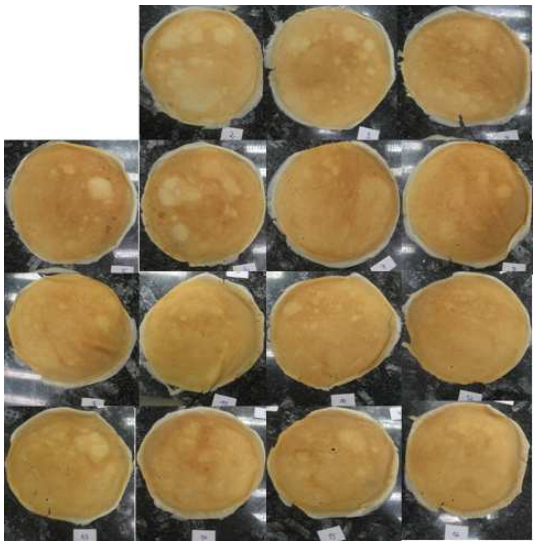

Figure 8.16: Application results obtained with the adaptive MMReO-based controller. For the carrying out of the application tests there is an internal normative in BSH. The first pancake is not considered because of this.

8.4 Discussion

It is well known that in traditional cookers based only on power control, users are prone to use more power than the cooking process actually needs, because they have no feedback about how high the temperature is. This waste of energy highly decreases the efficiency of the whole cooking process, despite the fact that the efficiency of the power electronics is very high. Therefore, an improvement in the efficiency during the whole cooking process could be achieved by means of pot temperature control.

This chapter has shown the excellent application results that can be obtained by means of a cooking pot temperature control. Depending on the sort of sensor chosen, an accurate temperature control for either high or low cooking process can be obtained, which clearly outperform standard power-based control. Besides, it has more advantages. For instance, the cooking pot temperature control ensures a correct food cooking minimizing the cooking time and avoids reaching too high temperatures, which burn the food, or too low temperatures, which cause underdone food.

Additionally, it can be used to perform more complicated cooking processes. For instance simmering, in which the food is submerged in water at a temperature from $88°C$ to $94°C$ that causes a great effect on the flavor of the food but that is almost impossible to carry out in a domestic cooker where the pot temperature is unknown. Moreover, it allows to the user to obtain almost exactly the same satisfactory cooking results when preparing

large batches of food, for instance several pancakes. In this case, by using the algorithms and ideas proposed in this Thesis, all of them are perfectly cooked presenting an homogeneous browning regardless of the order, which is generally difficult to achieve in household conditions.

Part IV

Conclusions

Chapter 9

Conclusions and Future Work

In this Thesis, we have contributed in different topics to develop a cooking pot temperature control for domestic induction hobs. This work mostly boils down to two stages. In the first one, motivated by the development of more efficient observation algorithms that could be used for estimating and controlling the cooking pot temperature, we have satisfactoryly extended the promising features of reset controllers to the observer framework. In the second one, we have studied the applicability of our theoretical results to its final application: the cooking pot temperature control for induction hobs. Contributions and conclusions obtained throughout this work are finally summarized in this chapter.

9.1 Conclusions

In this work, we have studied different topics to achieve an accurate cooking pot temperature control for domestic induction hobs. Conclusions that can be drawn from this work fall into two main areas, depending on their intrinsic interest, theoretical or practical.

Theoretical issues were addressed in a first stage, in which we aim at developing more efficient observation algorithms that could be used for estimating and controlling the cooking pot temperature. In particular, the following contributions and conclusions were obtained.

- Firstly, we successfully have extended the promising features of reset controllers, (i.e. quick transient response without overshooting) to the observer framework. Among the different reset conditions presented in the literature, it was found that reset-time independent formulations (i.e. zero crossing or sector condition) are more suitable for reset observers than the reset-time dependent formulation, resulting in a significantly better performance. Moreover, it was also found that the zero crossing reset condition and the sector reset condition behave exactly in the same way when all the initial states of the reset observer are set to zero, which is the initial configuration generally used in practice. Providing that the initial conditions are not set to zero, resultant performance will depend on the interrelation between system and observer dynamics, their initial conditions, and the likely presence of unknown disturbances.

- Secondly, we generalized our proposed reset observers to a wide class of systems, including time delay systems, nonlinear systems and systems affected by external disturbances. In all the cases, it was found that the reset observer was capable of outperforming other existing solutions, even if the system was affected by disturbances. The potential dangerous effect of external disturbances and the relevance of a proper tuning of the reset observer's gain justified the development of a method to automatically determine the optimal reset observer tuning parameters by minimizing the effect of the external disturbances on the estimation error. It was found that optimal reset observers designed through this method can behave better than other optimal designing methods proposed in the literature.

Afterwards, practical issues were tackled in a second stage, in which we aim at guaranteeing the applicability of our theoretical results to its final application: the cooking pot temperature control for induction hobs.

- Initially, a significant effort was made to determine the more suitable temperature sensor depending on the cooking process. It was found

that the retractable infrared sensor is especially well suited to control the pot temperature in cooking processes with high load. However, existing thermistor-based solution did not seem to be the best choice to control the pot temperature in low load cooking processes. For this reason, three novel sensing methods, which outperform the existing NTC thermistor-based solution in terms of robustness, accuracy, or time response, were developed. In particular, the contact spots minimize the effect of the air gap between the cooking pot bottom and the thermistors, resulting in significantly better heat transmission and measurement. The sensor line reduces the influence of the relative position between the cooking pot and the thermistors, resulting in a considerably more robust sensing system. The magnetic sensor estimates the changes of the temperature of the cooking pot by analyzing the changes of the magnetic and electrical properties of the cooking pot measured by the inductor itself, resulting in an almost instantaneous temperature sensor. Despite these promising features, it was found that all of them were infeasible in practice because they would sensibly increase the cost of the final product. For this reason, it was concluded that the NTC thermistor-based solution is the one that best balances the two most important features of a temperature sensor in practice, performance and cost, justifying its final choice to control the cooking pot temperature in low load cooking processes.

- Finally, the last contribution of this work was the application of our theoretical results to a real application. Several control-estimation algorithms were designed, tuned, implemented and tested by both experimental and application tests. After a performance comparison, it was found that an adaptive MMReO-based controller, which combines an adaptive PI controller with a more advanced multiple-model reset observer, is able to control the temperature of the cooking pot regardless the temperature sensor used. For this reason, it can be concluded that the development of an accurate temperature control for cooking pots in domestic induction hobs is affordable and possible.

9.2 Future Work

This Thesis has shown the potential benefits of combining the reset system formulation with the adaptive observer framework. However, due to the inherent deterministic behavior of our system under study, its applicability to stochastic systems has not been studied yet. A formal definition of the reset condition for stochastic systems would be interesting as well as challenging, and it would undoubtedly result in an exciting research line.

It is worth mentioning that some of the stability results presented in this Thesis might be somewhat conservative because they are mostly based on

quadratic Lyapunov functions. This is even more important for the reset observer for time delay systems, in which a delay independent approach was used in the stability analysis. In this case, it would be interesting to study a delay-dependent approach, and to explore different sorts of Lyapunov functions such as piece-wise quadratic Lyapunov functions or polynomial Lyapunov functions by using a sum of squares-based formulation which would result in a much less conservative solution.

Regarding the temperature sensors, it was shown that an infrared sensor generally outperforms any other sort of sensor in terms of accuracy, time response, and robustness. Currently, retractable infrared sensors are only able to measure the temperature of the cooking pot wall rather than the cooking pot bottom temperature, and hence, they cannot be used for controlling the temperature in low load cooking processes. For this reason, it would be interesting to explore whether an infrared sensor could be integrated below the glass ceramic, and from there, sensing the radiance emitted by the cooking pot bottom downwards through the glass ceramic. However, this idea is far from trivial and requires further research, due to the fact that the temperature is considerably higher in that point and could damage the infrared sensor's electronics.

Appendixes

Appendix A

Reset Systems at Fixed Reset Times

A.1 Problem Statement

In Chapter 3, a method to choose a fixed reset time interval for ReO has been presented, and a stability analysis that depends on the chosen reset interval has also been given. Although those results were characterized for ReOs, they can also be applied to reset controllers, which is a contribution that has value for itself. In this appendix, we formalize that idea, and we present a general mathematical description of a reset system reset at fixed times and its resultant closed-loop dynamics, that will depend on whether it is a reset controller or a reset observer.

Let us begin considering an LTI plant described by

$$P : \left\{ \begin{array}{rcl} \dot{x}_p(t) & = & A_p x_p(t) + B_p u(t) \\ y_p(t) & = & C_p x_p(t) \end{array} \right. \tag{A.1}$$

where $x_p(t) \in \mathbb{R}^{n_p}$ is the state vector, $u(t) \in \mathbb{R}$ is the plant input, $y(t) \in \mathbb{R}$ is the plant output, $A_p \in \mathbb{R}^{n_p \times n_p}$, $B_p \in \mathbb{R}^{n_p \times 1}$, and $C_p \in \mathbb{R}^{1 \times n_p}$ are known constant matrices. Moreover the pair (A_p, C_p) is assumed observable. Note that although reset elements have recently been extended to multiple-input multiple-output (MIMO) LTI systems in [57] for estimation purposes, we consider here single-input single-output (SISO) systems only, since the definition of a general formulation of reset controllers for MIMO systems is still an open research topic.

Following [41], let us consider the standard definition of reset controllers for LTI systems (A.1) based on the zero crossing condition that is given by

$$K : \left\{ \begin{array}{rcll} \dot{x}_k(t) & = & A_k x_k(t) + B_k e(t) & e(t) \neq 0, \\ x_k(t^+) & = & A_r x_k(t) & e(t) = 0, \\ u(t) & = & C_k x_k(t) & \end{array} \right. \tag{A.2}$$

where $x_k(t) \in \mathbb{R}^{n_k}$ is the reset controller state, $e(t) \in \mathbb{R}$ is the control error, $A_r \in \mathbb{R}$ is the reset matrix, $A_k \in \mathbb{R}^{n_k \times n_k}$, $B_k \in \mathbb{R}^{n_k \times 1}$, and $C_k \in \mathbb{R}^{1 \times n_k}$ are known constant matrices. Note that only autonomous and unforced systems are considered so that $e(t) = -y_p$.

In a similar way, let us introduce the dynamics of a reset observer for an LTI system (A.1). Following [58], reset observer dynamics based on the zero crossing condition [41] would be described as follows

$$O : \left\{ \begin{array}{rcl} \left. \begin{array}{rcl} \dot{\hat{x}}_p(t) & = & A_p \hat{x}_p(t) + B_p u(t) \\ & - & K_P C_p \tilde{x}_p(t) + K_I \zeta(t) \\ \dot{\zeta}(t) & = & A_\zeta \zeta(t) + B_\zeta C_p \tilde{x}(t) \\ \hat{y}_p(t) & = & C_p \hat{x}_p(t) \end{array} \right\} & & \tilde{y}_p(t) \neq 0, \\ \left. \begin{array}{rcl} \hat{x}_p(t^+) & = & A_r \hat{x}_p(t) \\ \zeta(t^+) & = & A_r \zeta(t) \\ \hat{y}_p(t^+) & = & \hat{y}_p(t) \end{array} \right\} & & \tilde{y}_p(t) = 0, \end{array} \right. \tag{A.3}$$

where $\hat{x}_p(t)$ is the estimated state, K_I and K_P are the integral and proportional observation gains respectively, $\zeta(t)$ is the reset integral term, $A_\zeta \in \mathbb{R}$

and $B_\zeta \in \mathbb{R}$ are two tuning scalars which regulate the transient response of ζ, A_r is the reset matrix, and $\tilde{y}_p(t) = C_p\tilde{x}(t) = C_p(x(t) - \hat{x}(t))$ is the output estimation error,

Then, the dynamics of the plant P and of either the reset controller K or the reset observer O can be combined into one description for the closed-loop dynamics of the resultant reset system as follows

$$\Sigma : \begin{cases} \left.\begin{array}{rcl} \dot{x}(t) & = & Ax(t) \\ y(t) & = & Cx(t) \end{array}\right\} & x(t) \notin \mathcal{M}, \\ \left.\begin{array}{rcl} x(t^+) & = & A_R x(t) \\ y(t^+) & = & y(t) \end{array}\right\} & x(t) \in \mathcal{M}, \end{cases} \tag{A.4}$$

where $x(t) \in \mathbb{R}^n$ is the closed-loop state vector, $y(t) \in \mathbb{R}$ is the reset system output, $A \in \mathbb{R}^{n\times n}$, and $C \in \mathbb{R}^{1\times n}$ are known constant matrices. $\mathcal{M}$ is the reset surface that is defined as in [43]. In particular, denoting $\mathcal{R}(X)$ and $\mathcal{N}(X)$ as the image and null subspace of the linear operator given by the matrix X, respectively, the reset surface $\mathcal{M}$ is defined as $\mathcal{M} = \mathcal{N}(C)\backslash\mathcal{M}_\mathcal{R}$ where $\mathcal{M}_\mathcal{R}$ is the after reset surface that represents the set of states $x(t)$ that belong both to the null space of C (and then the output $Cx(t) = 0$), and to the image space of A_R (they are after reset states).

It is worth noting that the structure of $x(t)$, A, C and A_R depends on whether the reset system is a reset controller or a reset observer. In particular, for a reset controller K, the resultant closed-loop state vector is given by $x(t) = (x_p^T(t),\, x_k^T(t))^T$ and the closed-loop matrix is as follows

$$A = \begin{bmatrix} A_p & B_pC_k \\ -B_kC_p & A_k \end{bmatrix}, \tag{A.5}$$

whereas for the reset observer O, $x(t)$ is defined as $x(t) = (\tilde{x}^T(t),\, \zeta^T(t))^T$ and its corresponding closed-loop matrix is given by

$$A = \begin{bmatrix} A_p - K_PC_p & -K_I \\ B_\zeta C_p & A_\zeta \end{bmatrix}, \tag{A.6}$$

note that in both cases the augmented reset matrix A_R and the augmented output matrix are defined as follows

$$A_R = \begin{bmatrix} I & 0 \\ 0 & A_r \end{bmatrix},\; C = \begin{bmatrix} C_p \\ 0 \end{bmatrix}^T. \tag{A.7}$$

Since the closed-loop reset system (A.4) can exhibit Zeno solutions, it has to be modified by imposing temporal regularization. We use the notation proposed by [42], which are based on including an auxiliary variable φ which guarantees that the time interval between any two consecutive resets is not smaller than $\theta \in \mathbb{R}^+$. Note that we consider LTI augmented reset systems Σ that can represent either a reset-control closed-loop or a reset-observer

closed-loop. Once temporal regularization is included, its dynamics are given by

$$\Sigma : \left\{ \begin{array}{l} \left.\begin{array}{rcl} \dot{x}(t) & = & Ax(t) \\ y(t) & = & Cx(t) \\ \dot{\varphi}(t) & = & 1 \end{array}\right\} \quad \text{if } x(t) \notin \mathcal{M} \vee \varphi \leq \theta, \\ \left.\begin{array}{rcl} x(t^+) & = & A_R x(t) \\ y(t^+) & = & y(t) \\ \varphi(t^+) & = & 0 \end{array}\right\} \quad \text{if } x(t) \in \mathcal{M} \wedge \varphi > \theta. \end{array} \right. \tag{A.8}$$

A.2 Simulation Examples

In this section, several examples are presented in order to show the effectiveness of the search method presented in Chapter 3. In the following, if a system is reset at fixed times according to (3.27) it will be denoted by FT reset system, whereas if it is reset according to the zero crossing condition (A.8) it will be denoted by ZC reset system.

Let us take the following example from [146] where the reset controller K is given by

$$A_k = -1,\ B_k = 4,\ C_k = 2,\ A_r = 0, \tag{A.9}$$

and the plant P is

$$A_p = \begin{bmatrix} -2 & 0 \\ 1 & 0 \end{bmatrix},\ B_p = \begin{bmatrix} 1 \\ 0 \end{bmatrix},\ C_p = \begin{bmatrix} 0 \\ 1 \end{bmatrix}^T, \tag{A.10}$$

and the resultant closed-loop matrix is as follows

$$A = \begin{bmatrix} -2 & 0 & 2 \\ 1 & 0 & 0 \\ 0 & -4 & -1 \end{bmatrix}. \tag{A.11}$$

Following the proposed search procedure Fig. A.1 is obtained. In this case, the minimum spectral radius results from $\Delta = 1.03$. The unstable poles of (A.11) have a damping ratio $\xi = -0.052$ and a natural frequency $\omega_n = 1.59$, and then $t_{peak} = \pi/1.59 \approx 1.98$. Since $\Delta < t_{peak}$, resetting the system every $\Delta = 1.03$ maximizes the performance of the transient response as it is shown in Fig. A.2.

Let us now consider a reset observer O that is given by

$$\begin{aligned} K_P = \begin{bmatrix} 0.05 \\ -1 \end{bmatrix},\ K_I = \begin{bmatrix} 15 \\ -15 \end{bmatrix}, \\ A_\zeta = 2.2,\ B_\zeta = 5,\ A_r = 0, \end{aligned} \tag{A.12}$$

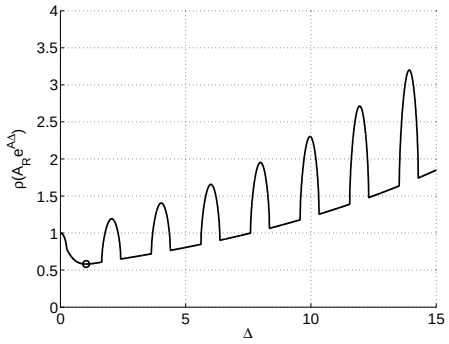

Figure A.1: $\rho(A_R e^{A\Delta})$ vs Δ for Example 1. Minimum value is represented by a circle and is obtained with $\Delta = 1.03$.

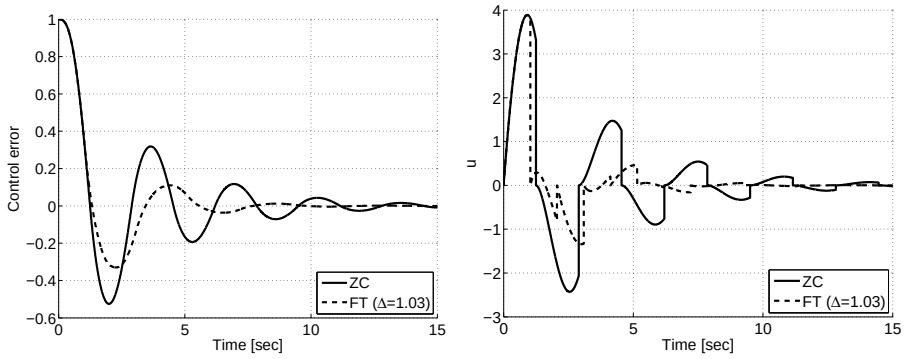

Figure A.2: Simulation results of Example 1. Solid lines have been obtained by using a ZC reset system. Dashed lines have been obtained by using an FT reset system with $\Delta = 1.03$.

and the plant P is

$$A_p = \begin{bmatrix} -2 & 0.1 \\ 0.1 & -0.9 \end{bmatrix},\ B_p = \begin{bmatrix} 0.5 \\ 2.5 \end{bmatrix},\ C_p = \begin{bmatrix} 1 \\ 0 \end{bmatrix}^T, \tag{A.13}$$

and the resultant closed-loop matrix is as follows

$$A = \begin{bmatrix} -2.05 & 0.1 & -15 \\ 1.1 & -0.9 & 15 \\ 5 & 0 & 2.2 \end{bmatrix}. \tag{A.14}$$

Similarly, Fig. A.3 is obtained by following the proposed search procedure. In this case, the minimum spectral radius is obtained with $\Delta = 5.4$, and the unstable poles of (A.14) have a damping ratio $\xi = -0.003$ and a natural frequency $\omega_n = 8.38$, and thus $t_{peak} = \pi/8.38 \approx 0.37$. Nonetheless, for this example since $\Delta \geq t_{peak}$, resetting the system every $\Delta = 5.4$ is ill-advised. In fact, Fig. A.4 shows how the ZC reset system clearly outperforms FT reset system as expected.

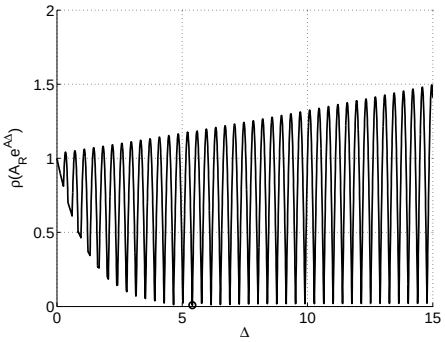

Figure A.3: $\rho(A_R e^{A\Delta})$ vs Δ for Example 2. Minimum value is represented by a circle and is obtained with $\Delta = 5.4$.

Let us now consider a reset observer O that is given by

$$K_P = \begin{bmatrix} 0.5 \\ -10 \end{bmatrix},\ K_I = \begin{bmatrix} 1 \\ 1 \end{bmatrix},$$
$$A_\zeta = 1,\ B_\zeta = 1,\ A_r = 0, \tag{A.15}$$

and the plant P is

$$A_p = \begin{bmatrix} 0.1 & 0.01 \\ -1 & -1 \end{bmatrix},\ B_p = \begin{bmatrix} 0.5 \\ 2.5 \end{bmatrix},\ C_p = \begin{bmatrix} 1 \\ 0 \end{bmatrix}^T, \tag{A.16}$$

and the resultant closed-loop matrix is as follows

$$A = \begin{bmatrix} -0.4 & 0.01 & -1 \\ 9 & -1 & -1 \\ 1 & 0 & 1 \end{bmatrix}. \tag{A.17}$$

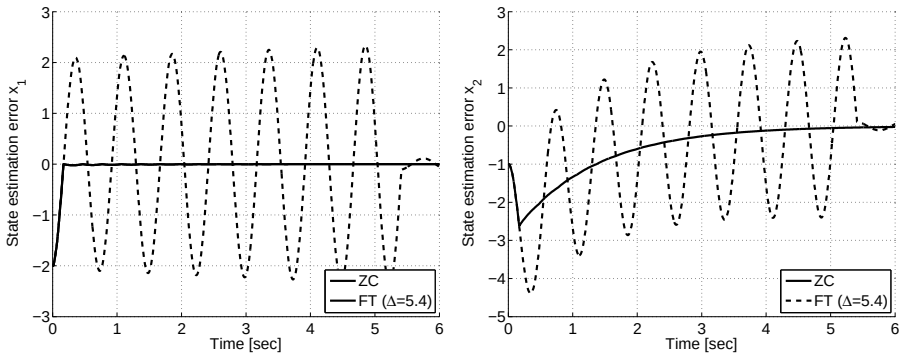

Figure A.4: Simulation results of Example 2. Solid lines have been obtained by using a ZC reset system. Dashed lines have been obtained by using an FT reset system with $\Delta = 5.4$.

In this example the proposed search procedure obtains the results given in Fig. A.5, where the minimum spectral radius is obtained with $\Delta = 1.31$. In addition, the unstable poles of (A.17) have a damping ratio $\xi = -0.424$ and a natural frequency $\omega_n = 0.805$, and thus $t_{peak} = \pi/0.805 \approx 4.31$. Since $\Delta < t_{peak}$, resetting the system every $\Delta = 1.31$ is recommended. In this case both approaches behave in a similar way. However, the FT reset system obtains a better response of the unknown variable x_2 at the expense of slightly deteriorating the estimate of the measured variable x_1 (see Fig. A.6).

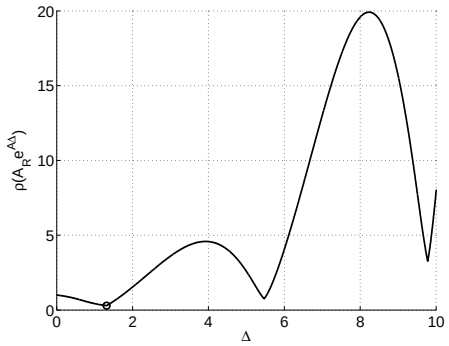

Figure A.5: $\rho(A_R e^{A\Delta})$ vs Δ of Example 3. Minimum value is represented by a circle and is obtained with $\Delta = 1.31$.

Discussion

Analyzing Figs. A.1, A.3, A.5 it can be seen that feasible and unfeasible regions appear alternatively and periodically depending on the chosen reset interval and closed-loop system dynamics. In particular, reset controllers

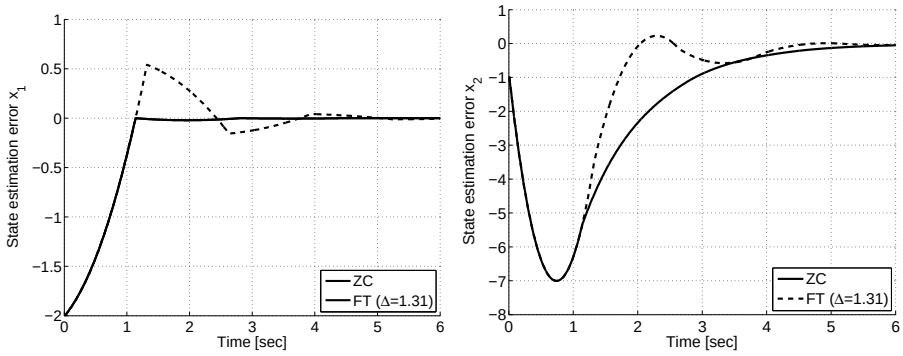

Figure A.6: Simulation results of Example 3. Solid lines have been obtained by using a ZC reset system. Dashed lines have been obtained by using an FT reset system with $\Delta = 1.31$.

(A.2) results in a specific closed-loop structure (A.5) that is specially well-suited for a fixed reset-time approach. Since its minimum $\rho(A_R e^{A\Delta})$ is bound to appear within the first feasible region (see Fig. A.1), some performance improvement is generally expected. On the other hand, the minimum $\rho(A_R e^{A\Delta})$ for reset observers (A.6) might appear beyond the first feasible region (see Fig. A.3). If so, a fixed reset-time approach results in a deteriorated transient response (see Fig. A.4) which highlights the necessity of a criterion to avoid this sort of situation.

Appendix B

Analytical Modeling

B.1 Introduction

In this appendix we present two state space models for the system cooking pot-induction hob. They are based on complete analytical modeling of the heat fluxes that take place in a cooking process. The main differences between both are the amount of load that each model considers, and the temperature sensor used. In particular, we firstly present an analytical model that characterizes the heat fluxes in high load cooking processes. In this case, the variable to be controlled is the cooking pot wall temperature that will be measured by the retractable infrared sensor. Secondly, we present another analytical model that characterizes the heat fluxes in low load cooking processes. In this case, the variable to be controlled is the cooking pot bottom temperature that will be measured by the NTC-thermistors beneath the glass-ceramic.

Both models will be really helpful in the development of temperature control algorithms, as well as in determining the main heat losses of the system. Temperature control is an important feature for hob manufacturers that allows their products to be distinguished from the others and it is also an important benefit for the users. They get important energy savings, safety, and better cooking results. On the other hand, the knowledge about the heat fluxes is important to develop more efficient pots. Combining the temperature control of the cooking process and more efficient pots, energy savings up to 80% could be achieved. Taking into account the amount of energy that every day is used around the world in cooking, this savings could be significant.

B.2 Model for High Load Cooking Processes

Before presenting the model, let us pay attention to Fig. B.1, where the main heat fluxes that take place in the system are presented. Thermal fluxes are represented by arrows. Red arrows represent losses, while black arrows represent the heat transferred from the base of the pan to the water. The heat is generated directly in the base of the pan due to the Foucault currents. Once it is hot, it heats the water, the glass and the walls of the pot. Here, it is assumed that the heat transferred from the base of the pot to the wall is negligible due to the small area of contact. Then, we assume the base heats up only the glass and the water. On the one hand, the heat received by the glass from the base of the pan is transferred through conduction to the surrounding glass, and this one loses the heat to the ambient. On the other hand, the heat received by the water is transferred to the walls of the pot and to the ambient through evaporation, convection and radiation. The walls, for their part, also lose the heat received from the water to the ambient through radiation and convection.

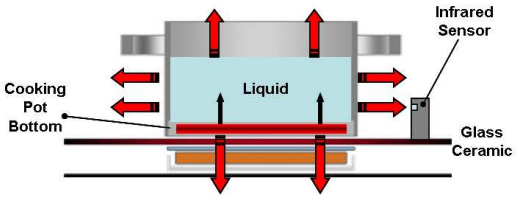

Figure B.1: Scheme that represents thermal fluxes and key temperatures. Red lines represent losses; black lines represent the heat transference between the water and the cooking pot bottom. There are thermal loses to the ambient from the liquid, the cooking pot and the glass ceramic. Cooking pot wall temperature is measured through the retractable infrared sensor.

Once the main fluxes of the system are briefly described, let us explain the process followed to get the model. First of all, the fundamental equations of the different heat transfer ways are presented in order to a better understanding. Afterwards, a power balance is set out, and then, the elements of the power balance are developed. From there, an electrical equivalent of the thermal model is constructed. Finally, to solve the electrical equivalent, it is transformed to state space model. Standard notation and equations of heat and mass transference have been used throughout this section [183], [184]. The parameters are in International System units, if other is not specified. The ways that heat can be transferred between two elements at different temperatures are three: radiation, convection and conduction.

The amount of energy transferred due to radiation, convection and conduction can be written easily as:

$$\begin{aligned} Q_{rad} &= \epsilon A \sigma (T_1^4 - T_2^4), \\ Q_{conv} &= hA(T_1 - T_2), \\ Q_{cond} &= \frac{kA}{L}(T_1 - T_2), \end{aligned} \tag{B.1}$$

where ϵ is the emissivity of the body; A is the area interchanging heat; σ is the Stefan-Boltzmann constant; T_1, T_2 are the temperatures of heat exchange; h is the convection coefficient; L is the length between T_1 and T_2 and k is the thermal conductivity.

The convection coefficient has to be calculated from the Nusselt number: $\mathrm{Nu} = Q_{conv}/Q_{cond} = hL/k$. This is the ratio of convective to conductive heat transfer. Then, it expresses the improvement in the heat transference through a fluid due to convection. L is the characteristic length and k is the thermal conductivity of the fluid. The Nusselt dimensionless number has to be calculated through different empirical expressions for each different situation. These expressions are usually complex and involve other dimensionless numbers as Rayleigh or Prandtl which will be explained below.

Two equations of power balance are presented according to the heat

fluxes in the Fig. B.1:

$$\begin{aligned} P &= Q_B + Q_{B-G} + Q_{B-L}, \\ Q_{B-L} &= Q_L + Q_{losses} + Q_e \end{aligned} \tag{B.2}$$

where P is the power generated by the hob in the cooking pot bottom, that is used in heating up the cooking pot bottom itself (Q_B), the liquid (Q_{B-L}) and the glass ceramic (Q_{B-G}). The heat transferred from the base to the liquid heats up the liquid (in this case water), resulting in energy losses through evaporation (Q_e) and through the ambient (Qlosses). Let us make some assumptions in order to simplify the model and then, each part of the equations will be explained: the temperature in the wall of the pan is equal to the temperature of the water; the temperature of the glass under the pan is equal to the temperature of the base; heat flux between the base and the wall of the pan is negligible, as it has been said before; heat losses from the glass to the inductor are negligible. In the case that the pan is covered with a lid, then we assume that there are no water leaks, and then $Q_e \approx 0$.

Specifically, Q_B is the variation of the internal energy of the base due to the increment or decrement of its temperature. It is called sensible energy. As the temperature of the base is assumed to be equal to the temperature of the glass, the sensible energy of the glass under the pot is included:

$$\begin{aligned} Q_B &= c_B m_B \frac{dT_B}{dt} + c_G m_G \frac{dT_G}{dt} \\ &= (c_B m_B + c_G m_G) \frac{dT_B}{dt} \end{aligned} \tag{B.3}$$

where c_B is the specific heat capacity of the base of the pot; m_B is the mass of the base of the pot; c_G is the specific heat capacity of the glass; m_G is the mass of the glass below the pot; T_B is the temperature of the base of the pot and T_G is the temperature of the glass down the pot assumed to be equal to the temperature of the base.

Q_{B-G} consists in the heat transferred by the base of the pan to the glass due to conduction because of the contact between the two surfaces. This flux includes the heat absorbed by the glass, and the heat lost by the glass to the ambient. As it is said before, the glass temperature is supposed to be equal to the temperature of the base, and the sensible energy of the glass is included in the sensible energy of the base. Consequently, this heat only considers losses to the ambient. This loss is due to conduction (B.1) of the glass in horizontal direction to the ambient.

Similarly, Q_{B-L} is the heat transmitted from the base to the liquid due to convection:

$$Q_{B-L} = h_{B-L} A_B (T_B - T_L), \tag{B.4}$$

where A_B is the pot base area and h_{B-L} is calculated through Nusselt number:

$$h_{B-L} = \mathrm{Nu}_{B-W} k/L, \tag{B.5}$$

where k is the conductivity of water and L is the height of water in the pot.

To calculate Nu, the rectangular enclosure approximation of Hollands et al (1976) [183] is used. It expresses the amount of heat transferred between two parallel surfaces at different temperatures in an enclosure:

$$\mathrm{Nu}_{B-W} = 1 + 1.44\left[1 - \frac{1708}{\mathrm{Ra}_{B-W}}\right] + \left[\frac{\mathrm{Ra}_{B-W}^{1/3}}{18} - 1\right], \tag{B.6}$$

for $\mathrm{Ra} < 108$, where Ra is the Raleigh number and is calculated with:

$$\mathrm{Ra}_{B-W} = \frac{g\beta(T_B - \frac{T_0+T_L}{2})(r/2)^3\mathrm{Pr}}{\upsilon^2}, \tag{B.7}$$

Here, Pr is the Prandtl dimensionless number of the fluid and can be obtained from thermodynamic tables; T_0 is the room temperature; r is the radius of the base of pot; υ is the cinematic viscosity of the fluid; g is the acceleration of gravity and β is the thermal expansion coefficient of the fluid. Note that in the previous equations, the properties of water and air are taken at the mean temperature of the two surfaces that are involved in the heat transference.

Q_L is the amount of heat absorbed by the water. As the temperature of the water is assumed to be equal to the temperature of the walls of the pot, this value includes the two heats:

$$\begin{aligned} Q_L &= c_L m_L \frac{dT_L}{dt} + c_W m_W \frac{dT_G}{dt} \\ &= (c_L m_L + c_W m_W)\frac{dT_L}{dt} \end{aligned} \tag{B.8}$$

where c_L is the specific heat capacity of the water; m_L is the mass of water filling the saucepan; c_W is the specific heat capacity of the walls of the pot; m_W is the mass of the walls of the pot; T_L is the temperature of the water and T_W is the temperature of the walls of the pot assumed to be equal to the temperature of the water.

Q_{losses} represents the sum of all losses due to convection and radiation that occur in the pot,

$$Q_{losses} = Q_{rad-W} + Q_{rad-T} + Q_{conv-W} + Q_{conv-T} \tag{B.9}$$

The values of Q_{rad-W} and Q_{rad-T} are the heat transferred due to radiation of the wall and the top of the pot, respectively and are direct application of (B.1). Q_{conv-W} is the heat transferred due convection of the air. This formula is more complicated due to the calculation of the convection coefficient Nu from empirical deduction that allows getting h. The wall cylinder Nusselt number in natural convection is:

$$\mathrm{Nu}_{conv-W} = \frac{4}{3}\left(\frac{7\mathrm{Ra}_{conv-W}\mathrm{Pr}}{100 + 105\mathrm{Pr}}\right) + 4\frac{(272 + 315\mathrm{Pr})H}{35(64 + 63Pr)2r}, \tag{B.10}$$

where H and r are the height and the radius of the cylinder respectively and Ra has to be calculated as follows:

$$\mathrm{Ra}_{conv-W} = \frac{g\beta(T_L - T_0)H^3\mathrm{Pr}}{\upsilon^2}. \tag{B.11}$$

On the other hand, Q_{conv-T}, which is the convection of the top surface of the cylinder, is calculated with the natural convection in horizontal surface formula:

$$\mathrm{Nu}_{conv-T} = \begin{cases} 0.54\mathrm{Ra}_{conv-T}^{1/4} & \text{for} 10^4 < \mathrm{Ra}_{conv-T} < 10^7, \\ 0.54\mathrm{Ra}_{conv-T}^{1/4} & \text{for} 10^7 < \mathrm{Ra}_{conv-T} < 10^{11}, \end{cases} \tag{B.12}$$

where the Rayleigh number is calculated as (B.11), but taking H as $r/2$, and T_L as the temperature of the top of the pot.

Q_e is the heat lost due to evaporation of water. It is calculated as:

$$Q_e = \frac{dm_L}{dt} h_{evap}, \tag{B.13}$$

where m_L is the mass of water filling the pot and h_{evap} is the enthalpy of evaporation of water (amount of energy needed to evaporate a certain quantity of water).

The key factor in this model is how to deal with the latent heat. There exist formulas which are useful to calculate the mass transfer when the amount of water transferred is very low. However, those formulas have large errors at high water temperatures and they are not applicable to boiling water. There are also formulas to calculate the amount of heat transferred by a surface to the water in boiling processes, but accurate models need complex calculus and algorithms. In this paper, an easy empirical way to calculate the evaporation in a pan is provided.

Let us start with the Chilton-Colburn analogy of mass transfer for low mass transference:

$$\frac{dm_L}{dt} = h_{mass} A(\rho_{v,s} - \rho_{v,\infty}), \tag{B.14}$$

where $\rho_{v,s}$ is the density of the vapour in the surface, $\rho_{v,\infty}$ is the density of the vapour, at the room temperature in a point of the room far enough from the surface; h_{mass} is similar to $h_{convection}$ but in this case Nusselt number has to be substituted by Sherwood (Sh) number which is calculated with Schmidt (Sc) number instead of Prandtl number:

$$\begin{aligned} h_{mass} &= \frac{\mathrm{Sh} D_{AB}}{L_c}, \\ \mathrm{Sh} &= 0.15(\mathrm{GrSc})^{1/3}, \\ D_{AB} &= \frac{1.87e^{-10}((T_L + T_\infty)/2)^{2.072}}{p_{atm}}, \end{aligned} \tag{B.15}$$

where L_c is the critical length of a circle $(r/2)$; Gr is the Grashof dimensionless number; D_{AB} is the diffusivity of water in air, similar to k in convection heat transfer (B.5) and p_{atm} is the atmospheric pressure in atmospheres. Dimensionless numbers Gr and Sc are calculated as follows:

$$\begin{aligned} \text{Gr} &= \frac{g(\rho_\infty - \rho_{sup})L_c^3}{(\rho_\infty + \rho_{sup})\upsilon^2/2}, \\ \text{Sc} &= \frac{\upsilon}{D_{AB}}, \end{aligned} \tag{B.16}$$

where ρ_∞ the density of the wet air in the room ρ_{sup} is the density of the wet air in the surface of the water.

This approximation is pretty correct at low temperatures but near the boiling point, it has up to 30% of error. Furthermore, the Chilton-Colburn analogy depends only on the temperature of water, but in water boiling the velocity of evaporation is dependent on the power applied, and the power applied has influence on the temperature of the base. Experimental tests show that (at least in induction hobs) at the minimum power to keep the system in boiling point, the velocity of evaporation is twice than predicted from Chilton-Colburn, and at maximum power provided by the hob, the velocity of evaporation rises to the quadruple. Therefore, a correction factor is needed to have accurate results. The proposed factor F_{ev} has an error smaller than 4% and depends on the temperature of the water and on the temperature of the base:

$$F_{ev} = 1 + \frac{T_L}{T_{sat}} + ((T_B - T_{sat})0.1 - 0.5)(\frac{T_L}{T_{sat}})^{40}, \tag{B.17}$$

where T_{sat} is the saturation temperature at the pressure of the room. Then (B.14), with the correction factor F_{ev} becomes

$$\frac{dm_L}{dt} = h_{mass}A(\rho_{v,s} - \rho_{v,\infty})F_{ev}, \tag{B.18}$$

Once the equations of heat transfer are presented, we need to join them in a global equation through the electrical equivalent just to build a state space model.

B.2.1 State Space Model

Thermal system can be seen as an electric circuit where temperatures are represented as voltages, heat fluxes as currents, capacitors represent heat capacity and the resistors represent the opposition to heat fluxes between the different elements. The resistances of the different kind of transmissions

are calculated as follows:

$$\begin{aligned} R_{cond} &= \frac{L}{kA}, \\ R_{conv} &= \frac{1}{hA}, \\ R_{rad} &= \frac{1}{\epsilon\sigma(T^2 - T_0^2)(-T_0)}, \end{aligned} \tag{B.19}$$

Starting with B.2, replacing its elements according to the power balance previously presented and applying the electrical equivalent resistors given in (B.19), the final equations of the heat transference balance are obtained:

$$\begin{aligned} P &= C_B \frac{dT_B}{dt} + \frac{T_B - T_0}{R_G} + \frac{T_B - (T_L + T_0)/2}{R_B}, \\ \frac{T_B - (T_L + T_0)/2}{R_B} &= C_L \frac{dT_L}{dt} + \frac{T_L - T_0}{R_{amb}} + Q_e, \end{aligned} \tag{B.20}$$

where T_B is the temperature of the base of the pan; T_0 is the room temperature; T_L is the temperature of water; $C_B = m_B c_B + m_G c_G$ includes heat capacity of the base and the glass under the pan; $C_L = m_L c_L + m_W c_W$ includes the heat capacity of water and of the wall of the pan; R_B is the thermal resistor of the base of the pan; R_G is the thermal resistor of the glass; Q_e is the latent heat and P is the power applied by the hob to the base of the pan. Finally R_{amb} is the thermal resistor of the ambient that includes the convection and radiation resistors of the wall of the pan and of the top of water. The resultant resistor is calculated:

$$\frac{1}{R_{amb}} = \frac{1}{R_{rad-T}} + \frac{1}{R_{rad-W}} + \frac{1}{R_{conv-T}} + \frac{1}{R_{rad-W}}. \tag{B.21}$$

The last factor that has to be included to finish the model is the efficiency of the power electronics and the inductor. For the electronic components, a 95% of efficiency is assumed and a 97% is assumed for the inductor. Then, $P = \eta_{elec}\eta_{ind}P_{cons}$ where η_{elec} is the efficiency of the electronic components; η_{ind} is the efficiency of the inductor and P_{cons} is the power consumed by the hob.

Finally, with the electrical equivalent and applying the Laplace transform with the variable changes, it is possible to obtain a state space model to represent the relation between the power supplied by the induction coil, and the temperatures of the system. Generally, linear time invariant systems are described as follows

$$\begin{aligned} \dot{x} &= A_p x + B_p u \\ y &= C_p x \end{aligned} \tag{B.22}$$

where $x \in \mathbb{R}^n$ is the state vector, $u \in \mathbb{R}^l$ is the input vector, $y \in \mathbb{R}^m$ is the system output vector, and A_p, B_p, C_p are constant $(n \times n), (n \times l), (m \times n)$

Table B.1: Nominal model parameters and their ranges

Parameter	Nominal Value	Variations
a_{11}	-0.0197	[-0.0461 -0.0048]
a_{12}	0.0097	[0.00230 0.02291]
a_{21}	0.0018	[0.00030 0.00540]
a_{22}	-0.0010	[-0.0029 -0.0002]
b_{11}	0.0018	[0.00120 0.00290]
b_{22}	0.0001	[0.00010 0.00040]

matrices. Then, by using an electrical equivalent model that represents the different heat transmissions which appear in our system, it is possible to obtain the following state space model:

$$\begin{aligned} \begin{bmatrix} \dot{\theta}_B \\ \dot{\theta}_W \end{bmatrix} &= \begin{bmatrix} a_{11} & a_{12} \\ a_{21} & a_{22} \end{bmatrix} \begin{bmatrix} \theta_B \\ \theta_W \end{bmatrix} + \begin{bmatrix} b_{11} & 0 \\ 0 & b_{22} \end{bmatrix} \begin{bmatrix} P \\ Q_E \end{bmatrix} \\ \theta_W &= \begin{bmatrix} 0 & 1 \end{bmatrix} \begin{bmatrix} \theta_B \\ \theta_W \end{bmatrix} \end{aligned} \tag{B.23}$$

where $\theta_B = T_B - T_0$ is the difference between the pot bottom temperature T_B and the ambient temperature, $\theta_W = T_W - T_0$ is the difference between the pot wall temperature T_W and the ambient temperature, P is the power supplied by the inductor coil which takes into account the efficiency of the electronics and of the inductor, and Q_E is the energy loss because of evaporation. Additionally, a_{11}, a_{12}, a_{21}, a_{22}, b_{11}, and b_{22} are uncertain parameters that depend on the pot and glass thermal properties, as well as on the different thermal losses of the system, which are given by

$$\begin{aligned} a_{11} &= \frac{R_G + R_B}{C_B R_G R_B}, & a_{12} &= \frac{1}{2C_B R_B}, & a_{21} &= \frac{1}{C_L R_B}, \\ a_{22} &= \frac{1}{C_L} \frac{2R_B - R_{amb}}{2R_B R_{amb}}, & b_{11} &= \frac{1}{C_B}, & b_{22} &= \frac{1}{C_L}, \end{aligned} \tag{B.24}$$

and whose nominal values and expected variation are summarized in Table B.1.

As conclusion, the proposed model considers the influence of all these parameters in heat fluxes, which is very important to determine the main contributions to heat losses. Once existing losses are well known, it is easier to avoid them in order to improve the efficiency of the cooking processes. This model considers the initial temperature and the mass of water; the temperature and humidity of the room; the emissivity, mass and the material of the pan; the power provided and the internal efficiency of the hob. It supplies also the possibility to put a lid on the cooking pot or the possibility to change the height over sea level where the cooking process is being car-

ried out. Height over sea level is important because atmospheric pressure changes, and therefore, the saturation temperature of water also changes.

B.2.2 Experimental Validation

Although multiple tests were carried out to show the robustness of the proposed model, only two tests are presented here for brevity, as an example of its accuracy. They were carried out at a cooking zone of 210 mm of diameter with different power levels to check the performance of the evaporation factor proposed in this section. Furthermore, despite the fact that the tests were done in different days, and hence, some room conditions changed, the model continues showing a good adjustment.

The first test (Fig. B.2) is performed at constant nominal power (2300 W) without lid. The test ends when 1.5 liter of water is evaporated. This far point is chosen to check whether the model is able to adapt itself to the evaporation velocity change when the amount of water considerably changes. During the whole test, the average error in mass is 0.0065 Kg and average error in temperature is $0.862°C$ that highlights the high accuracy of the presented model.

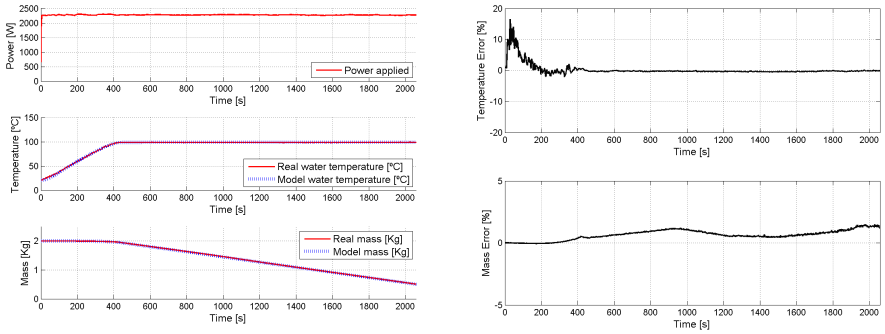

Figure B.2: Comparison of modeled behavior and real system through the observation of water temperature, mass water and power applied. Constant power applied of nominal level (2300 W) without lid. Average mass error = 0.0065 Kg. Average temperature error = $0.862°C$.

Fig. B.3 shows the second test carried out with a 210 mm cooking zone. In this case, supplied power is reduced to 50% when the water temperature reaches $90°C$. This results in a longer transition between the heating stage and the boiling stage. Consequently, this test allows us to check the accuracy in modelling this complex transition, which is no referenced in most studies focused on boiling or heating. Analyzing Fig. B.3, it is evident that the model shows a good behavior with an average mass error of 0.0022 Kg. and an average temperature error of $0.8240°C$.

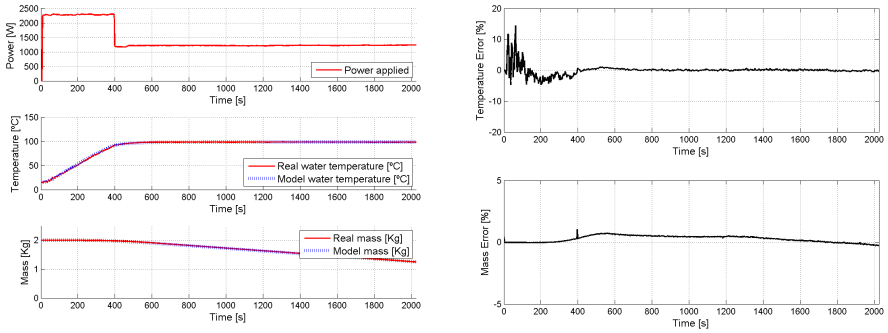

Figure B.3: Comparison of modeled behavior and real system through the observation of water temperature and water mass. Nominal power has been applied till the temperature has reached $90°C$. and 50% after that point. Average mass error = 0.0022 Kg. Average temperature error = $0.8240°C$.

B.3 Model for Low Load Cooking Processes

In a similar way, Fig. B.4, shows the main heat fluxes that occur in low load cooking processes. In particular, heat transmission is produced as follows. First, the heat is produced directly on the cooking pot bottom, and it is transmitted upwards, through the cooking pot layers, and downwards, through the glass ceramic. Furthermore, all heat losses have to be considered. There are several heat losses in our system: a radiation loss from the cooking pot to the air, a convection loss from the cooking pot to the air, and a convection loss from the glass ceramic to the air. There exists also, a contact resistor between the cooking pot bottom and the glass ceramic caused by the cooking pot bottom's evenness.

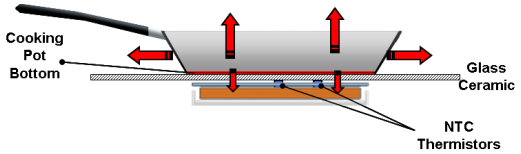

Figure B.4: Scheme that represents thermal fluxes and key temperatures. Red lines represent losses. Cooking pot bottom temperature is measured through the NTC thermistors.

Two equations of power balance are presented according to the heat fluxes shown in the Fig. B.4:

$$\begin{aligned} P &= Q_B + Q_{B-G} + Q_{B_{losses}}, \\ Q_{B-G} &= Q_G + Q_{G_{losses}} \end{aligned} \tag{B.25}$$

where P is the power generated by the hob in the cooking pot bottom, Q_B is the sensible heat associated with the cooking pot bottom, $Q_{B_{losses}}$ are

the heat losses of the cooking pot to the ambient due to both radiation and convection, Q_G is the sensible heat associated with the glass-ceramic, and $Q_{G_{losses}}$ are the heat losses of the glass ceramic to the ambient mostly due to convection, because the glass ceramic reaches lower temperatures than the cooking pot bottom while performing low load cooking processes.

Differences between power balance for high load (B.2) and low load (B.25) cooking processes require further comments. In high load cooking process, most part of the heat generated in the cooking pot bottom is transmitted upwards to the liquid, and only a small part is transmitted downwards to the glass ceramic. As a consequence, the resultant thermal gradient between the cooking pot and the glass ceramic is so small, that both elements can be assumed to be at the same temperature. However, this is no longer true while cooking with low load, because in this case, most of the heat is transmitted downwards to the glass-ceramic rather than being dissipated upwards to the air. For this reason, the power balance for low load cooking processes (B.25) considers a temperature gradient between the cooking pot and the glass-ceramic that will results in a considerably more accurate model.

As before, let us define every term of the power balance (B.25). In this case, Q_B only considers the variation of the internal energy of the cooking pot bottom due to the increment or decrement of its temperature, and is given by

$$Q_B = c_B m_B \frac{dT_B}{dt}, \tag{B.26}$$

where c_B is the specific heat capacity of the cooking pot, and m_B is the mass of the cooking pot.

Similarly, Q_G consists in the internal energy variation of the glass ceramic, and it is defined as follows

$$Q_G = c_G m_G \frac{dT_G}{dt}, \tag{B.27}$$

here c_G is the specific heat capacity of the glass ceramic, and m_G is the mass of the glass ceramic situated below the cooking pot.

Remaining terms correspond to heat losses associated with the cooking pot $Q_{B_{losses}}$ and the glass ceramic $Q_{G_{losses}}$, which are both computed as in (B.9) but characterizing each formula (B.10)-(B.12) with their respective parameters.

B.3.1 State Space Model

As previously, we can develop an equivalent electric circuit, in which electrical voltages represent temperatures, electrical current represent heat transmission, electrical capacitors represent thermal capacities, and every heat

flow is represented by a resistor. Replacing the elements of the power balance (B.25), and applying the electrical equivalent resistors results in:

$$\begin{aligned} P &= C_B \frac{dT_B}{dt} + \frac{T_B - T_0}{R_{B-amb}}, \\ \frac{T_B - T_G}{R_G} &= C_G \frac{dT_G}{dt} + \frac{T_G - T_0}{R_{G-amb}} \end{aligned} \tag{B.28}$$

where $C_B = c_B m_B$, $C_G = c_G m_G$, R_G is a contact resistor computed from (B.19), and

$$\begin{aligned} \frac{1}{R_{B-amb}} &= \frac{1}{R_{B-rad}} + \frac{1}{R_{B-conv}}, \\ \frac{1}{R_{G-amb}} &= \frac{1}{R_{G-rad}} + \frac{1}{R_{G-conv}}, \end{aligned} \tag{B.29}$$

that are obtained from (B.19) as well.

Finally, power balance (B.28) can be rearranged as state space model that represents the relation between the power supplied by the induction coil and the temperatures of the system. In this case state space model that characterizes low load cooking processes is given by:

$$\begin{aligned} \begin{bmatrix} \dot{\theta}_B \\ \dot{\theta}_G \end{bmatrix} &= \begin{bmatrix} a_{11} & 0 \\ a_{21} & a_{22} \end{bmatrix} \begin{bmatrix} \theta_B \\ \theta_G \end{bmatrix} + \begin{bmatrix} b_1 \\ 0 \end{bmatrix} P \\ \theta_G &= \begin{bmatrix} 0 & 1 \end{bmatrix} \begin{bmatrix} \theta_B \\ \theta_G \end{bmatrix} \end{aligned} \tag{B.30}$$

where $\theta_B = T_B - T_0$ is the difference between the pot bottom temperature T_B and the ambient temperature, $\theta_G = T_G - T_0$ is the difference between the glass ceramic temperature T_G and the ambient temperature, P is the power supplied by the inductor coil, which as previously, considers the efficiency of the electronics and of the inductor. Additionally, a_{11}, a_{21}, a_{22}, and b_1 are uncertain parameters that depend on the cooking pot and glass ceramic thermal properties which are given by

$$\begin{aligned} a_{11} &= \frac{-1}{R_{B-amb} C_B}, & a_{21} &= \frac{R_{G-amb}}{R_{G-amb} R_G C_G}, \\ a_{22} &= \frac{-(R_{G-amb} + R_G)}{R_{G-amb} R_G C_G}, & b_1 &= \frac{1}{C_B}. \end{aligned} \tag{B.31}$$

Consequently, there will be one different state-space model for each pot. The modeling process was repeated for a set of all the available pots; hence, a database with more than 150 simulation models was obtained. Table B.2 summarizes the nominal values of all model parameters and their variations.

Table B.2: Nominal model parameters and their ranges

Parameter	Nominal Value	Variations
a_{11}	-0.005	[-0.01 -0.0025]
a_{21}	0.01	[0.003 0.02]
a_{22}	-0.001	[-0.02 -0.003]
b_1	0.002	[0.00065 0.005]

B.3.2 Experimental Validation

Several tests are shown to check the accuracy of the proposed model. They are carried out at a cooking zone of 210 mm of diameter, in which a predefined power step is supplied to each cooking pot (see Fig. B.5). Each test consists in supplying 2300 watts for 60 seconds, and after that, 400 watts for 20 minutes more, which basically represents a typical power step that can be found in household conditions. Note that, users generally select a high power level to heat up quickly the cooking pot at the beginning of the cooking process, and afterwards, a lower power level to keep the cooking pot temperature under control.

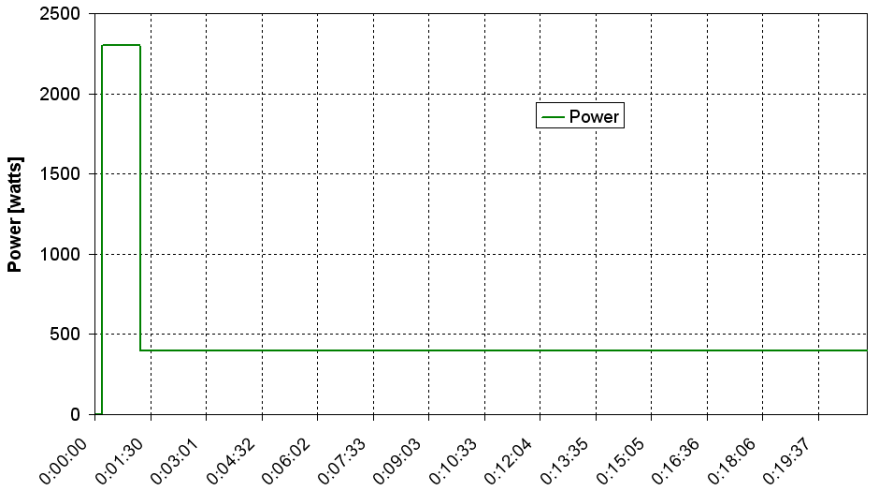

Figure B.5: Predefined power step used during validation tests.

As a sample of the performed tests, Fig. B.6 shows both estimated and actual temperature while using a cooking pot with a high concavity and little weight, conditions which are typical between enamel cooking pots. It is evident that the proposed model shows a considerable accuracy, resulting in average error in temperature lower than $5°C$. Despite the fact that this

error is higher than the one obtained with the model for high load cooking processes, it is worth mentioning that such accuracy is only required while cooking with liquids. As a matter of fact, $5°C$ of error could imply that the water is actually boiling instead of within the simmering range. However, this temperature error is not relevant while frying, roasting or grilling, as it was shown in the application tests of Chapter 8.

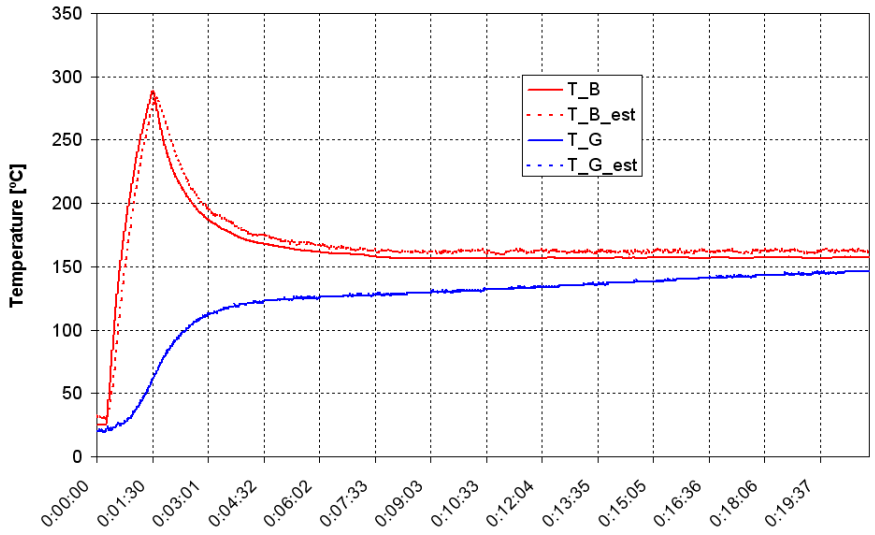

Figure B.6: Comparison of modeled behavior and actual system. Solid red line is the actual cooking pot bottom temperature. Dashed red line is the estimated cooking pot bottom temperature. Solid blue line is the actual glass ceramic temperature measured with the NTC-thermistors. Dashed blue line is the estimated glass ceramic temperature.

Finally, Fig. B.7 shows both estimated and actual temperature while using a multilayer cooking pot, which are heavier and less concave than enamel cooking pots (see Fig. B.8). As a consequence, the multilayer cooking pot reaches lower temperatures, in spite of the fact that the temperature measured by the NTC thermistors is higher. Nonetheless, the model keeps showing a considerable accuracy, because average error in temperature is still lower than $5°C$.

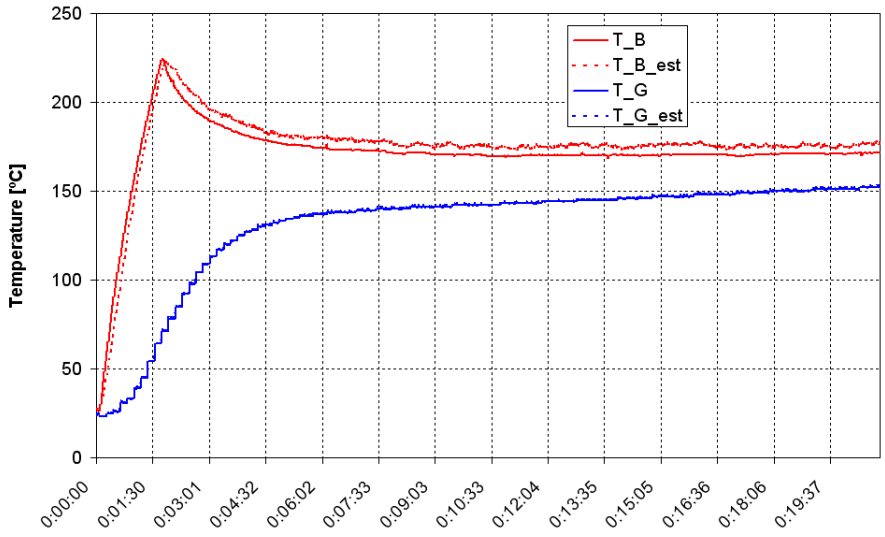

Figure B.7: Comparison of behavior of modeled and actual system. Solid red line is the actual cooking pot bottom temperature. Dashed red line is the estimated cooking pot bottom temperature. Solid blue line is the actual glass ceramic temperature measured with the NTC-thermistors. Dashed blue line is the estimated glass ceramic temperature.

Figure B.8: Enamel cooking pot (left). Multilayer cooking pot (right).

Bibliography

[1] E. E. Kriezis, T. D. Tsiboukis, S. M. Panas, and J. A. Tegopoulos. Eddy currents: theory and applications. *Proceedings of the IEEE*, 80(10):1559–1589, 1992.

[2] D. C. Jiles and D. L. Atherton. Theory of ferromagnetic hysteresis. *Journal of Magnetism and Magnetic Materials*, 61(1):48–60, 1986.

[3] F. Young. Induction heating for case hardening applications. *IEEE Trans. on Magnetics*, 13(6):1776–1785, 1977.

[4] N. S. Bayindir, O. Kukrer, and M. Yakup. DSP-based PLL-controlled 50-100 kHz 20 kW high-frequency induction heating system for surface hardening and welding applications. *IEE Proceedings-Electric Power Applications*, 150(3):365–371, 2003.

[5] P. K. Jain, J. R. Espinoza, and S. B. Dewan. Self-started voltage-source series-resonant converter for high-power induction heating and melting applications. *IEEE Trans. on Industry Applications*, 34(3):518–525, 1998.

[6] L. Mingyu, X. Hongbo, S. W. R. Lee, K. Jongmyung, and K. Daewon. Eddy current induced heating for the solder reflow of area array packages. *IEEE Trans. on Advanced Packaging*, 31(2):399–403, 2008.

[7] J. Acero, J. M. Burdio, L. A. Barragan, D. Navarro, R. Alonso, J. R. Garcia, F. Monterde, P. Hernandez, S. Llorente, and I. Garde. Domestic induction appliances. *IEEE Industry Applications Magazine*, 16(2):39–47, 2010.

[8] J. Acero, J. M. Burdio, L. A. Barragan, D. Navarro, R. Alonso, J. R. Garcia, F. Monterde, P. Hernandez, S. Llorente, and I. Garde. The domestic induction heating appliance: An overview of recent research. In *Proc. IEEE Applied Power Electronics Conference and Exposition (APEC)*, pages 651–657, 2008.

[9] S. Llorente, F. Monterde, J. M. Burdio, and J. Acero. A comparative study of resonant inverter topologies used in induction cooking. In *Proc. IEEE Applied Power Electronics Conference and Exposition (APEC)*, pages 1168–1174, 2002.

[10] J. M. Burdio, F. Monterde, J. R. Garcia, L. A. Barragan, and A. Martinez. A two-output series-resonant inverter for induction-heating cooking appliances. *IEEE Trans. on Power Electronics*, 20(4):815–822, 2005.

[11] J. M. Burdio, L. A. Barragan, A. Martinez, F. Monterde, D. Navarro, and J. Acero. Asymetrical voltage-cancellation control for full-bridge series resonant inverters. *IEEE Trans. on Power Electronics*, 19(2):461–469, 2004.

[12] Nam-Ju Park, Dong-Yun Lee, and Dong-Seok Hyun. A power-control scheme with constant switching frequency in class-d inverter for induction-heating jar application. *IEEE Trans. on Industrial Electronics*, 54(3):1252–1260, 2007.

[13] I. Millan, D. Puyal, J. M. Burdio, C. Bemal, and J. Acero. Improved performance of half-bridge series resonant inverter for induction heating with discontinuous mode control. In *Proc. IEEE Applied Power Electronics Conference and Exposition (APEC)*, pages 1293–1298, 2007.

[14] J. Acero, R. Alonso, J. M. Burdio, L.A. Barragan, and D. Puyal. Analytical equivalent impedance for a planar circular induction heating system. *IEEE Trans. on Magnetics*, 42(1):84–86, 2006.

[15] C. Carretero, J. Acero, R. Alonso, J. M. Burdio, and F. Monterde. Temperature influence on equivalent impedance and efficiency of inductor systems for domestic induction heating appliances. In *Proc. IEEE Applied Power Electronics Conference and Exposition (APEC)*, pages 1233–1239, 2007.

[16] G. Cooke. Fire safety engineering applied to the domestic chip-pan fire problem. *Building Engineer*, pages 22–24, 2005.

[17] U. Has, J. Schieferdecker, and D. Wassilew. Temperature control for food in pots on cooking hobs. *IEEE Trans. on Industrial Electronics*, 46(5):1030–1034, 1999.

[18] O. Aldana, R. Braulio, J. R. Garcia, S. Llorente, F. Monterde, D. Paesa, and C. Sagues. Induction cooking hob with at least one induction heating element and at least one temperature sensor. EP2094059. 2009.

[19] H. Durrant-Whyte. *Integration, Coordination and Control of Multi-sensor Robot systems*. Kluwer Academic Publishers, 1988.

[20] J. Manyika and H. Durrant-Whyte. *Data Fusion and Sensor Management. A Decentralized Information-Theoretic Approach*. Ellis Howrwood publishers, 1994.

[21] I. Horowitz. A synthesis theory for linear time-varying feedback systems with plant uncertainty. *IEEE Trans. on Automatic Control*, 20(4):454–464, 1975.

[22] Y. Chait and O. Yaniv. Multiple-input/single-output computer-aided control design using the quantitative feedback theory. *Int. Journal of Robust and Nonlinear Control*, 3(1):47–54, 1993.

[23] Ali Altowati, Kai Zenger, and Teuvo Suntio. QFT-based robust controller design for a DC-DC switching power converter. In *Proc. of the IEEE European Conference on Power Electronics and Applications*, pages 1–11, 2007.

[24] A. Baños. Nonlinear quantitative feedback theory. *Int. Journal of Robust and Nonlinear Control*, 17(2):181–202, 2007.

[25] K. Glover and J. C. Doyle. State-space formulae for all stabilizing controllers that satisfy an h1-norm bound and relations to risk sensitivity. *Systems and Control Letters*, 11(3):167–172, 1988.

[26] J. C. Doyle, K. Glover, P. P. Khargonekar, and B. A. Francis. State space solutions to standard H2 and H1 control problems. *IEEE Trans. on Automatic Control*, 34(8):831–847, 1989.

[27] R. Naim, G. Weiss, and S. Ben-Yaakov. H-infinity control applied to boost power converters. *IEEE Trans. on Power Electronics*, 34(4):677–683, 1997.

[28] P. Gahinet, A. Nemirovski, A. J. Laud, and M. Chilali. *LMI Control Toolbox*. The MathWorks Inc., 2001.

[29] R. Kalman. A new approach to linear filtering and prediction problems. *Transactions of the ASME–Journal of Basic Engineering*, 82(Series D):35–45, 1960.

[30] D. G. Luenberger. Observing the state of a linear system. *IEEE Trans. Mil. Electron.*, 8:74–80, 1964.

[31] D. G. Luenberger. An introduction to observers. *IEEE Trans. on Automatic Control*, 16(6):596–602, 1971.

[32] M. J. Milford. *Robot Navigation from Nature: Simultaneous Localisation, Mapping, and Path Planning Based on Hippocampal Models.* Springer Tracts in Advanced Robotics, 2010.

[33] B. Ristic, S. Arulampalam, and N. Gordon. *Beyond the Kalman filter: particle filters for tracking applications.* Artech House, 2004.

[34] M. Zeitz. The extended Luenberger observer for nonlinear systems. *Systems and Control Letters*, 9(2):149–156, 1987.

[35] K. S. Narendra and A. M. Annaswamy. *Stable Adaptive Systems.* Dover Publications, 2005.

[36] Q. Zhang. Revisiting different adaptive observers through a unified formulation. In *Proc. of the IEEE Conference of Decision and Control*, pages 3067–3072, 2005.

[37] J. L. Chang. Applying discrete-time proportional integral observers for state and disturbance estimations. *IEEE Trans. on Automatic Control*, 51(5):814–818, 2006.

[38] J. Jung, J. Hwang, and K. Huh. Optimal proportional-integral adaptive observer design for a class of uncertain nonlinear systems. In *Proc. of the IEEE American Control Conference*, pages 1931–1936, 2007.

[39] E. Vahedforough and B. Shafai. Design of proportional integral adaptive observers. In *Proc. of the IEEE American Control Conference*, pages 3683–3688, 2008.

[40] J. Clegg. A nonlinear integrator for servomechanisms. *Trans. of the A.I.E.E.*, 77(Part-II):41–42, 1958.

[41] O. Beker, C. Hollot, Y. Chait, and H. Han. Fundamental properties of reset control systems. *Automatica*, 40(6):905–915, 2004.

[42] D. Nesic, L. Zaccarian, and A. R. Teel. Stability properties of reset systems. *Automatica*, 44(8):2019–2026, 2008.

[43] A. Baños, J. Carrasco, and A. Barreiro. Reset times dependent stability of reset systems. *IEEE Trans. on Automatic Control*, 56(1):217–223, 2011.

[44] J. Zheng and M. Fu. A reset state estimator using an accelerometer for enhanced motion control with sensor quantization. *IEEE Trans. on Control System Technology*, 18(1):79–90, 2010.

[45] D. Paesa, C. Franco, S. Llorente, G. Lopez-Nicolas, and C. Sagues. On robust PI adaptive observers for nonlinear uncertain systems with

bounded disturbances. In *Proc. of the 18th IEEE Mediterranean Control Conference*, pages 1031–1036, 2010.

[46] D. Paesa, A. Baños, and C. Sagues. Reset observers for linear time-delay systems. a delay-independent approach. In *Proc. of the IEEE Conference on Decision and Control*, 2011. (Accepted).

[47] D. Paesa, J. Carrasco, and C. Sagues. On the design of reset systems with unstable base: a fixed reset-time approach. In *Proc. of the 37th Annual Conference of the IEEE Industrial Electronics Society*, 2011. (Accepted).

[48] D. Paesa, C. Franco, S. Llorente, G. Lopez-Nicolas, and C. Sagues. Reset adaptive observer for a class of nonlinear systems. *IEEE Trans. on Automatic Control*, (Accepted).

[49] D. Paesa, A. Baños, and C. Sagues. Optimal reset adaptive observer design. *Systems and Control Letters*, 60(10):877–883, 2011.

[50] O. Aldana, S. Llorente, D. Paesa, and C. Sagues. Hob with a cover plate. WO2010081637. 2010.

[51] M. Almolda, C. Franco, S. Llorente, D. Paesa, and C. Sagues. Heating zone for a domestic appliance for preparing food. EP2328383. 2011.

[52] J. Acero, R. Alonso, J. I. Artigas, C. Carretero, C. Franco, S. Llorente, D. Paesa, and C. Sagues. Cook top comprising at least one temperature sensor. WO2011055279. 2011.

[53] C. Franco, J. Acero, R. Alonso, C. Sagues, and D. Paesa. Inductive sensor for temperature measurement in induction heating applications. *IEEE Sensors Journal*, (Submitted).

[54] D. Paesa, C. Franco, S. Llorente, G. Lopez-Nicolas, and C. Sagues. QFT-based robust simmering control for domestic induction cookers using an infrared sensor. In *Proc. of the 45th IEEE Industry Applications Society Annual Meeting*, pages 1–6, 2010.

[55] D. Paesa, C. Franco, S. Llorente, G. Lopez-Nicolas, and C. Sagues. Adaptive simmering control for domestic induction cookers. *IEEE Trans. on Industry Applications*, 47(5):2257–2267, 2011.

[56] D. Paesa, S. Llorente, C. Sagues, and O. Aldana. Adaptive observers applied to pan temperature control of induction hobs. *IEEE Trans. on Industry Applications*, 45(3):1116–1125, 2009.

[57] D. Paesa, C. Franco, S. Llorente, G. Lopez-Nicolas, and C. Sagues. Reset observers applied to MIMO systems. *Journal of Process Control*, 21(4):613–619, 2011.

[58] D. Paesa, C. Franco, S. Llorente, G. Lopez-Nicolas, and C. Sagues. Reset adaptive observers and stability properties. In *Proc. of the 18th IEEE Mediterranean Control Conference*, pages 1435–1440, 2010.

[59] C. Franco, D. Paesa, C. Sagues, and S. Llorente. Analytical modeling of a saucepan in an induction hob. In *Proc. of the 18th IEEE Mediterranean Control Conference*, pages 298–303, 2010.

[60] O. Aldana, S. Llorente, D. Paesa, and C. Sagues. Hob having a temperature sensor. WO2010139598. 2010.

[61] C. Franco, S. Llorente, D. Paesa, and C. Sagues. Heating zone for a domestic appliance for preparing food. EP2339893. 2011.

[62] D. Paesa, C. Franco, and C. Sagues. Sistema de sensado para la reducción de la temperatura en la superficie de cocción. Primer Premio en la categoría de Equipos de Investigación de la Universidad de Zaragoza. Premio BSH-UZ a la innovación en la empresa 2009.

[63] A. Radke and Z. Gao. A survey of state and disturbance observers for practitioners. In *Proc. of the IEEE American Control Conference*, pages 5183–5188, 2006.

[64] G. Luders and K. S. Narendra. A new canonical form for an adaptive observer. *IEEE Trans. on Automatic Control*, 19(2):117–119, 1974.

[65] G. Kreisselmeir. Adaptive observers with exponential rate of convergence. *IEEE Trans. on Automatic Control*, 22(1):2–8, 1977.

[66] A. J. Van Der Schaft. On nonlinear observers. *IEEE Trans. on Automatic Control*, 30(12):1254–1256, 1985.

[67] G. Bastin and M. R. Gevers. Stable adaptive observers for nonlinear time varying systems. *IEEE Trans. on Automatic Control*, 33(7):650–658, 1988.

[68] R. Marino. Adaptive observers for single output nonlinear systems. *IEEE Trans. on Automatic Control*, 35(9):1054–1058, 1990.

[69] R. Marino and P. Tomei. Global adaptive observers for nonlinear systems via filtered transformations. *IEEE Trans. on Automatic Control*, 37(8):1239–1245, 1992.

[70] R. Marino and P. Tomei. Adaptive observers with arbitrary exponential rate of convergence for nonlinear systems. *IEEE Trans. on Automatic Control*, 40(7):1300–1304, 1995.

[71] Q. Zhang and A. Clavel. A new approach to adaptive observer design for MIMO systems. In *Proc. of the IEEE Conference on Decision and Control*, pages 1545–1550, 2001.

[72] Q. Zhang. Adaptive observer for multiple-input multiple-output (MIMO) linear time-varying systems. *IEEE Trans. on Automatic Control*, 47(3):525–529, 2002.

[73] Q. Zhang and A. Clavel. Adaptive observer with exponential forgetting factor for linear time varying systems. In *Proc. of the IEEE Conference on Decision and Control*, pages 3886–3891, 2001.

[74] R. Marino and G.L Santosuosso. Robust adaptive observers for nonlinear systems with bounded disturbances. In *Proc. of the IEEE Conference on Decision and Control*, pages 5200–5205, 1999.

[75] R. Marino and G.L Santosuosso. Robust adaptive observers for nonlinear systems with bounded disturbances. *IEEE Trans. on Automatic Control*, 46(6):967–972, 2001.

[76] J. A. R. Vargas and E. M. Hemerly. Nonlinear adaptive observer design for uncertain dynamical systems. In *Proc. of the IEEE American Control Conference*, pages 1307–1308, 2000.

[77] P. Garimella and B. Yao. Nonlinear adaptive robust observer design for a class of nonlinear systems. In *Proc. of the IEEE American Control Conference*, pages 4391–4396, 2003.

[78] J. B. Pomet and L. Praly. Adaptive nonlinear regulation: Estimation from the lyapunov equation. *IEEE Trans. on Automatic Control*, 37(6):729–740, 1992.

[79] J. Jung, K. Huh, H. K. Fathy, and J. L. Stein. Optimal robust adaptive observer design for a class of nonlinear systems via an h-infinity approach. In *Proc. of the IEEE American Control Conference*, pages 3637–3642, 2006.

[80] C. Kravaris, V. Sotiropoulos, S. Georgiou, N. Kazantzis, M. Q. Xiao, and A. J. Krener. Nonlinear observer design for state and disturbance estimation. *System and Control Letters*, 56(11-12):730–735, 2007.

[81] G. H. Hostetter and J. Meditch. On the generalization of observers to systems with unmeasurable, unknown inputs. *Automatica*, 9(6):721–724, 1973.

[82] Y. Park and J. L. Stein. Closed-loop state and input observer for systems with unknown inputs. *International Journal of Control*, 48(3):1121–1136, 1988.

[83] J. Chen, R. Patton, and H. Zhang. Design of unknown input observers and robust fault detection filters. *International Journal of Control*, 63(1):85–105, 1996.

[84] M. Corless and J. Tu. State and input estimation for a class of uncertain systems. *Automatica*, 34(6):757–764, 1998.

[85] Q. P. Ha and H. Trinh. State and input simultaneous estimation for a class of nonlinear systems. *Automatica*, 40(10):1779–1785, 2004.

[86] E. Alcorta and P.M. Frank. Deterministic nonlinear observer-based approaches to fault diagnosis: a survey. *Control Engineering Practice*, 5(5):663–670, 1997.

[87] C. Edwards, S. K. Spurgeon, and R. J. Patton. Sliding mode observers for fault detection and isolation. *Automatica*, 36(4):541–553, 2000.

[88] B. Basseville. Detecting changes in signals and systems - a survey. *Automatica*, 24(3):309–326, 1988.

[89] A. Emami-Naeini, M. M. Akhter, and S. M. Rock. Effect of model uncertainty on failure detection the threshold selector. *IEEE Trans. on Automatic Control*, 33(12):1106–1115, 1988.

[90] B. Shafai and R. L. Carroll. Design of proportional-integral observer for linear time-varying multivariable systems. In *Proc. of the IEEE Conference on Decision and Control*, pages 597–599, 1985.

[91] B. Shafai, S. Beale, H. H. Niemannv, and J. Stoustrup. LTR design of discrete-time proportional integral observer. *IEEE Trans. on Automatic Control*, 41(7):1056–1062, 1996.

[92] B. Shafai, C.T. Pi, S. Nork, and S.P. Linder. Proportional integral adaptive observer for parameter and disturbance estimations. In *Proc. of the IEEE Conference of Decision and Control*, pages 4694–4699, 2002.

[93] H. Sadaka, B. Shafai, and R. Sipahi. Robust PI observer design for linear time-delay systems. In *Proc. of the Multi-conference on Systems and Control*, pages 1209–1213, 2009.

[94] K. K. Busawon and P. Kabore. On the design of integral and proportional integral observers. In *Proc. of the IEEE American Control Conference*, pages 3725–3729, 2000.

[95] P. Kabore and K. Busawon. Disturbance attenuation using proportional integral observers. *International Journal of Control*, 74(6):618–627, 2001.

[96] M. Athans, D. Castañon, K. Dunn, C. Greene, L. Wing, N. Sandell, and A. Willsky. The stochastic control of the F-8C aircraft using a multiple model adaptive control (MMAC) method-Part I: Equilibrium flight. *IEEE Trans. on Automatic Control*, 22(5):768–780, 1977.

[97] K. S. Narendra and J. Balakrishnan. Improving transient response of adaptive control systems using multiple models and switching. *IEEE Trans. on Automatic Control*, 39(9):1861–1866, 1994.

[98] K. S. Narendra and J. Balakrishnan. Adaptive control using multiple models. *IEEE Trans. on Automatic Control*, 42(2):171–187, 1997.

[99] S. Fekri, M. Athans, and A. Pascoal. RMMAC: A novel robust adaptive control scheme - Part I: Architecture. In *Proc. of the IEEE Conference on Decision and Control*, pages 1134–1139, 2004.

[100] R. Orjuela, B. Marx, J. Ragot, and D. Maquin. Proportional-integral observer design for nonlinear uncertain systems modelled by a multiple model approach. In *Proc. of the IEEE Conference on Decision and Control*, pages 3577–3582, 2008.

[101] A. M. Nagy, B. Marx, G. Mourot, G. Schutz, and J. Ragot. State estimation of the three-tank system using a multiple model. In *Proc. of the IEEE Conference on Decision and Control*, pages 7795–7800, 2009.

[102] R. Orjuela, B. Marx, J. Ragot, and D. Maquin. On the simultaneous state and unknown input estimation of complex systems via a multiple model strategy. *IET Control Theory and Applications*, 3(7):877–890, 2009.

[103] P. J. Antsaklis and A. Nerode. Guest editorial hybrid control systems: An introductory discussion to the special issue. *IEEE Trans. on Automatic Control*, 43(4):457–460, 1998.

[104] M. Egerstedt. Behavior based robotics using hybrid automata. *Lecture Notes in Computer Science*, 1790:103–116, 2000.

[105] C. Tomlin, G. Pappas, and S. Sastry. Conflict resolution for air traffic management: a study in multi-agent hybrid systems. *IEEE Trans. on Automatic Control*, 43(4):509–521, 1998.

[106] B. Lennartson, M. Tittus, B. Egardt, and S. Pettersson. Hybrid systems in process control. *IEEE Control Systems Magazine*, 16(5):45–56, 1996.

[107] B. Brogliato. *Nonsmooth Mechanics*. New York: Springer-Verlag, 1999.

[108] J. Buck. Synchronous rhythmic flashing of fireflies ii. *The Quarterly Review of Biology*, 63(3):265–289, 1988.

[109] C. S. Peskin. *Mathematical Aspects of Heart Physiology*. New York: Courant Institute of Mathematical Sciences, 1975.

[110] J. Lygeros, K. H. Johansson, S. N. Simic, J. Zhang, and S. S. Sastry. Dynamical properties of hybrid automata. *IEEE Trans. on Automatic Control*, 48(1):2–17, 2003.

[111] R. Goebel, R. G. Sanfelice, and A. R. Teel. Hybrid dynamical systems. *IEEE Control Systems Magazine*, 29(2):28–93, 2009.

[112] D. Liberzon and S. Morse. Basic problems in stability and design of switched systems. *IEEE Control Systems Magazine*, 19(5):59–70, 1999.

[113] H. Lin and P. J. Antsaklis. Stability and stabilizability of switched linear systems: A survey of recent results. *IEEE Trans. on Automatic Control*, 54(2):308–322, 2008.

[114] A. S. Morse. *Control Using Logic-Based Switching*. Springer-Verlag, 1997.

[115] R. W. Brockette. *Asymptotic stability and feedback stabilization*. Birkhauser, 1997.

[116] R. A. Decarlo, M. S. Branicky, S. Pettersson, and B. Lennartson. Perspectives and results on the stability and stabilizability of hybrid systems. *Proceedings of the IEEE, Special issue on Hybrid Systems*, 88(7):1069–1082, 2000.

[117] D. Liberzon. *Switching in Systems and Control*. Birkhauser, 2003.

[118] A. S. Morse. Supervisory control of families of linear set-point controllers part i: exact matching. *IEEE Trans. on Automatic Control*, 41(10):1413–1431, 1996.

[119] J. Hespanha and A. S. Morse. Stability of switched systems with average dwell-time. In *Proc. of the IEEE Conference on Decision and Control*, pages 2655–2660, 1999.

[120] S. Boyd, L. E. Ghaoui, E. Feron, and V. Balakrishnan. *Linear Matrix Inequalities in System and Control Theory*. SIAM - Society for Industrial Applied Mathematics, 1994.

[121] J. Daafouz, R. Riedinger, and C. Iung. Stability analysis and control synthesis for switched systems: A switched lyapunov function approach. *IEEE Trans. on Automatic Control*, 47(11):1883–1887, 2002.

[122] L. Fang, H. Lin, and P. J. Antsaklis. Stabilization and performance analysis for a class of switched systems. In *Proc. of the IEEE Conference on Decision and Control*, pages 3265–3270, 2004.

[123] M. A. Wicks, P. Peleties, and R. A. DeCarlo. Construction of piecewise lyapunov functions for stabilizing switched systems. In *Proc. of the IEEE Conference on Decision and Control*, pages 3492–3497, 1994.

[124] M. A. Wicks, P. Peleties, and R. A. DeCarlo. Switched controller design for the quadratic stabilization of a pair of unstable linear systems. *European Journal of Control*, 4:140–147, 1998.

[125] D. Liberzon, J. P. Hespanha, and A. S. Morse. Stability of switched linear systems: A lie-algebraic condition. *System and Control Letters*, 37(3):117–122, 1999.

[126] Z. Sun. Stabilizability and insensitivity of switched linear systems. *IEEE Trans. on Automatic Control*, 49(7):1133–1137, 2004.

[127] X. Xu and P. J. Antsaklis. Stabilization of second-order lti switched systems. *International Journal of Control*, 73(14):1261–1279, 2000.

[128] K. R. Krishnan and I. Horowitz. Synthesis of a non-linear feedback system with significant plant-ignorance for predescribed system tolerances. *International Journal of Control*, 19(4):689–706, 1974.

[129] I. Horowitz and P. Rosenbaum. Nonlinear design for cost of feedback reduction in systems with large parameter uncertainty. *International Journal of Control*, 21(6):977–1001, 1975.

[130] Y. Chait and C. V. Hollot. On horowitzs contributions to reset control. *International Journal of Robust and Nonlinear Control*, 12(4):335–355, 2002.

[131] H. Hu, Y. Zheng, Y. Chait, and C.V. Hollot. On the zero-input stability of control systems with clegg integrators. In *Proc. of the IEEE American Control Conference*, pages 408–410, 1997.

[132] Q. Chen, Y. Chait, and C. Hollot. Analysis of reset control systems consisting of a fore and second order loop. *Journal of Dynamic Systems, Measurement, and Control*, 123(2):279–283, 2001.

[133] O. Beker, C.V. Hollot, Q. Chen, and Y. Chait. Stability of a reset control system under constant inputs. In *Proc. of the IEEE American Control Conference*, pages 3044–3045, 1999.

[134] Q. Chen, C.V. Hollot, and Y. Chait. Bibo stability of reset control systems. In *Proc. of the IEEE Conference on Decision and Control*, pages 251–256, 2000.

[135] O. Beker, C.V. Hollot, and Y. Chait. Stability of a MIMO reset control system under constant inputs. In *Proc. of the IEEE Conference on Decision and Control*, pages 2780–2781, 1999.

[136] O. Beker, C.V. Hollot, and Y. Chait. Forced oscillations in reset control systems. In *Proc. of the IEEE Conference on Decision and Control*, pages 4825–4826, 2000.

[137] O. Beker, C. Hollot, and Y. Chait. Stability of limit-cycles in reset control systems. In *Proc. of the IEEE American Control Conference*, pages 4681–4682, 2001.

[138] K. Gu, V. L. Kharitonov, and J. Chen. *Stability of Time-Delay Systems*. Birkhauser, 2003.

[139] A. Barreiro and A. Baños. Delay-dependent stability of reset systems. *Automatica*, 46(1):216–221, 2010.

[140] A. Baños and A. Barreiro. Delay-independent stability of reset systems. *IEEE Trans. on Automatic Control*, 52(2):341–346, 2009.

[141] L. Zaccarian, D. Nesic, and A. R. Teel. First order reset elements and the clegg integrator revisited. In *Proc. of the IEEE American Control Conference*, pages 563–568, 2005.

[142] T. Loquen, S. Tarbouriech, and C. Prieur. Stability analysis for reset systems with input saturation. In *Proc. of the IEEE Conference on Decision and Control*, pages 3272–3277, 2007.

[143] W. H. T. M. Aangenet, G. Witvoet, W. P. M. H. Heemels, M. J. G. van de Molengraft, and M. Steinbuch. An LMI-based $\mathcal{L}_2$ gain performance analysis for reset control systems. In *Proc. of the IEEE American Control Conference*, pages 2248–2253, 2008.

[144] Y. Guo, Y. Wang, L. Xie, and J. Zheng. Stability analysis and design of reset systems: Theory and an application. *Automatica*, 45(2):492–497, 2009.

[145] A. Baños, J. Carrasco, and A. Barreiro. Reset times dependent stability of reset systems. In *Proc. of the European Control Conference*, pages 4792–4798, 2007.

[146] A. Baños, J. Carrasco, and A. Barreiro. Reset times-dependent stability of reset system with unstable base system. In *Proc. of the IEEE Int. Symp. Ind. Electron.*, pages 163–168, 2007.

[147] O. Beker, C. Hollot, and Y. Chait. Plant with integrator: An example of reset control overcoming limitations of linear feedback. *IEEE Trans. on Automatic Control*, 46(11):1797–1799, 2001.

[148] A. Fernandez, A. Barreiro, A. Baños, and J. Carrasco. Reset control for passive teleoperation. In *Proc. of the 34th Annu. Conf. IEEE Ind. Electron. Soc.*, pages 2935–2940, 2008.

[149] A. Fernandez, A. Barreiro, A. Baños, and J. Carrasco. Reset control for passive bilateral teleoperation. *IEEE Trans. on Industrial Electronics*, 58(7):3037–3045, 2011.

[150] A. Vidal and A. Baños. Reset compensation for temperature control: Experimental application on heat exchangers. *Chemical Engineering Journal*, 159:170–181, 2010.

[151] A. Vidal, A. Baños, J. C. Moreno, and M. Berenguel. PI+CI compensation with variable reset: application on solar collector fields. In *Proc. of the 34th Annu. Conf. IEEE Ind. Electron. Soc.*, pages 321–326, 2008.

[152] A. Baños and A. Vidal. Definition and tuning of a PI+CI reset controller. In *Proc. of the European Control Conference*, pages 4792–4798, 2007.

[153] L. Zaccarian, D. Nesic, and A. R. Teel. Set-point stabilization of SISO linear systems using first order reset elements. In *Proc. of the IEEE American Control Conference*, pages 5808–5809, 2007.

[154] T. Loquen, S. Tarbouriech, and C. Prieur. Stability of reset control systems with nonzero reference. In *Proc. of the IEEE Conference on Decision and Control*, pages 3386–3391, 2008.

[155] C. Wood, A. Chmielewski, and D. Zoltan. Measurement of seebeck coefficient using a large thermal gradient. *Review of Scientific Instruments*, 59(6):951–954, 1988.

[156] R. L. Rosenbaum. A survey of some secondary thermometers for possible applications at very low temperatures. *Review of Scientific Instruments*, 41(1):37–40, 1970.

[157] F. Lacy. Evaluating the resistivity-temperature relationship for rtds and other conductors. *IEEE Sensors Journal*, 11(5):1208–1213, 2011.

[158] R. W. A. Scarr and R. A. Setterington. Thermistors, their theory, manufacture and application. *Proceedings of the IEE - Part B: Electronic and Communication Engineering*, 107(35):395–405, 1960.

[159] O. Saburi and K. Wakino. Processing techniques and applications of positive temperature coefficient thermistors. *IEEE Transactions on Component Parts*, 10(2):53–67, 1963.

[160] G. Moore. Acoustic thermometry. a sound way to measure temperature. *IEEE Electronics and Power*, 30(9):675–677, 1984.

[161] Y. J. Lee, B. T. Khuriyakub, and K. C. Saraswat. Temperature measurement in rapid thermal processing using acoustic techniques. *Review of Scientific Instruments*, 65(4):974–976, 1994.

[162] P. R. N. Childs, J. R. Greenwood, and C. A. Long. Review of temperature measurement. *Review of Scientific Instruments*, 71(8):974–976, 2000.

[163] M. Schneider, M. Thaler, U. Has, S. Stolz, and M. Zeraschi. Cooking appliance with temperature sensor. US6158329. 2000.

[164] U. Has, K. Horn, and M. Neuhauser. Sensor-controlled cooktop with a sensor unit arranged below the cooktop plate. US6225607. 2001.

[165] U. Has and F. Ziegler. Cooking place for use as electrical generator with e.g. electrical consumer, has infrared sensor arranged in direction of cookware that is arranged on hob, where infrared sensor is connected to control unit. DE102007058945. 2007.

[166] S. Koide and S. Hiejima. Temperature controlled induction heating and cooking apparatus. USP4617441. 1986.

[167] J. Kalkkuhl, T. A. Johansen, and J. Ldemann. Improved transient performance of nonlinear adaptive backstepping using estimator resetting based on multiple models. *IEEE Trans. on Automatic Control*, 47(1):136–140, 2002.

[168] W. H. T. M. Aangenet, G. Witvoet, W. P. M. H. Heemels, M. J. G. van de Molengraft, and M. Steinbuch. Performance analysis of reset control systems. *International Journal of Robust and Nonlinear Control*, 20(11):1213–1233, 2010.

[169] Y. Guo, Y. Wang, L. Xie, H. Li, and W. Gui. Optimal reset law design of reset control systems with application to HDD systems. In *Proc. of the IEEE Conference on Decision and Control*, pages 5287–5292, 2009.

[170] W. J. Rugh. *Linear System Theory*. Prentice Hall, 1996.

[171] M Trinh, P. S. Teh, and T. L. Fernando. Time-delay systems: Design of delay-free and low-order observers. *IEEE Trans. on Automatic Control*, 55(10):2434–2438, 2010.

[172] P. A. Ioannou and J. Sun. *Robust Adaptive Control*. Prentice Hall, 1996.

[173] A. Gauzzi, J. Le Cochec, G. Lamura, B. J. Jnsson, V. A. Gasparov, F. R. Ladan, B. Plaais, P. A. Probst, D. Pavuna, and J. Bok. Very high resolution measurements of the penetration depth of superconductors by a novel single coil inductance technique. *Review of Scientific Instruments*, 80(5):2147–2153, 2000.

[174] M. Enokizono and H. Tanabe. Numerical analysis of high frequency induction heating including temperature dependence of material characteristics. *IEEE Trans. on Magnetics*, 31(4):2438–2444, 1995.

[175] D.R. Lide. *CRC Handbook of chemistry and physics: a ready-reference book of chemical and physical data*. CRC Press, 2003.

[176] Z. Liu, F. L. L. Luo, and M. H. Rashid. QFT-based robust and precision motion control system for a high speed direct-drive XY table positioning mechanism. In *Proc. of the IEEE Industry Applications Society Annual Meeting*, volume 1, pages 293–300, 2003.

[177] C. Lucas, M. M. Shanehchi, P. Asadi, and P. M. Rad. A robust speed controller for switched reluctance motor with nonlinear QFT design approach. In *Proc. of the IEEE Industry Applications Society Annual Meeting*, volume 3, pages 1573–1577, 2000.

[178] O. Yaniv. *Quantitative Feedback Design of Linear and Nonlinear Control Systems*. Kluwer Academic Publishers, 1999.

[179] J. Acero, D. Navarro, L. A. Barragan, I. Garde, and J. M. Burdio. FPGA-based power measuring for induction heating appliances using sigma-delta A/D conversion. *IEEE Trans. on Industrial Electronics*, 54(4):1843–1852, 2007.

[180] D. Koenig. Unknown input proportional multiple-integral observer design for linear descriptor systems: application to state and fault estimation. *IEEE Trans. on Automatic Control*, 50(2):212–217, 2005.

[181] K. Ogata. *Modern Control Engineering*. Prentice Hall, 2009.

[182] O. Lucia, J. M. Burdio, I. Millan, J. Acero, and D. Puyal. Load-adaptive control algorithm of half-bridge series resonant inverter for domestic induction heating. *IEEE Trans. on Power Electronics*, 56(8):3106–3116, 2009.

[183] Y. A. Cengel. *Heat and mass transfer. A practical approach*. Mcgraw-Hill, 2007.

[184] F. P. Incropera and D. P. Dewitt. *Fundamentals of Heat and Mass Transfer*. John Wiley & Sons Inc, 2001.